# Study of solar neutrino energy spectrum above 4.5 MeV in Super-Kamiokande-I

Chikaori Mitsuda

Doctoral Program
in Fundamental Science and Energy Technology
Graduate School of Science and Technology
Niigata University

February 2004

# Acknowledgment

First of all, I would like to express my great appreciation to my adviser Prof. Kazumasa Miyano. He introduced me to experimental physics and gave me ample encouragement. Unfortunately, he retired in March, 2003. He was unable to see the completion of this thesis. Nevertheless, his great support and excellent advice are manifested in this thesis.

Next, I must thank Prof. N.Tamura and Prof. H.Miyata. They always encouraged and supported me. Especially, Prof. N.Tamura guided me to complete this thesis. He always encouraged me by his words. I got many significant words from him. Prof. H.Miyata gave me many questions and advises in the private discussions with him. His advises were useful to drive forward my study.

I acknowledge Prof. Y.Totsuka, previous spokesman of the Super-Kamiokande experiments and Prof. Y.Suzuki, current spokesman. They gave me the opportunity to participate in such an enthusiastic time of the study of the neutrino oscillation. Prof. Y.Suzuki, previous leader of solar neutrino analysis group, supported me to study solar neutrino analysis.

Special acknowledgement goes to Prof. M.Nakahata. I learned from him all of the experimental physics. He always gave me insightful words to aim at physical results. His serious attitude showed me the style of a true scientist. He gave me lots of advice on analysis and many opportunities to study experimental physics.

I am grateful to all members of the solar neutrino analysis group. Without their excellent works, this thesis would never have been completed. I would like to thank Prof. Y.Fukuda, Dr. Y.Takeuchi, and Dr. Y.Koshio, and Dr. K.Ishihara for their suggestions and advice about solar neutrino analysis.

I would like to thank all the Super-Kamiokande collaborators for help with the experiments. Especially, Prof. T.Kajita, Prof. Y.Itow, Prof. K.Kaneyuki, Prof. S.Moriyama, Dr. M.Miura, Dr. M.Shiozawa, and Dr. Y.Obayashi, the members in USA: Prof. B.Svoboda, Dr. M.Vagins, Dr. M.Smy, Dr. G.Guillian, Dr. M.Malek, and Mr. D.Liu, and the member in Korea: Dr. J.H.Yoo, I often had useful discussions with them about the experiment. Particular thanks goes to Mr. Y.Gando, Mr. M.Ishitsuka and all the SK graduate students. They always encouraged me.

I also would like to deeply thank all graduate students in the High Energy Physics group at Niigata university. The good conversation with members always refreshed me. I could make myself at ease in my laboratory. Especially, Mr. Allister & Maricel Sanchez gave me a great support for the English correction of this thesis. I want to thank him very much. I gratefully acknowledge my best friends to support me throughout my life.

Finally, I thank my parents and my sisters very much for supporting to continue studying physics. Without their help and understanding throughout my physicist life, I would never accomplish my study. This thesis is dedicated to them.

# Abstract

Super-Kamiokande-I (SK-I) was operated for solar neutrino observation from May 31, 1996 to July 15, 2001. The measurement of the solar neutrino energy spectrum above 4.5 MeV is presented in this thesis.

The deficit of solar neutrino flux compared to the predicted flux by solar standard model (SSM) has been discussed for over 30 years, and is called the "solar neutrino problem". The solution of the problem was recently concluded to be neutrino oscillation. For the oscillation mechanism, there are possible four solutions (SMA, LMA, LOW and VO). To solve the oscillation mechanism, a number of different fits to solar neutrino mixing and mass square difference as oscillation parameters were performed using 1496 days of solar neutrino data in SK-I. A global fit combining SK data with the solar neutrino interaction rates measured by Homestake, SNO, Gallex/GNO and SAGE prefers a single allowed area, the Large Mixing Angle solution, at the 98.9% confidence level (C.L.) [2].

In order to decide the oscillation parameter, we need more precise measurements and more statistics. Furthermore, we need to discuss an energy spectrum for the lower energy region so that we can examine the distortion of solar neutrino energy spectrum due to neutrino oscillation. In this thesis, the energy spectrum, including 4.5∼5.0 MeV energy range, is discussed. The analysis threshold in SK-I has been limited to 5.0 MeV be the radon background in SK detector. By the reduction of radon background and understanding the behavior of radon in SK, we succeeded in observing for the first time the solar neutrino flux of the 4.5∼5.0 MeV energy bin using 511 days (from September 17, 1999 to July 15, 2001) of solar neutrino data in SK-I. Using 511 days data set, the distortion of energy spectrum is discussed. Moreover, a number of different fits to solar neutrino mixing and mass square difference were performed. The results including 4.5∼5.0 MeV data favored LMA and LOW solution by 95% C.L. and gives strong credit to the various results gathered up to now from different aspect. Finally, it is suggested to lower the energy threshold in the future for energy spectrum analysis of the solar neutrino.

# Contents

# List of Figures

# List of Tables

# Chapter 1

# Introduction

Over 4.6 billion years, a huge amount of energy is produced in the Sun through nuclear fusion. As it shines, it radiates energy at a rate of $3.8\times10^{26}$ J per seconds. The generated energy is primarily released as photons, which slowly diffuse their way to the surface of the Sun over the course of $\sim 10^5$ years. We are usually looking at the surface information of the Sun, which is transmitted by photons, by traditional optical observations. However, all information these photons might contain regarding the nuclear reactions that created them is lost in the repeated interactions these photons undergo as they percolate out of the Sun. On the other hand, the neutrinos which are created in the core can provide direct information of the center of the Sun. Because, the neutrinos have very small reaction cross section, even in the highest density regions of the Sun. Solar neutrinos can pass through very dense matter that we never achieve on the earth and they travel the long distance of $1.5\times10^8$ km from the Sun to the earth. Thus, the study of solar neutrinos can serve as important test for theories of stellar evolution and structure.

The study of neutrinos is also interesting from particle physics perspective. The neutrino, denoted $\nu$, is a particle whose existence was proposed by W.Pauli in 1930 to explain the apparent energy deficit in $\beta$ decay. It was discovered in the 1950s by F.Reines and C.L.Cowan who observed neutrinos radiated from a reactor. The neutrino is a lepton which has a spin of (1/2), no electric charge, and possibly a very small mass. There are three types of neutrinos. Each type is associated with charged massive leptons, such as electrons, muons, and tau leptons. A neutrino interacts with other particles only via the weak interaction, so that the cross section of interaction is very small. Owing to this small interaction cross section, one can observe the solar core by the solar neutrino. Such characteristic conditions provide us an opportunity to investigate almost unknown properties of neutrinos such as their mass and magnetic moment.

The first solar neutrino detection experiment was carried out by R.Davis and his collaborators using neutrino capture by $^{37}$Cl. This experiment operated until 1998 and the latest results show that the observed flux is 33% of the expected flux. Successive observations have reported significant solar neutrino deficits, too. This is known as the solar neutrino problem. The most likely solution for the deficits is neutrino oscillation, which is a phenomenon where a neutrino changes its flavor while propagating. It has been assumed that neutrinos are massless, but the neutrino oscillation indicates that at least some flavors of neutrinos are massive.

Super-Kamiokande (SK) measures the energy of recoil electrons via elastic scattering of the solar neutrinos and electrons in real-time. Therefore, it has the ability to observe both a distortion of the energy spectrum and daytime-nighttime variation of the flux. In SK, solar neutrino data has been accumulated since 1996. The observed solar neutrino energy spectrum is unique in the world so far. The first detector operation of SK (SK-I) had been done from April 1, 1996 to July 15, 2001 [1].

Solar neutrino has been observed by four old different experiment and new two experiments: the Homestake experiment which uses Cl nuclei as a target [8], Kamiokande which used electrons in $H_2O$ molecules, and GALLEX [18]/GNO [13] and SAGE [22] which use Ga as a target, and as new experiments SK which uses same principle as Kamiokande, and SNO which use heavy water, $D_2O$ molecules [27]. All experiments have confirmed 'Solar neutrino problems' and solar neutrino oscillations between two active flavors. From most recent results, electron densities in the Sun and the earth can strongly affect the oscillation probability.

In this thesis, neutrino oscillations between two active neutrinos, $\nu_e$ and $\nu_{\mu,\tau}$, is examined by using recoil electron energy spectrum of solar neutrino. Then, the distortion of energy spectrum with 4.5∼5.0 MeV data for various solutions of neutrino oscillation is discussed using 511 days SK-I data selected from the full data of SK-I 1496 days. It also treated the technical aspect of background reduction to lower the energy threshold from 5.0 to 4.5 MeV.

A detailed description about the theoretical and experimental background is given in Chapter 2. SK and its current status with other solar neutrino experiments throughout the world is discussed in Chapter 3. In Chapter 4, the methods on how to reconstruct the vertex, direction, and energy of an event are presented. Calibrations of the SK detector are described in Chapter 5. The general data reduction in SK solar neutrino analysis is explained in Chapter 6. Up to Chapter 6, the outline of solar neutrino analysis in SK is being introduced.

From Chapter 7, the approach to observe low energy solar neutrino is described. Especially, the radon background reduction from the hardware aspect is explained in Chapter 7. As the main topic of this thesis, the tight data reduction to analyze 4.5∼5.0 MeV data is presented in Chapter 8. Chapter 9 gives the results of 511 days data set and the observed solar neutrino flux in the 4.5∼5.0 MeV energy region. The distortion of solar neutrino energy spectrum above 4.5 MeV is discussed in Chapter 10. Chapter 11 presents the conclusions of this thesis and future prospects to lower the energy threshold in the future of SK.

# Chapter 2

# The Standard Solar Model and Solar Neutrino Observation

In this chapter, the theory and other solar neutrino experiments are explained. As the theory, an account of the Standard Solar Model (SSM), and the Mikheyev, Smirno, Wolfenstein (MSW) effect are given. The SSM describes stellar evolution and predicts the flux of solar neutrinos. The MSW effect, which describes the propagations of massive neutrinos through matter, opens a pioneering way to solve the contradiction between the SSM prediction and observed data. Deficits in the observed solar neutrino flux, which is widely known as the solar neutrino problem, are also explained. Lastly, as the most likely solution of the solar neutrino problem, the neutrino oscillation is explained.

## 2.1 The Sun and the Standard Solar Model

The Sun is an astronomical laboratory. Because of its proximity to the Earth, we are able to obtain information about the Sun that is not accessible for other stars. We can measure with precision solar parameters that are known to only one or two significant figures for any other star. For example, we can determine precise values for the solar mass, radius, geometric shape, photon spectrum, total luminosity, surface chemical composition, and age. They are listed in Table 2.1

| Parameter | Value |
|---|---:|
| Photon luminosity | $3.86\times10^{33}$ erg s$^{-1}$ |
| Neutrino luminosity | $0.023L_\odot$ |
| Mass($M_\odot$) | $1.99\times10^{33}$ g |
| Radius($R_\odot$) | $6.96\times10^{10}$ cm |
| Effective surface temperature | $5.78\times10^{3}$ K |
| Age | $4.57\times10^{9}$ yr |
| Initial helium abundance by mass | 0.27 |
| Initial heavy element abundance by mass | 0.020 |
| Depth convictive zone | $0.26R_\odot$ |
| Central density | 148 g cm $^{-3}$ |
| Central temperature | $15.6\times10^{6}$ K |
| Central hydrogen abundance by mass | 0.34 |

Table 2.1: Lists some of the main physical characteristics of the Sun[Dicke, Kuhn, and Libbrecht (1985) [28]]

In order to understand the solar neutrino problem, one needs to know the main ingredients of the theory of stellar evolution that are used in the construction of the solar models. The Sun is assume to be spherical and to have evolved quasi-statically (from one approximately equilibrium configuration to another approximately equilibrium configuration) for a period of about $5 \times 10^9$ yr. Evolution is manifested by the loss of photons from the surface of the star, which in turn is balanced by the burning of protons into $\alpha$-particles in the core of the Sun. It produces an intense flux of electron neutrinos as a consequence of nuclear fusion reactions whose combined effect is

$$4\mathrm{p} \rightarrow {}^{4}\mathrm{He} + 2\mathrm{e}^{+} + 2\nu_{\mathrm{e}}. \tag{2.1}$$

Positrons annihilate with electrons. Therefore, when considering the solar thermal energy generation, a relevant expression is

$$4\mathrm{p} + 2\mathrm{e}^{-} \rightarrow {}^{4}\mathrm{He} + 2\nu_{\mathrm{e}} + 26.73\ \mathrm{MeV} - E_{\nu}, \tag{2.2}$$

where $E_\nu$ represents the energy taken away by neutrinos, with an average value being $E_\nu \sim 0.6$ MeV. The thermal energy of 26.73 MeV is released for every four protons burned. Each conversion of four protons to an $\alpha$-particle is known as a termination of the chain of energy-generating reactions that accomplishes the nuclear fusion. The thermal energy that is supplied by nuclear fusion ultimately emerges from the surface of the Sun as sunlight. Energy is transported in the deep solar interior mainly by photons, which means that the opacity of matter to radiation is important. The pressure that supports the Sun is provided largely by the thermal motions of the electrons and ions.

Some of the principal approximations used in constructing standard solar models deserve special emphasis because of their fundamental roles in the calculations. These approximations have been investigated carefully for possible sources of departure from the standard scenario.

1. Hydrostatic equilibrium
   The Sun is assumed to be in hydrostatic equilibrium, that is, the radiative and particle pressures of the model exactly balance gravity.
2. Energy transport by photons or by convective motions
   In the deep interior, where neutrinos are produced, the energy transport is primarily by photon diffusion.
3. Energy generation by nuclear reactions
   The primary energy source for the radiated photons and neutrinos is nuclear fusion, although the small effects of gravitational contraction (or expansion) are also included.
4. Abundance changes caused solely by nuclear reactions
   The initial solar interior is presumed to have been chemically homogeneous. In region of the model that are stable to matter convection, changes into the local abundances of individual isotopes occur only by nuclear reactions.

A standard solar model is the end product of a sequence of models. A standard solar model is based on the standard theory of stellar evolution. A variety of input information is needed in the evolutionary calculations. In this thesis, the adopted SSM is a model developed by Bahcall, Basu, and Pinsonneault. It is called "BP2000"($\Phi_{\nu_e} = 5.05 \times 10^6 \cdot \mathrm{cm}^{-2} \cdot \mathrm{s}^{-1}$) from now on. The most elaborate SSM, BP2000 is constructed with the best available physics and input data. Though they used no helioseismological constraints in defining the SSM, the calculated sound speed as a function of the solar radius shows an excellent agreement with helioseismologically determined sound speed to precision of 0.1% rms throughout essentially the entire Sun. This greatly strengthens confidence in the solar model. The BP2000 prediction for the flux is shown in Table 2.2. Contributions to the event rates in chlorine and gallium solar neutrino experiments from each neutrino-producing reaction are listed in Table 2.3.

By "the standard solar model," we mean the solar model that is constructed with the best available physics and input data. All of the solar models we consider, standard or "deviant" models, are required to fit the observed luminosity and radius of the Sun at the present epoch, as well as the observed heavy-element-to-hydrogen ratio at the surface of the Sun. No helioseismological constraints are used in defining the standard model. Naturally, standard models improve with time, as the input data are made more accurate, the calculation techniques become faster and more precise, and the physical description is more detailed.

Figure 2.1 shows the procedure of Solar Standard Model which have been changed by precise physical data. The figure also shows the experimental results using Chlorine as a target of the solar neutrino. Even if the solar standard model was slightly changed, there is still a deficit of solar neutrinos between the predicted flux and the observed flux.

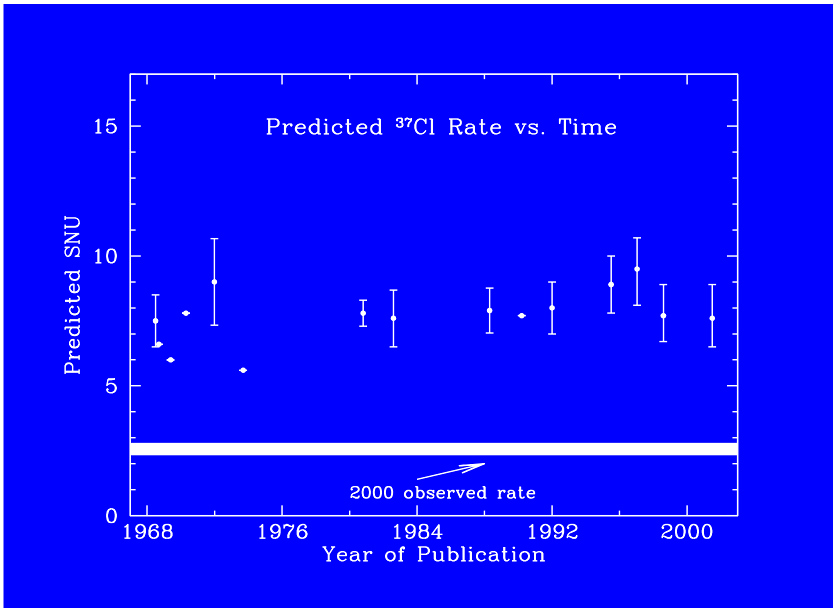

Figure 2.1: The procedure of Solar Standard Model (http://www.sns.ias.edu/~jnb/).

The SSM predicted $^8$B solar neutrino flux is proportional to the low-energy cross section factor $S_{17}(0)$ for the $^7$Be(p, $\gamma$)$^8$B reaction. The BP2000 [29] and Turck-Chieze *et al.* . [30] models adopted $S_{17}(0) = 19^{+4}_{-2}$ eV·b. Inspired by the recent precise measurement of the low-energy cross section for the $^7$Be(p, $\gamma$)$^8$B reaction by Junghans *et al.*. [31], Bahcall *et all.* [32] calculated the SSM predictions using $S_{17}(0) = 22.3 \pm 0.9$ eV·b. The results are: the $^8$B solar neutrino flux of $5.931.00^{+0.14}_{-0.15} \times 10^6$cm$^{-2}$s$^{-1}$, the chlorine capture rate of $8.59^{+1.1}_{-1.2}$SNU, and gallium capture rate of $130^{+9}_{-7}$SNU.

The standard solar model of BP2000 is constructed with the OPAL equation of state (Rogers Swenson, & Iglesias 1996 [33]) and OPAL opacities(Iglesias & Rogers 1996), which are supplemented by the low temperature opacities of Alexander & Ferguson (1994). The model was calculated using the usual mixing length formalism to determine the convective flux.

The principal change in the input data is the use of the Grevesse & Sauval (1998) improved standard solar composition in the OPAL opacities [33] and in the calculation of the nuclear reaction rates. The refinements in this composition redetermination come from many different sources, including the use of more accurate atomic transition probabilities in interpreting solar spectra. The OPAL equation of state and the Alexander and Ferguson opacities are not yet available with the composition recommended by Grevesse & Sauval(1998).

A present-epoch solar luminosity is estimated 1369 Wm$^2$[$4\pi \times$ AU$^2$] for all the models.

| Reaction | Abbr. | Flux($\mathrm{cm}^{-2}\ \mathrm{s}^{-1}$) |
|---|---|---|
|  | pp chain |  |
| $\mathrm{pp} \rightarrow \mathrm{d}\ \mathrm{e}^{+}\nu$ | *pp* | $5.95(1.00^{+0.01}_{-0.01})\times10^{10}$ |
| $\mathrm{pe}^{-}\mathrm{p} \rightarrow \mathrm{d}\ \nu$ | *pep* | $1.40(1.00^{+0.015}_{-0.015})\times10^{8}$ |
| $^{3}\mathrm{He}\ \mathrm{p} \rightarrow\ ^{4}\mathrm{He}\ \mathrm{e}^{+}\nu$ | *hep* | $9.3\times10^{3}$ |
| $^{7}\mathrm{Be}\ \mathrm{e}^{-} \rightarrow\ ^{7}\mathrm{Li}\ \nu + (\gamma)$ | $^{7}$Be | $4.77(1.00^{+0.10}_{-0.10})\times10^{9}$ |
| $^{8}\mathrm{B}\ \mathrm{e}^{-} \rightarrow\ ^{8}\mathrm{Be}\ \mathrm{e}^{+}\nu$ | $^{8}$B | $5.05(1.00^{+0.20}_{-0.16})\times10^{6}$ |
|  | CNO cycle |  |
| $^{13}\mathrm{N} \rightarrow\ ^{13}\mathrm{Ce}^{+}\nu$ | $^{13}$N | $5.48(1.00^{+0.21}_{-0.17})\times10^{8}$ |
| $^{15}\mathrm{O} \rightarrow\ ^{15}\mathrm{Ne}^{+}\nu$ | $^{15}$O | $4.80(1.00^{+0.25}_{-0.19})\times10^{8}$ |
| $^{13}\mathrm{F} \rightarrow\ ^{17}\mathrm{Oe}^{+}\nu$ | $^{17}$F | $5.63(1.00^{+0.25}_{-0.25})\times10^{6}$ |

Table 2.2: Neutrino-producing reactions in the Sun (the first column) and their abbreviations(second column) and neutrino fluxes(third column). [Bahcall, Basu, and Pinsonneault (2000) [29]]

For the neutrino fluxes, more recent best estimate value used a solar luminosity of 1366.2 W $\mathrm{m}^2[4\pi \times \mathrm{AU}^2] = 3.842\times10^{33}\mathrm{erg}\cdot\mathrm{s}^{-1}$(Frohlich & Lean 1998 [34]; Crommelynck *et al.* 1995 [35]). The difference between these two values for the luminosity is 0.2%, For the calculations of uncertainties in neutrino flux productions, we assume a $1\sigma$ uncertainty of 0.4%. The uncertainty in the predicted solar neutrino fluxes due to the luminosity is an order of magnitude smaller than the total uncertainty in predicting the neutrino fluxes.

The nuclear reaction rates were evaluated with the subroutine exportenergy.f(Bahcall & Pinsonneault 1992) [36], using the reaction data in Adelberger *et al.* (1998) [37] and with electron and ion weak screening as indicated by recent calculations of Gruzinov & Bahcall (1998 [38], Salpeter 1954 [39]). The model incorporates helium and heavy-element diffusion using the exportable diffusion subroutine of Thoul(Thoul, Bahcall, & Loeb 1994 [40]; Bahcall & Pinsonneault 1995 [41]). An independent and detailed treatment of diffusion by Turcotte *et al.* (1998 [42]) yields results for the impact of diffusion on the computed solar quantities that are very similar to those obtained here.

For the standard model, the evolutionary calculations were started at the main-sequence stage. The model has a radius of 695.98 Mm. The ratio of heavy elements to hydrogen(Z/X) at the surface of the model is 0.0230, which is chosen to be consistent with the value obtained by Grevesse & Suaval(1998) [43]. A Krishna-Swamy $T-\tau$ relation ship for the atmosphere was used. The adopted solar luminosity is $\mathrm{L}_{\odot} = 3.844\times10^{33}\mathrm{erg}\cdot\mathrm{s}^{-1}$ and the solar age is $4.57\times10^{9}$ yr (Bahcall & Pinsonneault 1995 [44]).

The uncertainties in the neutrino fluxes and in the experimental event rates were calculated by including the published errors in all experimental quantities and by taking account of the correlated influence of different input parameters using the results of detailed solar model calculations. The procedure for calculating the uncertainties has been developed over the past three decades and is described in detail in Bahcall(1989, 1992, 1995, BBp98, Bahcall & Pinsonneault). The uncertainties in the nuclear fusion cross sections (except for *hep* $\nu$) were taken from Adelberger et all.(1998) [37], the neutrino cross sections and their uncertainties are from Bahcall(1994 [45],1997 [46]) and Bacall *et al.* (1996) [47], the luminosity and age uncertainties were adopted from Bahcall & Pinsonneault(1995) [48], the $1\sigma$ fractional uncertainty in diffusion rate was taken to be 1.5%(Thoul *et al.* 1994 [49]), and the opacity uncertainty was determined by comparing the results of fluxes computed using the model Livermore opacities(Bahcall & Pinsonneault 1992 [50]). The adopted 1 $\sigma$ uncertainty in the heavy-element abundance of

$$\sigma(Z/X) = \pm0.061(Z/X). \tag{2.3}$$

| Source, Abbr. | Chlorine(SNU) | Gallium(SNU) | SK |
|---|---|---|---|
| | pp chain | | |
| *pp* | 0.0 | 69.7 | 0.0 |
| *pep* | 0.2 | 2.8 | 0.0 |
| *hep* | 0.04 | 0.1 | 0.0 |
| $^7$Be | 1.15 | 34.2 | 0.001 |
| $^8$B | 5.76 | 12.1 | 0.999 |
| | CNO cycle | | |
| $^{13}$N | 0.09 | 3.4 | 0.0 |
| $^{15}$O | 0.33 | 5.5 | 0.0 |
| $^{17}$F | 0.0 | 0.1 | 0.0 |
| Total | $7.6^{+1.3}_{-1.1}$ | $128^{+9}_{-7}$ | 1.0 |

Table 2.3: Solar neutrino detection rates in chlorine and gallium for each flux measurements experiments. For SK, the ratio to the total flux is also shown. [Bahcall, Basu, and Pinsonneault (BP2000) [29]]

This uncertainty spans the range of values recommended by Grevesse(1984), Grevesse & Noels(1993), and Grevesse & Sauval (1998) [51] [52] [53]. In support of the larger uncertainty used in BP2000, the difference between the Grevesse & Noels (1993) values of Z/X = 0.0230 is 1 $\sigma$ according to above equation. The calculated errors are asymmetric in many cases because these asymmetries in the uncertainties in neutrino fluxes and experimental event rates result from asymmetries in the uncertainties of some of the input parameters, for example, the important *pp*, $^7$Be + p, $^{14}$N + p, fusion reactions and the effect of excited states on neutrino absorption cross sections.

## 2.2 Nuclear energy generation in the Sun and the solar neutrino fluxes

The Sun shines by converting protons into $\alpha$-particles. About 600 million tons of hydrogen are burned every second to supply the solar luminosity. The SSM predicts that over 98% of solar energy is produced from the pp-chain reaction which is the conversion of four protons into $^4$He.

$$4\mathrm{p} \rightarrow\ ^4\mathrm{He}^* + 2\mathrm{e}^+ + 2\nu_\mathrm{e} \tag{2.4}$$

The energy produced per pp-chain reaction is 26.731 MeV. Figure 2.4 shows the reaction tree of the pp-chain.

There is another reaction series called the CNO(carbon-nitrogen-oxygen) cycle. Figure 2.5 shows the schematic overview of the CNO cycle.

The reaction rate (number of reactions per unit volume per unit time) between two nuclear species is described by the formula

$$R_{12} = \frac{n(1)n(2)}{(1+\delta_{12})}\langle\sigma v\rangle_{12}, \tag{2.5}$$

where $n(1), n(2)$ are the number densities of particles of type 1 and 2, $\sigma$ is their interaction cross section, and $v$ the magnitude of their relative velocity.

As described above, the temperature in the core is about 1.5×10$^7$ K. Thus, the protons in the core do not have enough energy to overcome the Coulomb repulsion. The solar nuclear fission occurs only via the quantum mechanical tunneling effect.

The energy dependence of the fusion cross sections can be represented most simply by a formula, in which the geometrical factor, the De Broglie wavelength squared, and the barrier penetration factor have both been removed, leaving a function $S(E)$ that varies smoothly in the absence of resonances. The conventional definition is:

$$\sigma(E) \equiv \frac{S(E)}{E} \exp(-2\pi\eta), \tag{2.6}$$

where

$$\eta(E) = Z_1 Z_2 \frac{e^2}{\hbar v}. \tag{2.7}$$

$$\eta(E) = \frac{Z_1 Z_2 e^2}{h} \sqrt{\frac{\mu}{2E}}. \tag{2.8}$$

$$\mu = \frac{A_1 A_2}{A_1 + A_2}. \tag{2.9}$$

where $E$ is the center-of-mass energy, $\eta$ is the Sommerfeld parameter, and $Z_1, Z_2$ are the charge numbers of the nuclei, and $\mu$ is the reduced mass of the system, and $A_1, A_2$ are the masses of the nuclei.

The quantity $\exp(-2\pi\eta)$ is known appropriately as the Gamow penetration factor. The value of $S(E)$ at the zero energy is known as the cross section factor, $S_0$.

In the condition i which the WKB approximation is valid. $S(E)$ is continuous and varies slowly. Then $S(E)$ can be expanded as follows:

$$S(E) = S(0) + S'(0)E + \frac{1}{2}S''(0)E^2. \tag{2.10}$$

The $S(0)$ for the solar nuclear fusion reactions are summarized in reference paper [76].

In CNO cycle, high temperature ($T_c > 10^8$ K) is required. So, in the current core temperature ($T_c \sim 10^7$ K), the contribution to total energy generation is suppressed to 2%.

The origins of predicted solar neutrino fluxes are shown in figure 2.2.

Neutrino fluxes from continuum sources (such as pp and $^8$B) are given in units of counts per cm$^2$ per second. The pp chain is responsible for more than 98% of energy generation in the standard solar model. Neutrino produced in the carbon-nitrogen-oxygen CNO chain are not important energetically and are difficult to detect experimentally. The arrows at the top of the figure indicate the energy thresholds for the ongoing neutrino experiments.

The probability of converting an electron-type neutrino to a muon or tau neutrino in the Sun depends on the profile of the electron number density as a function of solar radius. For particular values of the electron density, neutrino energy, and neutrino mass, neutrinos can be resonantly converted from one type of neutrino to another. The Mikheyev-Smirnov resonance occurs if the electron density at a radius r satisfies

$$\frac{\mathrm{n_{e,res}(r)}}{\mathrm{N_A}} \approx 66 \cos 2\theta_\mathrm{v} \left(\frac{\mid \Delta \mathrm{m}^2 \mid}{10^{-4}\mathrm{eV}}\right)\left(\frac{10\mathrm{MeV}}{\mathrm{E}}\right), \tag{2.11}$$

where $n_e$ is the electron number of density measured in cm$^{-3}$, $N_A$ is Avogadro's number, $\theta_v$ is the neutrino mixing angle in vacuum, $\mid \Delta m^2 \mid$ is the absolute value of the difference in neutrino masses between two species that are mixing by neutrino oscillations, and $E$ is the neutrino energy.

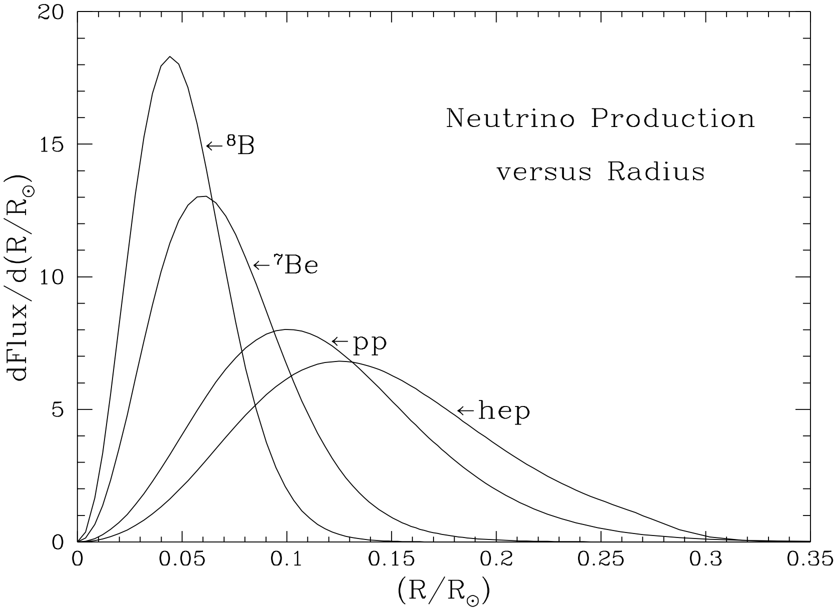

Figure 2.2: This graph shows where in the Sun the different solar neutrino fluxes originate (http://www.sns.ias.edu/j̃nb/).

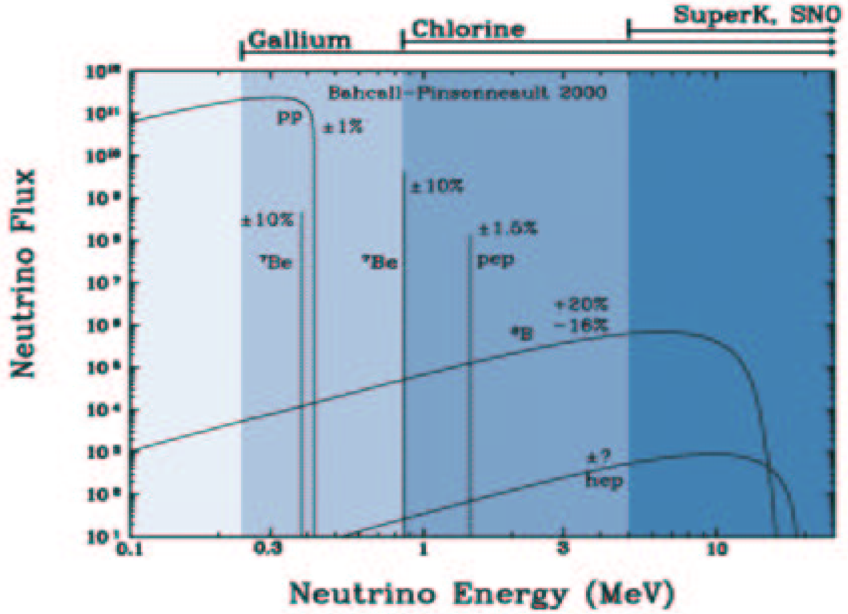

Figure 2.3: The solar neutrino energy spectrum(http://www.sns.ias.edu/j̃nb/).

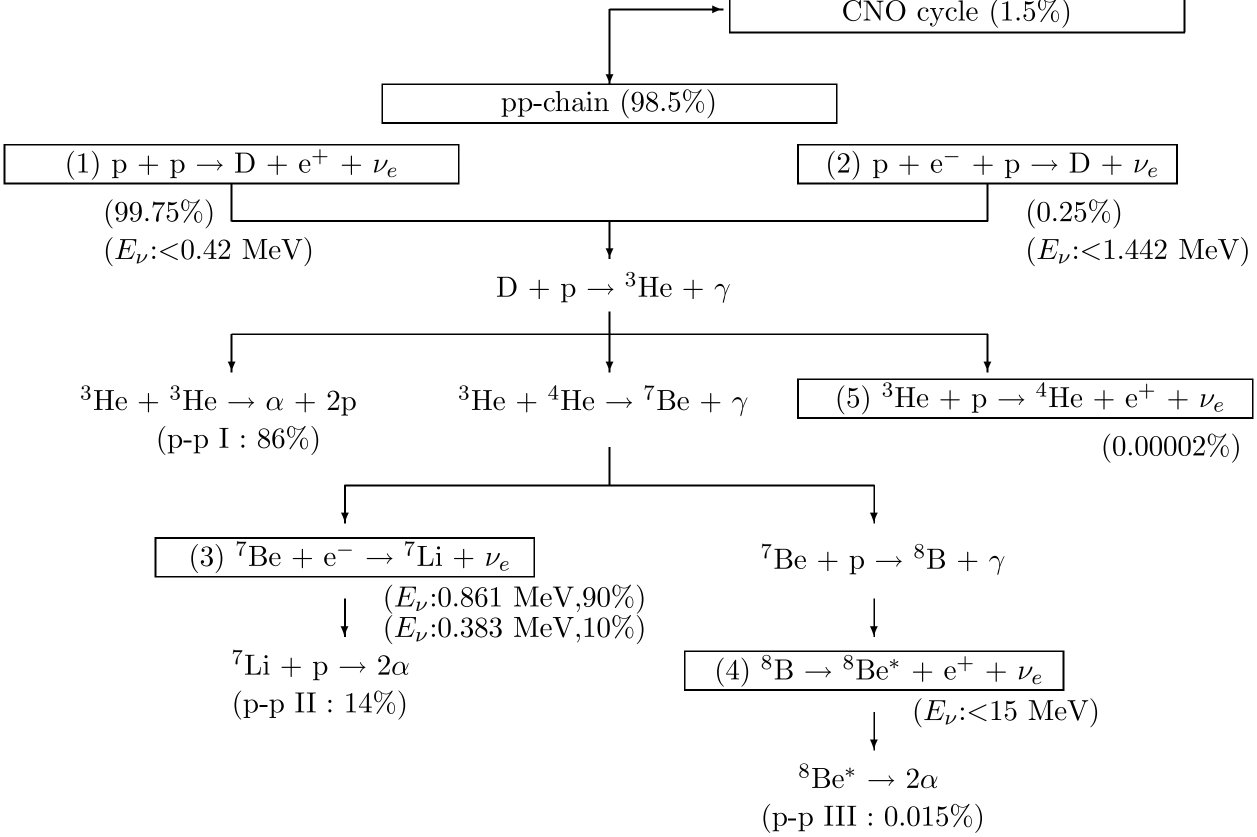

Figure 2.4: The pp-chain.

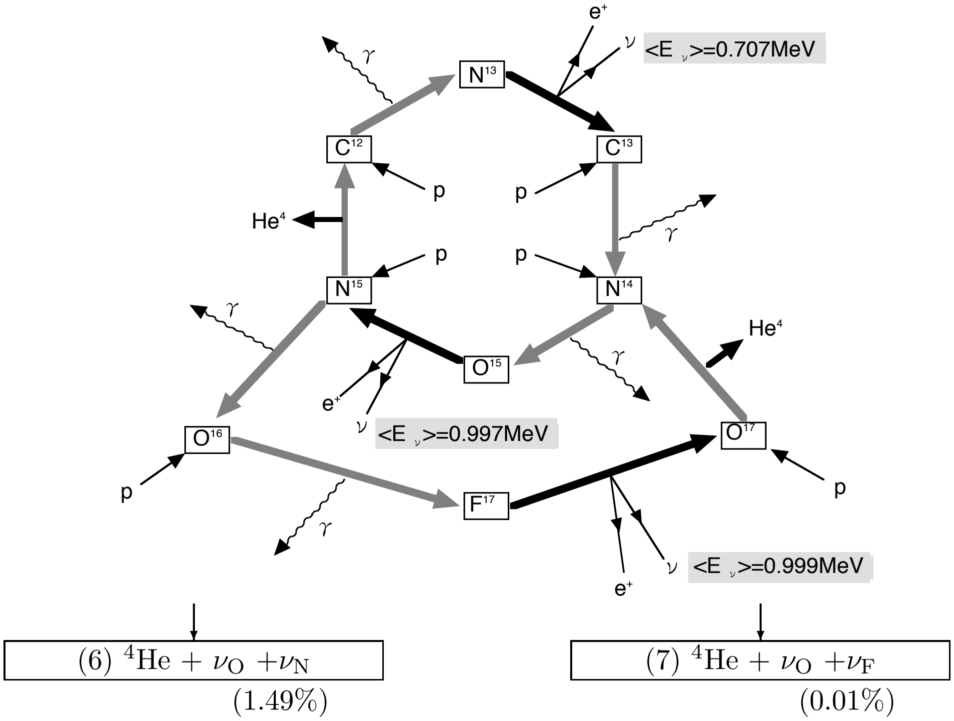

Figure 2.5: The CNO cycle.

Figure 2.6 give the electron number density as a function of solar radius for the standard model (BP2000). For the so-called LOW MSW solutions and for all MSW solutions with $\theta_v \sim \pi/4$, the resonance radius falls in the outer part of the Sun.

There are no accurate values for the electron density in the outer parts of the Sun, $r \geq 0.8 R_\odot$. The straight line in the figure is an approximations to the electron number density in the standard solar model of Bahcall & Ulrich (1998) [54].

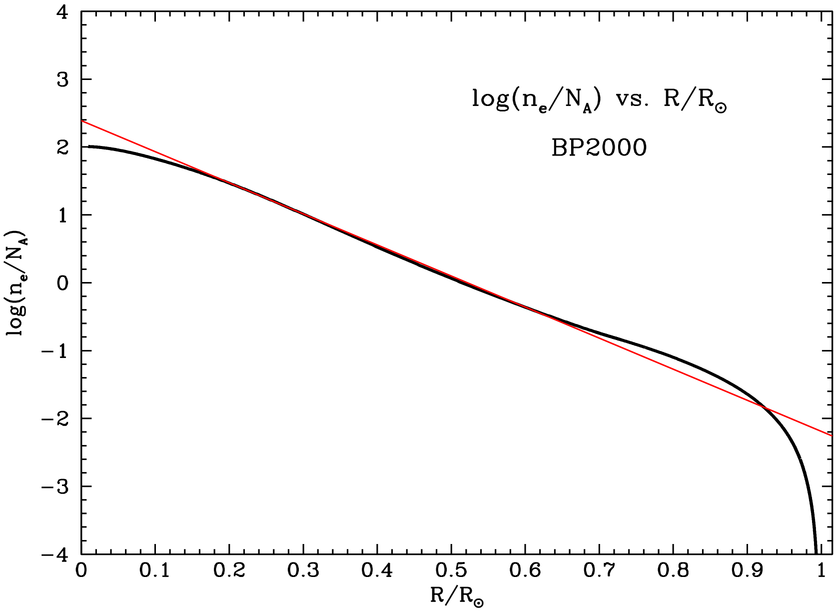

Figure 2.6: Electron number density, $n_e$, vs. solar radius for the standard solar model (BP2000). The straight-line fit shown is an approximation given by Bahcall (1989).(http://www.sns.ias.edu/˜jnb/)

## 2.3 The $^8$B neutrino flux

As shown in Table 2.2, a $^8$B neutrino is produced via the $\beta^+$ decay of $^8$B. The energy levels of $^8$B decay are shown in figure 2.7. The energy spectrum of $^8$B neutrinos is obtained by measurements of the $^8$B $\beta$ decay spectrum and the $\alpha$ spectrum from the subsequent $^8$Be decay. The $^8$B $\beta$ decay spectrum with the momentum above 8 MeV/c is measured using a $\beta$-spectrometer [55]. The error of the absolute momentum calibration is estimated using the $^{12}$B $\beta$ spectrum shape ($Q_{\beta^-} = 13.4$ MeV) and is obtained to be ±0.090 MeV. The delayed $\alpha$ spectrum of $^8$Be is measured by several experimental groups [56] [57] [58]. These $\alpha$ decay data are compared and used to fit the $\beta$ decay data. The best-fit $\alpha$ spectrum and its uncertainty are obtained from this over constrained comparison. The $^8$B neutrino spectrum is determined using the best-fit $\alpha$ spectrum. This is shown in figure 2.8. The spectra allowed by $\pm 3\sigma$ uncertainties are also shown on the same figure. The uncertainty of the $^8$B neutrino energy spectrum is caused by the experimental uncertainty of the $\alpha$ spectrum measurement. A more detailed explanation is given in Ref. [59]. Details about $^7$Be and *hep* neutrino fluxes are given in appendix A.

## 2.4 Solar neutrino experiments

A pioneering solar neutrino experiment by Davis and collaborators using $^{37}$Cl started in the late 1960's. Since then, chlorine and gallium radiochemical experiments and water Čerenkov experiments with light and heavy water targets have made successful solar neutrino observations.

Observation of solar neutrinos directly addresses the theory of stellar structure and evolution, which is the basis of the standard solar model (SSM). The Sun, as a well-defined neutrino source,

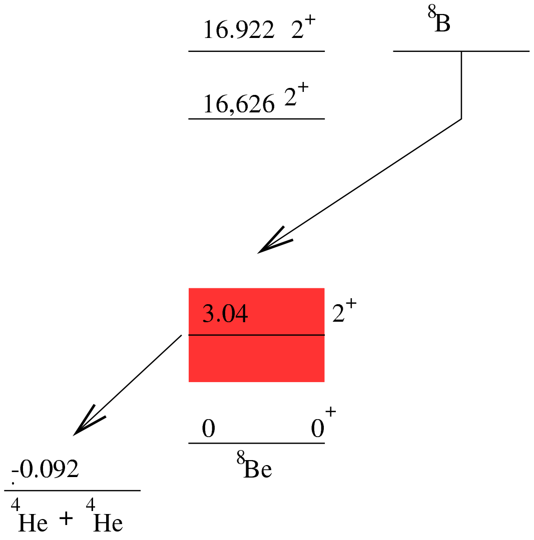

Figure 2.7: Energy levels in the $^8\mathrm{B}\beta^+$ $^8\mathrm{Be}(2\alpha)$ decay chain. The gray zone shows the $2^+$ states of $^8\mathrm{Be}^*$.

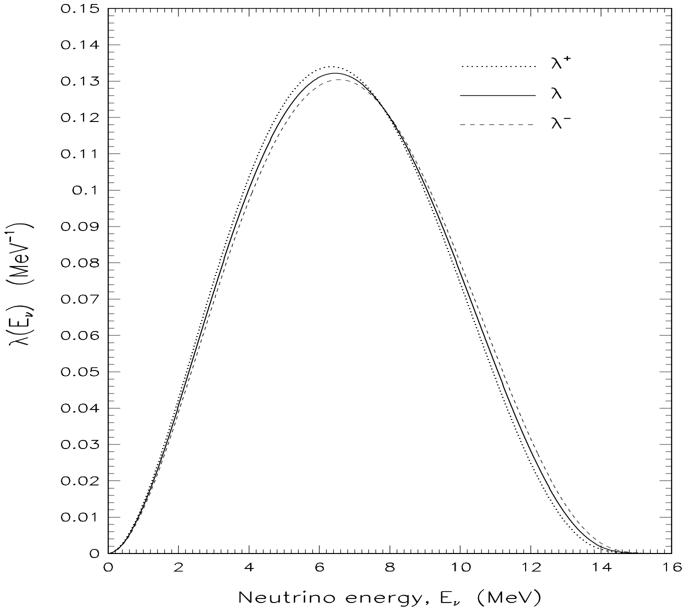

Figure 2.8: The best-estimate (standard) $^8$B neutrino spectrum $\lambda$, together with the spectra $\sigma^\pm$ allowed by the maximum $\pm 3\sigma$ theoretical and experimental uncertainties. (http://www.sns.ias.edu/~jnb/)

also provides extremely important opportunities to investigate nontrivial neutrino properties such as nonzero mass and mixing, because of the wide range of matter density and the very long distance from the Sun to the Earth.

From the very beginning of the solar-neutrino observation, it was recognized that the observed flux was significantly smaller than the SSM prediction provided nothing happens to the electron neutrinos after they are created in the solar interior. This deficit has been called "The solar neutrino problem". The initial result from Sudbury Neutrino Observatory (SNO) on the solar neutrino flux measured via charged-current reaction $\nu_\mathrm{e} + \mathrm{d} \rightarrow \mathrm{e}^- + \mathrm{p} + \mathrm{p}$, combined with Super-Kmioknade's high statistics flux measurement via $\nu_\mathrm{e} + \mathrm{e}$ elastic scattering, provided direct evidence for flavor conversion of solar neutrinos. The most probable explanation is neutrino oscillation which can also solve the solar neutrino problem. Figure 2.9 shows the ratio between the predicted solar neutrino fluxes for each target and the observed solar neutrino fluxes in each experiment. The uncertainties for the observed solar neutrino fluxes are given for each experiment. The errors for the predicted solar fluxes for each target is due to the uncertainties of the SSM (BP2000). In Table 2.4, the detailed results for total solar neutrino fluxes are given for each experiment of solar neutrino observation.

| Experiment | $^{37}\mathrm{Cl} \rightarrow {}^{37}\mathrm{Ar}$ SNU | $^{71}\mathrm{Ga} \rightarrow {}^{71}\mathrm{Ge}$ SNU | $^{8}\mathrm{B}\nu$ flux $10^6\mathrm{cm}^{-2}\mathrm{s}^{-1}$ |
|---|---|---|---|
| Homestake<br>(CLEVELAND 98 [11]) | $2.56 \pm 0.16 \pm 0.16$ | - | - |
| GALLEX<br>(HAMPEL 99 [14]) | - | $77.5 \pm 6.2^{+4.3}_{-4.7}$ | - |
| GNO<br>(ALTMANN 00 [12]) | - | $65.8^{+10.2}_{-9.6}{}^{+4.3}_{-4.7}$ | - |
| SAGE<br>(ABDURASHI 99B [21]) | - | $67.2^{+7.2}_{-7.0}{}^{+3.5}_{-3.0}$ | - |
| Kamiokande<br>(FUKUDA 96 [3]) (elastic-scattering) | - | - | $2.80 \pm 0.19 \pm 0.33$ |
| Super-Kamiokande-I<br>(FUKUDA 01 [6])(elastic-scattering) | - | - | $2.32 \pm 0.03^{+0.08}_{-0.07}$ |
| SNO<br>(AHMAD 02 [26]) (charged-current) | - | - | $1.76^{+0.06}_{-0.05} \pm 0.09$ |
| SNO<br>(AHMAD 02 [26]) (elastic-scattering) | - | - | $2.39^{+0.24}_{-0.23} \pm 0.12$ |
| SNO<br>(AHMAD 02 [26]) (neutral-current) | - | - | $5.09^{+0.44}_{-0.43}{}^{+0.46}_{-0.43}$ |
| SSM (BP2000 [29]) | $7.6^{+1.3}_{-1.1}$ | $128^{+9}_{-7}$ | $5.05(1.00^{+0.20}_{-0.16})$ |
| SSM (TURCK-CHIEZE 01 [30]) | $7.44 \pm 0.96$ | $128 \pm 8.6$ | $4.95 \pm 0.72$ |

Table 2.4: Recent results from the seven solar neutrino experiments and a comparison with standard solar model predictions. [K. Hagiwara *et al.* (particle Data Group), Phys. Rev. D 66, 010001 (2002) (URL: http://pdg.lbl.gov)]

### 2.4.1 Radiochemical Experiments

Radiochemical experiments exploit electron neutrino absorption on nuclei followed by their decay through orbital electron capture. The produced Auger electrons are counted. The Homestake chlorine experiment in USA uses the reaction:

$$^{37}\mathrm{Cl}+\nu_{\mathrm{e}}\rightarrow\ ^{37}\mathrm{Ar}+\mathrm{e}^{-}. \tag{2.12}$$

Three gallium experiments (GALLEX and GNO at Gran Sasso in Italy and SAGE at Baksan in Russia) use the reaction

$$^{71}\mathrm{Ga}+\nu_{\mathrm{e}}\rightarrow\ ^{71}\mathrm{Ge}+\mathrm{e}^{-}. \tag{2.13}$$

The produced $^{37}$Ar and $^{71}$Ge atoms are both radioactive, with half lives ($\tau_{1/2}$) of 34.8 days and 11.43 days, respectively. After an exposure of the detector for two to three times $\tau_{1/2}$, the reaction products are chemically extracted and introduced into a low-background proportional counter, and are counted for a sufficiently long period to determine the exponentially decaying signal and a constant background.

### Homestake

The first solar neutrino observation was carried out by R. Davis and his Brookhaven collaborators in 1968 [9]. Their detector consisted of a horizontal steel tank, 6.1 m in diameter and 14.6 m long, containing 615 m$^3$ of $C_2Cl_4$. It was located in the Homestake Gold Mine in Lead, South Dakota, United States. The average overburden for the detector was 4200± 100 meter water equivalent (m.w.e).

In order to detect solar neutrinos, they used the inverse $\beta$ reaction $^{37}\mathrm{Cl}(\nu_{\mathrm{e}},\mathrm{e}^{-})^{37}\mathrm{Ar}$. At the end of each exposure of about eight months, $^{37}$Ar was collected by purging the $C_2Cl_4$ with He gas. He, carrying with it Ar, was cleaned by a condenser (-40°C) and a molecular sieve trap before a charcoal trap. This charcoal trap was cooled by liquid $N_2$ (-196°C) to freeze and absorb Ar (freezing point of Ar is -189°C). Then the trap was warmed (+200°C) an Ar was transferred to a small system to measure the volume. After that, Ar was transferred to gas chromatographic system. It separated Ar from the heavier gases, such as Kr, Xe, and Rn. Then the volume of Ar was measured and transferred to the proportional counter. Ar was mixed with $CH_4$ whose volume was 7% of the Ar volume. The number of $^{37}$Ar was determined by observing their decay electrons. The decay electrons with an energy of 2.8 keV represents 81.5% of all decays. An additional 8.7% of the decays invokes a K orbital electron capture together with emission of a $\gamma$-ray (2.6∼2.8 keV). 10% of those $\gamma$-rays converts and deposits an energy of 2.8 keV. The reaction threshold of $^{37}$Cl neutrino absorption is 0.814 MeV, so the dominant components of neutrino sources were $^7$Be neutrinos and $^8$B neutrinos. The contributions of *pep* neutrinos and neutrinos from CNO-cycle were small because their fluxes are small. The energy of $^7$Be neutrinos is 0.861 MeV, so it can excite just the Gamow-Teller transition to the $^{37}$Ar ground state. $^8$B neutrinos can excite $^{37}$Cl to numerous states. The interaction cross section is calculated from the $\beta$ decay $^{37}\mathrm{Ca}(\beta^{+})^{37}\mathrm{K}$, which is an isospin mirror of $^{37}\mathrm{Cl}(\nu_{\mathrm{e}},\mathrm{e}^{-})^{37}\mathrm{Ar}$ [10]. The number of events predicted by the SSM and the measured capture rate are given in Table 2.4. SNU is a unit which is the number of interactions per $10^{36}$ targets per second. The ratio of the measured rate to the SSM prediction is 0.34±0.06 [11].

### GALLEX,GNO and SAGE

GALLEX and SAGE were radiochemical experiments using Ga. A solar neutrino was detected by inverse $\beta$ interaction $^{71}\mathrm{Ga}(\nu_{\mathrm{e}},\mathrm{e}^{-})^{71}\mathrm{Ge}$. The energy threshold of absorption in 232.69±0.15 keV. So, *pp* neutrinos could be detected by these detectors. The K and L Auger electrons from $^{71}$Ge decay have energies of 10.4 keV and 1.2 keV, respectively. The lifetime for $^{71}$Ge electron capture has been measured as $\tau_{1/2}$ = 11.43±0.03 day [65].

The GALLEX detector was located at Gran Sasso Underground Laboratory at the depth of 3800 m.w.e [18]. The detector observed solar neutrinos from 1991 to 1997 [17] [16] [15] [14].

The target consisted of 101 tons (53.5 $\mathrm{m}^3$) of $\mathrm{GaCl_3}$, of which 12 tons were $^{71}$Ga. At the end of each 20 day exposure about 1 mg of Ge carriers were added to extract $^{71}$Ge chemically. The $\mathrm{GeCl_4}$ was volatile and purged with $\mathrm{N_2}$ gas. Then it converted $\mathrm{GeH_4}$ and filled a proportional counter with Xe, The proportional counter was enclosed in NaI veto counter surrounded by lead shielding and counted the K and L Auger electrons for period of 90 days. The detector was calibrated twice with neutrino source $^{51}$Cr of known intensity [66]. $^{51}$Cr emits neutrinos with energies of 428 keV (9.0%), 747 keV (8163%) and 752 keV (8.5%), which is similar to the energies of *pp* and $^7$Be Solar neutrinos. The source was introduced inside of the detector. The source emitted about $6\times10^{13}$ neutrinos per second just after the installation. This flux was 10 times larger than that of solar neutrinos. After 3 months calibration, the flux was reduced to 1/10 of the initial one. The $^{51}$Cr calibration showed that the observed neutrino detection efficiency was consistent with the estimated value. The result of $^{51}$Cr calibration is [19]:

$$\frac{\sigma(^{51}\mathrm{Cr})^{\mathrm{GALLEX}}_{\mathrm{measured}}}{\sigma(^{51}\mathrm{Cr})_{\mathrm{BU88}}} = 0.93 \pm 0.08, \tag{2.14}$$

where $\sigma(^{51}\mathrm{Cr})^{\mathrm{GALLEX}}_{\mathrm{measured}}$ is the absorption cross section of $^{71}$Ga measured by the $^{51}$Cr calibration as GALLEX. $\sigma(^{51}\mathrm{Cr})_{\mathrm{BU88}}$ is the calculated cross section by Bahcall and Urlich [67] and it is $59.2\times10^{-46}(1\pm0.1)\mathrm{cm}^{-2}$. Another test was performed at the end of the experiment by adding $^{71}$As to the target solution [68]. $^{71}$As decays ($\beta^+$ 32% and electron capture 68%) with the half-life of 2.72 days into $^{71}$Ge. By using the $^{71}$Ge from $^{71}$As decay, the efficiency of extraction was studied and it was found to be consistent with expectation. The ratio of the measured rate to the SSM prediction in GALLEX [14] (+ GNO [12]) is 0.58±0.07. The number of events predicted by the SSM and the measured capture rate are given in Table 2.4.

The SAGE detector is situated in a tunnel in the northern Causaus mountains in southern Russia at the depth of about 4700 m.w.e [22]. Solar neutrino observation began in 1990. The target is 50 tons of metallic Ga. At the end of an exposure period (typically one month), a small amount ( a few hundred mg) of Ge carrier is added to each detector. Then $^{71}$Ge is extracted chemically by a solution of dilute HCl and $\mathrm{H_2O_2}$. The $\mathrm{GeCl_4}$ is then transformed into $\mathrm{GeH_4}$ and mixed with Xe to be filled in proportional counters to count the K Auger electrons. Each sample counted for a period of 2 $\sim$ 3 months. $^{51}$Cr calibration was performed in SAGE too. The result is [69] [23] [24]:

$$\frac{\sigma(^{51}\mathrm{Cr})^{\mathrm{SAGE}}_{\mathrm{measured}}}{\sigma(^{51}\mathrm{Cr})_{\mathrm{BU88}}} = 0.95 \pm 0.12, \tag{2.15}$$

The ratio of the measured rate to the SSM prediction is 0.59±0.07 [21]. The number of events predicted by the SSM and the measured capture rate are given in Table 2.4.

### 2.4.2 Kamiokande and Super-Kamiokande experiments

Kamiokande and Super-Kamiokande in Japan are real-time experiments utilizing $\nu\ e$ scattering

$$\nu_{\mathrm{x}} + \mathrm{e}^- \to \nu_{\mathrm{x}} + \mathrm{e}^- \tag{2.16}$$

in a large water-$\check{C}$erenkov detector. It should be noted that the reaction is sensitive to all active neutrinos, $\mathrm{x} = \mathrm{e}, \mu, \mathrm{and}\tau$. However, the sensitivity to $\nu_\mu$ and $\nu_\tau$ is much smaller than the sensitivity to $\nu_e$, $\sigma(\nu_{\mu,\tau}\ e) \approx 0.16\sigma(\nu_e\ e)$. The solar neutrino flux measured via $\nu\ e$ scattering is deduced assuming no neutrino oscillations.

These experiments take advantage of the directional correlation between the incoming neutrino and the recoil electron. This feature greatly helps the clear separation of the solar neutrino signal from background. Due to the high thresholds(7 MeV in Kamiokande-II and 5 MeV in Super-Kamiokande-I) the experiments could observe pure $^8$B solar neutrinos.

Kamiokande was a water Čerenkov detector which was located near SK. Purified water of 3000 m$^3$ was contained in a stainless steel tank of 15.6 m diameter and 16.1 m height. The inner detector had 946 50cm-PMTs viewing 2140 m$^3$ of purified water. The comparison between Kamiokande detector and Super-Kamiokande detector is shown Table 2.5. The observation of solar neutrinos in the Kamiokande-II collaboration started in 1987 using recoil electrons via neutrino-electron elastic scattering [4]. The vertex, direction, and energy of each event were reconstructed using Čerenkov photons. Solar neutrino events could be extracted using direction correlation to the Sun. The energy threshold was $\sim 7.0$ MeV. Therefore, $^8$B neutrinos and *hep* neutrinos could be observed. The Kamiokande-II experiment came to an end at the beginning of 1995. The ratio of the measured rate to the SSM prediction is $0.55\pm0.13$ [3]. The number of events predicted by the SSM and the measured capture rate are given in Table 2.4.

Super-Kamiokande will be discussed in detail later. In this section, only an overview will be given. Super-Kamiokade is a 50k ton second-generation solar neutrino detector, which is characterized by a significantly larger counting rate than then first generation experiments [1]. This experiment started the observation of solar neutrino in April 1996. The average solar neutrino flux is smaller than, but consistent with, the Kamiokande-II result. The flux measured in the nighttime is slightly larger than the flux measured in daytime, but it is only a $1.3\sigma$ effect [2]. Super-Kamiokande also observed the recoil-electron energy spectrum. The Super-Kamiokande-I experiment was closed in July 2001. Now, Super-Kamiokande-II experiment which started from November 2003 is running. The ratio of the measured rate to the SSM prediction is $0.47\pm0.02$ [2]. The number of events predicted by the SSM and the measured capture rate are given in Table 2.4. In Table 2.5, the comparison between Kamiokande-II and Super-Kamiokande-I is presented.

| Parameters | SK-I | Kamiokande-II | Remarks |
|---|---|---|---|
| Total size | 41mh×39m$\phi$ | 16mh×19m$\phi$ | |
| Total volume | 50000t | 4500t | |
| Fiducial volume | 32000t | 2140t | supernova neutrino |
| | 22500t | 1040t | proton decay |
| | 22500t | 680t | solar neutrino |
| Thickness of outer detector | 2.6m∼2.75m | 1.2m∼1.5m | |
| Number of PMT | 11146 | 948 | inner detector |
| Photosensitive coverage | 40% | 20% | |
| PMT timing resolution | ∼2.2ns | ∼4ns | |
| PMT energy resolution | 2.6%/$\sqrt{E}$ | 3.6%/$\sqrt{E}$ | electrons at E (GeV) |
| | 2.5% | 15% | muons ($E \leq$1 GeV) |
| PMT energy resolution | 21.3%/$\sqrt{E/5\text{MeV}}$ | 24.9%/$\sqrt{E/5\text{MeV}}$ | electrons (E≤50MeV) |
| PMT position resolution | 50cm | 100cm | 10 MeV electron |
| PMT position resolution | ∼10cm | ∼50cm | $p \rightarrow e^+\pi^0$ |
| PMT angular resolution | 25° | 26° | 10 MeV electron |
| PMT angular resolution | 1.5° | 2.7° | through-going muon |
| Energy threshold (Trigger) | 4.5 MeV | 5.2 MeV | |
| Energy threshold (Analysis) | 5.0 MeV | 7.0 MeV | Solar neutrino |
| Selection of electron/muon | 99% | | 0.03<$p_e$<1.33 GeV/$c$ |
| | 99% | | 0.2<$p_\mu$<1.5 GeV/$c$ |
| Selection of electron/muon | | 80% | stopping-muon |

Table 2.5: Comparison between Super Kamiokande and Kamiokande

### 2.4.3 SNO experiment

In 1999, a new real-time solar neutrino experiment, SNO (Sudbury Neutrino Observatory) in Canada started observation. SNO is an imaging water Čerenkov detector located at a depth of 6010 m of water equivalent in the INCO, LTD. Creighton mine near Sudbury, Ontario. It features 1000 metric tons of ultra-pure $D_2O$ to intercept about 10 neutrinos per day contained in a 12 m diameter spherical acrylic vessel. This sphere is surrounded by a shield of ultra-pure $H_2O$ contained in a 34 m high barrel-shaped cavity of maximum diameter 22 m. A stainless steel structure 17.8 m in a diameter supports 9456 20-cm photomultiplier tubes with light concentrators. Approximately 55% of the light produced within 7 m of the center of the detector will strike a PMT.

Events are defined by a multiplicity trigger of 18 or more PMTs exceeding a threshold of $\sim$ 0.25 photo-electrons within a time window of 93 ns. The trigger reaches 100% efficiency at 23 PMTs. For every event trigger, the time and charge response of each participating PMT are recorded. Solar neutrino are extracted using the angle between the reconstructed direction from the Sun to the Earth.

Calibration of the PMT time and charge pedestals, slopes, offsets, charge vs. time dependencies, and second order rate dependencies are performed using electronic pulser and pulsed light sources. Optical calibration is obtained using a diffuse source of pulsed laser light at 337, 365, 386, 420, 500, and 620 nm wavelengths. The absolute energy scale and uncertainties are established with triggered $^{16}$N source (predominantly 6.13-MeV $\gamma$'s) deployed over two planar grids within the $D_2O$ and a linear grid in the $H_2O$. The resulting Monte Carlo predictions of detector response are tested using a $^{252}$Cf neutron source, which provides an extended distribution of 6.25 MeV $\gamma$ rays from neutron capture, and a $^3$H(p.$\gamma$)$^4$He source providing 19.8 MeV $\gamma$ rays. The volume weighted mean response is approximately nine PMT hits per MeV of electron energy.

SNO measures $^8$B solar neutrino via the reactions

$$\nu_{\mathrm{e}} + \mathrm{d} \rightarrow \mathrm{e}^- + \mathrm{p} + \mathrm{p} \text{ Charged-Current CC} \tag{2.17}$$

$$\nu_{\mathrm{x}} + \mathrm{d} \rightarrow \nu_{\mathrm{x}} + \mathrm{p} + \mathrm{n} \text{ Neutral-Current NC} \tag{2.18}$$

$$\nu_{\mathrm{x}} + \mathrm{e}^- \rightarrow \nu_{\mathrm{x}} + \mathrm{e}^- \text{ Elastic-Scattering ES} \tag{2.19}$$

The Q-value of the CC reactions is -1.4 MeV and the electron energy is strongly correlated with neutrino energy. Thus the CC reaction provides an accurate measure of the shape of the $^8$B solar neutrino spectrum. The contributions from the CC reaction nd $\nu_e$ scattering can be distinguished by using different $\cos\theta_{sun}$ distribution where $\cos\theta_{sun}$ is the angle with respect to the direction from the Sun to the Earth. The forward peak of $\cos\theta_{sun} = 1$ arises from the kinematics of the ES reaction, while CC electrons are expected to have a distribution which is (1-0.345$\cos\theta_{sun}$) by detector response.

The threshold of the NC reaction is 2.2 MeV. In the pure $D_2O$, the signal of the NC reaction is neutron capture in deuterium, producing a 6.25 MeV $\gamma$ ray. In this case, capture efficiency is low and the deposit energy is close to the detection threshold of 5.0 MeV. In order to enhance both the capture efficiency and the total $\gamma$ ray energy (8.6 MeV), 2.5 tons of NaCl has been added to the heavy water in the second phase of the experiment. The chlorine ($^{35}$Cl) has a high absorption cross-section for thermal neutrons, resulting in a gamma ray cascade peaked at around 8 MeV. The neutron capture efficiency will be about 83%. The background for this process will be neutrons produced by photo disintegration of the deuteron, arising chiefly from the 2.45 MeV and 2.63 MeV gamma rays in the $^{232}$Th and $^{238}$U chains. Special care was taken so that the salt is at the highest level of cleanliness. In addition, installation of discrete $^3$He neutron counter is planned for the NC measurement in the third phase.

The energy threshold in SNO is 6.75 MeV as an effective kinetic energy. The reported data were recorded between November 2, 1999 and January 15, 2001 and correspond to a live time of 240.95 days [27].

The ratio of the measured rate to the SSM prediction is 0.47±0.1 for ES reaction. The number of events predicted by the SSM and the measured capture rate are given in Table 2.4.

Though the results has poor statistics yet, it is consistent with the high statistics Super-Kamiokande-I result. Thus the SNO group compared their CC result with Super Kamiokande ES result, and obtained evidence of active non-$\nu_e$ component in the solar neutrino flux.

More recently, in September 7, 2003, the SNO collaboration reported the first result on the $^8$B solar neutrino flux measurement via NC reaction in salt phase. The total flux measured via NC reaction is consistent with the solar model predictions [26].

## 2.5 Solar neutrino problem

Figure 2.9 compares the predictions of the standard solar model with the total observed rates in the six solar neutrino experiments: chlorine, Super Kamiokande, Kamiokande, GALLEX, SAGE, and SNO. The model predictions are color coded with different colors for the different predicted neutrino components. For both the experimental values and the predictions, the 1 sigma uncertainties are indicated by cross hatching. This figure explains the "four solar neutrino problems" that suggest that new neutrino physics is required to explain the results of the solar neutrino experiments. The problems exist because it is assumed, following the minimal standard model, that essentially nothing happens to the neutrinos after they are created in the center of the Sun.

In all six cases, the blue experimental values are significantly less than the model predictions. The difference (by a factor of three or more) between the chlorine measurement of Ray Davis and the standard solar model prediction was the "solar neutrino problem" for two decades. The discrepancy between measured and predicted absolute rates was strengthened at the beginning of the 1990's by the measurement by the Kamiokande experiment of the $^8$B neutrino flux. For Kamiokande, which has a threshold of 7.5 MeV (compared to 0.8 MeV for the chlorine experiment), the discrepancy is approximately a factor of two. The discrepancy in absolute rates is the first "solar neutrino problem."

A second solar neutrino problem, namely, is that the rate of just the $^8$B neutrinos observed in Kamiokande exceeds the total measured rate in the chlorine experiment if the energy spectrum of the solar neutrinos is not changed by new neutrino physics. This problem is exacerbated by the fact that significant contributions are also expected in the chlorine experiment from $^7$Be neutrinos and from CNO neutrinos. The predicted rate from the $^7$Be neutrinos is well determined, especially since the related $^8$B neutrinos are observed to be depleted only by a factor of two.

The GALLEX and SAGE experiments present the third, essentially independent solar neutrino problem. The total observed rate is accounted for by the pp neutrinos, whose flux is an accuracy of 1 %. Therefore, the gallium experiments do not leave any room for the reliably calculated $^7$Be neutrinos. This is the reason why the third solar neutrino problem is sometimes referred to as "the problem of the missing $^7$Be neutrinos." Moreover, both the GALLEX and SAGE experiments have been directly calibrated with a radioactive source, $^{51}$Cr, that emits neutrinos with similar energies to the $^7$Be neutrinos.

Most recently and perhaps most dramatically, the SNO experiment has shown that the CC rate (from electron type neutrinos only) in a deuterium detector is only 0.35 of the standard model prediction. The Super-Kamiokande experiment, which measures the CC rate plus–with reduced efficiency–the muon and tau neutrinos, observes 0.46 of the standard model prediction. The fact that Super-Kamiokande observes 0.46 (with some sensitivity to all three neutrinos) and SNO observes only 0.35 of the standard rate (from only electron type neutrinos) proves that some electron type neutrinos become muon and tau neutrinos after they are created in the center of the Sun.

It is clear from above flux results that the results from all the solar-neutrino experiments, except the most recent SNO NC result, indicate significantly less flux than expected from BP2000 SSM. There has been a consensus that a consistent explanation of all the results of solar neutrinos observation is unlikely within the framework of astrophysics using the solar neutrino spectra given by the standard electroweak model. Many authors made solar model independent analyses constrained by the observed solar luminosity [26], where they attempted to fit the measured solar neutrino capture rates and $^8$B flux with normalization-free, undistorted energy spectra. All these attempts only obtained solutions with very low probabilities.

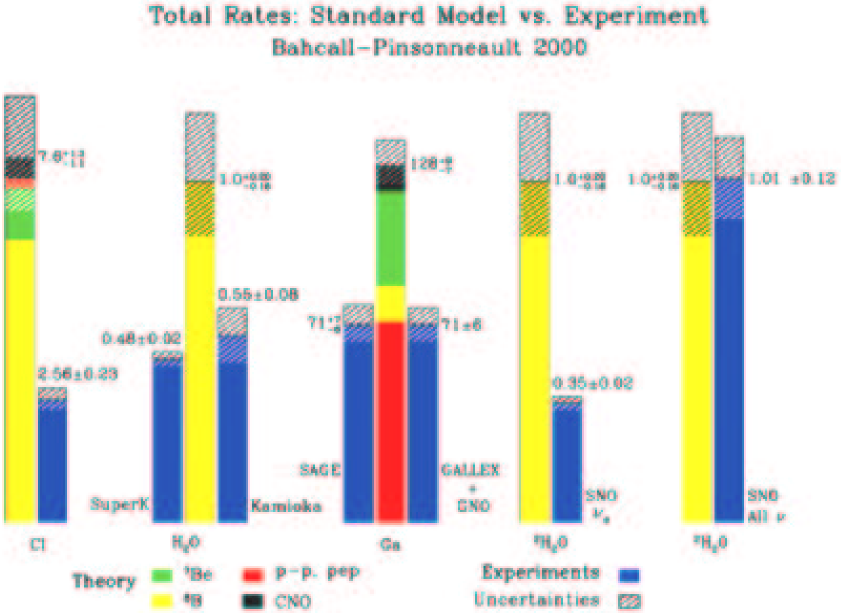

Figure 2.9: This color viewgraph compares the predictions of the standard solar model with the total observed rates in the six solar neutrino experiments: chlorine, Super Kamiokande, Kamiokande, GALLEX, SAGE, and SNO. (http://www.sns.ias.edu/j̃nb/)

Predicted Ratio to SSM

$$\mathrm{R_{Cl}} = 0.0 \cdot \mathrm{SSM_{pp}} + 0.15 \cdot \mathrm{SSM_{Be}} + 0.76 \cdot \mathrm{SSM_{B8}} \tag{2.20}$$

$$\mathrm{R_{Ga}} = 0.56 \cdot \mathrm{SSM_{pp}} + 0.27 \cdot \mathrm{SSM_{Be}} + 0.1 \cdot \mathrm{SSM_{B8}} \tag{2.21}$$

$$\mathrm{R_{SK}} = 0.0 \cdot \mathrm{SSM_{pp}} + 0.0 \cdot \mathrm{SSM_{Be}} + 0.999 \cdot \mathrm{SSM_{B8}} \tag{2.22}$$

Flux results to SSM from measurements

$$\phi(\mathrm{pp}) \sim 0.9 \times \phi\mathrm{SSM(pp)} \tag{2.23}$$

$$\phi(\mathrm{Be}) \sim 0.0 \times \phi\mathrm{SSM(Be)} \tag{2.24}$$

$$\phi(\mathrm{B8}) \sim 0.5 \times \phi\mathrm{SSM(B8)} \tag{2.25}$$

To explain the deficit in the framework of the SSM, some probabilities are discussed such as the temperature in the core $T_c$ and the cross section of $^7$Be proton capture The temperature in the core influences the rate of nuclear fission. If the $T_c$ is much lower than the value used in the SSM, then all of the neutrino flux is decreased. The temperature dependence of the $^8$B neutrino flux is $\phi \sim T_c^{18}$, although that of the $^7$Be neutrino flux is $\phi \sim T_c^8$ [87]. Thus, a large reduction in the $^7$Be neutrino flux results in a much larger reduction in the $^8$B neutrino flux in the SSM.

The ratio of proton capture $^7$Be is 0.1 % of that of electron capture by $^7$Be. So, if $S_{17}(0)$ is larger than expected by 2 orders of magnitude, then the results can be explained. The estimated error of $S_{17}(0)$ is 25% at 1 $\sigma$. The uncertainty of $^7$Be electron capture rate is also studied and found to be less than 2%.

Therefore, the data suggest that the solution to the solar neutrino problem requires nontrivial neutrino properties. Figure 2.10 shows fluxes of solar neutrino calculated from observed neutrino fluxes in SK and SNO experiments.

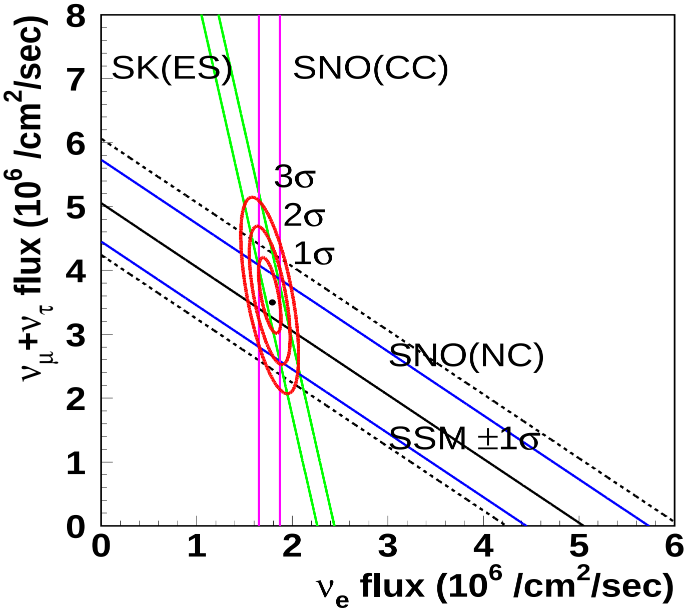

Figure 2.10: Fluxes of $^8$B solar neutrinos, $\phi(\nu_e), \phi(\nu_{\mu,\tau})$, deduced from the SK's ES result and SNO's CC, NC, and ES results. The standard solar model prediction is also shown. The bands represent the $1\sigma$ error. The contours show the 68%, 95%, and 99% joint probability for flux results.

## 2.6 Neutrino oscillation mechanism

In this section, the theory of neutrino oscillations is described. It is regarded as the most likely solution of the solar neutrino problem.

### 2.6.1 Vacuum oscillation

If neutrinos have mass and different generations mix as quark do, the observed neutrino flavor will change as they propagate. This phenomenon occurs because the propagation eigenstate, namely a mass eigenstate, of a neutrino is not a flavor eigenstate. Currently it is believed that there are three kinds of neutrinos, namely, $\nu_e$, $\nu_\mu$, and $\nu_\tau$. For simplicity, only two flavor oscillations between $\nu_e$ and $\nu_\mu$ is taken into account here.

Mixing between two generations can be expressed as follow:

$$\begin{pmatrix} \mid \nu_e\rangle \\ \mid \nu_\mu\rangle \end{pmatrix} = \begin{pmatrix} \cos\theta & \sin\theta \\ -\sin\theta & \cos\theta \end{pmatrix} \begin{pmatrix} \mid \nu_1\rangle \\ \mid \nu_2\rangle \end{pmatrix} \equiv U \begin{pmatrix} \mid \nu_1\rangle \\ \mid \nu_2\rangle \end{pmatrix} \tag{2.26}$$

where $\mid \nu_{1,2}\rangle$ are the mass eigenstates, $\theta$ is the mixing angle, and $U$ is the mixing matrix. From now on, $i, j$ denote 1 or 2 and $a, b$ denote e or $\mu$. The propagation of mass eigenstates is expressed as:

$$\mid \nu_i(t)\rangle = e^{-iE_i t} \mid \nu_i(0)\rangle \tag{2.27}$$

where $t$ is the time and $E_i$ is the energy of a neutrino for mass eigenstate $i$. $E_i$ is approximated as follow,

$$E_i = \sqrt{p^2 + m_i^2} \simeq p + \frac{m_i^2}{2p} \simeq E + \frac{m_i^2}{2E} \tag{2.28}$$

where $m_i$ is the mass of eigenstate $i$. Equation (2.26) can be rewritten as:

$$\mid \nu_a(t)\rangle = \sum_i U_{ai} \mid \nu_i(t)\rangle \tag{2.29}$$

substitution of (2.27) in (2.29) yields:

$$\begin{aligned} \mid \nu_a(t)\rangle &= \sum_i U_{ai} e^{-iE_i t} \mid \nu_i(0)\rangle & (2.30) \\ &= \sum_i \sum_b U_{ai} U^{-1}_{ib} e^{-iE_i t} \mid \nu_b(0)\rangle & (2.31) \end{aligned}$$

Therefore, the amplitude that the same flavor is maintained is,

$$\begin{aligned} \langle \nu_a \mid \nu_a(t)\rangle &= \sum_i \sum_b U_{ai} U^{-1}_{ib} e^{-iE_i t} \langle \nu_a \mid \nu_b(0)\rangle & (2.32) \\ &= \sum_i \sum_b U_{ai} U^{-1}_{ib} e^{-iE_i t} \delta_{ab} & (2.33) \\ &= \sum_i U_{ai} U^{-1}_{ia} e^{-iE_i t} & (2.34) \end{aligned}$$

The probability that the same flavor is kept, $P(a \to a, t)$, is:

$$\begin{aligned} P(a \to a, t) &= \mid \langle \nu_a \mid \nu_a(t)\rangle \mid^2 & (2.35) \\ &= \sum_i \sum_j U_{ai} U^{-1}_{ia} U_{aj} U^{-1}_{ja} e^{-i(E_i - E_j)t} & (2.36) \end{aligned}$$

Finally substituting equation (2.26) in (2.36) yields:

$$P(a \to a, t) = 1 - \sin^2 2\theta \sin^2 \frac{\Delta m^2}{4E} t \tag{2.37}$$

where $\Delta m^2 = m_2^2 - m_1^2$. Therefore, the probability that an electron neutrino generated at $t = 0$ remains an electron neutrino after time $t$, or distance $L$ (assuming $t = L$ in natural units (c=1)) becomes:

$$\begin{aligned} P(\nu_e \to \nu_e, L) &= 1 - \sin^2 2\theta \sin^2 \frac{\Delta m^2}{4E} L \\ P(\nu_e \to \nu_e, L) &= 1 - \sin^2 2\theta \sin^2 \frac{\pi L}{L_V} & (2.38) \end{aligned}$$

where

$$L_V = \frac{4\pi E}{\Delta m^2} = 2.48 \frac{E(\text{MeV})}{\Delta m^2(\text{eV}^2)} (m) \tag{2.39}$$

is the oscillation length in the vacuum.

The vacuum oscillation phenomenon is searched for by several experiments which use accelerators or reactors as neutrino source. However, these experiments did not find the phenomenon. Recently, observations of atmospheric neutrinos (which are decay products of mesons ($\pi$'s, K's, or $\mu$'s) created in interactions of primary cosmic rays (protons and nuclei) in the atmosphere), by Super-Kamiokande confirmed that neutrino oscillation does occur between $\nu_\mu \leftrightarrow \nu_\tau$ channel[1]. The atmospheric neutrinos generated on the opposite side of the Earth travel about $1 \times 10^4$km. Therefore, the observation of 1 GeV atmospheric neutrinos has sensitivity for $\Delta m^2$ down to $\sim 2.5 \times 10^{-3}$eV$^2$. Actually, the observations suggest that non-oscillation is rejected at the 6.2$\sigma$

---

[1] or $\nu_\mu \leftrightarrow \nu_s$ channel; where $\nu_s$ is sterile neutrino

level from the zenith angle distribution of neutrino events and the double ratio of muon neutrino and electron neutrino flux of measured to expected values, and that the allowed region of $\Delta m^2$ is $10^{-3} \sim 10^{-2}\mathrm{eV}^2$ [70].

Another aspect of vacuum oscillation is expected for solar neutrinos, if $\Delta m^2$ between $\nu_e$ and $\nu_\mu$ is suitable. The distance between the Sun and the Earth is about $1.5\times10^{11}$m, and typical energy of the $^8$B neutrinos is about 10 MeV, therefore, if the $\Delta m^2$ is of order $10^{-10}\mathrm{eV}^2$ and the mixing angle is sufficiently large, a seasonal deviation from the expected value of $\nu_e$ flux time variation caused by the elliptical orbit of the Earth may be observed. And the shape of the $^8$B neutrino energy spectrum is distorted due to the energy dependence of the vacuum oscillation length. Since this oscillation is caused by a just agreement of the vacuum oscillation length and the orbital radius, this is called the 'Just-so' solution. In order to verify this solution, high statistical solar neutrino events, hence, massive detectors like Super-Kamiokande, are needed.

### 2.6.2 Neutrino oscillation in matter

Wolfenstein suggested that neutrino oscillations in matter are different from those in vacuum due to an additional potential the $\nu_e$ experiences. With analogy to optics, the phase factor of propagation of the neutrino is changed from $ipx$ to $ipn_lx$, where $n_l$ is the index of refraction of flavor $l$. $n_l$ is represented as follow [71],

$$n_l = 1 + \frac{2\pi N}{p^2} f_l(0) \tag{2.40}$$

where $N$ is the number of density of scatters and $f_l(0)$ is the forward scattering amplitude. An electron, a muon and a tau neutrino interact with an electron, a proton and a neutron via a neutral current interaction. For solar neutrino energy, only electron neutrinos can interact with an electron via a charged current interaction (figure 2.11). This causes the difference in $f_l(0)$ for an electron neutrino from the other type neutrinos, and this additional phase shift causes neutrino oscillation in matter to differ from that in vacuum. Since S.P.Mikheyev, A.Yu.Smirnov

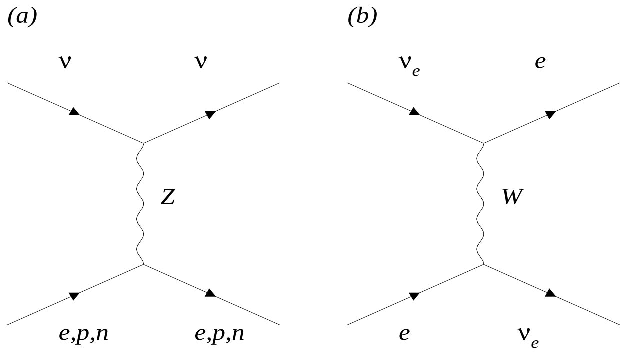

Figure 2.11: The Feynman diagrams of neutrino interaction in matter. Figure (a) shows neutral current interaction via Z boson exchange between a neutrino and an electron, a proton or a neutron. Figure (b) shows charged current interaction via W boson exchange between an electron neutrino and an electron.

applied this theory to the solar neutrino problem, this effect is called the 'MSW effect'. The MSW effect could solve the solar neutrino problems, if $\Delta m^2 \sim 10^{-5}$ and $\sin^2 2\theta \simeq 10^{-3} \sim 1$. In order to explain the MSW effect mathematically, let us consider the propagation of a neutrino in matter. Again, only two flavor eigenstates are considered for simplicity. The time development equation of flavor eigenstates in matter is

$$i\frac{d}{dt}\begin{pmatrix} |\nu_e(t)\rangle \\ |\nu_\mu(t)\rangle \end{pmatrix} = \left\{ U \begin{pmatrix} E_1 & 0 \\ 0 & E_2 \end{pmatrix} U^{-1} + \begin{pmatrix} V_C + V_N & 0 \\ 0 & V_N \end{pmatrix} \right\} \begin{pmatrix} |\nu_e(t)\rangle \\ |\nu_\mu(t)\rangle \end{pmatrix} \tag{2.41}$$

where $V_C$ and $V_N$ represent the effective potential for neutral and charged current interactions, respectively. The diagonal component of $V_N$ can be absorbed into a common phase, $e^{-i\int V_N dt}$. $V_C$ is calculated to be $\sqrt{2}G_F N_e$, where $G_F$ is the Fermi coupling constant and $N_e$ is the electron density. Equation (2.41) is rewritten,

$$i\frac{d}{dt}\begin{pmatrix} |\nu_e(t)\rangle \\ |\nu_\mu(t)\rangle \end{pmatrix}$$

$$M_{eff} = \frac{1}{2E}\left\{ \frac{1}{2}(m_1^2 + m_2^2 + A)I + \frac{1}{2}\begin{pmatrix} -\Delta m^2 \cos 2\theta + A & \Delta m^2 \sin 2\theta \\ \Delta m^2 \sin 2\theta & \Delta m^2 \cos 2\theta - A \end{pmatrix} \right\} \begin{pmatrix} |\nu_e(t)\rangle \\ |\nu_\mu(t)\rangle \end{pmatrix} \tag{2.42}$$

where

$$A = 2\sqrt{2}G_F N_e E \tag{2.43}$$

and $I$ is the $2 \times 2$ unit matrix. Eigenvalues of the matrix are regarded as effective masses of two mass eigenstates in matter. The eigenvalues are

$$m_{im}^2 = \frac{m_1^2 + m_2^2 + A}{2} \pm \frac{1}{2}\sqrt{(\Delta m^2 \cos 2\theta - A)^2 + \Delta m^4 \sin^2 2\theta} \qquad (i = 1, 2) \tag{2.44}$$

and the eigenstate in matter is

$$\begin{pmatrix} |\nu_{1m}\rangle \\ |\nu_{2m}\rangle \end{pmatrix} = \begin{pmatrix} \cos\theta_m & -\sin\theta_m \\ \sin\theta_m & \cos\theta_m \end{pmatrix} \begin{pmatrix} |\nu_e\rangle \\ |\nu_\mu\rangle \end{pmatrix} \tag{2.45}$$

where $\theta_m$ is the effective mixing angle in matter and given by,

$$\begin{aligned} \tan 2\theta_m &= \frac{\tan 2\theta}{1 - \dfrac{A}{\Delta m^2 \cos 2\theta}} \\ \tan 2\theta_m &= \frac{\tan 2\theta}{1 - \dfrac{L_V}{L_e \cos 2\theta}} \end{aligned} \tag{2.46}$$

with $L_e = \sqrt{2}\pi / G_F N_e$. Thus, if the following relation is satisfied, the mixing angle in matter becomes maximal ( $\theta_m = \pi/4$ ) even if the vacuum mixing angle is small.

$$L_V = L_e \cos 2\theta \qquad \text{or} \qquad \Delta m^2 \cos 2\theta = 2\sqrt{2}G_F N_e E \tag{2.47}$$

This condition is called 'resonance condition'. The electron density at which the resonant condition is satisfied is denoted as $N_{e,res} \equiv \Delta m^2 \cos 2\theta / 2\sqrt{2}G_F E$.

Let us consider solar neutrinos. As shown in figure 2.6, the electron density varies as a function of solar radius.

It is largest in the center where nuclear fusion happens and it decreases as the radius increases. Therefore, a neutrino with energy larger than the critical energy $E_{crit}$, always passes through a position where resonance condition is satisfied. The critical energy is given by:

$$E_{crit} = \frac{\Delta m^2 \cos 2\theta}{2\sqrt{2}G_F N_{e,c}} = 6.6 \cos 2\theta \left( \frac{\Delta m^2}{10^{-4}\mathrm{eV}^2} \right) \text{ MeV} \tag{2.48}$$

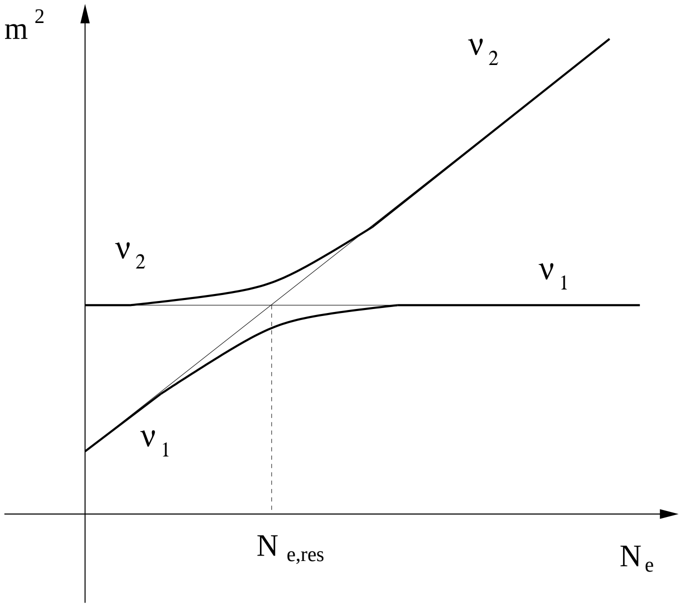

Figure 2.12: MSW effect in the Sun.

where $N_{e,c}$ is the electron density in the center of the Sun. Figure 2.12 shows the mass eigenvalues of two neutrino mass eigenstates in matter as a function of electron density. If the energy of a neutrino is greater than $E_{crit}$, $\theta_m \cong \pi/2$ from equation (2.46), hence, $\mid \nu_e\rangle$ is almost $\mid \nu_2\rangle$. While the mass eigenstates propagate from the center of the Sun to the surface of it, the mass of the eigenstates changes as shown in figure 2.12. When a neutrino passes the resonance region, $\theta_m$ becomes $\pi/4$ and the mixing becomes maximal. If the variation of the electron density is reasonable (see eq(2.50)), the main component of flavor $\mid \nu_2\rangle$ state changes from $\mid \nu_e\rangle$ to $\mid \nu_\mu\rangle$ adiabatically, if the vacuum mixing angle $\theta$ is small enough. Therefore, a neutrino which is produced as an electron neutrino becomes a muon neutrino when it reaches the surface where the electron density is almost zero. The condition which allows the transition of neutrino flavor from $\nu_e$ to $\nu_\mu$ adiabatically is called adiabatic condition.

Actually, level jumping from $\mid \nu_2\rangle$ to $\mid \nu_1\rangle$ occurs. The probability of this jump, $P_{jump}$, is approximately calculated by L.D.Landau and C.Zener [72],

$$P_{jump} = \exp\left(-\frac{\pi}{4}\frac{\sin^2 2\theta}{E\cos 2\theta}\frac{\Delta m^2}{\left|\frac{1}{N_e}\frac{dN_e}{dr}\right|}\right) \tag{2.49}$$

The adiabatic condition holds if $P_{jump} \ll 1$, namely,

$$\sin^2 2\theta\Delta m^2 \geq E\cos 2\theta \left|\frac{1}{N_e}\frac{dN_e}{dr}\right| \tag{2.50}$$

Figure 2.13 shows the example of the MSW effect in the Sun, where $E/\Delta m^2$ and $\sin^2 2\theta$ are $6.0\times10^5$ and 0.001, respectively. As shown in figure 2.13, the resonance occurs at $R/R_\odot \simeq 0.3$ and it is found that $\nu_e$ is converted to $\nu_\mu$ with about 35% probability.

As the MSW effect for certain parameter range in $\Delta m^2$ and $\sin^2 2\theta$ may convert an $\nu_e$ into a $\nu_\mu$ on its way out of the Sun, it is possible for part of this parameter range that the $\nu_\mu$ are converted back to $\nu_e$ when passing through the Earth. Figure 2.14 shows the electron density distribution as a function of the radius of the Earth. This effect leads to the prediction that the observed electron neutrino flux at night when neutrinos go through the Earth may be larger than that during the day when the neutrinos come directly from the Sun. This is called the 'day-night

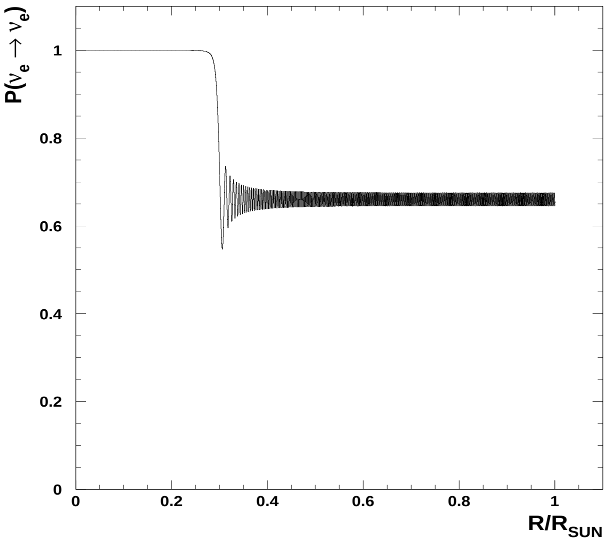

Figure 2.13: Survival probability $P(\nu_e \to \nu_e, L)$ as a function of the solar radius when $E/\Delta m^2 = 6.0 \times 10^5$ and $\sin^2 2\theta = 0.001$.

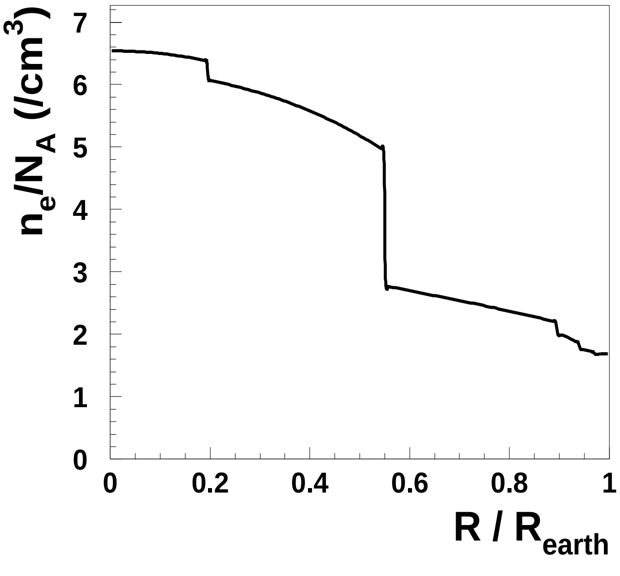

Figure 2.14: The electron density distribution as a function of the radius of the Earth[73].

effect'. Again, like the seasonal effect, in order to study this effect, a high statistics observation is necessary. Figure 2.15 shows the probability $P(\nu_e \to \nu_e)$ distribution as a function of $\frac{E}{\Delta m^2}$ for day-time and night-time ($\theta_z = 0, 180°$, respectively, where $\theta_z$ is the zenith angle defined in figure 2.16). The energy dependence of survival probability of $\nu_e$ leads to a distortion of energy spectrum.

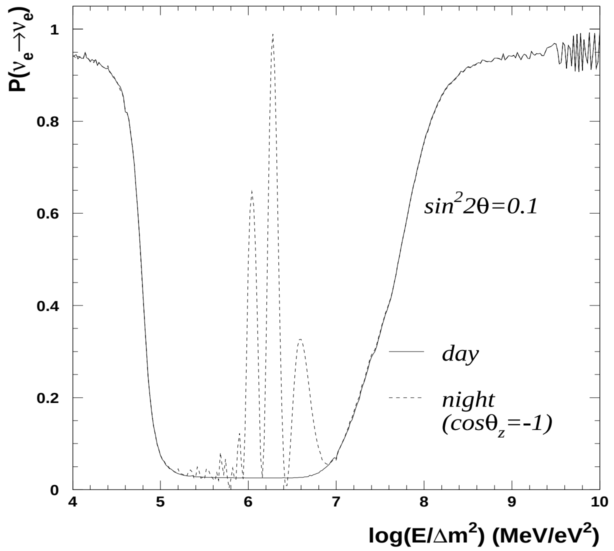

Figure 2.15: The probability $P(\nu_e \to \nu_e)$ at some place on the Earth surface is drawn as a function of $\frac{E}{\Delta m^2}$ both for day-time (solid line) and night-time ($\theta_z = 180°$) (broken line), where $\sin^2 2\theta = 0.1$.

## 2.7 The evidence of solar neutrino oscillation

Denoting the $^8$B solar neutrino flux obtained by the SNO CC measurement as $\phi^{\rm CC}_{\rm SNO}(\nu_{\rm e})$ and that obtained by the Super Kamiokande $\nu_e$ scattering as $\phi^{\rm ES}_{\rm SK}(\nu_{\rm x})$, $\phi^{\rm CC}_{\rm SNO}(\nu_{\rm e}) = \phi^{\rm ES}_{\rm SK}(\nu_{\rm x})$ is expected for the standard neutrino physics. However, SNO's initial data [27] indicate

$$\phi^{\rm ES}_{\rm SK}(\nu_{\rm x}) - \phi^{\rm CC}_{\rm SNO}(\nu_{\rm e}) = (0.57 \pm 0.17) \times 10^6 {\rm cm}^{-2}{\rm s}^{-1}. \tag{2.51}$$

The significance of the difference is $> 3\sigma$, implying direct evidence for the existence of a non-$\nu_e$ active neutrino flavor component in the solar neutrino flux. A natural and most probable explanation of neutrino flavor conversion is neutrino oscillation. Note that both the SNO [26] and Super Kamiokande [2] flux results were obtained by assuming the standard $^8$B neutrino spectrum shape. This assumption is justified by the measured energy spectra in both of the experiments.

From the measured $\phi^{\rm CC}_{\rm SNO}(\nu_{\rm e})$ and $\phi^{\rm ES}_{\rm SK}(\nu_{\rm e})$, the flux of non-$\nu_e$ active neutrinos, $\phi(\nu_{\mu \text{ or } \tau})$, and the total flux of active $^8$B solar neutrinos, $\phi(\nu_{\rm x})$, can be deduced:

$$\phi(\nu_\mu \text{ or } \nu_\tau) = (3.69 \pm 1.13) \times 10^6 {\rm cm}^{-2}{\rm s}^{-1} \tag{2.52}$$

$$\phi(\nu_{\rm x}) = (5.44 \pm 0.99) \times 10^6 {\rm cm}^{-2}{\rm s}^{-1} \tag{2.53}$$

The last equation is a solar model independent result and therefore tests solar models. It shows very good agreement with the $^8$B solar neutrino flux predicted by the BP2000 SSM.

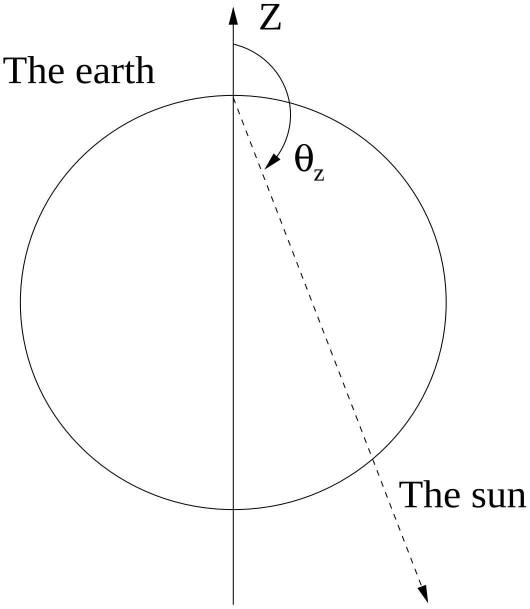

Figure 2.16: The definition of zenith angle.

The most recently reported SNO's results including data of salt phase are

$$\phi^{\rm CC}_{\rm SNO}(\nu_{\rm e}) = (1.59^{+0.08}_{-0.07}({\rm stat.})^{+0.06}_{-0.08}({\rm syst.})) \times 10^6{\rm cm}^{-2}{\rm s}^{-1} \tag{2.54}$$

$$\phi^{\rm ES}_{\rm SNO}(\nu_{\rm e}) = (2.21^{+0.31}_{-0.26}({\rm stat.}) \pm 0.10({\rm syst.})) \times 10^6{\rm cm}^{-2}{\rm s}^{-1} \tag{2.55}$$

$$\phi^{\rm NC}_{\rm SNO}(\nu_{\rm e}) = (5.21 \pm 0.27({\rm stat.}) \pm 0.38({\rm syst.})) \times 10^6{\rm cm}^{-2}{\rm s}^{-1} \tag{2.56}$$

The resultant $\phi(\nu_\mu \text{ or } \nu_\tau)$ from SK and SNO flux results is

$$\phi(\nu_\mu \text{ or } \nu_\tau) = (3.62 \pm 0.48) \times 10^6{\rm cm}^{-2}{\rm s}^{-1} \tag{2.57}$$

where the statistical an systematic errors are added in quadrature. Now $\phi(\nu_\mu \text{ or } \nu_\tau)$ is $7.5\sigma$ above 0, providing stronger evidence for neutrino oscillation.

## 2.8 Global analysis of the solar neutrino data

A number of solar neutrino flux results in Super Kamiokande and all radio chemical solar neutrino experiments yielded various solutions in terms of two neutrino oscillations. For example, Bahcall, Krastev, and Smirnov [74] found at 99.7% confidence level eight allowed descrete regions in two neutrino oscillation space. From the flux constrained results, these are five solutions for active neutrinos (LMA, SMA, LOW, VAC, and Just So$^2$) and three separate solutions for sterile neutrinos (SMA(sterile), VAC(sterile), and Just So$^2$(sterile)). LMA, SMA, LOW, VAC, are abbreviations of large mixing angle, small mixing angle, low probability or low mass, and vacuum, respectively. The summary of solutions is shown in Table 2.6.

The best-fit points for the five solutions for active neutrinos are shown below.

- LMA : $\Delta {\rm m}^2 = 4.2 \times 10^{-5}{\rm eV}^2, \tan^2\theta = 0.26$
- SMA : $\Delta {\rm m}^2 = 5.2 \times 10^{-6}{\rm eV}^2, \tan^2\theta = 5.5 \times 10^{-4}$
- LOW : $\Delta {\rm m}^2 = 7.6 \times 10^{-8}{\rm eV}^2, \tan^2\theta = 0.72$

| Effect | Solution<br>for Active neutrino | Solution<br>for sterile neutrino |
|---|---|---|
| Vacuum Oscillations | VAC(active) | VAC(sterile) |
| MSW effect | LMA(active) | - |
| | SMA(active) | SMA(sterile) |
| | LOW(active) | - |
| | Just So$^2$(active) | Just So$^2$(sterile) |

Table 2.6: Expected solution from flux constrains of SK and radiochemical experiments.

- Just So$^2$ : $\Delta\mathrm{m}^2 = 5.5 \times 10^{-12}\mathrm{eV}^2, \tan^2\theta = 1.0$
- VAC : $\Delta\mathrm{m}^2 = 1.4 \times 10^{-10}\mathrm{eV}^2, \tan^2\theta = 0.38$

For the three solutions for sterile neutrinos, the best-fit points are similar to the corresponding solutions for active neutrinos. The oscillation allowed region for each solution from flux constrains of SK, SNO(CC:Charged current results) and radiochemical experiments is shown in figure 2.17.

The survival probability of expected energy spectrum for each solution is shown in figure 2.18. The top figure shows the predicted energy spectrum from BP2000 SSM. The solid lines for LAM and LOW solutions indicates the night-time spectrum. The dashed lines indicates the day-time spectrum. The horizontal axis is the neutrino energy (MeV).

The survival probability of the expected energy spectrum and day-night energy spectrum (zenith spectrum named in Super Kamiokande) for typical parameter values of oscillation solutions are dependent on recoil electron energy strongly like as the shown figure. So, the information of the spectra shape can be used to distinguish between possible solutions.

In addition to above flux informations, the Super Kamiokande day-night spectrum and SNO results constrains the probable solution. Especially, Super-Kamiokinde-I results of the energy and zenith spectrum have effect on determination of solar neutrino oscillation parameter remarkably because of the large statistical and precise measurements. Without SK data, the strongest constraint of the parameters is a $\chi^2$ fit to the charged-current neutrino rates from GALLEX/GNO, SAGE, Homestake, and SNO experiments.

However, SK data breaks the degeneracy in $\chi^2$ of these regions by analyzing the shape of the zenith-angle spectrum which combines spectrum and daily variation analysis. Here we utilize the zenith angle spectrum from the entire SK-I data set collected between May 31st, 1996 and July 15th, 2001 (1496 live days). There is no indication of spectral distortion, the $\chi^2$ to an undistorted spectrum is 4.6 for 7 degrees of freedom (71% C.L.). No significant daily variation is found, the day/night rate asymmetry is

$$\mathrm{Asym.}_{\mathrm{day,night}} = \frac{\phi_{\mathrm{day}}(\nu_{\mathrm{e}}) - \phi_{\mathrm{night}}(\nu_{\mathrm{e}})}{1/2(\phi_{\mathrm{day}}(\nu_{\mathrm{e}}) + \phi_{\mathrm{night}}(\nu_{\mathrm{e}}))} = -0.021 \pm 0.020(\mathrm{Stat.})^{+0.013}_{-0.012}(\mathrm{Syst.}) \qquad (2.58)$$

If the SMA solution was really a solution of the neutrino oscillation, the survival probability of energy spectrum will increase with energy, while it is almost flat for the LMA and LOW solutions.

Figure 2.19 shows the result of the zenith angle spectrum fit. The SMA and VAC regions are excluded since they require a distorted $^8$B neutrino spectrum. The lower part of the LMA and the upper part of the LOW solution predict daily variations and are therefore disfavored. The excluded areas are independent of the SSM neutrino fluxes.

Since there is no indication of a distortion of the SK zenith spectrum, an analysis of the zenith spectrum shape alone can only yield excluded regions. However, if the $^8$B flux is known,

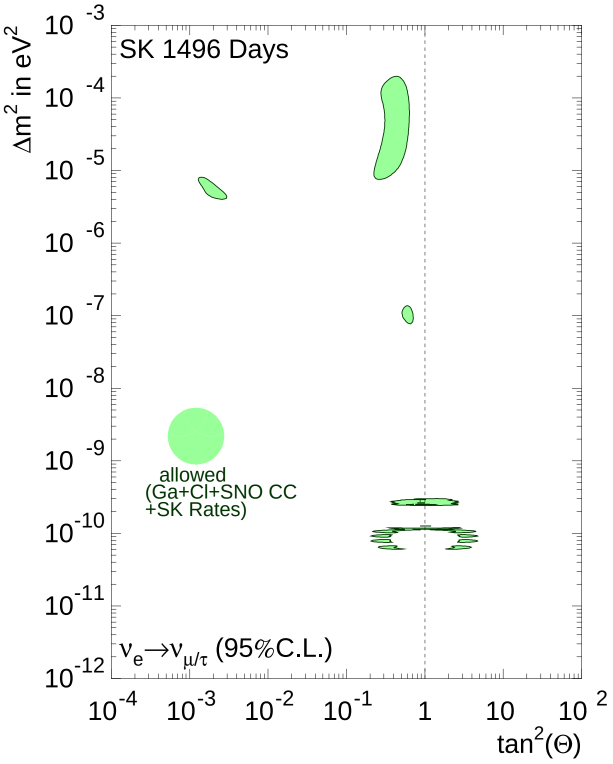

Figure 2.17: The 95% C.L. allowed regions which satisfy all four flux measurements: Chlorine, Gallium, SK and SNO(CC).

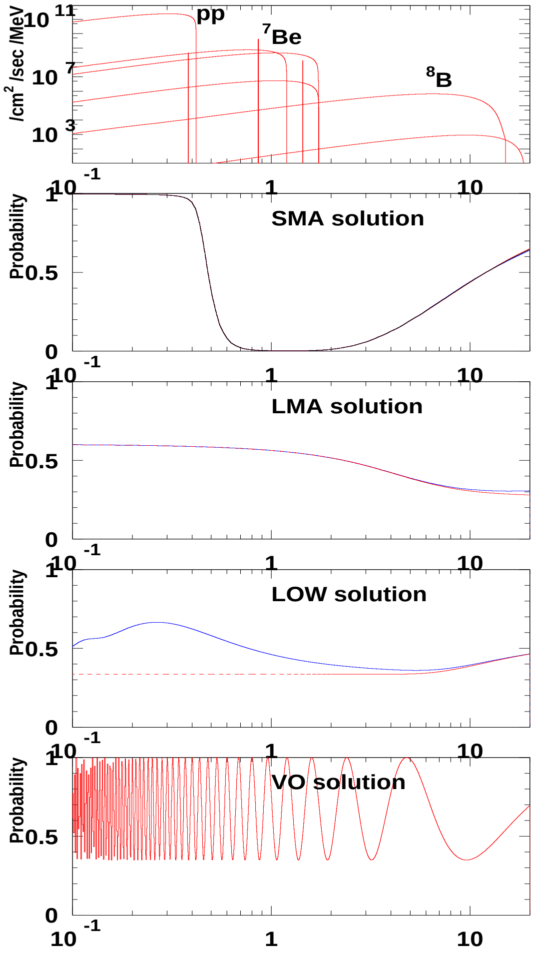

Figure 2.18: The expected energy spectrum for each oscillation solution and day-night time energy spectrum for LMA and LOW solutions. The horizontal axis is the neutrino energy (MeV).

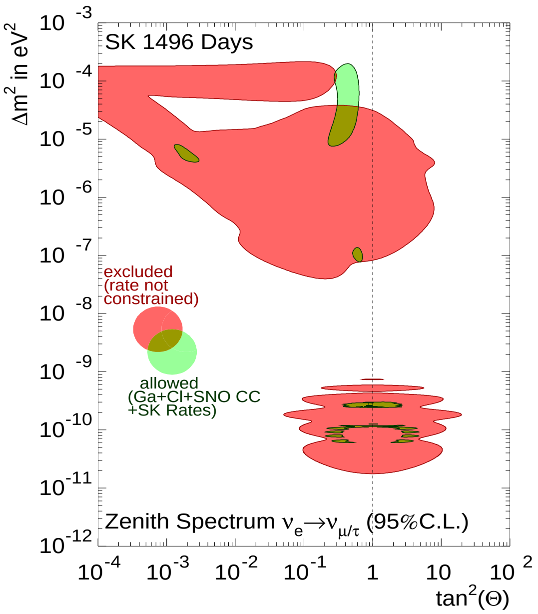

Figure 2.19: SSM flux independent excluded areas using the SK zenith spectrum shape alone overlaid with the allowed regions.

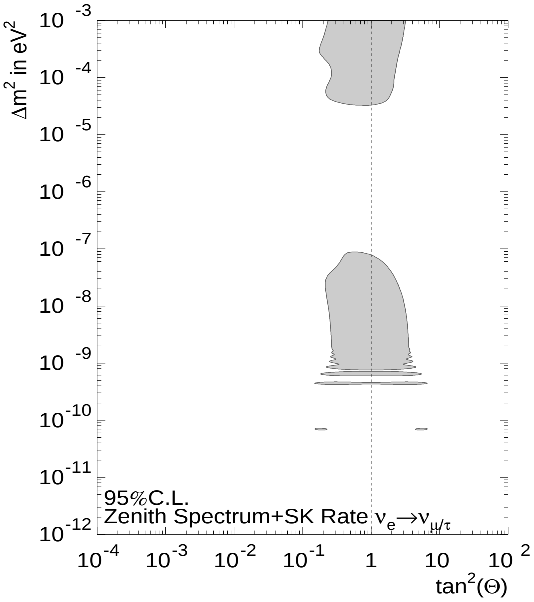

Figure 2.20: Allowed areas using only SK data and the SSM $^8$B neutrino flux prediction. Both allowed regions indicate large neutrino mixing.

the SK rate can be predicted. Then, the zenith spectrum shape can be combined with the SK rate into a single measurement. Figure 2.20 shows the allowed regions using SK rate between SSM and observed flux and zenith angle spectrum in combination with the $^8$B flux prediction and uncertainty of the SSM. The remained allowed regions is two: the LMA and quasi-VAC solution.

Finally, a comparison between the SK rate and SNO's charged-current rate yields another $^8$B flux constraint which is independent on the SSM, so a combination of the SK rate and zenith angle spectrum with the SNO charged-current rate need not rely on any neutrino flux prediction. Figure 2.21 shows the determination of the oscillation solution from the all solar neutrino data combination (Homestke, GALLEX/GNO, SAGE, SK, ,and SNO(CC, NC reaction)).

The combined fit to the charged-current interaction rates measured by several experiments result in many allowed regions of neutrino mixing and mass square difference: LMA, SMA, LOW, Just-So, VAC. The absence of spectral distortion and daily variations of the SK solar neutrino interactions rate strongly constrains these regions rejecting SMA, LOW, and VAC solutions at 95% C.L., while leaving only the higher mass square difference LMA and the quasi-VAC region. When all solar neutrino data are combined with SK data, only the higher mass square difference LMA solutions remain at 98.9% C.L.. The best fit parameter is like following.

$$\Delta m^2 = 6.9 \times 10^{-5} \mathrm{eV}^2, \tan^2\theta = 0.38 \tag{2.59}$$

Thus the combined results of all solar neutrino experiments can be used to determine a unique region of oscillation parameters that explains the famous solar neutrino problem.

The LMA solutions means the following phenomenon. A $\nu_\mu$ converted from $\nu_e$ in the Sun may oscillate back to $\nu_e$ via the MSW effect in the Earth. So the day-night time results might be different for a certain parameter region. This is called "neutrino regeneration". In the Earth, the resonance condition is represented as follows [72]:

$$\Delta \mathrm{m}^2 \approx 4 \times 10^{-6} \mathrm{eV}^2 (\rho / 5 \mathrm{Y_e g cm}^{-3}) \tag{2.60}$$

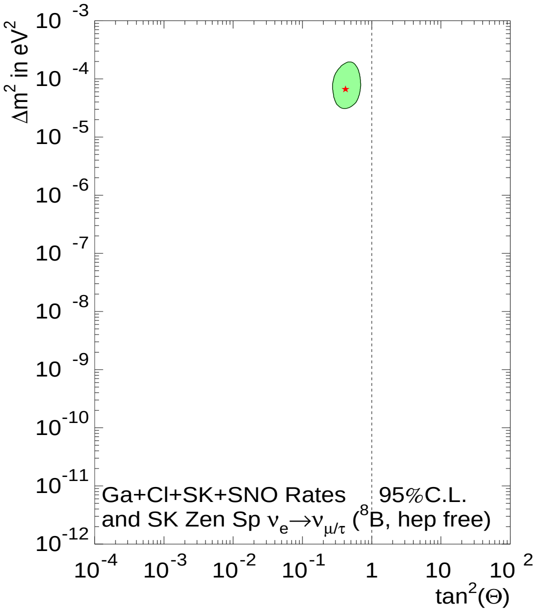

Figure 2.21: The combined fit to SK data and all rates favor the LMA solution. The best fit point is indicated by the asterisk. All fits are independent of the SSM $^8$B flux and *hep* flux.

where the density of the Earth $\rho = 3.5 \sim 13 \text{gcm}^{-3}$, the neutrino energy $E_\nu \sim 10MeV$ and the electron number per atomic number $Y_e 1/2$. The oscillation length of the resonance in $L_{M,res} \sim 6.8 \times 10^8 \text{cm}/\sin 2\theta$. It is of the order of the diameter of the Earth ($1.3{\times}10^3$cm), even if $\sin 2\theta$ is large.

# Chapter 3

# Super Kamiokande

In this chapter, the detection principle and the components of the SK detector are described in detail. The cross section for $\nu_e - e$ elastic scattering and $\check{C}$erenkov radiation is explained. The water purification system and air purification system to reduce the background of radioactivity in SK is also presented. The DAQ system is described in detail. About the detector simulation, the explanation is presented in appendix B.

## 3.1 Detection principle in Super-Kamiokande

When a charged particle having a velocity of $v$ travels in a medium the index of refraction of which is $n$, $\check{C}$erenkov photons are emitted if $v > c/n$, where $c$ is the light velocity in vacuum. $\check{C}$erenkov photons are emitted into a forward cone around the particle track with opening angle of $\theta$ measured from the direction of the particle. $\theta$ is given by:

$$\cos\theta = \frac{1}{n\beta} \quad (\beta \equiv \frac{v}{c}) \tag{3.1}$$

In the case of pure water, ($n = 1.334$), $\theta$ is about 42° for $\beta \simeq 1$. The number of $\check{C}$erenkov photons ($dN$) generated in the wavelength interval $d\lambda$ per track length $dx$ is,

$$dN = 2\pi\alpha \left(1 - \frac{1}{n^2\beta^2}\right) \frac{1}{\lambda^2} dx d\lambda \tag{3.2}$$

$\alpha$ is the fine structure constant. The number of $\check{C}$erenkov photons in the wavelength range of 300~600nm, which is the sensitive region of the PMTs, is about 340 in water per 1cm track length for a charged particle having a unit charge and velocity of $\beta \simeq 1$. The energy threshold for an electron to emit $\check{C}$erenkov photons is $\frac{n}{\sqrt{n^2-1}} m_e \simeq 0.78$ MeV, where $m_e = 0.511$ MeV is the rest mass of an electron.

A neutrino interacts with electrons via neutral and charged current interaction:

$$\nu + \mathrm{e} \rightarrow \nu + \mathrm{e} \tag{3.3}$$

The differential cross section $d\sigma_{\nu e}$ of neutrino-electron elastic scattering is given by:

$$\frac{d\sigma_{\nu e}}{dT_e} = \frac{G_F^2 m_e}{2\pi} \left\{ A_0 + B_0 \left(1 - \frac{T_e}{E_\nu}\right)^2 + C_0 \frac{m_e T_e}{E_\nu^2} \right\} \tag{3.4}$$

where $T_e$ is the scattered electron's kinetic energy, $E_\nu$ is the incident neutrino energy, $G_F = 1.16636 \times 10^{-11}$ MeV$^{-2}$ is the Fermi coupling constant. The order of magnitude for the cross section is set by the first coefficient $\frac{G_F^2 m_e}{2\pi} = 4.31 \times 10^{-45}$ (cm$^2$/MeV). The parameters, $A_0, B_0, C_0$

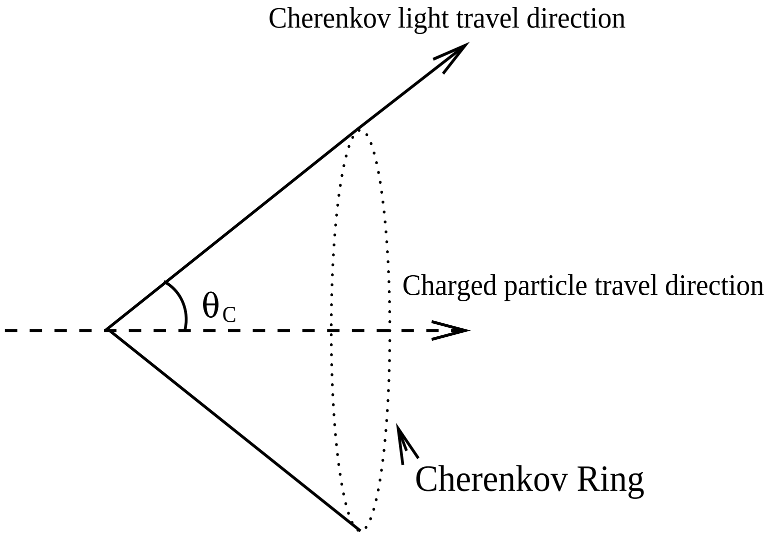

Figure 3.1: The definition of the $\check{C}$erenkov angle.

in equation (3.4), are defined as:

$$\begin{aligned} A_0 &= (g_V + g_A)^2, \quad B_0 = (g_V - g_A)^2, \quad C_0 = g_A^2 - g_V^2 && (3.5)\\ g_V &= 2\sin^2\theta_W + \frac{1}{2}, \quad g_A = +\frac{1}{2} \quad \text{for } \nu_e && (3.6)\\ g_V &= 2\sin^2\theta_W - \frac{1}{2}, \quad g_A = -\frac{1}{2} \quad \text{for } \nu_\mu \text{ or } \nu_\tau && (3.7) \end{aligned}$$

where $\theta_W$ is the Weinberg angle and $\sin^2\theta_W = 0.2317$. The total cross section $\sigma_{\nu e}$ is calculated by integrating equation (3.4) for $T_e$ from 0 to $T_{max}$,

$$\begin{aligned} \sigma_{\nu e} &= \int_0^{T_{max}} \frac{d\sigma_{\nu e}}{dT_e} dT_e \\ &= \frac{G_F^2 m_e}{2\pi}\left[A_0 T_{max} + \frac{B_0 E_\nu}{3}\left\{1 - \left(1 - \frac{T_{max}}{E_\nu}\right)^3\right\} + \frac{C_0}{2}\frac{m_e T_{max}^2}{E_\nu^2}\right] && (3.8) \end{aligned}$$

where $T_{max}$ is maximum kinetic energy for the recoil electron in (3.3),

$$T_{max} = \frac{E_\nu}{1 + \frac{m_e}{2E_\nu}} \tag{3.9}$$

The differential and total cross sections of $\nu$-e scattering with radiative corrections are calculated by [77]. Some of the Feynman diagrams for the electro-magnetic one loop contributions are drawn in figure 3.2. These corrections reduce the total cross section by about 2%. For the highest energy $^8$B neutrinos, the cross section is reduced by about 4%. In $\nu_\mu$-e scattering there is no contribution from charged current interactions at low energies. Total cross sections for $\nu_e$-e and $\nu_\mu$-e scattering with radiative corrections as a function of incident neutrino energy are drawn in figure 3.3. The total cross section for the $\nu_e$-e scattering is about 6 times larger than that for $\nu_\mu$-e scattering due to the contribution of the charged current interaction. Hence, if an electron neutrino is converted to another type of neutrino ($\nu_\mu$ or $\nu_\tau$), the event rate of $\nu$-e scattering decreases.

The differential cross section in the case of incident neutrino energy of 10 MeV for $\nu_e$+e→ $\nu_e$+e scattering is shown in figure 3.4 [77].

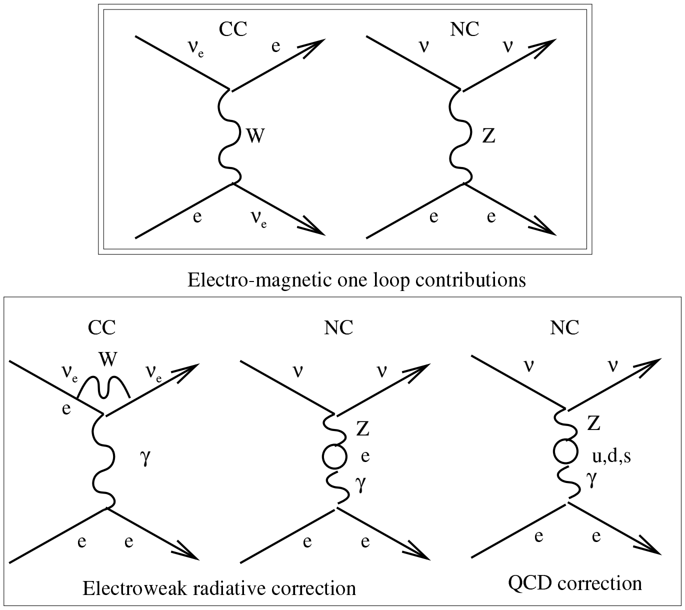

Figure 3.2: A Feynman diagram for one-loop QCD correction and Feynman diagrams for one-loop electroweak radiative correction.

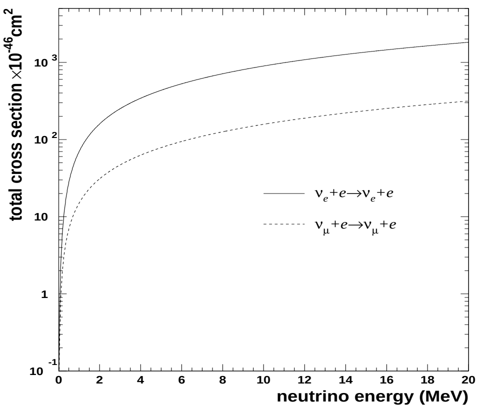

Figure 3.3: Total cross sections for $\nu_e$-e and $\nu_\mu$-e scattering as a function of energy of an incident neutrino.

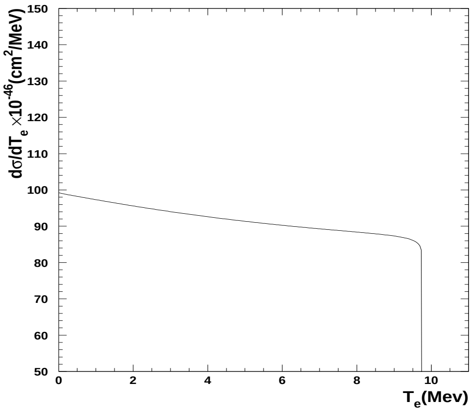

Figure 3.4: Differential cross section of $\nu_e$+e→ $\nu_e$+e scattering for an incident neutrino energy of 10 MeV. The horizontal axis is the kinetic energy of a recoil electron.

The recoil electron energy spectrum $F(T_e)$ is calculated to be:

$$F(T_e)dT_e = \left\{ \int_0^{E_{\nu,max}} \frac{d\sigma_{\nu e}(E_\nu, T_e)}{dT_e} \phi(E_\nu) dE_\nu \right\} dT_e \tag{3.10}$$

where $\phi(E_\nu)$ is energy spectrum of the neutrinos and $E_{\nu,max}$ is the maximum neutrino energy. In the case of $^8$B solar neutrinos, the energy spectrum of the recoil electrons is shown in figure 3.5.

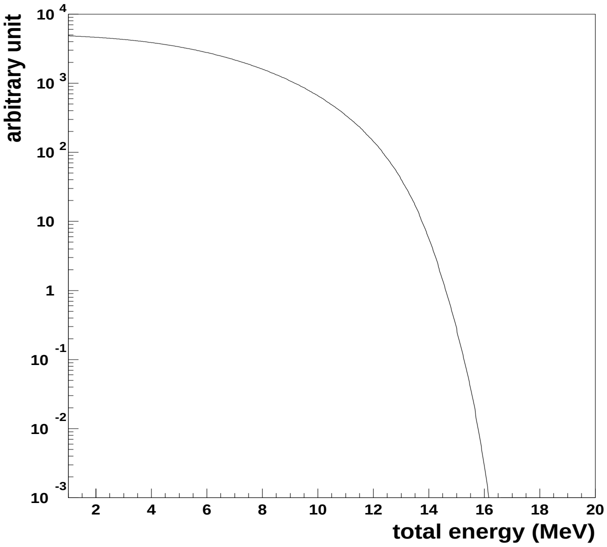

Figure 3.5: The energy spectrum of recoil electrons $^8$B solar neutrino scattering. The horizontal axis is the total energy of the electrons.

The scattering angle $\theta$ is determined by the kinematical condition,

$$\cos\theta = \frac{1 + \dfrac{m_e}{E_\nu}}{\sqrt{1 + \dfrac{2m_e}{T_e}}} \tag{3.11}$$

When the neutrino energy is high enough compared with the electron mass, the scattering angle can be approximated by:

$$\theta \leq \sqrt{\frac{2m_e}{T_e}} \tag{3.12}$$

Therefore, the recoil electron keeps the information about incident neutrino's direction. However, because of multiple scattering in the water, the angular resolution is limited to about 27° for an electron energy of 10 MeV.

The advantage of using water Čerenkov counters for the observation of solar neutrinos is that the detector can measure the precise time when an electron is scattered, and the energy and direction of the recoil electron. Hence, it is possible to measure how much the electron neutrino flux changes between day and night, or seasonally. Also the energy spectrum of the incident neutrinos can be inferred from the measured energies of the recoil electrons.

## 3.2 Detector description

SK was commissioned and data taking began April, 1996. It was shut down for maintenance and upgrade in July 2001, after logging 1,678 live days of running with high efficiency. In this paper, this initial 1996∼2001 running period will be treated, referred to as SK-I. Figure 3.6 is the integrated total live-time as a function of elapsed day from April 1, 1996 to July 15, 2001.

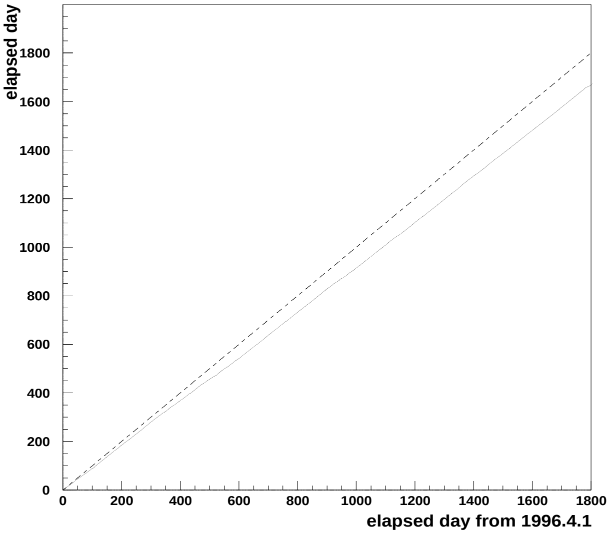

Figure 3.6: The integrated live time from the beginning of SK. The dashed line is expected total live time.

SK is a water Čerenkov detector located underground in the Kamioka mine in Gifu Prefecture, Japan. Its latitude and longitude are 36°25' N and 137°18' E, respectively. The average rock over burden above SK is 2800 m.w.e. A schematic view of the detector is given in figure 3.7. The reason why the detector is underground is to shield against cosmic ray muons. Compared to ground level, the intensity of muons is reduced by about 1/100000 at the depth of the SK detector. The muon rate in SK is 1.88Hz.

Measured background radiation rates for $\gamma$ rays and neutrons near the Kamiokande cavity dome [1] are shown in table 3.1.

| Particle | Energy range | Rate |
|---|---|---|
| $\gamma$ rays | $E_\gamma > 0.5$ MeV | $0.1\ \mathrm{cm^{-2}s^{-1}sr^{-1}}$ |
| | $E_\gamma > 5$ MeV | $2.7\ \times^{-6}\mathrm{cm^{-2}s^{-1}sr^{-1}}$ |
| Neutrons | $E_n \leq 0.05$ MeV | $1.4\ \times 10^{-5}\mathrm{cm^{-2}s^{-1}sr^{-1}}$ |
| | $0.05 < E_n \leq 2.5\times10^6$ MeV | $2.5\ \times 10^{-5}\mathrm{cm^{-2}s^{-1}sr^{-1}}$ |
| | $2.5\times10^6 < E_n \leq 2.5\times10^7$ MeV | $0.33\ \times 10^{-5}\mathrm{cm^{-2}s^{-1}sr^{-1}}$ |

Table 3.1: Measured background radiation rates for $\gamma$ rays and neutrons near the Kamiokande cavity.

A cylindrical stainless steel tank forms the SK detector. The tank, whose total height is 41.4 m and diameter is 39.3 m, holds 50,000 $\mathrm{m}^3$ of ultra pure water with a water and air purification system, photomultiplier tubes (PMTs), electronics and online data acquisition system, and off-line computer facilities. SK is split into two optically separate detectors: inner and outer summarized in table 3.2. The separation between the inner and outer detectors is provided by a stainless steel structural grid. Tyvek, and polyethylene black sheets. Although the inner and outer detectors are optically separated, water can flow between the two detectors.

The local detector coordinate system of SK is shown in figure 3.8.

The wall of the cave is covered by "Mineguard", a polyurethane material made by the Canadian company Urylon, which blocks radon emanating from the rock.

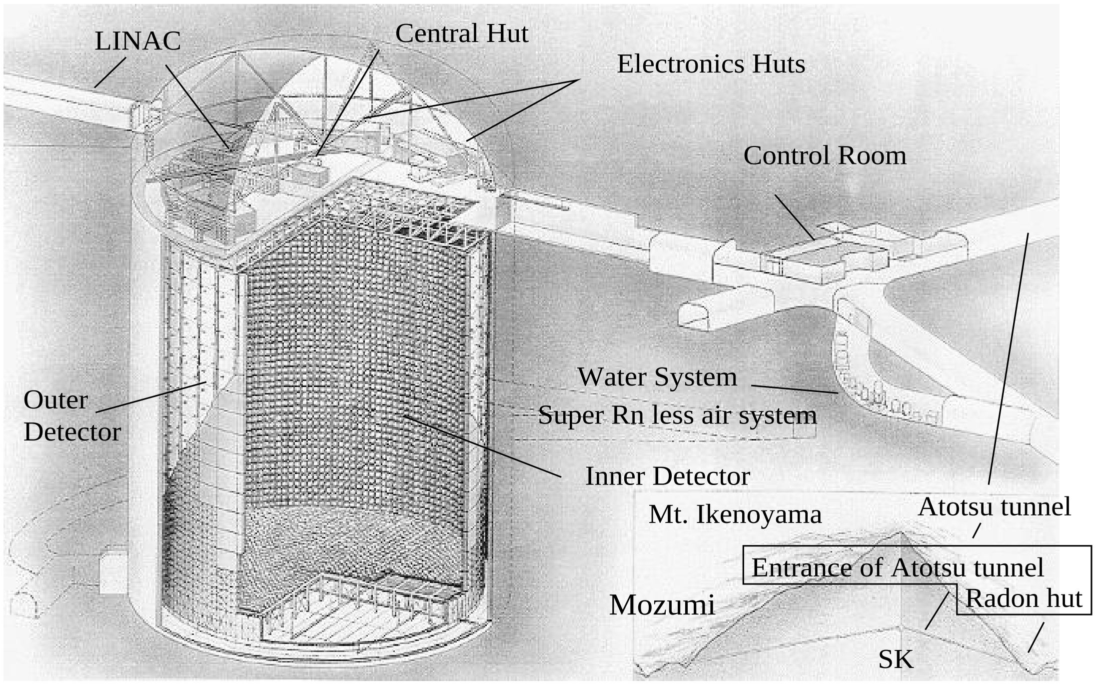

Figure 3.7: Overview of the Super-Kamiokande.

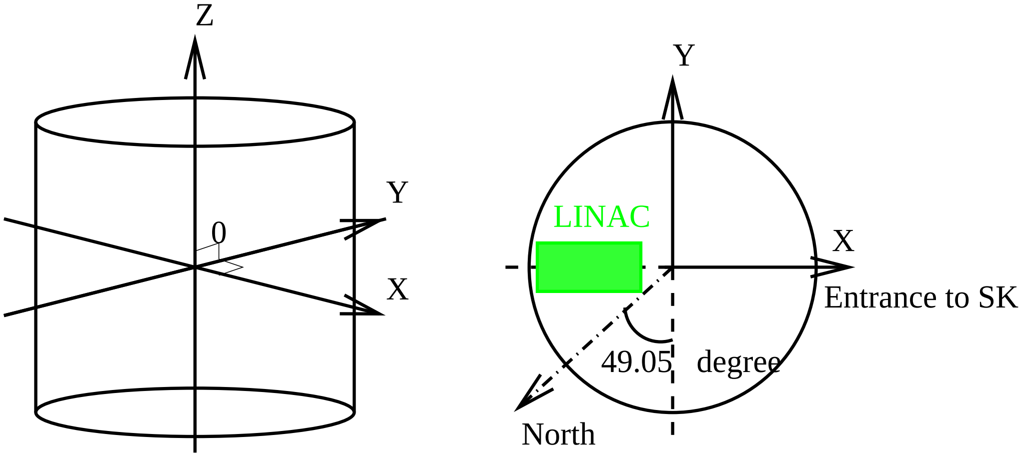

Figure 3.8: The local detector coordinate system of SK.

The tank is sealed tightly to keep the mine's radon rich air outside. Radon gas is the most serious background for the solar neutrino analysis. The concentration of radon gas in the dome is about 1500 Bq/m$^3$ in summer time and 30 Bq/m$^3$ in winter time. This large difference is caused by the flow of air in the mine. Air blows into the mine in the winter and out of the mine in the summer.

| Item | Value |
|---:|---|
| Tank dimension | 39.3m in diameter×41.4m in height |
| volume | 50 ktons |
| Inner part dimension | 33.8m in diameter×36.2m in height |
| volume | 18 ktons |
| Number of PMT | 748 (top and bottom) and 7650 (barrel) |
| Outer part thickness | 2.6 m on top and bottom |
| | 2.75 m on barrel |
| volume | 32 ktons |
| Number of PMT | 302 (top), 308 (bottom) and 1275 (barrel) |
| Fiducial area thickness | 2m (5.5 R.L. and 3.3 N.L.) from the inner wall |
| Fiducial area volume | 22.5 ktons |

Table 3.2: Several parameters of Super-Kamiokande detector. R.L and N.L mean radiation length and nuclear interaction length, respectively.

We use 11,146 20-inch PMTs in the inner detector and 1885 8-inch PMTs in the outer detector, as summarized in table 3.2.

### 3.2.1 The inner detector

The inner detector is a cylinder of 36.2 m in height and 33.8 m in diameter. It encloses 32.481 m$^3$ of water, which is viewed by 11,146 inward-facing 50 cm diameter photomultiplier tubes (PMTs), which will be explained later. All of the PMTs and two of the outer detector PMTs constitutes one super-module. Figure 3.9 is schematic view of a super module. In the inner detector, PMTs are placed at intervals of 70 cm, and the ratio of PMT area to all area (photo coverage) is 40.41%. The wall of the tank is covered with black polyethylene terephthalate sheets (called "black sheet") behind the inner PMTs to suppress the reflection of Čerenkov light and the leakage of light from or to the outer detector.

Super-Kamiokande can detect events over a wide range of energy, from 4.5 MeV to over 1 TeV. Each ID PMT has a dynamic range from 1 photoelectron (pe) to 300 pe. For low energy events used for solar neutrino studies, the energy of event is calculated from the number of PMT hits, while for high energy is measured terms of net charge detected PMTs.

### 3.2.2 The outer detector

The outer detector surrounds the inner detector and provides an almost uniformly thick (1.95∼2.20 m) $4\phi$ active veto. The purpose of the outer detector is to active veto cosmic ray muons, and to decrease the detection of $\gamma$ rays from the surrounding rock.

The outer detector is reviewed by 1,885 outward-pointing 20 cm diameter PMTs (HAMAMATSU R1408) with 60 cm square wavelength shifter plates [1] to increase the photo coverage. All outer surfaces in the outer detector are covered with a reflective material, White Tyvek, to enhance light collection in the OD. Thus, all surfaces of the outer tank are covered with white tyvek sheets with a reflectivity of above 80%.

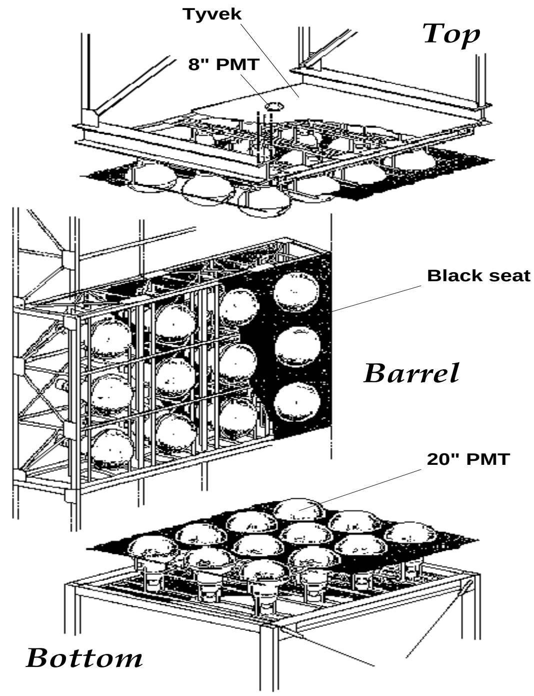

Figure 3.9: A super-module supports twelve ID PMTs and two OD PMTs.

## 3.3 ID photomultiplier tube

We use 50 cm diameter PMTs (HAMAMATSU R3600-05) in the ID. A schematic view of a PMT is given is figure 3.10. It was originally developed by the HAMAMATSU Photonics Company and Kamiokande collaborations and improved for use in SK [1]. The improved photons are the following :

- The 1 photo electron(p.e.) peak has become clearer by optimizing the structure of the dynode as shown in figure 3.11.
- A lager area for the dynode has reduced the influence of the residual geomagnetic field. Hence, the timing resolution (i.e. the transit time spread) at the 1 p.e level has become better (5 nsec → 3 nsec).

The glass body of the PMT is made of Prevex glass of 5 mm thickness which is transparent to light down to 330 nm in wavelength. The photocathode area is coated with Bialkali material (Sb-K-Cs). The quantum efficiency is a function of light wavelength is shown in figure 3.12. It is 22% at 390 nm.

The dynode has Venetian blind structure with 11 stages, which provides a large photosensitive area. The dark noise rate caused by thermal electrons from the photocathode is shown figure 3.13. The average dark rate is stable around 3.14 kHz after 2 months from the start of SK. The value of supplied voltage which gives a gain of $10^7$ is 2000 V. The average transit time is about 100 nsec for multi p.e. light. For single p.e. light, the variation of the transit time of PMTs is about 10 nsec in a supplied voltage range 1500 to 2000 V.

The large size of the PMTs makes them susceptible to the geomagnetic field. To obtain a uniform response from the PMTs, the geomagnetic field (450 mG in natural conditions) must be reduced to less the 100 mG [1]. Compensation coils are used accomplish this in SK and the residual magnetic field in kept at less than 100 mG in every position of the detector.

Some of the PMTs are dead by short circuit or some other unknown response. The time variation in the number of dead PMTs is shown figure 3.14. The fraction of the dead PMTs is about 1.4%.

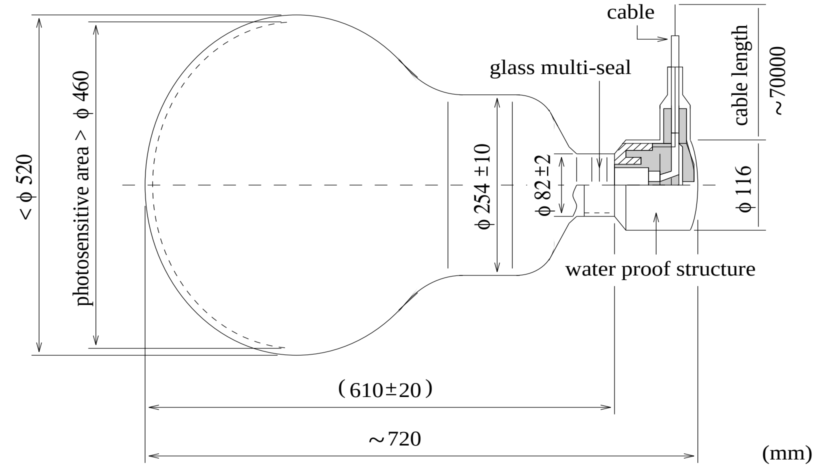

Figure 3.10: Schematic view of a 50 cm photomultipiler tube (HAMAMATSU R3600-05).

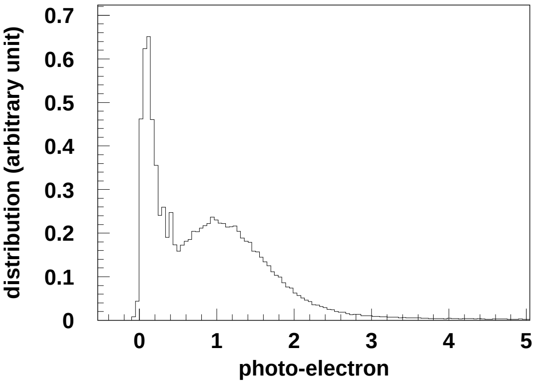

Figure 3.11: The single p.e. distribution from 50 m PMTs. There is a clear peak around 1 p.e.. A spike near the lowest region is caused by photo-electron that miss the first dynode.

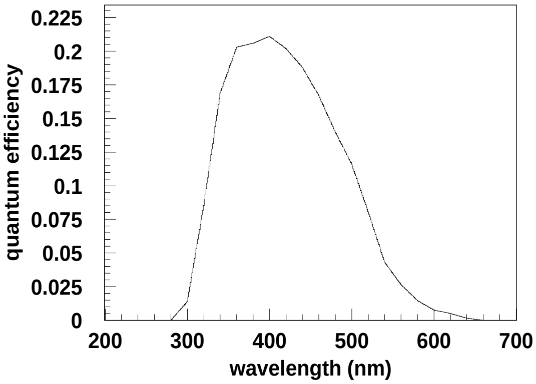

Figure 3.12: The quantum efficiency of the PMTs and the relative Čerenkov spectrum as a function of light wavelength.

Figure 3.15 shows the time variation of high and low energy trigger rate from the beginning of SK-I in ID detector. The right plot is high energy trigger rate and the left plot is low energy trigger rate.

## 3.4 The water purification system

In purities in the SK water can cause strong attenuation and scattering of Čerenkov light. Moreover, if they are radioactive, like $^{222}$Rn and $^{220}$Rn, they could become a possible source of background to the solar neutrino events, because the $\beta$-decay of their daughter nucleus causes a

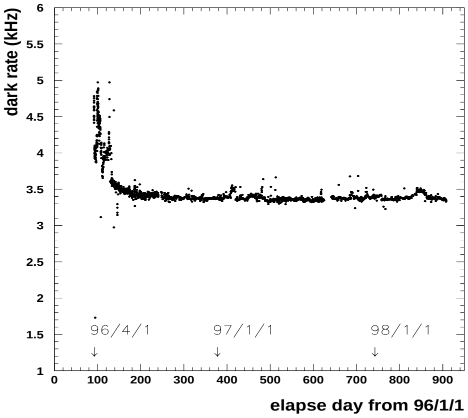

Figure 3.13: The time variation of dark rate from the beginning of SK.

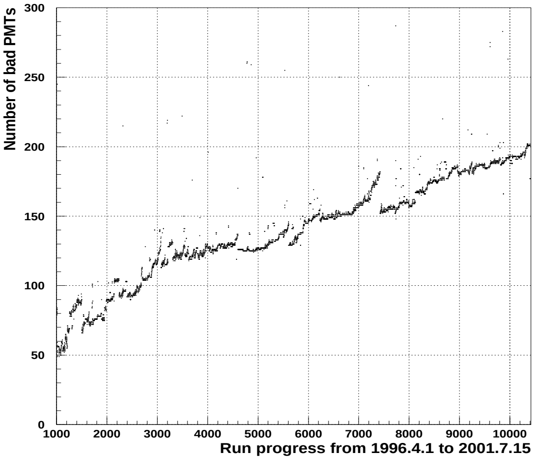

Figure 3.14: The time variation of the number of dead PMTs from the beginning of SK.

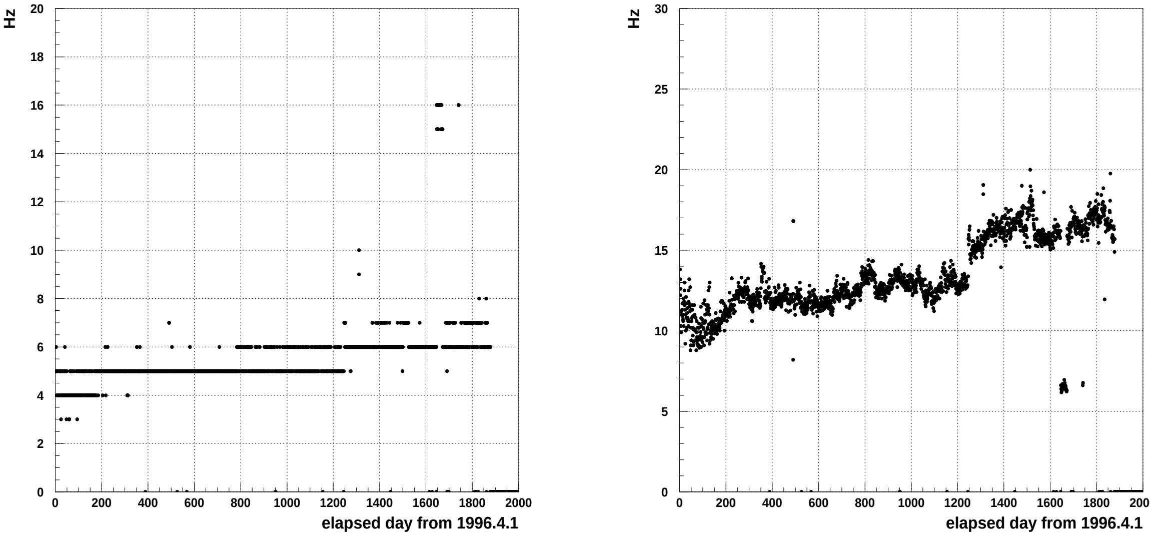

Figure 3.15: The time variation of high and low energy trigger rate from the beginning of SK.

similar event as solar neutrino event which means $\nu_e - e$ elastic scattering. The decay chain of $^{222}$Rn is shown in figure 3.20. None of the electrons or $\gamma$ rays from the decay chain have energy above threshold for this analysis 4.5 MeV. However, because of finite energy resolution of SK, such low energy electrons are sometimes observed as electrons with energy above 4.5 MeV. So, the purity of the water is essential for solar neutrino observation in SK.

The SK water purification system has been modified and upgraded with Organo Corporation. In this section, the basic components of the system is explained. The details of the modification and upgrading of the water system is explained in chapter 7 in detail.

The source of water in SK is an underground aquifer in the Kamiokande mine. The water purification system makes highly purified water from the mine water. Figure 3.16 is a basic schematic view of the water purification system. The water passes through the following components:

- 1 $\mu$m normal filter :
  Remove relatively large particles. Some of Rn also rejected with dust.

- Heat exchanger(HEX) :
  Water pumps increase the water temperature. The heat exchanger decrease the temperature down to about 12∼13°C to inhibit bacterial growth and to suppress the water convection in the SK tank.

- Ion exchanger(IEX) :
  Removes metal ion ($\mathrm{Fe}^{2+}, \mathrm{Ni}^{2+}, \mathrm{Co}^{2+}$) impurities in the water. It can also remove $^{218}$Po which is a daughter nucleus as a result of the decay of $^{222}$Rn and easily ionize. The water resistance is best indication of the concentration of the ion in the water. If no ion is in the water, the water resistance will be expected 18.2 M$\Omega$. In the SK water, the water resistance is 17.9∼18.2 M$\Omega$.

- UV sterizer(UV) :
  To kill bacteria. The documentation states the number of bacteria can be reduced to less than $10^3 \sim 10^4$/100ml.

- Rn-less-air dissolving system :
  Dissolve Rn less air in water to improve the Rn removal efficiency of the vacuum de-gasifier.

- Reverse Osmosis filters (RO) :
  Reverse osmosis by a high performance membrane which removes even organisms on the other of 100 modular weight. The output water is put back into the mine stream. The dissolving oxygen in the out put water is 10.8 $\mu$g/L after VD.

- Vacuum De-gasifier (VD) :
  Removes gases (Rn, Oxygen, etc) dissolved in water; about 96% of the dissolved radon gas is removed at this stage.

- Cartridge Polisher (CP) :
  High performance ion exchangers using high quality ion exchanger material.

- Ultra Filter (UF) :
  Removes sub-$\mu$m contamination. After the Ultra filter, the water is returned to the detector. The UF removes 10% of the water passed through. That water is recirculated through the water purification system again via the following equipment, which is shown by the dashed line in the figure.

- Membrane Degasifier (MD) :
  A membrane degasifier (MD) also removes radon dissolved in water. It is made of 30 hollow fiber membrane modules and a vacuum pump. A flow rate of 30 L/min of Rn-less

air from the air purification system is supplied to the MD system as purge gas. The typical pressure in the MD system is 2.6 kPa. The typical concentration of dissolved oxygen after the MD is 0.3 mg/L. The measured removal efficiency for radon is about 83%.

Usually, the water purification system supplies the purified water from the bottom of the tank and removes it from the top of the tank. The maximum capacity of the flow rate is 70 ton/hour. usually, the flow rate is 35 ton/hour. A summary of the quality of the purified water is given in table 3.3.

| Impurities | Reduction efficiency |
|---|---|
| $^{222}$Rn | $\sim$99% |
| $O_2$ | $\sim$96% |
| Dust $> 0.1\mu$m | $\sim$99.7% |
| Bacteria | $\sim$100% |
| Ion | $\sim$99% |

Table 3.3: The summary of the quality of the purified water.

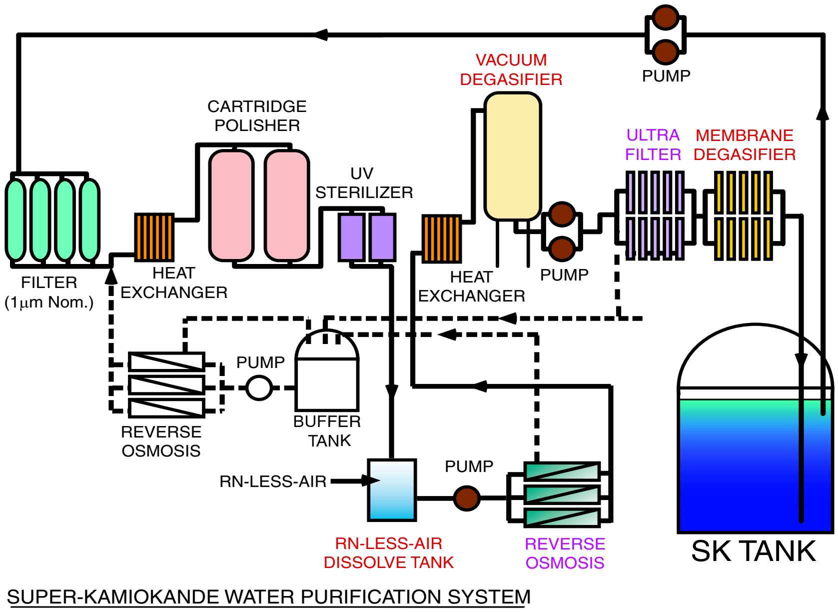

Figure 3.16: A schematic view of the water purification system.

## 3.5 The air purification system

SK is situated in mine, and the $^{222}$Rn concentration in the mine air is 50$\sim$2000 mBq/m$^3$. Therefore the detector is literally surrounded by the source of Rn gas. The rock dome above the water tank and the hallway are covered with Mineguard polyurethane material, which prevents Rn gas emanation from rocks. Double doors at all entrances also limit the amount of mine air that entries the detector area.

To keep radon levels in the dome area and water purification system below 100 Bq/m$^3$, fresh air is continuously pumped at approximately 10 m$^3$/min from outside the mine through an air duct along 1.8 km Atotsu tunnel to the experimental area. This flow rate generates a slight

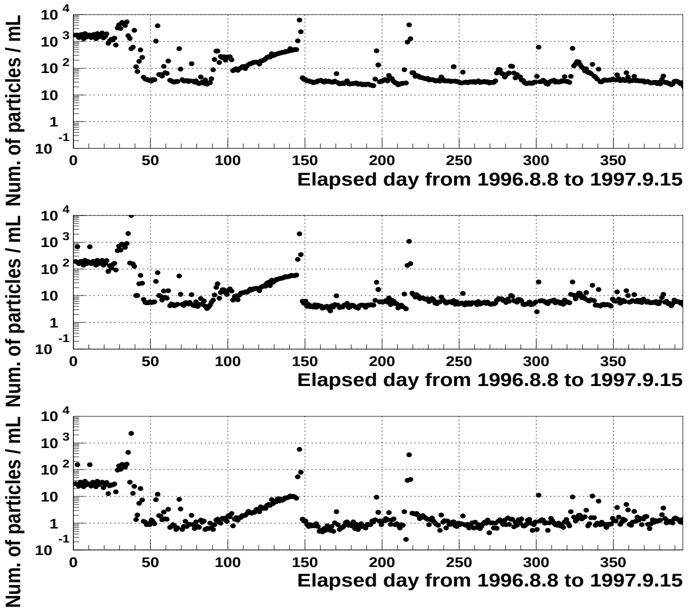

Figure 3.17: The time variation of the number of particles in the purified water. Each figure shows the number of particles of 0.1,0.2, and 0.3 $\mu$ size respectively from the top figure.

over-pressure in the SK experimental area, minimizing the entry of ambient mine air. A "Radon hut" in figure 3.7 was constructed near the Atotsu tunnel entrance to house equipment for the dome air system : a 40 hp air pump with 10 m$^3$/min/15 PSI pump capacity, air dehumidifier, carbon filter tanks, and control electronics. Fresh air from an intake (initially located at the Radon hut) is fed in to the air pump, and is then pumped through a dehumidifier, a carbon filter tank, and finally through a 1.8 km air duct from the Atotsu entrance to the experimental area. An extended intake pipe was installed at a location approximately 25 m above Atotsu tunnel entrance, where radon level concentration was found to remain at 10$\sim$30 Bq/m$^3$ all year long. Thus the 10 m$^3$/min fresh air flow from the Radon hut keeps the radon levels in the experimental area at approximately 30$\sim$50 Bq/m$^3$ throughout the year.

A part of the fresh air from the Radon hut is purified to Rn-less air with the air purification system. Figure 3.18 is a schematic view of the air purification system. It consists of three compressors, a buffer tank, driers, filters, and activated charcoal filters. The components of the air purification system as follows:

- Compressor : Takes in air from outside the mine and pressurizes it 7$\sim$8.5 atom.
- 0.3,0.1,0.01 $\mu$m filter : Removes dust in air.
- Air drier : Absorbs moisture since the radon reduction efficiency of the carbon column dependents on the humidity air.
- Carbon column (8 m$^3$): CO (Activated charcoal) absorbs Rn.
- Active charcoal (50 L) : Active charcoal cooled to -41°C traps the Rn.

Finally, after the air purification system, Rn reduction efficiency is $\sim$99.98% [1]. Figure 3.21 and figure 3.22 are the time variations of the radon concentration in various air.

Rn-less air is mainly supplied to $\sim$60 cm gap between the water surface and the top of the Super-Kamiokande tank. The Rn-less air is kept at a slight overpressure to help prevent ambient radon-laden air from entering the detector. Typical flow rates, dew point, and residual radon concentration are 18 m$^3$/hour, $\sim$-80(+1 kg/cm$^2$)°C, and a few mBq/m$^3$, respectively.

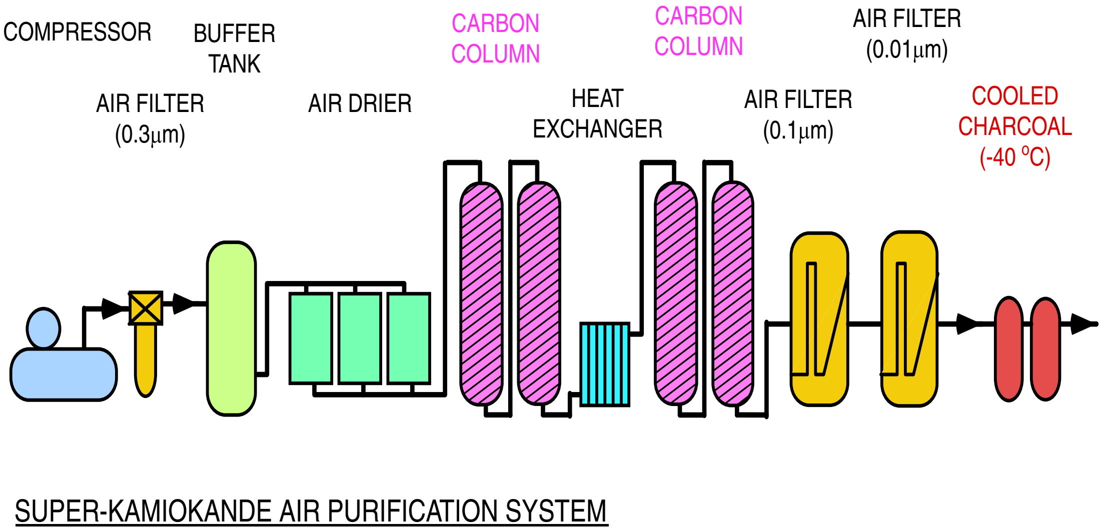

Figure 3.18: A schematic view of the air purification system.

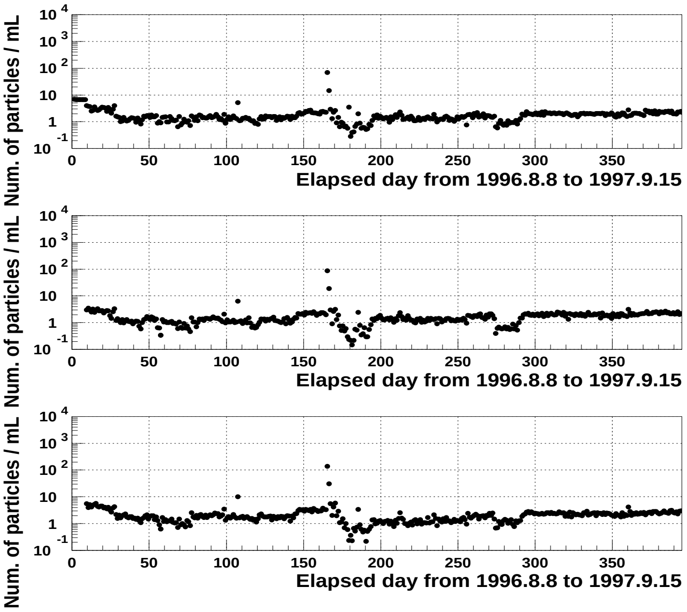

Figure 3.19: The time variation of the number of particles in the purified air. Each figure shows the number of particle of 0.1,0.2, and 0.3 $\mu$ size respectively from the top figure.

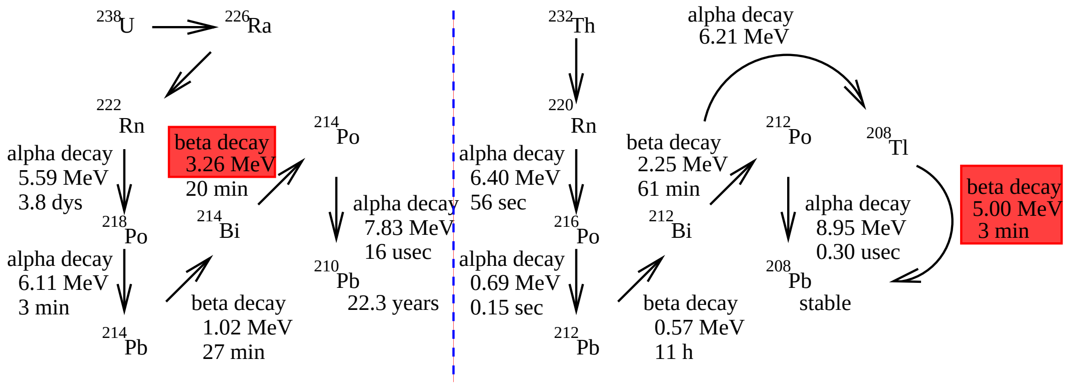

Figure 3.20: Rn decay series. The left side shows Uranium series of Rn. The right side shows Thorium series of Rn.

Table 3.4 is the summary of the radon concentration in the various samples. Table 3.5 is the list of the temperature condition at the various points.

| Standard Samples | Rn concentration(Bq/m$^3$) |
|---|---|
| Fresh air | 0.5∼1.0 |
| Air in the underground | $1.0\times10^3\sim4.0\times10^6$ |
| Water in the underground | $3.0\times10^3\sim4.0\times10^7$ |
| Kamioka Samples | Rn concentration(Bq/m$^3$) |
| Air in the mine | winter $8.0\times10^1\sim1.0\times10^2$ |
| | summer $6.0\times10^3\sim1.0\times10^4$ |
| Dome air on the tank | $5\times10^1\sim6.0\times10^1$ |
| Purified air after the system | $3.0\times10^{-3}\sim4.0\times10^{-3}$ |
| Purified air in the tank gap | $1.0\times10^{-2}\sim2.0\times10^{-2}$ |
| Purified water after the system | $6.0\times10^{-3}\sim10.0\times10^{-3}$ (before upgrade) |
| | $<1.0\times10^{-3}$ (after upgrade) |
| Purified water in the SK tank | $\sim5.0\times10^{-3}$ (before upgrade) |
| | $1.0\times10^{-3}\sim2.0\times10^{-3}$ (after upgrade) |
| Return water from the SK tank | $1.0\times10^{-2}\sim1.5\times10^{-2}$ (before upgrade) |
| | $<2.0\times10^{-3}$ (after upgrade) |

Table 3.4: The summary of the Rn concentration. Before and after mean before water system upgrading and after water system upgrading respectively.

## 3.6 The data acquisition system

### 3.6.1 The inner detector system

An overview of the data acquisition (DAQ) system is shown in figure 3.23. The signal cables which come from PMTs of ID and OD are extended on the top of the tank, where the electronics systems are located. The ID PMT signal cables (70m) are fed into ATM (Analog Timing Module) modules in a TKO (Tristan-KEK-Online) system. A TKO crate contains a GONG module (GO or NoGO, which distributes control signals as a master module to its slave modules), a SCH module (Super Controller Header, which is a bus-interface module between TKO and VME (Versa Module Europe)), and 20 ATM modules (which digitize analog signals from PMTs for

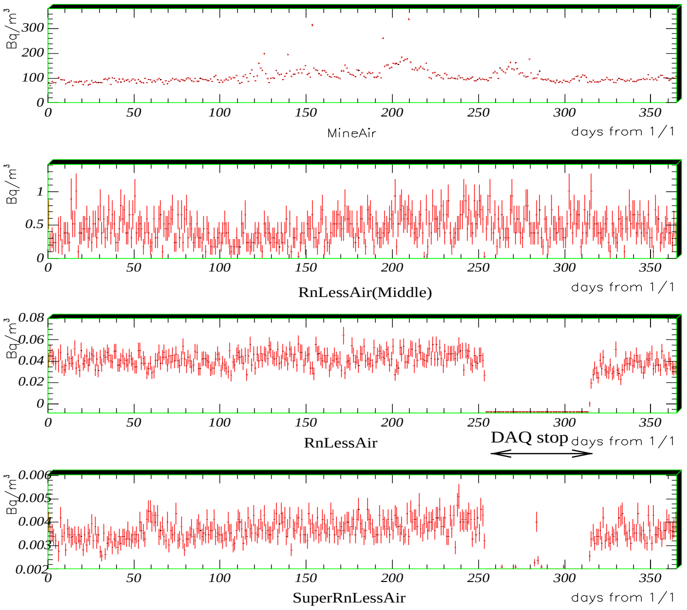

Figure 3.21: The time variation of the radon concentration in various air of the water purification system site. The top figure is the radon concentration in mine air. The second figure is the radon concentration in radon less air in middle point of air purification system. The third figure is the radon concentration in radon less air before cooled charcoal in air purification system. The fourth figure is the radon concentration super radon less air after all air purification system.

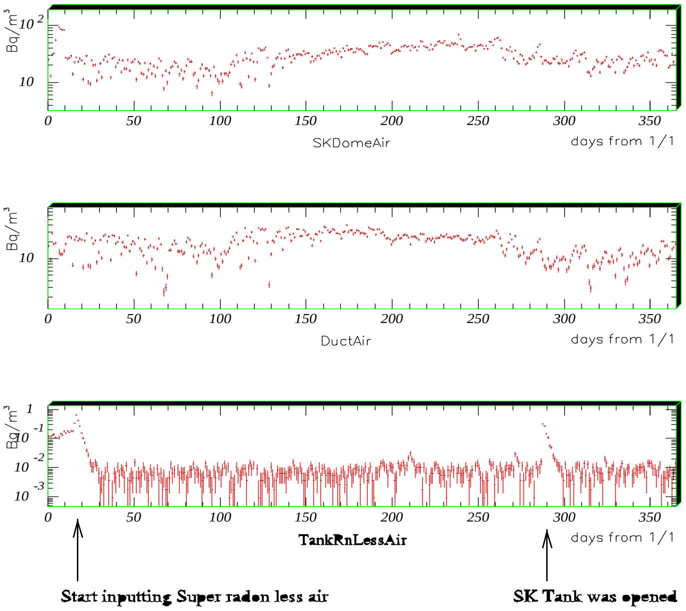

Figure 3.22: The time variation of the radon concentration in various air of the SK dome site. The top figure is the radon concentration in the dome air on SK tank. The second figure is the radon concentration in the duct air from outside of mine. The third figure is the radon concentration of air in the gap between the water surface and top of the SK tank.

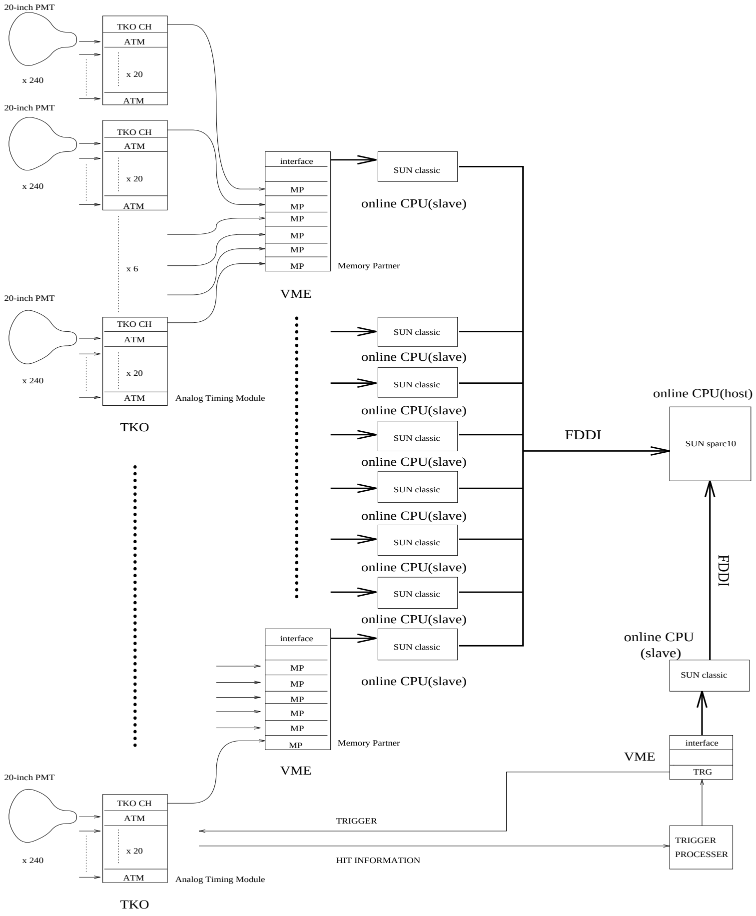

Figure 3.23: An overview over the DAQ system.

| Sample | Temperature(°C)) |
|---|---|
| Purified water after the system | 12.7 |
| Purified water in the SK tank | 14.1∼14.2 |
| Purified air after the system | 17.0 |
| Dew point of the Purified air | -78.5 |
| Dome air on the tank | 20.6 |

Table 3.5: The summary of the temperature in various places.

|  | data per 1 channel |  |  |  |  |  |  |  |  |  |  |  |  |  |  |  |
|---|---|---|---|---|---|---|---|---|---|---|---|---|---|---|---|---|
|  | 15 | 14 | 13 | 12 | 11 | 10 | 09 | 08 | 07 | 06 | 05 | 04 | 03 | 02 | 01 | 00 |
| 1st word | 0 | 0 | event number (8bit) |  |  |  |  |  |  |  | AB | 0 | channel |  |  |  |
| 2nd word | 0 | 1 | 0 | 0 | TDC data (12bit) |  |  |  |  |  |  |  |  |  |  |  |
| 3rd word | 1 | 0 | 0 | 0 | ADC data (12bit) |  |  |  |  |  |  |  |  |  |  |  |

Table 3.6: The data structure of ATM for 1 channel.

timing and charge information and are controlled as slave modules by GONG). There exist 12 TKO crates in a electronics hut and 4 huts in total. Each electronics hut controls 1/4 of the ID. A central hut houses the trigger electronics. One ATM module handles 12 PMTs, hence, 934 ATMs are used in SK.

In the first stage of an ATM module [78], the analog signal from a PMT is split into 4. One copy is used for external monitoring of analog signals, another copy is sent to a discriminator after an amplification by a factor 100, and the other copy are sent to the TAC/QAC [79] (Time to Analog Converter, charge to Analog Converter) circuits. If the amplified signal exceeds the threshold level of the discriminator, a rectangular signal of 200nsec width and -15mV amplitude is added to the HITSUM output of the ATM module. From the added output of all ATM modules ID trigger are derived. The threshold of the discriminator is set to the equivalent of 0.2p.e.. The two TAC/QACs for each channel enable the ATM to work dead-time free. This indicates that SK can handle $\mu$-e decay events (the typical time difference is 2.2$\mu$sec) or high rate events (i.e. supernovae bursts; about 1kHz in the case of supernovae explosion at the center of the Galaxy). The TAC circuit translates time into an integrated charge, which is proportional to the time difference between the PMT hit and the timing of the global trigger, and the QAC circuit integrates the charge from the PMT within 400nsec. The integrated charges are held by capacitors. If the global trigger signal is not issued within about 1.3$\mu$sec after a PMT hit, the integrated charges are discharged automatically. If the global trigger signal is issued, the charges are digitized by an ADC (Analog to Digital Converter), and the digitized data are stored in a 1024 word FIFO (First In/First Out) memory. The ATM provides 1.3$\mu$sec full range in time with 0.3nsec resolution and 600pC full range in charge with 0.2pC ($\simeq$0.1p.e.) resolution. The association of a signal to an event is done by an event number. The event number is incremented by a TRG (TRiGger) module in the central hut which issues the global trigger signal, and the event number (16bit) is distributed with the trigger to the electronics huts. The GONG in each TKO crate receives the event number and distributes the lower 8bit of it to the ATMs. The data structure of one signal recorded in the FIFO of the ATM is shown in table 3.6, where AB indicates which of the two TAC/QACs was used and 'channel' is a unique channel number identifying the PMT and its electronics channel.

### 3.6.2 The outer detector system

The DAQ system for the outer detector is completely different. The OD PMT signals are fed to QTC (Charge to Time Converter) module after separation from the positive HV by pickoff cards. The QTC module, which deals with 48 PMT signals and discriminates the signals with a threshold of 0.25p.e., generates rectangular pulses. Each pulse is put out with 200nsec delay after a signal comes and the width of the pulse is proportional to the charge integrated within a 200nsec gate. These pulses, which have timing and charge information, are sent to a FASTBUS TDC module. The QTCs also generate HITSUM signals, which are used to generate the outer detector trigger.

If a global trigger is issued, the QTC signals are digitized in the TDC modules. The TDC module, which can handle 96 channels, is able to record for time range of 32$\mu$sec. The recording range is tunable relative to the global trigger timing.

The readout of the digitized data is controlled by a FSCC (FASTBUS Smart Crate Controller). The data are sent to a DC2-DM115, which latches the TDC data into its memory, and written into a DPM (Dual Ported Memory) modules which plays a role like SMPs (see following section) in the DAQ of the ID. Finally the data are read out by a workstation.

### 3.6.3 Trigger system

The all HITSUM signals issued by the ATMs are summed up in each electronics hut with summing modules, and the summed HITSUM signals from the four electronics huts are again summed up in the central hut. In this summation, the pulse height contributions from individual hits drop from -15 to -11 mV. The summed signal is AC-coupled into a discriminator to subtract the changing offset generated by the dark noise rate of the 1,1146 inner PMTs. A trigger is issued, when the HITSUM signal exceeds a discriminator threshold. The threshold level is set to -320mV, i.e. if the number of hit PMTs exceeds 29hits in a 200nsec time window, a global trigger is generated. This trigger level is called Low Energy (LE) trigger. The rate at which LE triggers are issued is about 10Hz. There are other kinds of similar triggers named Super Low Energy (SLE) trigger (The data taking with SLE trigger started in May 1997) and High Energy (HE) trigger. The trigger thresholds of SLE and HE are -260mV and -340mV, and the event rate of these are 100Hz and 3Hz, respectively. Since the rate of SLE trigger was too high to handle in the off-line system, an intelligent online event reduction system is used to reject the events near the wall of ID which dominate the SLE trigger (A recent off-line computer upgrade would allow to take the full SLE rate.). As a result of this trigger, the event rate from the SLE trigger is reduced to about 16Hz. The OD also generates its own trigger. The threshold of the OD trigger is 19hits in 200nsec time window and the rate is about 3Hz, which is almost entirely due to cosmic ray muons.

The global trigger is then fed to the TRG module (VME specification). The TRG increments the 16 bit event number and distributes the event number signal and the global trigger signal to all GONGs, records the time at which the global trigger was issued using an internal 50MHz 48bit clock. The TRG also records the trigger ID indicating which trigger was issued by an 8bit data word. The identification bit of trigger ID is shown in table 3.7. The method to issue the global trigger is drawn in figure 3.24.

The threshold of the SLE trigger was changed 7 times in SK-I period to take data with lower energy. The summary is shown in table 3.8

### 3.6.4 Real-time data process

For events issuing only the SLE trigger (typically below 6.5 MeV) , a soft ware trigger which is called Intelligent Trigger (IT) is applied. This is a real-time fiducial volume cut procedure. Most very low energy events are due to $\gamma$ rays from the ID wall materials and the rock surrounding

| Trigger bit | type of trigger |
|---|---|
| 0 | LE |
| 1 | HE |
| 2 | SLE and Fission Trigger(for Ni calibration) |
| 3 | OD trigger |
| 4 | Periodical Trigger |
| 5 | Calibration Trigger |
| 6 | Online Veto Start |
| 7 | Online Veto Stop |

Table 3.7: The trigger ID. Periodical Trigger is a kind of random trigger issued every 6 seconds. Online Veto Start and Stop mark the duration of a possible online veto, which is issued if more than 64 events happen within 120$\mu$sec.

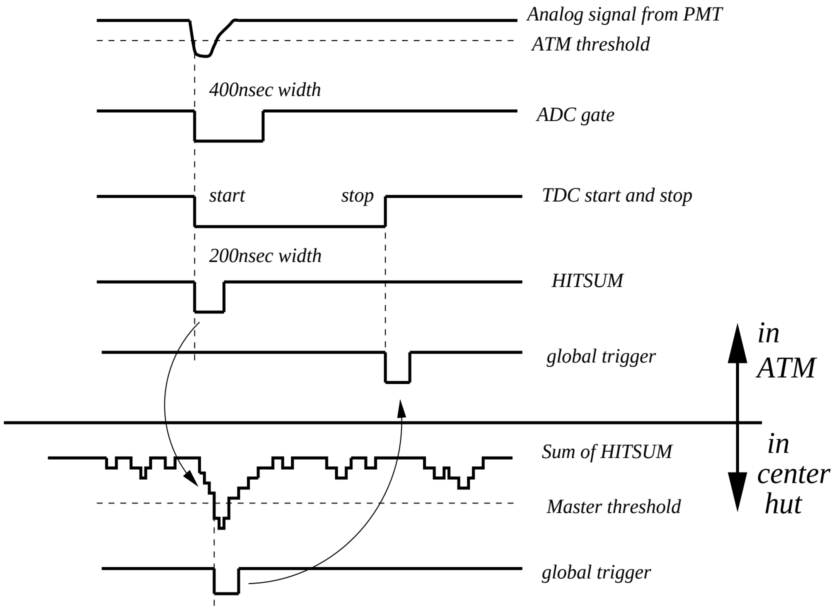

Figure 3.24: Trigger generation.

| Trigger threshold | Period | Event rate(Hz) |
|---|---|---|
| LE (-320 mV)(29 ID hits) | 1996.5.31 ∼ 1999.12.22 | 11 |
| LE (-302 mV)(29 ID hits) | 1999.12.22 ∼ 2001.7.15 | 11 |
| SLE (-260 mV)(24 ID hits) | 1997.5.29 ∼ 1999.5.13 | 106.6 |
| SLE (-250 mV)(23 ID hits) | 1999.5.13 ∼ 1999.9.17 | 172.2 |
| SLE (-222 mV)(20 ID hits) | 1999.9.17 ∼ 1999.12.22 | 540.6 |
| SLE (-212 mV)(19 ID hits) | 1999.12.22 ∼ 2000.7.11 | 561.5 |
| SLE (-186 mV)(17 ID hits) | 2000.7.11 ∼ 2000.7.31 | 1678. |
| SLE (-212 mV)(19 ID hits) | 2000.7.31 ∼ 2000.9.27 | 532.3 |
| SLE (-186 mV)(17 ID hits) | 2000.9.27 ∼ 2001.7.15 | 1678. |

Table 3.8: The summary of the switch of LE and SLE trigger threshold.

the tank, so the vertexes are distributed near the wall. The IT eliminates those events, keeping only 8% of the incoming events at the SLE threshold = -212 mV.

The data stream of the IT diverges from the online host computer. The online host computer sends the data which issues only the SLE trigger to 12 CPUs (IT CPUs), which reformat the data and reconstruct event vertex.

Fast vertex reconstruction by IT is required to keep up with the high data rate. For this purpose, a fast vertex reconstruction algorithm (Hayai fitter) is applied to the data before the usual one, which is described in chapter 4. First, the fitter makes a list of all hit PMTs that has a neighboring hit PMT in space (distance within 10 m) and time (hit within 33.3 nsec). A timing distribution is made from set of PMTs, and the number of PMTs in a sliding window of 16.7 nsec width examined. The set of PMTs that belongs to the window with largest number of hit PMTs is less than 5.

The initial vertex for the subsequent grid search is obtained as the centroid of the selected hit PMTs. In order to prevent starting a vertex too close to the wall, the vertex is moved 2 meters away from the ID wall. Then the Hayai fitter searches the vertex which gives the maximum "*goodness*" which is defined as follows :

$$goodness \equiv f(a)\frac{1}{N_0}\sum_{i=1}^{N_0}\exp(-\frac{(t_i - t_i^{exp} - T_{offset})^2}{2\sigma^2}) \tag{3.13}$$

where $f(a)$ is a function which reflects the shape of the expected Čerenkov cone from the true vertex. $a$ is the magnitude of the anisotropy defined as follows :

$$\begin{aligned} a &= \mid \overrightarrow{a} \mid \\ &= \mid \frac{\sum_{i=1}^{N_0} q_i \frac{\overrightarrow{d_i}}{|\overrightarrow{d_i}|}}{\sum_{i=1}^{N_0} q_i} \mid \end{aligned} \tag{3.14}$$

$N_0$ is the number of selected hit PMTs. $t_i$ is the detection time of i-th hit PMT. $T_{offset}$ is the time offset to make the center of $(t_i - t_i^{exp} - T_{offset})$ zero. $\overrightarrow{d_i}$ is the distance vector from the trial vertex to the i-th hit PMT. The trial vertexes are uniformly distributed with step size of 1.86 m. $t_i^{exp}$ is the expected detection time of i-th PMT, defined as follows :

$$t_i^{exp} = T_0 + \frac{\mid \overrightarrow{d_i} \mid}{c/n} \tag{3.15}$$

| address | data | | |
|---|---|---|---|
| | 31·········16 | 15·········0 | |
| 1 | 0000 | 16 bit event number | GONG |
| 2 | Module address | channel and 8bit event counter | ATM |
| 3 | Module address | TDC data | ATM |
| 4 | Module address | ADC data | ATM |
| 5 | Module address | channel and 8bit event counter | ATM |
| · | · · · | · · · | ATM |

Table 3.9: The data format of SMP. The right side line means the origin of data. Module address is the address of an ATM in a TKO crate. 'address' is the data address in SMP.

where n is the refractive index of water.

When the vertex which maximizes the *goodness* is found the location of the vertex is examined. If the distance between the reconstructed vertex and the ID wall is less than 2 m, the vertex is rejected.

After this fast reduction, the normal vertex reconstruction is also applied. The vertex reconstruction method is explained in next section. Events whose reconstructed vertex is located within 2 m of the ID wall is rejected. The reduction efficiency of the IT dependents on the SLE trigger rate. For example, when the SLE trigger threshold = -212 mV, 92% of events are rejected. The event identification number of remaining events are sent to reformatter machine. Only the data for the these events are reformatted and sent to the off-line host.

### 3.6.5 The ID online and offline system

The digitized PMTs data stored in the FIFO of the ATMs are read out through the SCH by a SMP (Super Memory Partner, VME specification), which possesses 2Mbyte internal memory. One SMP collects the data from one TKO crate in the fixed format shown in table 3.9. The data size per one channel is 12 bytes. Six SMPs are controlled by one workstation, S4/CL (Sun SPARCclassic), which is called 'slave machine'. There are 8 slave machines and each electronics hut has 2. Therefore, one slave machine controls the data from about 1400 PMTs. The 6 SMPs' data are read out by block transfer. The data of all slave machines are sent to a workstation, S4/10 (Sun SPARCstation 10), called 'host machine' via FDDI (high speed ring network with optical fiber cable). The TRG is controlled by another workstation, S4/CL, called the 'trigger machine', and information related to the trigger are sent to the host machine through it. Yet another workstation, a S4/20 (Sun SPARCstation 20) collecting OD data, is called an 'anti slave', and its data are sent to the host machine via FDDI. The host machine builds the event from the slave machines on the basis of the event counter information. The reconstructed data are sent on to another workstation (UltraSPARC, 'reformat machine'), which changes the online format to an off-line format (ZBS, Zebra Bank System), which is easy to handle in the analysis.

The reformatted data are sent to the off-line computer system. The system is composed of a VPX2105 called 'sukop' and 10 S4/20 workstations called 'sukeve(1∼10)' with a MTL (Magnetic Tape Library) system, which has a capacity of 12Tbyte (until January of 1998). Since February 1998, the system is completely replaced. PetaSite made by SONY can store about 100Tbyte of data and the flow rate of data read out is enlarged 14 times as compared to the old MTL system (from 10.8MByte/s to 144Mbyte/s). The sukop machine transforms the ADC and TDC counts of the ATM data to the real charge (pC) and time (nsec), respectively, using the tables provided by various detector and electronics calibration. This process is called 'TQreal'. The size of data with real charge and time is 27Gbyte/day. These data are distributed to the 10 sukeve machines, on which the reconstruction of events (vertex, direction, energy, etc) are carried out for solar neutrino, atmospheric neutrino, and up-going muon events.

After reconstruction, these data are recorded on the Data Storage system. A figure summarizing the online and offline system is shown in figure 3.25.

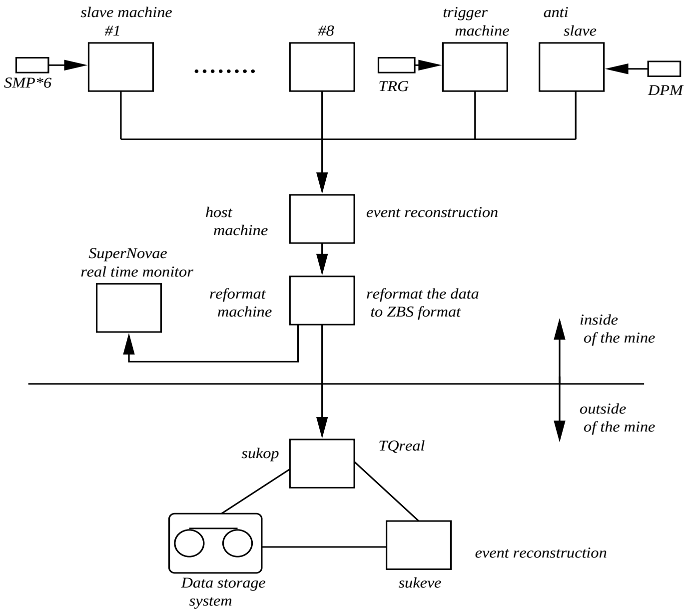

Figure 3.25: The summary figure of on and offline system.

# Chapter 4

# Event Reconstruction

The event reconstruction algorithms used for the solar neutrino analysis is described in this chapter.

First, vertex reconstruction which uses the time information of hit PMTs is described. The second step is the reconstruction of the event direction using the pattern of hit PMTs. After these reconstructions, the effective number of hit PMTs, $N_{eff}$, is calculated. $N_{eff}$ is converted into energy by using a conversion function obtained from LINAC calibration, which is described in next section. Additionally, muon track reconstruction described in appendix C.

## 4.1 Vertex reconstruction

The timing information from the hit PMTs is used to reconstruct the vertex position. The path length of an electron recoiling from the neutrino interaction is less than 10 cm. It is negligible in comparison with the vertex resolution of approximately 1 m. Therefore, the vertex treated as a point in vertex reconstruction program.

Prior to the reconstruction, the PMT timing information is evaluated to remove hit caused b random noise and reflected light. A trial timing distribution of hit PMTs is shown figure 4.1 To select the PMTs which are used for vertex reconstruction, the following time window method is used :

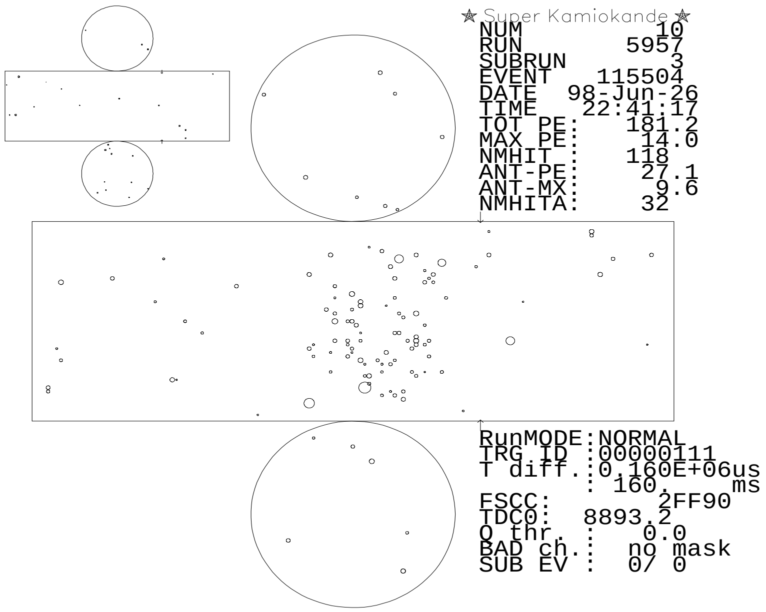

Figure 4.1: Event display of a typical low energy event.

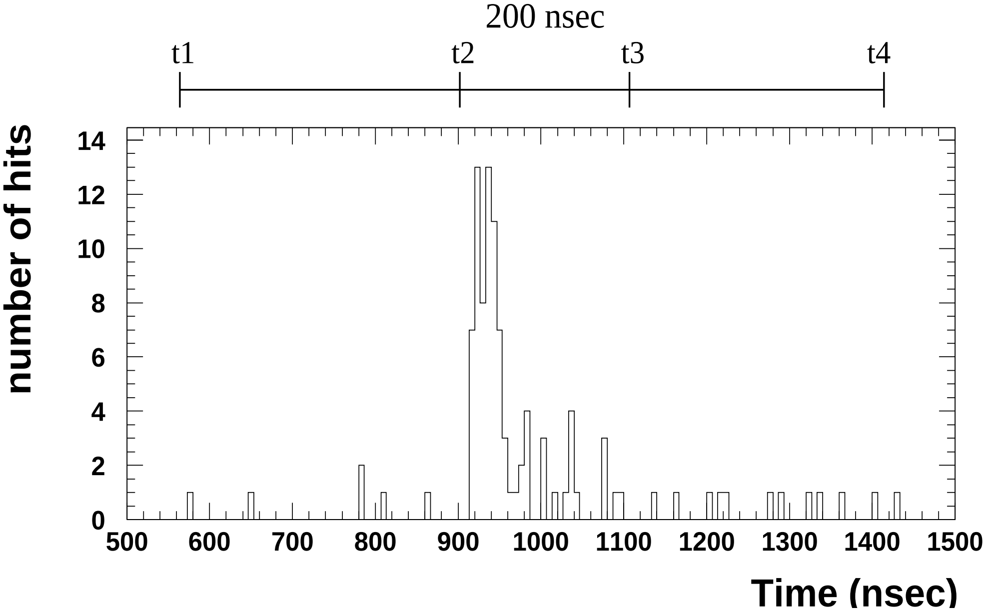

Figure 4.2: Absolute time distribution of hit PMTs in the event in figure 4.1.

1. Sort the hit PMTs in chronogical order and locate the 200 nsec time window which contains the maximum number of hit PMTs ($N_{sg}$)

2. Estimate the number of dark noise hits, $N_{bg}$ by the relation :

$$N_{bg} \equiv \frac{t_3 - t_2}{(t_2 - t_1 + (t_4 - t_3))}(N_{hit}(t_1 \sim t_2) + N_{hit}(t_3 \sim t_4)) \tag{4.1}$$

   $t_1 \sim t_4$ are defined in figure 4.2.

3. Reduce the width of the window in 19 nsec steps to optimize the significance of the signal. The significance, $S$, is defined as follows :

$$S \equiv \frac{N_{hit}(t_2 \sim t_3) - N_{bg}}{\sqrt{N_{bg}}} \tag{4.2}$$

   Only the hit PMTs within the time within the time window with maximum $S$ are used for vertex reconstruction.

The vertex point is found by using a grid search method. The distance between the grid points used in the initial stage of vertex reconstruction is 397.5 cm. The vertex is placed on a grid point, and for the grid point, the "*goodness*" of vertex reconstruction is calculated by following equation. The calculation is repeated for every point on the grid.

$$goodness(x,y,z) \equiv \frac{1}{\sum_{i=1}^{N_{hit}} \frac{1}{\sigma^2}} \times \sum_{i=1}^{N_{hit}} \frac{1}{\sigma^2} \exp\left(\frac{(t_{res,i}(x,y,z) - t_{center}(x,y,z))^2}{2\sigma^2}\right) \tag{4.3}$$

where (x,y,z) is the position of the grid point. $N_{hit}$ is the number of hit PMTs selected by the time window method. $\sigma$ is the PMT time resolution, which is 5 nsec for all PMTs. $t_{res}$ is the residual time of i-th hit PMT which is defined as follows :

$$t_{res,i} \equiv t_i - \frac{n}{c}\sqrt{(x-x_i)^2 + (y-y_i)^2 + (z-z_i)^2} \tag{4.4}$$

where $t_i$ is the time of the i-th hit PMT. $t_{center}$ is the mean time of the distribution of $t_{red,i}$. $n$ is the reflective index of water and $c$ is the speed of light in the vacuum. $(x_i, y_i, z_i)$ is the position of the i-th hit PMT. In an ideal case, all of the $t_{res}$ are equal, and the *goodness* will be 1. The distance between the grid points is reduced to 5 cm as the trials converge upon the final vertex. Figure 4.3 shows a distribution of the *goodness* using events from LINAC calibration. Figure 4.4 shows the reconstructed vertex of the same events. The resolution of vertex reconstruction is measured by LINAC calibration by LINAC calibration system, and found to be ~75 cm for electron energy 10 MeV. A full explanation of the LINAC calibration in chapter 5.

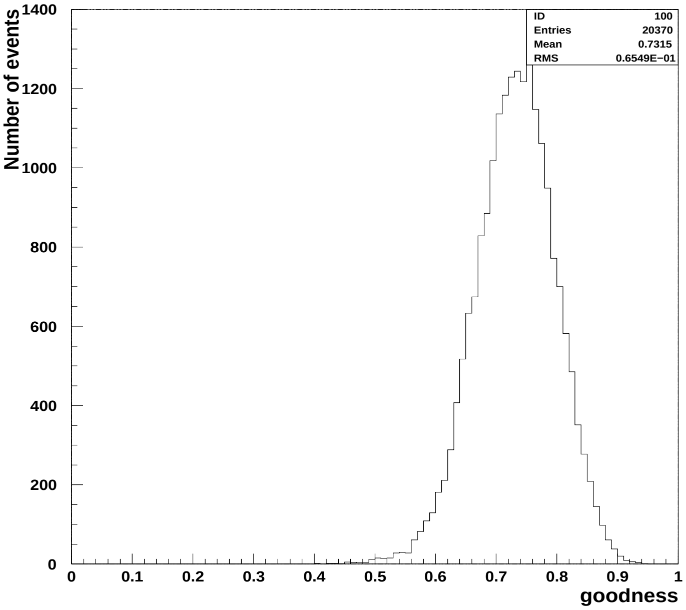

Figure 4.3: Projection of the *gooodness* distribution for LINAC calibration events at the position (x=-388.9cm, y=-70.7cm, z=-6cm) with the electron beam energy 6.98 MeV.

## 4.2 Direction reconstruction

Once the vertex position of an event has been determined, the direction can be reconstructed by examining the pattern of hit PMTs created by the Čerenkov ring. In an ideal case, the event pattern is expected to be a clear ring with an opening angle of 42° about the direction of the electron's path. However, photons can be scattered in the water, reflected off the PMTs and the black sheet. Also, the electron may undergo multiple scattering. All of these effects cause the Čerenkov ring to be smeared. The hit PMTs which are used to reconstruct the direction are selected using a 50 nsec timing window from the TOF (Time-Of-Fright) subtracted time distribution. A maximum likelihood method is used to determine the direction. The likelihood function is defined as :

$$L(\overrightarrow{d}) \equiv \sum_{i=1}^{N_{hit}} \log(P_i(\cos\theta_{dir})) \times \frac{\cos\theta_i}{a(\theta_i)} \tag{4.5}$$

$$\theta_i \equiv \arccos(\frac{\overrightarrow{d_i} \cdot \overrightarrow{p_i}}{|\overrightarrow{d_i}| \cdot |\overrightarrow{p_i}|}) \tag{4.6}$$

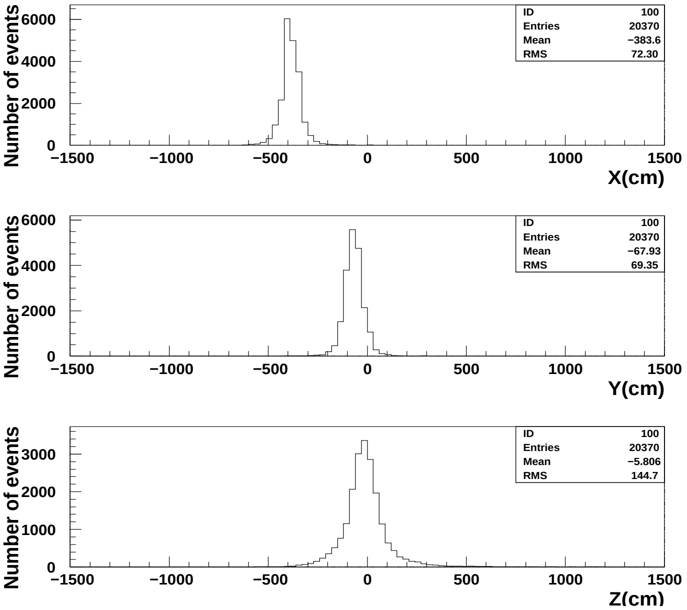

Figure 4.4: Projection of the reconstructed vertex distribution for LINAC calibration events at the position (x=-388.9cm, y=-70.7cm, z=-6cm) with the electron beam energy 6.98 MeV.

$P_i(\cos\theta_{dir})$ is probability density function for the angle of Čerenkov photons relative to the recoil electron momentum. Figure 4.5 shows the distribution of $P_i(\cos\theta_{dir})$. $\theta_i$ is the angle of incidence of the Čerenkov photon on the i-th PMT. $\overrightarrow{p_i}$ is the vector from the reconstructed vertex to the position of the i-th hit PMT. $\overrightarrow{d_i}$ is the direction vector that the i-th hit PMT is facing. $a(\theta_i)$ is acceptance of the PMT photo cathode as function of $\theta_i$. The distribution $a(\theta_i)$ is presented in figure 4.6. A grid search method is used to find which 9°,4°,1.6°. The mean value of the multiple scattering angle is about 27° for electrons with an energy of 10 MeV. So the step sizes are small enough to reconstruct the direction of low energy electrons. Figure 4.7 shows the reconstructed direction of the same events in figure 4.4. The resolution of the direction reconstruction is measured with LINAC calibration data, and found to be $\sim 27°$ for electron energy of 10 MeV. A full explanation of the LINAC calibration system is given in chapter 5.

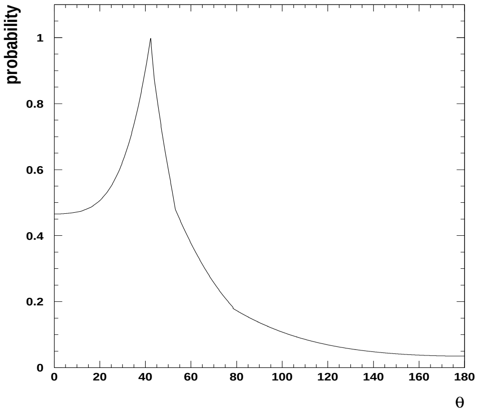

Figure 4.5: The unnormalized probability density function for Čerenkov photon directions with respect to initial electron direction for 10 MeV/c electrons.

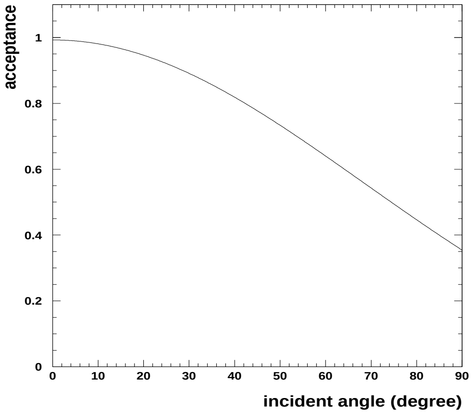

Figure 4.6: The acceptance function of the PMT.

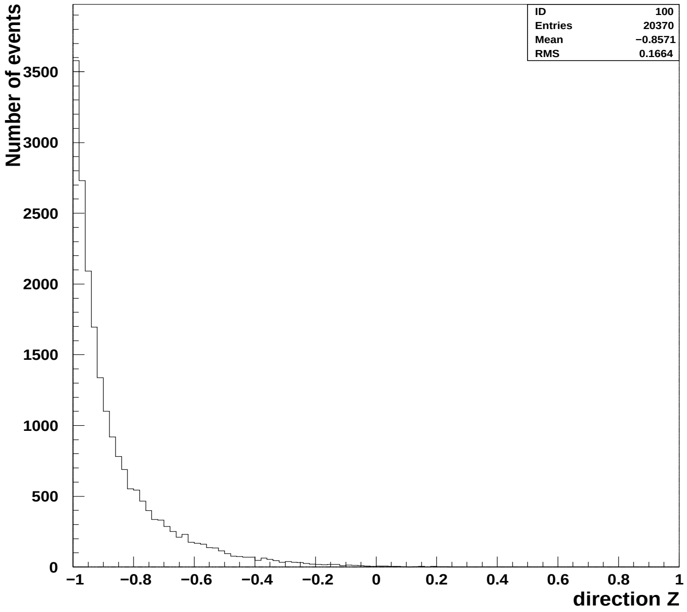

Figure 4.7: Projection of the direction cosine distribution for LINAC calibration events at the position (x=-388.9cm, y=-70.7cm, z=-6cm) with the electron beam energy 6.98 MeV.

## 4.3 Energy reconstruction

As indicated in chapter 2, the measurement of the energy spectrum shape is the most important key to investigate the neutrino oscillation with solar neutrinos. Hence, the energy determination has to be done carefully. As discussed earlier, almost all hit PMTs catch only a single photo-electron in a solar neutrino event. The total charge of the event is not a good indicator for the energy of the recoil electron, because charge resolution at the single photo-electron level of a 50cm-PMT is not good (∼50%) enough to estimate the total number of emitted Čerenkov photons. Accordingly, in SK, the energy is calculated from the number of hit PMTs within a 50nsec timing window ($N_{50}$). However, the number of hit PMTs is still not a good energy indicator, since it has large position dependence (For example, the measured mean $N_{50}$ using $\gamma$-rays from Ni(n,$\gamma$)Ni reactions is different by about 10% between the central position ($\boldsymbol{x} = (0,0,0)$) and an edge position of the fiducial volume ($\boldsymbol{x} = (0,0,+16\mathrm{m})$).). In order to give uniform response over the fiducial volume (The fiducial volume is the inner part of the ID, where the distance from the wall is greater than 2m. It contains 22.5 ktons water.), various corrections are applied. The corrected number of hits, $N_{eff}$, is defined by:

$$N_{eff} = \sum_{i=1}^{N_{50}} \frac{N_{all}}{N_{alive}} (\alpha_i + \alpha_{tail} - \alpha_{dark}) S(\theta_i, \phi_i) e^{\frac{R(\boldsymbol{x}_0, \boldsymbol{x}_i)}{\lambda}} p_i \tag{4.7}$$

The corrections are classified as follows.

### Dead PMT correction

In order to reduce the effective difference of the energy scale caused by the variation of the number of available PMTs with time, a factor $N_{all}/N_{alive}$ is used. Here $N_{all}$ is the total number of PMTs in the inner detector of SK (i.e. 11146), and $N_{alive}$ is the number of available PMTs in the detector and the remaining PMTs are dead ones (see figure 3.14).

### Multi photo-electron hits correction

If an event happens at near the fiducial volume edge toward the nearest ID wall, an observed number of hit PMTs become effectively small, since a Čerenkov ring of the event become small, which causes multi photo-electron hits on one PMT. The expected number of photo-electrons received by individual PMTs is estimated from the occupancy of the surrounding tubes. If the averaged number of photo-electrons is $\eta_i$ per one PMT area in the region surrounding the $i$-th PMT, a probability, $A_i$, that the surrounding PMTs do not hit is calculated from a Poisson distribution: $A_i = \frac{\eta_i^0 e^{-\eta_i}}{0!} = e^{-\eta_i}$. For a while, when the number of hit PMTs and the number of alive PMTs surrounding the $i$-th PMT are $n_i$ and $N_i$ (normally $N_i = 3 \times 3 = 9$) respectively, the probability $A_i$ is equal to $(N_i - n_i)/N_i = 1 - n_i/N_i$. Hence, the averaged number of photo-electrons in the area is computed to be:

$$\eta_i = \log\left(\frac{1}{1-\varepsilon_i}\right) \tag{4.8}$$

where $\varepsilon_i = n_i/N_i$. The total number of photo-electrons in the region is $N_i\eta_i$. Therefore, the expected number of photo-electrons received by the $i$-th PMT, $\alpha_i$, is given by:

$$\alpha_i = \frac{N_i\eta_i}{n_i} = \frac{\log(1/(1-\varepsilon_i))}{\varepsilon_i} \tag{4.9}$$

If $\varepsilon_i = 1$, we set $\alpha_i = 3$, which is obtained by extrapolating $\varepsilon_i$ to 1 in equation (4.9) as shown in figure 4.8.

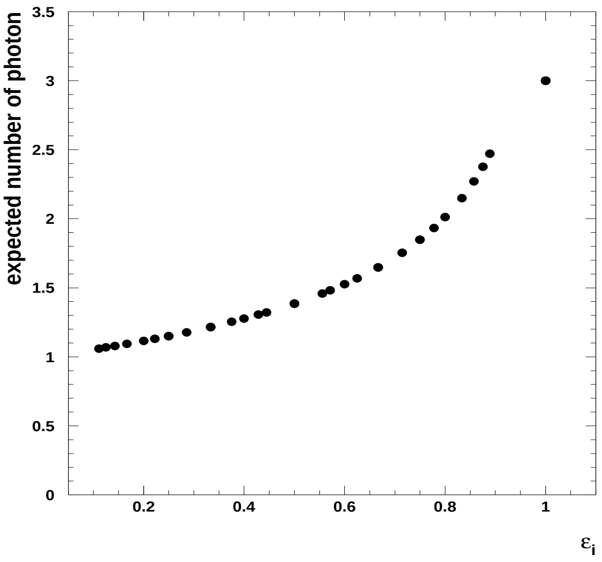

Figure 4.8: The expected number of photo-electrons received by one PMT as a function of $\varepsilon_i$.

### Recovery for reflected Čerenkov photons

In order to recover the reflected Čerenkov photons which hit PMTs with a considerable time lag ($\leq$ 50nsec), a factor $\alpha_{tail}$ is multiplied, which is defined by:

$$\alpha_{tail} = \frac{N_{100} - N_{50}}{N_{50}} \tag{4.10}$$

where $N_{100}$ is same as $N_{50}$ except that the time window on the TOF subtracted timing is 100nsec.

### Correction for dark noise hits

In order to drop contribution of dark noise hits from observed $N_{50}$ (The dark noise ($\sim$ 3.3kHz) contribute about 2 hits in a 50nsec window.), a following factor $\alpha_{dark}$ is subtracted:

$$\alpha_{dark} = \frac{N_{alive} R_{dark} \times 100 \cdot 10^{-9}}{N_{50}} \tag{4.11}$$

where $R_{dark}$(Hz) is the mean dark rate evaluated on a run to run basis (see figure 3.13).

### Correction for effective photo-cathode coverage

$S(\theta_i, \phi_i)$ is the effective photo-cathode area from the view of $\theta_i$, $\phi_i$ direction, where $\theta_i$ is the incident angle to the $i$-th PMT and $\phi_i$ is the azimuth angle. A $\phi$ dependence is caused by the arrangement of PMTs as shown in figure 4.9. The function $S(\theta, \phi)$ is shown in figure 4.10.

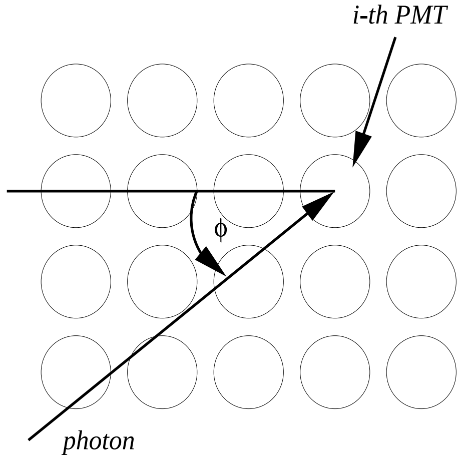

Figure 4.9: The arrangement of PMTs and the definition of the azimuth angle $\phi$.

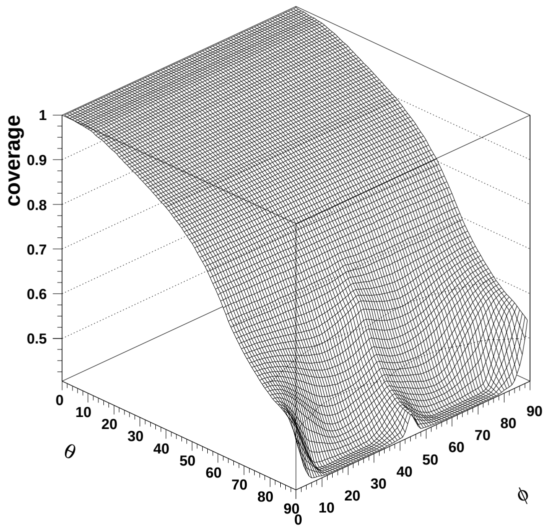

Figure 4.10: Effective photo-cathode area as a function of $\theta_i$, $\phi_i$ direction.

### Water transparency correction

In order to compensates changes in the attenuation of Čerenkov light in water and recovers the associated position dependence of the energy scale, a factor $e^{\frac{R(\boldsymbol{x}_0,\boldsymbol{x}_i)}{\lambda}}$ is multiplied, where $\lambda$ is the water transparency measured from the Čerenkov light output of electrons from the decay of stopping muons. It is a function of time. The details of the calculation of $\lambda$ are described in chapter 5.

### Correction for quantum efficiency

The last term $p_i$ is the quantum efficiency correction factor. 375 PMTs were produced in a pre-series to the main PMTs. The quantum efficiency of these PMTs is found to be larger(This fact was established from the occupancy distribution by Ni calibration measurement. See chapter 5.). The factor is given by:

$$p_i = \begin{cases} 0.833 & \text{(375 PMTs)} \\ 1.000 & \text{the other PMTs} \end{cases} \tag{4.12}$$

The non-uniformity of $N_{eff}$ in the fiducial volume is measured to be $\sim 1\%$ using $\gamma$-rays from Ni(n,$\gamma$)Ni reaction and monochromatic electron beam (LINAC).

A calculation of an MeV value from $N_{eff}$ is discussed in subsection 5.4.2.

# Chapter 5

# Calibration

In this chapter, details and results of the SK detector calibration are given. First of all, the fundamentals of the detector, namely uniformity of gain and timing adjustment for all PMTs, have to be investigated, using a Xe light source, a Ni-Cf calibration source and a laser light source. To know the water transparency in the SK tank a direct measurement of the water transparency is carried out using a laser light source and a CCD camera. To monitor the variation, decay electrons from stopping $\mu$ are used.

In order to measure the energy spectrum of solar neutrinos, a liner accelerator for electrons (LINAC) is installed at the detector to calibrate the detector with electrons of energy 4.0$\sim$16 MeV. Uniformity of the energy scale in direction and time is investigated by spallation events, the Ni-Cf source and the $\mu$ decay electron events.

Angular and vertex resolution measured in the LINAC calibration and the trigger efficiency obtained with the Ni-Cf calibration and DT calibration are also described.

## 5.1 PMT gain monitoring

Uniformity of gain for all PMTs is monitored by two methods, i.e. a Xe light source for decision of the relative gain and a Ni-Cf $\gamma$-ray source for decision of the absolute gain.

### 5.1.1 Xe calibration for relative gain of the PMTs

The gain of all PMTs has to be the same to make detector response uniform. As described in chapter 3, the relative gain of all PMTs is adjustable by changing high voltage $V(10^7$ gain$)$. In order to check the relative gain of all PMTs and the stability of gain uniformity, a Xe calibration system is used. Figure 5.1 shows an overview of the Xe light system. An advantage to using a Xe-lamp is that intensity of the output light is stable within 5%. The light generated by the Xe-lamp go through a UV-pass (Ultra-Violet) filter and an optical fiber and is sent to a scintillator ball in the tank. A role of the UV-pass filter is to pass only ultraviolet light which can be absorbed by the scintillator ball. The scintillator ball is a spherical acrylic ball mixed with BBOT wavelength shifter and MgO. BBOT absorbs the Xe light passing through the UV filter and emit 450nm wavelength light, which is similar to $\check{C}$erenkov light wavelength. MgO is diffuser to emit the light uniformly. The intensity of the output light is monitored by two silicon photo-diodes and a 5cm PMT.

Charge observed in each PMT is corrected with PMT acceptance, light attenuation in water and non-uniformity of the scintillator ball, which are measured independently.

In checking the relative gain of PMTs, the charge of each PMT should be corrected with the acceptance of each PMT, light attenuation in water and the non-uniformity of the scintillator ball. The corrected charge is defined by following equation :

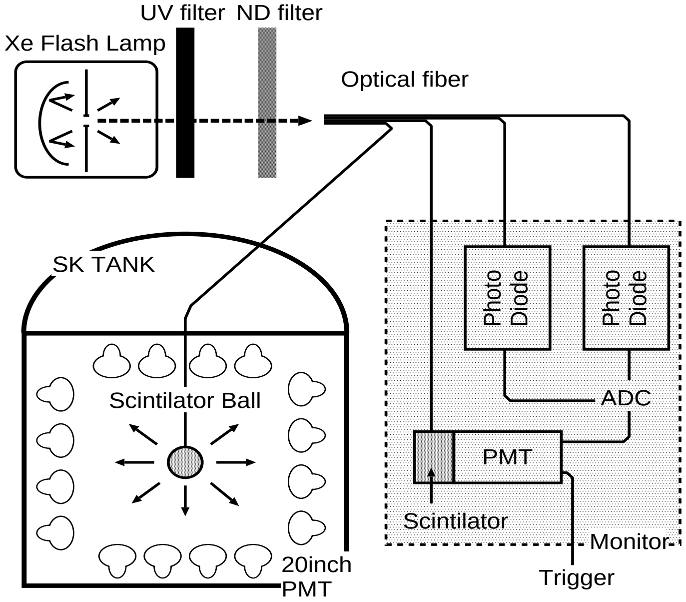

Figure 5.1: Overview of the Xe calibration system.

$$Q_{cor} \equiv \frac{Q \times r}{\exp(-\frac{r}{\lambda}) f_{acc}(\theta_{PMT}) f_{ball,\theta}(\theta) f_{ball,\phi}(\theta,\phi)} \tag{5.1}$$

where

- $Q$ Charge of a PMT
- $r$ Distance from scintillator ball of a PMT
- $f_{acc}$ Function for acceptance correction
- $f_{ball,\theta}$ Function to correct the zenith angle dependent non-uniformity of the scintillator ball
- $f_{ball,\phi}$ Function to correct the azimuth angle dependent non-uniformity of the scintillator ball

Figure 5.2 shows distribution of the corrected charge for all PMTs. The gain of all PMTs is consistent within 7%. The stability of the overall gain for long time period is also studied and it is found to be stable within 2% for 5 measurements in one year.

### 5.1.2 Ni-Cf calibration for absolute gain of the PMTs

With the Xe calibration system the gain of all PMTs can be adjusted at large output charge (100∼200p.e.). Hence, it is relevant for high energy events, such as cosmic ray muon events. For solar neutrino events, the uniformity for single photo-electron PMT response, namely single p.e. efficiency is essential. For that purpose a Ni-Cf calibration source is used.

A schematic view of the Ni-Cf calibration system is shown figure 5.3.

The source is also used to evaluate the systematic error of vertex reconstruction and obtain trigger efficiency The Ni-Cf source emits $\gamma$-rays with a maximum energy of 9.00 MeV. The $\gamma$-rays cause Compton-electrons, which emit Čerenkov photons. In this case, signal on hit PMTs is at the 1p.e. level. Hence, the peak value of the output charge of one PMT indicates the absolute

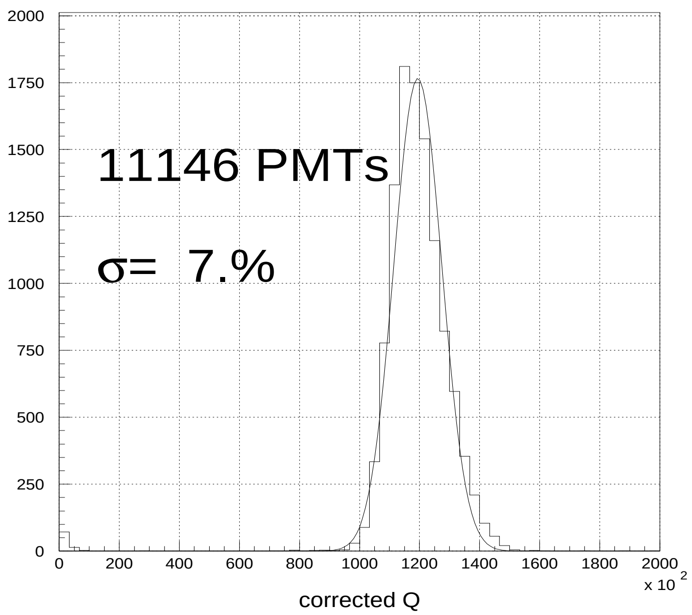

Figure 5.2: The distribution of the corrected charge for all PMTs.

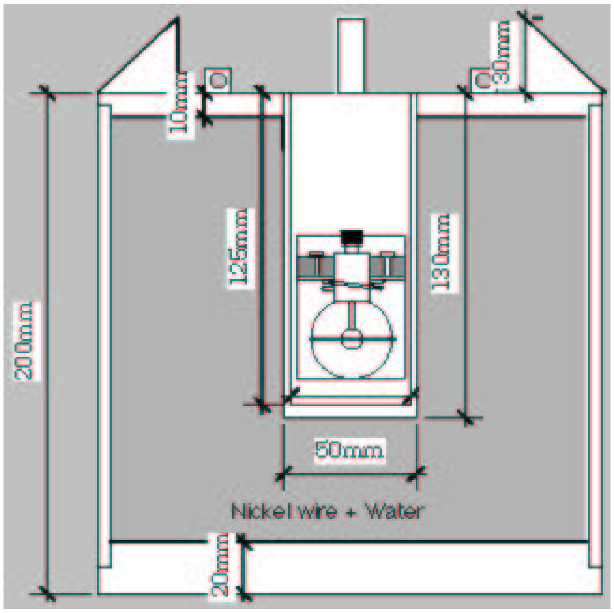

Figure 5.3: A schematic view of the Ni-Cf calibration system. Cf is situated at the center of the container.

gain. Figure B.3 shows distribution of the output charge for single photo-electron response of a triggered PMT. Mean value of the distributions for all PMTs is 2.055 pC/1p.e..

A parameter indicating the uniformity of the 1p.e. efficiency is represented by the occupancy with a correction for water transparency defined as (number of hits)/(number of total events) for each PMT. Distribution of the averaged occupancy for each layer of barrel part is shown in figure 5.4. Position that the layer number equal one is bottom part and 51 is top part. Figure 5.4 shows a clear increase of the occupancy at the bottom and at the top. This is due to the reflection of light on the PMTs and geometrical condition of the PMT arrangement, and is reproduced in the MC simulation.

The open marks in figure 5.4 are different from the other filled points by about 20%. The reason is that these layers include the PMTs (375 PMTs) produced in earlier period which have higher 1p.e. efficiency. The Xe calibration adjusts the gain so that the output charge of all PMTs become same. Therefore high voltage values of these 375 PMTs are set lower. However, the occupancy measured by the Ni-Cf source reveals differences in the 1p.e. efficiency, because 1p.e. efficiency is independent of applied high voltage. The difference in the 1p.e. efficiency is taken into account in the calculation of electron energy as described in equation (4.7).

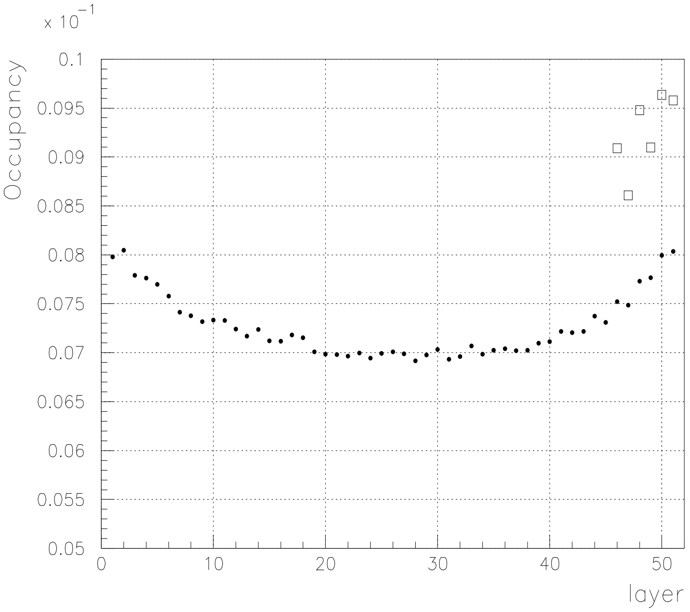

Figure 5.4: Distribution of the averaged occupancy for each layer of the barrel part.

## 5.2 Timing calibration of the PMTs

In order to get vertex position where an event occurs accurately, relative timing and timing resolution of all PMTs have to be known. If the relative timing is different PMT by PMT, an adjustment of the timing have to be performed. To do so, a light source of short time width, ∼a few nano seconds, is required. Figure 5.5 shows a schematic view of a laser system which measures the timing response of all PMTs. The light source is a $N_2$ laser which can produce sufficiently intense light of 337nm wavelength, which width is moderately short (∼3nsec).

The wavelength of the generated light is converted to 384nm by a DYE laser. Light intensity is controlled using an attenuation filter. The light is divided into two. One light is sent to a diffuser ball in the water tank through an optical fiber, the other is used for monitoring and triggering. The diffuser ball contains a $TiO_2$ tip and LUDOX. LUDOX is silica gel with 20nm glass fragments. The tip is located at the center of the LUDOX. The light is diffused by the tip and the LUDOX without an additional timing spread.

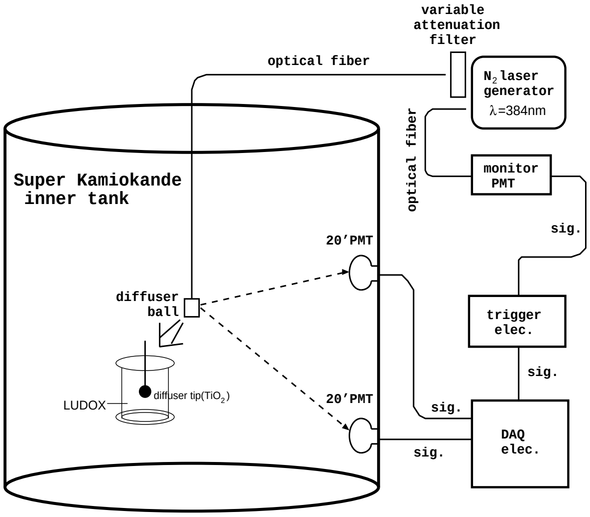

Figure 5.5: The schematic view of the laser system.

By changing the intensity of the light output, the charge dependence of the absolute timing and timing resolution of the PMTs is established. Figure 5.6 shows a so-called 'TQ map', which characterizes the timing response of a PMT. The horizontal axis is the number of observed photo-electrons and the vertical axis is the hit timing. The charge dependence of hit timing is mainly due to slewing in the discriminator on the ATM. The timing resolution also depends on the detected number of photo-electrons. The typical timing resolution for a 1p.e. signal is 3nsec.

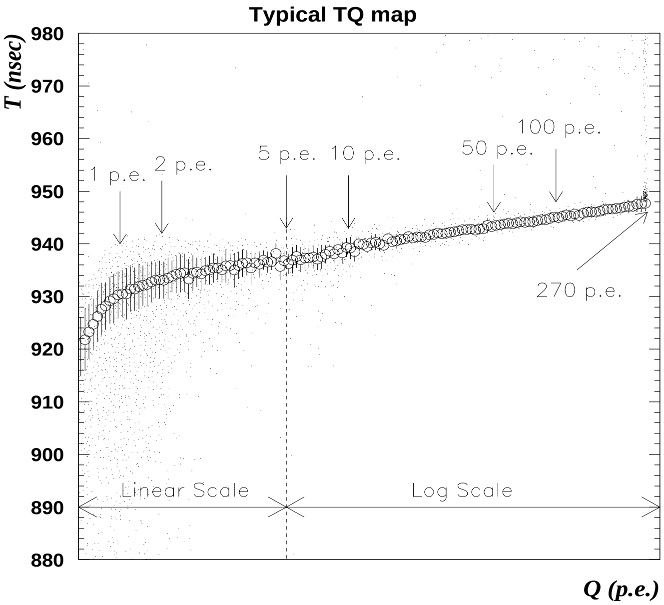

Figure 5.6: The TQ map of one PMT. The details of this figure are described in the text.

## 5.3 Water transparency measurements

Water transparency in the SK tank is an important parameter to characterize the response of the detector to the solar neutrino events, since it determines the number of Čerenkov photons which arrive at the PMTs. There are two aspects of the measurement of the water transparency, i.e. one is wavelength dependence which is important for MC simulation in the step of the Čerenkov photon propagation, the other is its long term variation.

### 5.3.1 Direct measurement of the water transparency

A direct measurement of the water transparency is carried out with the system shown in figure 5.7. Source of light is a $N_2$ dye laser which is able to produce monochromatic light with wavelengths from 337 to 600nm. The light is split into two, one of which is sent to a diffuser ball in the water tank and the other is used to monitor intensity of the light output through an optical fiber with a 5cm PMT. The diffuser ball is a spherical acrylic ball with MgO. Intensity of the light emerging from the acrylic ball is measured by a CCD camera at the top of the tank. By varying the distance between the diffuser ball and the CCD camera, the water transparency can be extracted without knowledge of the absolute light output of the system. The water transparency $\lambda_{tra}$ is given by:

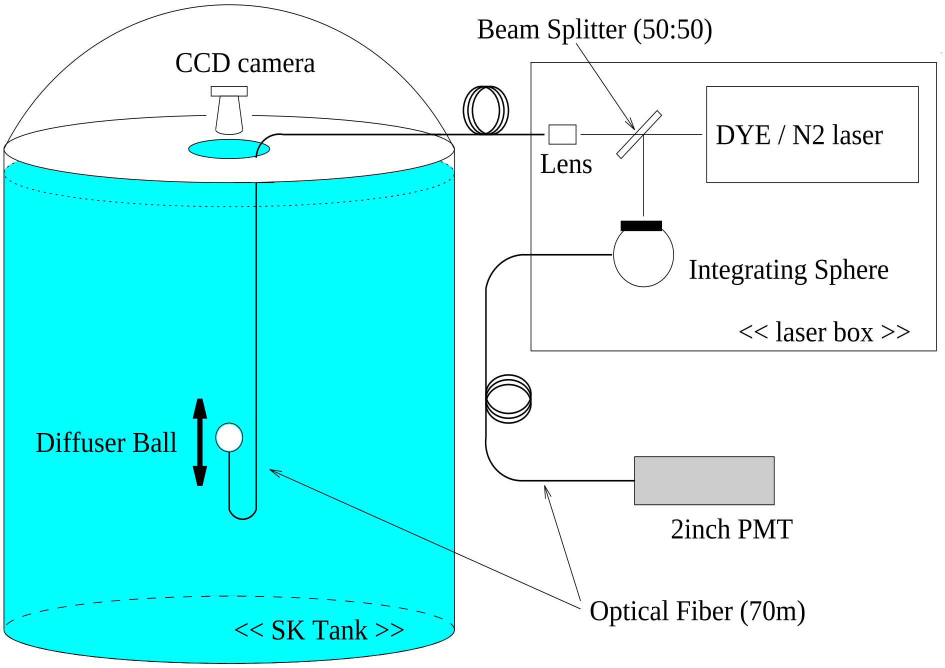

Figure 5.7: System for the direct measurement of the water transparency.

$$I(d) = \exp\left(-\frac{d}{\lambda_{tra}}\right) I_0 \tag{5.2}$$

where $I_0$ is the intensity of the light source, $I(d)$ is the measured intensity at the distance of $d$. Figure 5.8 shows the measured intensity $I_{CCD}$ normalized to the output charge of the monitoring PMT $I_{PMT}$ as a function of $d$ at a wavelength of 420nm. The fit result for $\lambda_{tra}$ is 97.9±3.5m. Figure B.1 shows water attenuation coefficient defined as $1/\lambda_{tra}$ as a function of the wavelength. The open points are the results of measurements. The line is used in the SK detector MC simulation.

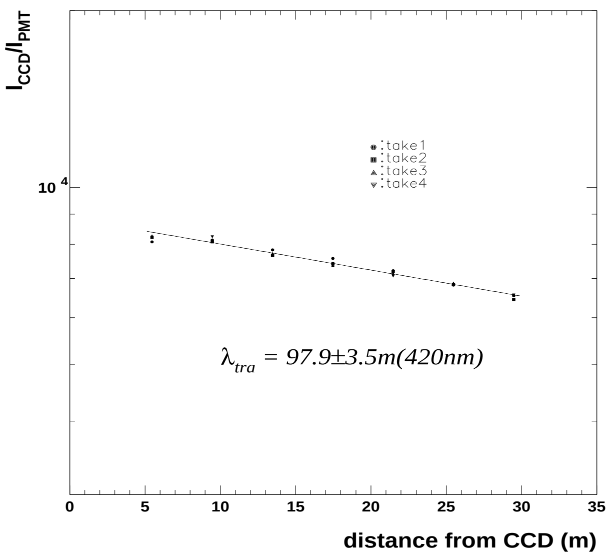

Figure 5.8: The measurement of the water transparency. $I_{CCD}/I_{PMT}$ vs $d$ is shown. The inverse of the slope in the figure is the water transparency; 97.9±3.5m at a wavelength of 420nm. Four different data sets are overlaid (take1∼4).

### 5.3.2 Monitoring water transparency by penetrating muons

The water transparency is monitored continuously using $\mu$ decay electron events. Though this method can only measure the water transparency averaged over the Čerenkov spectrum, the time variation of the water transparency caused by change of filter performance of the water purification system can be measured day by day, since about 1500 $\mu$ decay events happen every day. Figure 5.9 shows a schematic view of how the water transparency is calculated. To begin with, the relevant PMTs, which are within a 50nsec window after TOF subtraction (same as $N_{50}$ defined in chapter 4) and seen under an opening angle with respect to the direction of the decay electron within 32∼52°, are selected. These PMTs are projected onto a sphere with radius $R$, and the center at the vertex position of the event. On the sphere, these PMTs come to lie on a ring. The ring is divided into 36 equal parts as shown in figure 5.9. The $i$-th segment on the sphere has effective charge $\Delta Q_i$:

$$\Delta Q_i = \sum_{j=1}^{N_i} q_j \mathrm{exp}\left(\frac{d_j - R}{\lambda_e}\right) \tag{5.3}$$

where $N_i$ is the number of PMTs included in the $i$-th segment, $q_j$ is the acceptance corrected charge of the $j$-th PMT, $d_j$ is the distance from the vertex position to the $j$-th PMT position, and $\lambda_e$ is the water transparency to be calculated. In ideal case, all $\Delta Q_i$ $(i = 1, 36)$ should be equal:

$$\Delta Q_1 = \Delta Q_2 = \cdots = \Delta Q_{36} = \Delta Q \tag{5.4}$$

Since each segment can be regarded small, equation (5.3) can be rewritten:

$$\Delta Q = \exp\left(\frac{r}{\lambda_e}\right) q(r) \tag{5.5}$$

where $r \equiv \sum_{j=1}^{N_i} d_j/N_i$ is the mean distance, $q(r) \equiv \sum_{j=1}^{N_i} q_j$, and $R$ is set to 0.

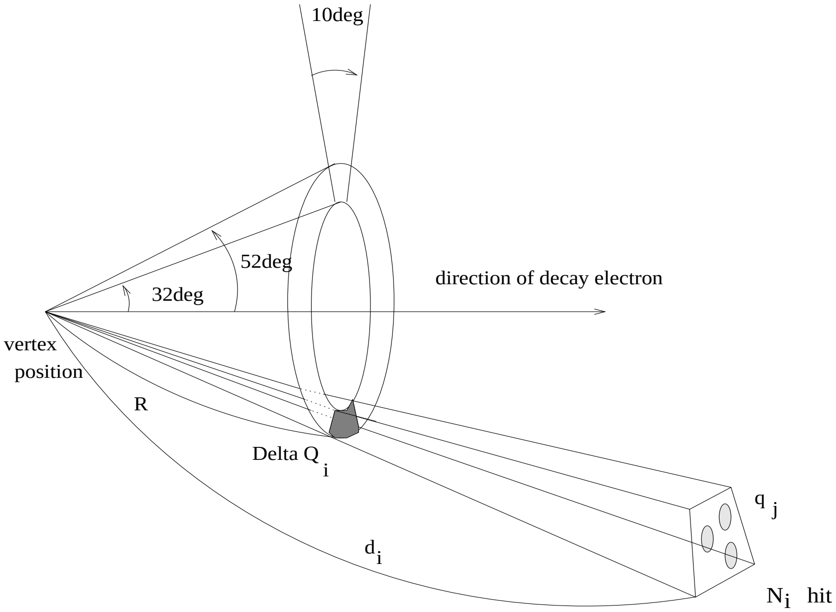

Figure 5.9: The schematic view of how to calculate the water transparency from a $\mu$ decay electron event.

$\Delta Q$ is different from event to event since the energies of the $\mu$ decay electrons are different, following the Michel spectrum. $q(r)$ follows this energy distribution, leading to:

$$\overline{q(r)} = \exp\left(-\frac{r}{\lambda_e}\right)\overline{\Delta Q} \tag{5.6}$$

$$\log(\overline{q(r)}) = -\frac{r}{\lambda_e} + \log(\overline{\Delta Q}) \tag{5.7}$$

where the upper bar means an average over the corresponding variable. From $\log(\overline{q(r)})$ and $r$, $\lambda_e$ can be calculated. Figure 5.10 shows $\log(\overline{q(r)})$ as a function of $r$. The slope is the inverse of $\lambda_e$. Figure 5.11 shows the time variation of the water transparency measured by this method. One point corresponds to one week. The first significant increase is due to a replacement of Ultra Filters and another increase is due to an exchange of the 1$\mu$m filters. The water transparency for each day is used in the energy calculation of equation (4.7).

Figure 5.12 shows the tank height dependence of the water transparency by above method. The height of the tank is divided to three of top, center and bottom. The measured transparencies for each zone are basically same tendency. However, the averaged transparency is slightly different by zone in table 5.1. Because the SK purified water is supplied from bottom usually, the transparency in bottom zone is better than top zone. The dust from the SK tank material goes up gradually from the bottom to the top by water convection. This tendency of the transparency for each zone, it is described in chapter 7 that the radon events in the SK tank is accumulated in the bottom zone, indicates that the radon events are independent of the dust in the tank.

| Zone | Averaged transparency (cm) |
|---|---|
| Top | 8708.8±64.4 |
| Center | 9906.7±64.4 |
| Bottom | 10200.8±64.4 |

Table 5.1: The averaged transparency for each zone. The error is statistical error.

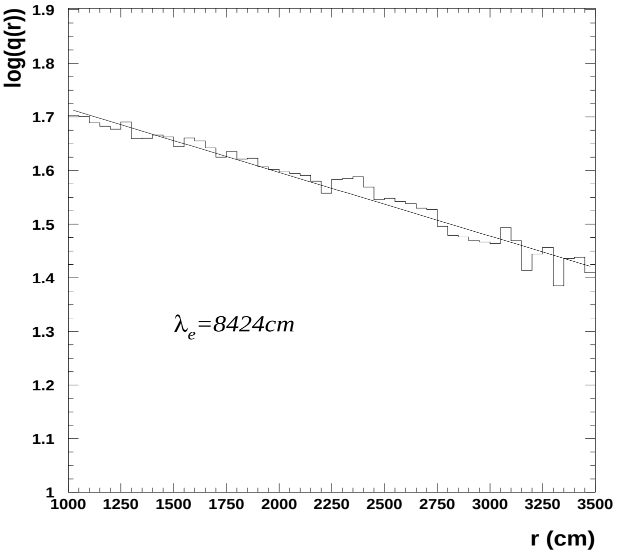

Figure 5.10: This figure shows $\log(\overline{q(r)})$ as a function of $r$. The slope measures the inverse of $\lambda_e$.

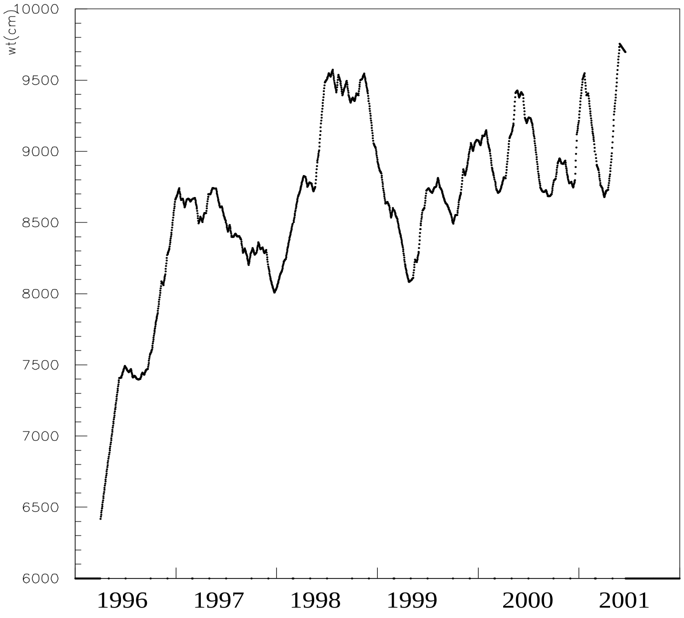

Figure 5.11: Measured time variation of the water transparency from April 1, 1996

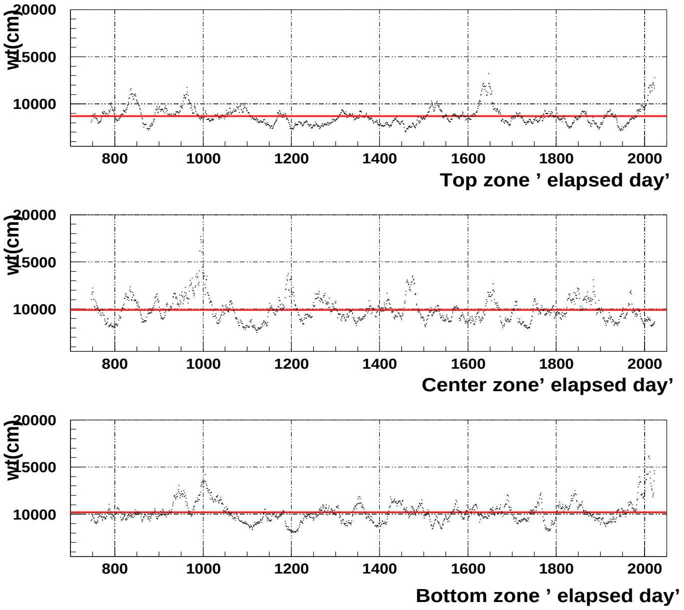

Figure 5.12: Measured time variation of the water transparency from April 1, 1996 for each zone. The solid lines are the averaged transparency for each zone.

## 5.4 Energy calibration by LINAC

The determination of the absolute energy scale is most important for the measurement of the energy spectrum of the recoil electrons scattered from solar neutrinos. In order to search for possible distortion of the energy spectrum by neutrino oscillations, for example the small angle solution of the MSW effect, the absolute energy must be calibrated with an accuracy of ∼1%. A Ni-Cf calibration source was used for the absolute energy calibration at Kamiokande and beginning of SK for solar neutrinos. However it has systematic uncertainties by itself which are large enough to spoil the measurement of the energy spectrum distortion. The main sources of uncertainty are the neutron capture cross sections and decay lines of $^{60}$Ni and $^{62}$Ni. A LINAC (LINear ACcelerator [104]) system which can inject electrons, that energy is similar to that of the recoil electrons, to the detector directly is most suitable for that purpose, since it has smaller systematic uncertainties. In this section, details of the absolute energy calibration with the LINAC are described. Uncertainties arising in the LINAC calibration are also discussed. More details of the LINAC calibration are given in [104].

### 5.4.1 The LINAC system

Figure 5.13 shows an overview of the LINAC calibration system. An electron LINAC is located 4.2m above and 13m away from the water tank in a mine tunnel. The LINAC was used at the hospital of Miyazaki Medical University as a cure for cancer. Electrons from an electron gun, which is specially improved in order to reduce the current to suitable level, allowing that only one electron is injected in to the tank, go through an acceleration tube in which the electrons are accelerated with microwaves of 2$\mu$sec width. The frequency of generation of the microwave is adjustable in a range of 10∼66Hz. The broad momentum of the electrons is determined by an input power to the acceleration tube, which is also adjustable. The electron energy range that the LINAC can generate is from 4.5 MeV to 16 MeV. Current of the electron beam can be changed by adjusting the output current of the electron gun. The accelerated electrons are bent by a magnet (D1 magnet) at the angle of 15 degrees. The electric current of the D1 magnet selects the momentum of the electrons fundamentally with two collimators near the magnet. Reduction factor of the electron current is about $10^{-6}$. The selected electrons go through a

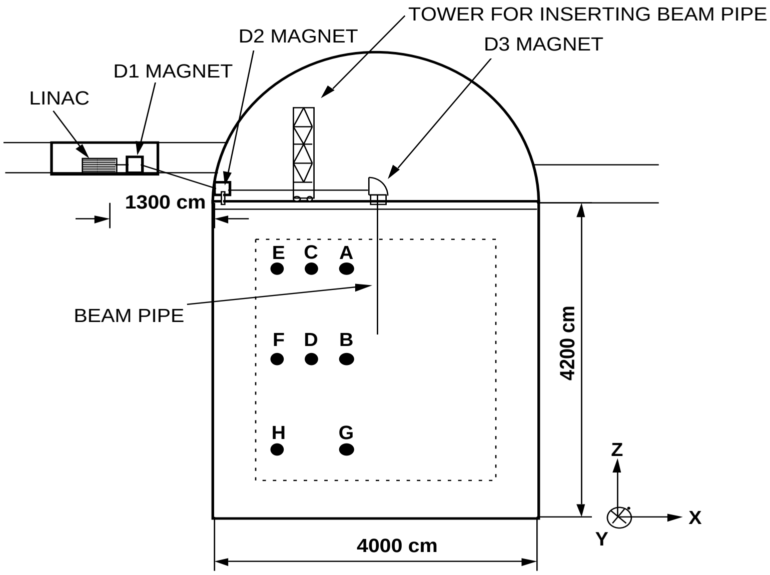

Figure 5.13: The overview of the LINAC calibration system.

beam pipe surrounded by rock as shown in figure 5.13. The rock plays a role to stop $\gamma$-rays generated by the collisions of the unselected electrons with the collimators or the beam pipe. By MC simulation, the probability that the $\gamma$-rays can penetrate the rock and OD is estimated to be less than $10^{-9}$. The electron momentum is further selected by a collimator before the D2 magnet. The momentum spread after this collimator is 0.5% at FWHM. Again many $\gamma$-rays are generated by this collimator. Lead blocks located under the collimator stop the radiation. The electrons passing thought the collimator are bent 15 degrees back to the horizontal direction by the D2 magnet. The electron beam traveling horizontally on the tank is bent again 90 degrees by the D3 magnet and injected downward to the tank. Quadrupole magnets (Q-magnets) located before and after the D3 magnet focus the electron beam on the end point of the beam pipe. Energy loss by bremsstrahlung at the D3 magnet is negligible small ($\sim 1.5 \times 10^{-8}$ MeV for total energy of 10 MeV).

Figure 5.14 shows the structure of the beam pipe end point. In left side in figure 5.14, upper

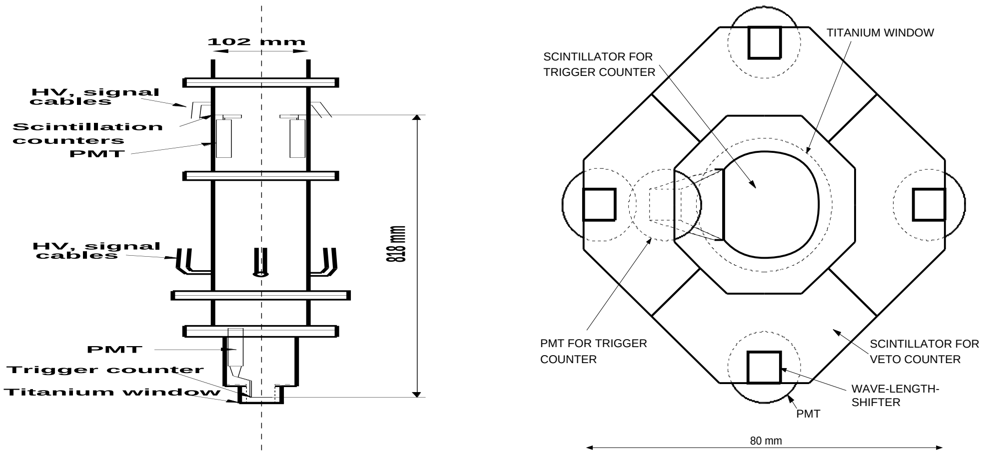

Figure 5.14: The end point of the beam pipe. Left figure shows side view and right figure shows top view.

scintillation counters are used for optimizing the beam profile at the end point and as a veto

| Position | $x$(cm) | $y$(cm) | $z$(cm) |
|---|---|---|---|
| A | $-388.9$ | $-70.7$ | 1228 |
| B | $-388.9$ | $-70.7$ | 27 |
| C | $-813.1$ | $-70.7$ | 1228 |
| D | $-813.1$ | $-70.7$ | 27 |
| E | $-1237$ | $-70.7$ | 1228 |
| F | $-1237$ | $-70.7$ | 27 |
| G | $-388.9$ | $-70.7$ | $-1173$ |
| H | $-1237$ | $-70.7$ | $-1173$ |

Table 5.2: The list of the positions where LINAC data was taken.

counter. A lower scintillation counter, with radius of 12mm and thickness of 1mm is used as a trigger counter. Last point of the beam pipe is covered by a 100 $\mu$m thick titanium window of 15mm radius which partitions the vacuum ($10^{-4\sim-5}$ torr) and water.

Electric currents of the D2 and the D3 magnet are set so that the electron beam hit the trigger counter maximumly. The current of the D1 magnet is set to a fixed value, selecting the electron momentum. Q-magnet current is calculated by a MC simulation of beam transportation. The beam intensity is adjusted to 0.1 electron per microwave in order to reduce the injection of more than 2 electrons in the tank water. The beam intensity can be also monitored on the water tank using monitoring scintillation counter located before the D3 magnet. By comparing the beam intensity on the tank and at the end cap, the degree of beam loss can be calculated. The loss gets worse as the beam momentum becomes small (about 80% at 5 MeV/c electron momentum). The missing electrons have a possibility to induce a $\gamma$-ray background. Discussion related with the background problem is given later.

The LINAC beam calibration about details is described in appendix D.

### 5.4.2 Energy calibration of SK detector

The injection of the electron beam to the SK detector was done at 8 positions. List of the 8 positions in terms of the detector coordinates defined in figure 5.13 is shown in table 5.2. A schematic view of the 8 positions is also shown in figure 5.13. At each position, an electron beam is injected with 6∼7 different momenta and about $2\times10^4$ events hitting the trigger counter are taken. The trigger logic used for the LINAC calibration is drawn in figure 5.15. In order to get the measured energy in the SK detector, at first, events issuing LINAC trigger are selected. Further, multiple electron events, that have more than two electrons injected to the SK detector accidentally in one event, are rejected. These events can be eliminated easily by counting number of peaks in the TOF subtracted time distribution of the hit PMTs. For example, figure 5.16 shows the TOF subtracted time distributions for the events selected as having one, two, or three electron multiplicity. About 5% LINAC triggered events are dropped by this selection. Figure 5.17 shows scatter plot of reconstructed vertex distribution with histograms of its projections on the $x$ and $z$ axes for finally selected events. The injection point is $\boldsymbol{x}$=($-388.9$cm,$-70.7$cm,$+27$cm) and the beam momentum is 16.31 MeV/c.

The measurement of the $N_{eff}$ in SK detector is done as follows. At first the measured $N_{eff}$ is plotted to one-dimensional histogram as shown in figure 5.18. Next, a Gaussian fit is applied to the distribution in a range from $-1\sigma$ to $+2\sigma$. A measured $N_{eff}$ value is defined as a mean value of the Gaussian fit and energy resolution is defined as (sigma of the Gaussian fit)/(the mean).

In order to get absolute energy scale, namely the relation between $N_{eff}$ and total electron energy, a MC simulation is used. A direct correlation between LINAC beam energy and the measured $N_{eff}$ value is not useful for that purpose, because there exists ∼1% non-uniformity

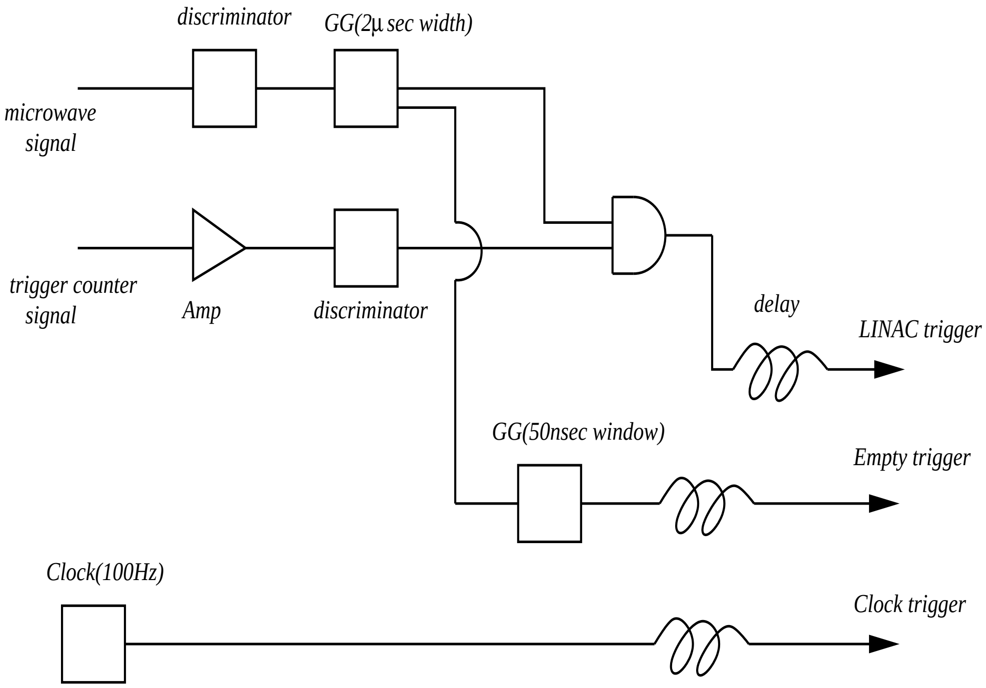

Figure 5.15: The trigger logic for the LINAC calibration. LINAC trigger is used for event selection. The other trigger is for study of beam correlated background.

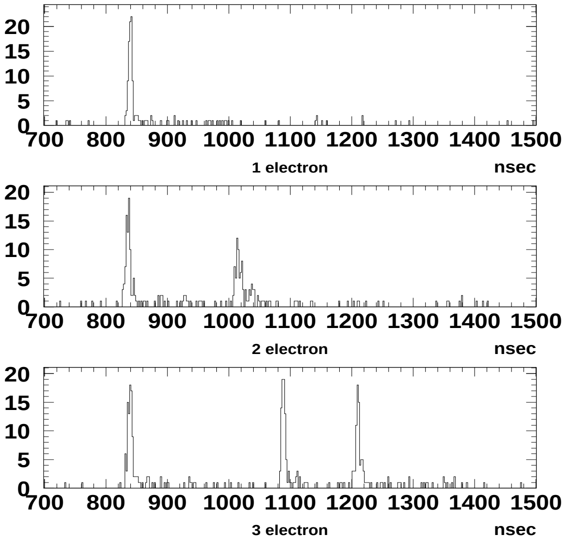

Figure 5.16: The TOF subtracted time distribution for the events selected as one, two, or three electron multiplicity. Each histogram represents one event that is representative of its class.

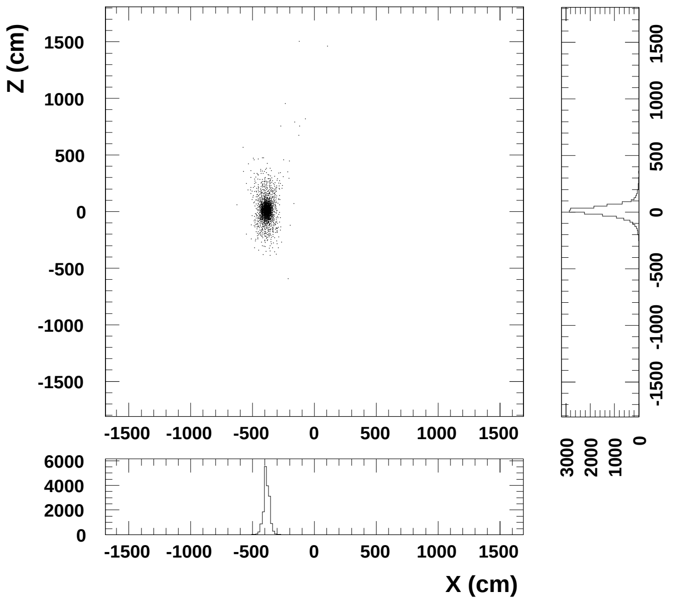

Figure 5.17: The scattered plot of the reconstructed vertex distribution with histograms of its projections on the $x$ and $z$ axes. The injection position is $\boldsymbol{x}$=(−388.9cm,−70.7cm,+27cm) and the beam momentum is 16.31 MeV/c.

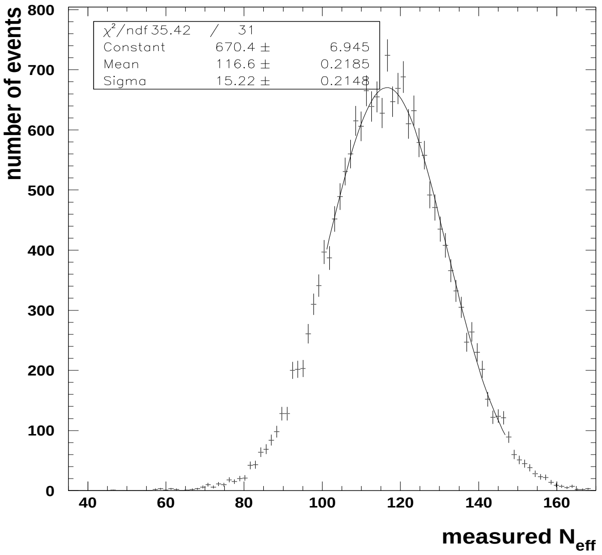

Figure 5.18: The measured $N_{eff}$ distribution in the SK detector at the position of $\boldsymbol{x}$=(−388.9cm,−70.7cm,+27cm) and beam momentum of 16.31 MeV/c.

of $N_{eff}$ in the fiducial volume and the LINAC calibration is done for only 8 positions with one (downward) direction, and the correlation cannot be easily extrapolated to the total fiducial volume and all direction. A MC simulation which includes the LINAC system configuration (namely the beam pipe, the trigger counter, and the Ti window) is carried out for various tuning parameters (collection efficiency and coefficients of scattering and absorption of light in water: see chapter 3). The input electrons are injected in the beam pipe from before the trigger counter to a downward direction with the beam spread corresponding to the size of the trigger counter. MC simulation data are also analyzed as same way as the LINAC data, and measured $N_{eff}$ values of both are compared. The tuned parameters for which the MC simulation best agrees with the LINAC data are selected.

With the best-tuned MC simulation, about $6\times10^4$ events are generated in the fiducial volume for electrons of total energy of 4, 5, 6, 7, 10, 15, 30 and 50 MeV. The distribution of the $N_{eff}$ for total energy of 10 MeV is shown in figure 5.19. A Gaussian fit is applied to the distribution to reduce the distribution to a value. An MeV value for the total energy of the electrons is obtained by fitting a 4-th order polynomial function as shown in figure 5.20. A fitting accuracy is about ±0.1%. Thus the energy observed in SK, $E_{SK}$ is defined by in our current MC simulation

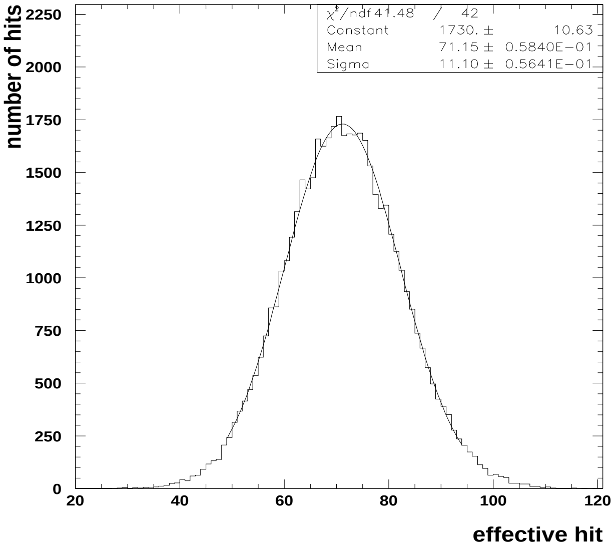

Figure 5.19: The distribution of the $N_{eff}$ for the electron events of total energy of 10 MeV. A Gaussian fit is applied to get the peak value of the distribution.

$$\begin{aligned} E_{SK} = 0.80586 + 0.12982N_{eff} - 0.17176 \cdot 10^{-4}N_{eff}^2 \\ +0.19489 \cdot 10^{-6}N_{eff}^3 - 0.32113 \cdot 10^{-9}N_{eff}^4 \end{aligned} \tag{5.8}$$

If higher order terms are ignored, the conversion from the $N_{eff}$ to the energy is approximately represented as 1 MeV$\simeq$7.71 effective hits.

The measured energy distribution of the LINAC data and the MC simulation for seven beam energies at the position $\boldsymbol{x}$=(−1237cm,−70.7cm,+1228cm) is shown in figure 5.21. Agreement is very good including width of the energy distribution Further, figure 5.22 shows an energy spectrum of 10.78 MeV/c LINAC data summing the data of 8 positions (cross marks) with the corresponding MC (boxes, each box height corresponds to square sum of MC statistical error and energy resolution systematic error(2%), which is described later). As shown in the figure, the MC simulation reproduces the detector response to electrons even up to a $3\sigma$ tail of the spectrum.

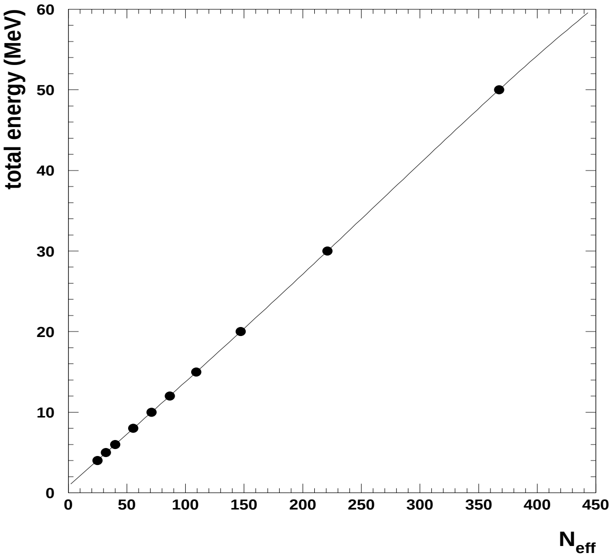

Figure 5.20: A 4-th order polynomial fit to the correlation between the peak values of the $N_{eff}$ and the total energies of the electrons.

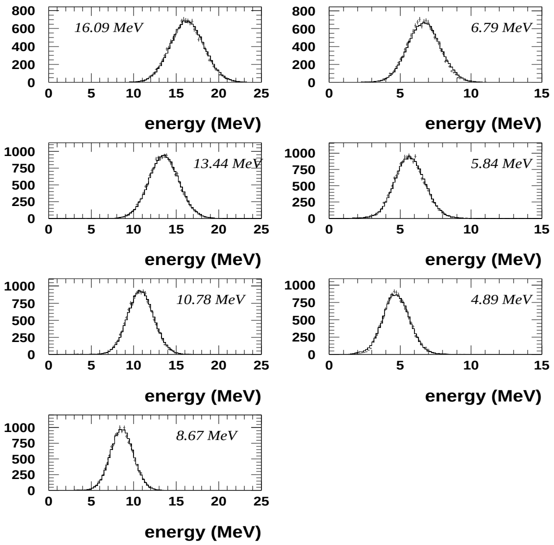

Figure 5.21: LINAC data and MC simulation measured energy distribution for seven beam energies at a position $\boldsymbol{x}$=(−1237cm,−70.7cm,+1228cm). The cross marks are the LINAC data and histograms are the MC simulation.

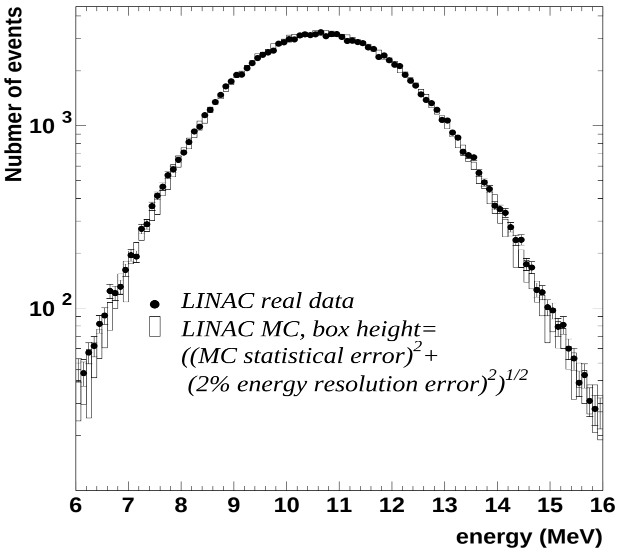

Figure 5.22: Summed energy spectrum for real data (cross marks) and MC simulation (boxes) over the LINAC 8 positions with the beam momentum of 10.78 MeV/c.

The LINAC calibration data are used for tuning of the parameters in the SK detector MC simulation. However, there still remain systematic discrepancies between data and MC. Another useful aspect of the LINAC calibration data is to evaluate remaining systematic difference between the LINAC data and the MC simulation. Energy deviation between them for each beam energy and at each position is shown in figure 5.23. Error bars of all marks are statistical at each point and for each beam energy. From now on, the LINAC data is denoted as 'LINAC' and the MC simulation as 'MC'. The energy systematic difference is evaluated for two classifications, i.e. energy dependence and position dependence, and these are shown in figure 5.24. Figure 5.24 (a) and (b) shows position averaged and energy averaged deviation between data and MC, respectively. Outside error bars in figure 5.24(a) are systematic uncertainty of the LINAC calibration. The systematic uncertainties about details is described in appendix D. Inner error bars are statistically combined error and the rightest mark in figure 5.24(a) is combined difference for all momenta and at all positions. These values are used for an evaluation of the systematic error of the solar neutrino flux and the measurement of the energy spectrum. The detailed discussion of it is given later. In figure 5.24(a), though the deviation have energy dependence, all points stay within ±0.5%. These figures are used for evaluating energy correlated systematic errors as described in next section.

Energy resolution is also investigated. Figure 5.25 shows the energy resolution as a function of the electron total energy at each position for the LINAC data (a) and the MC simulation (b). Position averaged deviation of the energy resolution as a function of the electron total energy is also shown in figure (c). Although the energy resolution is not a tunable parameter, the deviation between the LINAC data and the MC simulation is consistent within 2%.

The energy systematic energy resolution difference is evaluated for two classifications, i.e. energy dependence and position dependence, and these are shown in figure 5.26. Figure 5.26 (a) and (b) shows position averaged and energy averaged deviation between data and MC, respectively.

The time and directional uniformity by LINAC calibration about details is described in appendix D.

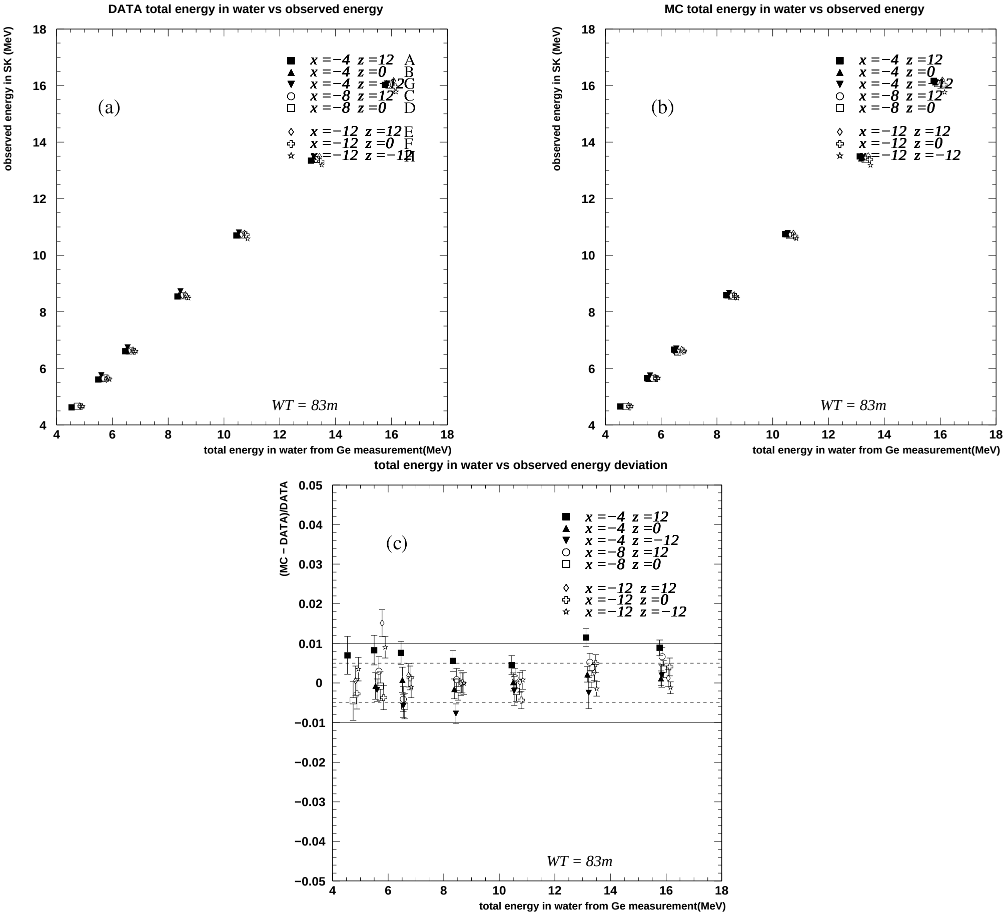

Figure 5.23: The energy deviation between the LINAC data and the MC simulation for seven beam energies and at 8 positions for LINAC data(a) and MC simulation(b). Figure (c) shows the deviation of the energy resolution at each position. A∼H mean the positions defined in table 5.2.

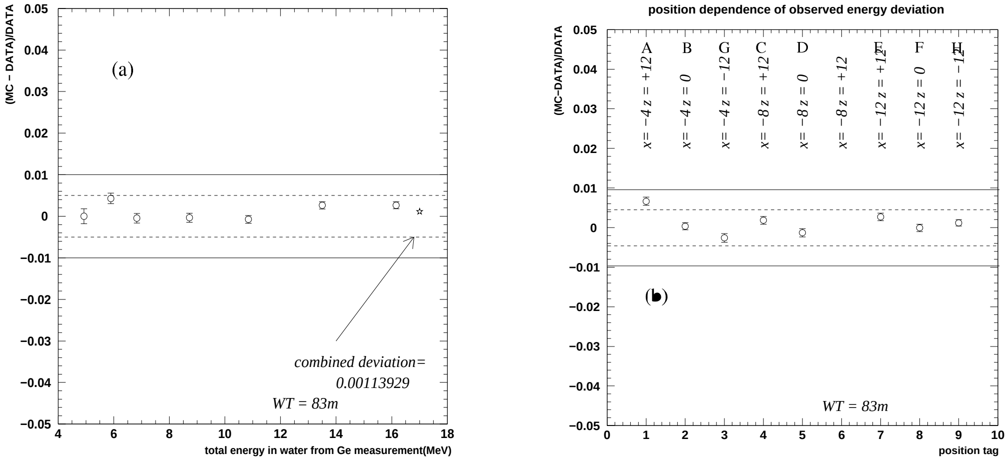

Figure 5.24: The systematic energy difference between the LINAC data and the MC simulation, (a) energy dependence (position averaged deviation) and (b) position dependence (energy averaged deviation). Outside error bars of figure(a) are the LINAC system systematic uncertainty described later. Inside error bars are the statistical error. Error bars of figure(b) are only statistical error.

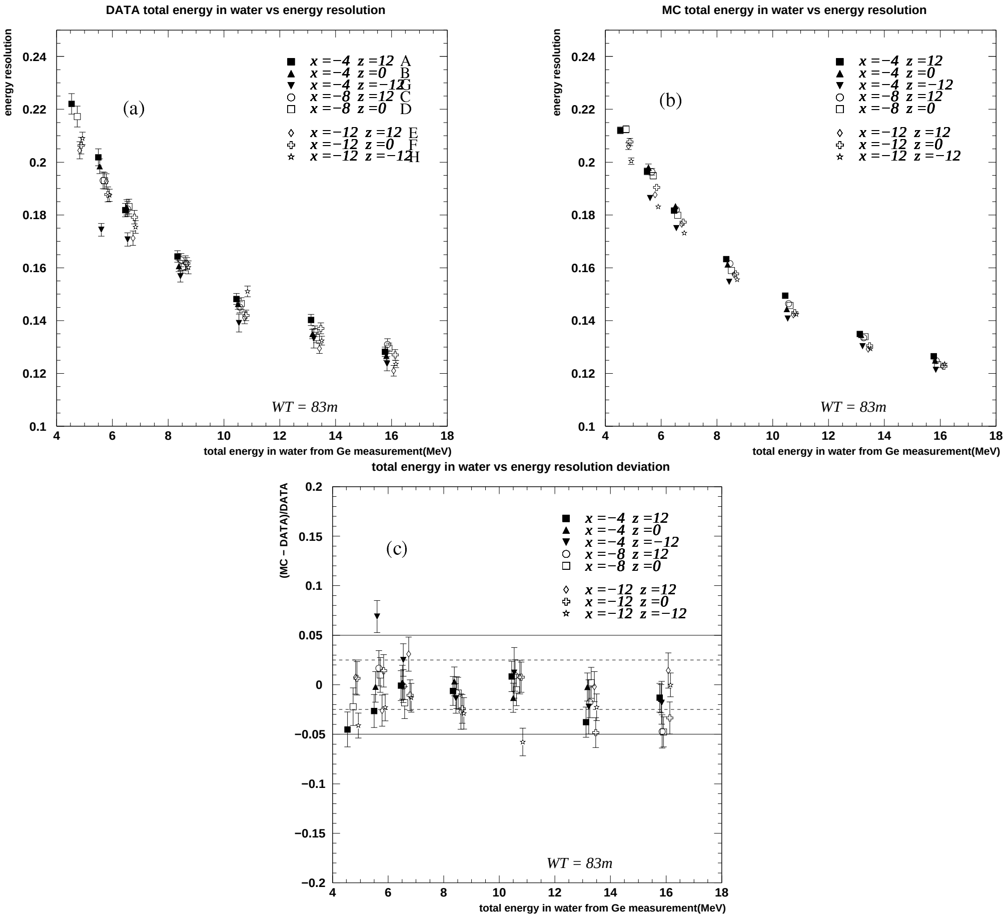

Figure 5.25: The energy resolution as a function of the electron total energy at each position for LINAC data(a) and MC simulation(b). Figure (c) shows the deviation of the energy resolution at each position.

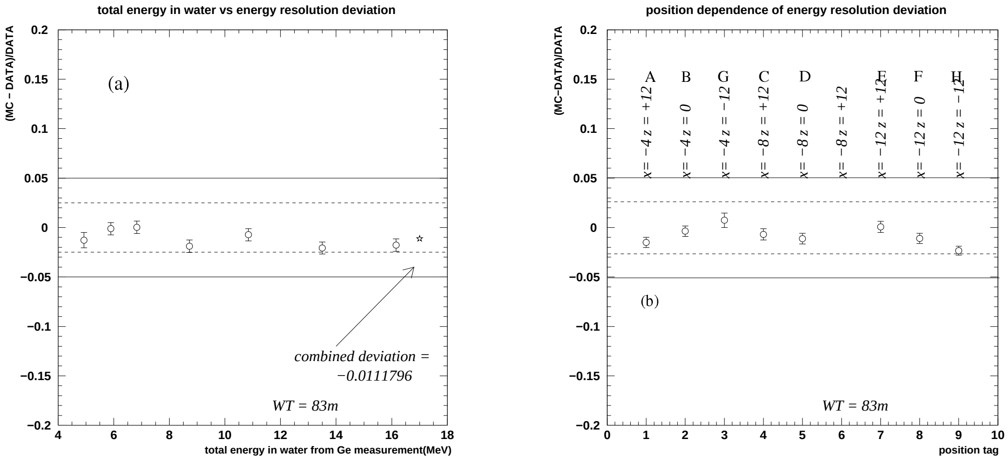

Figure 5.26: The systematic energy resolution difference between the LINAC data and the MC simulation, (a) energy dependence (position averaged deviation) and (b) position dependence (energy averaged deviation). Outside error bars of figure(a) are the LINAC system systematic uncertainty described later. Inside error bars are the statistical error. Error bars of figure(b) are only statistical error.

## 5.5 Angular resolution

Angular resolution at SK detector is measured by the LINAC calibration. Though the LINAC system can measure the angular resolution for only one direction (downward), it provides a crucial test of the detector simulation. Figure 5.27 shows distributions of an opening angle between the direction of the beam injection and the reconstructed direction for LINAC data (cross) and MC simulation (histogram) at a position $\boldsymbol{x}=(-1237\text{cm},-70.7\text{cm},+1228\text{cm})$ for 7 electron momenta. Agreement is excellent. The angular resolution is defined as an angle which includes 68% of the reconstructed directions around the beam direction. Energy dependence of the angular resolution at 8 positions for LINAC data and MC simulation are shown in figure 5.28(a) and (b) respectively. Figure 5.28 (c) shows deviation between LINAC and MC for 7 momenta and at 8 positions. Though the angular resolution of MC simulation is larger than that of LINAC data and the deviation has some position dependence, almost all points are consistent within 5%. Error bars of figure 5.28(a),(b),(c) are only the statistical error. Figure 5.28(d) shows the position combined deviation. Error bars of 5.28(d) are variances at each beam momentum in figure 5.28(c). This slight disagreement between LINAC and MC causes a comparatively large systematic error for the measured solar neutrino flux value.

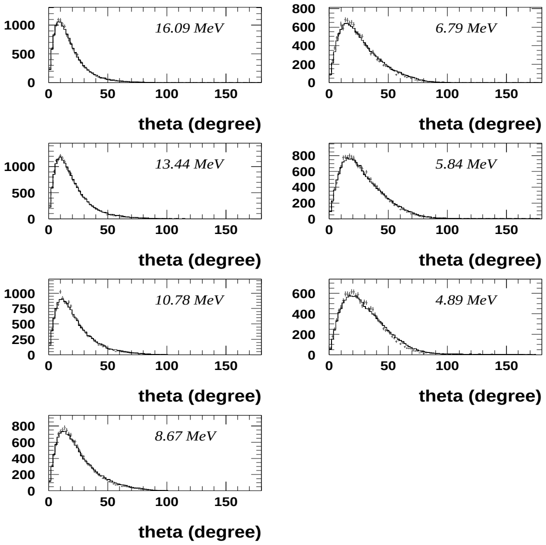

Figure 5.27: An opening angular distribution at $\boldsymbol{x}=(-1237\text{cm},-70.7\text{cm},+1228\text{cm})$ for 7 electron momenta. The cross marks are the LINAC data and histograms are the MC simulation.

## 5.6 Vertex resolution and shift

The LINAC system can also calibrate vertex resolution. Figure 5.29 shows distributions of distance from the end point of the beam pipe to the reconstructed vertex position at a beam injection position $\boldsymbol{x}=(-1237\text{cm},-70.7\text{cm},+1228\text{cm})$ for 7 beam momenta. Again cross marks are for LINAC data and histograms are the MC simulation. Vertex resolution is defined as a spherical radius which includes 68% reconstructed vertex position around the end point. Figure 5.30 shows (a) the vertex resolution as a function of the electron total energy at 8 positions for LINAC data, (b) same as (a) but for the MC simulation, (c) deviation between (a) and (b), (d) deviation combined for the 8 positions. Error bars of the figures are the same as those of figure 5.28. The timing resolution of the ID PMTs for single photo-electron response in the MC simulation is adjusted so that the vertex resolutions of the LINAC data and the MC simulation

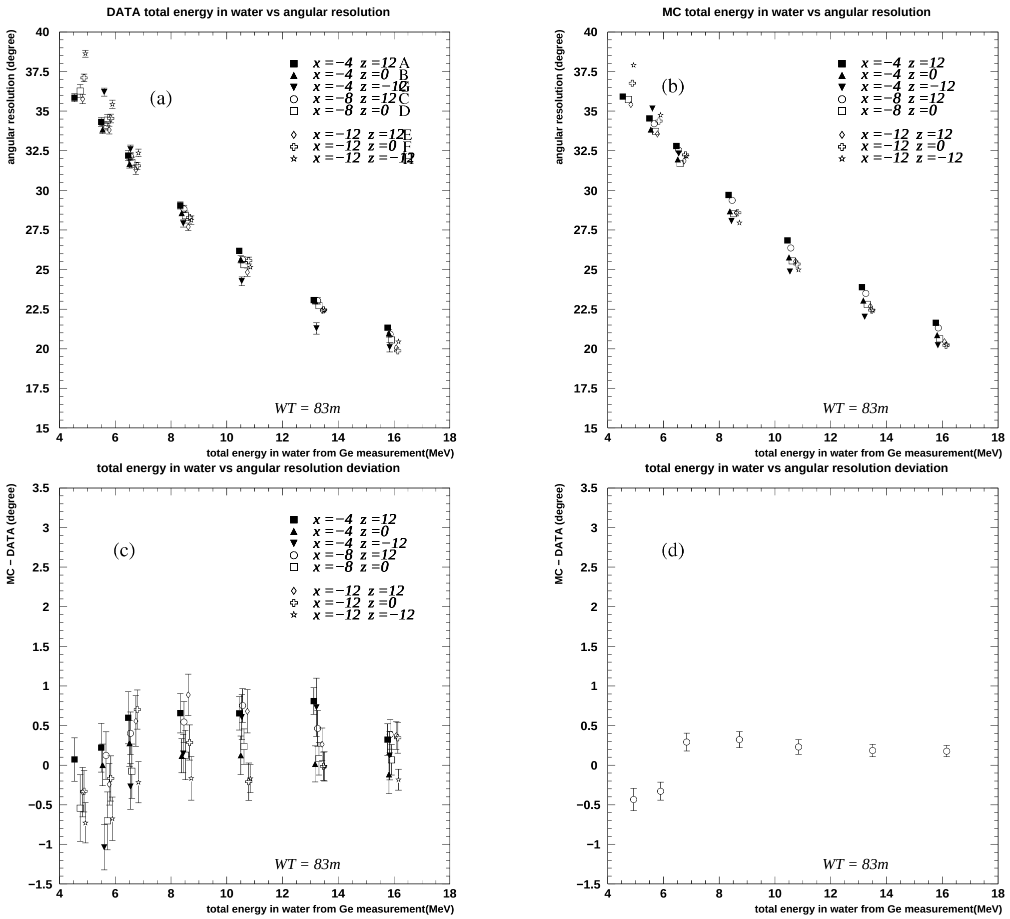

Figure 5.28: Angular resolution as a function of the electron total energy. (a) is for LINAC data, (b) is for MC simulation, (c) is the deviation between LINAC and MC at 8 positions and 7 momenta and (d) is the position combined deviation. Explanations of error bars of the figures are given in text.

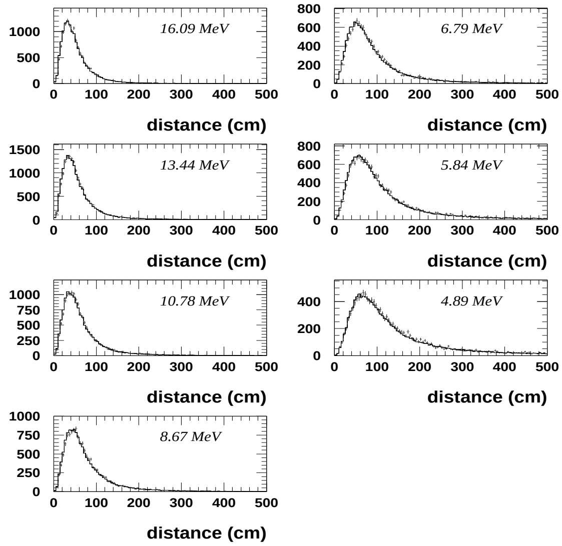

Figure 5.29: Distributions of distance from the end point of the beam pipe to the reconstructed vertex position at a beam injection position $\boldsymbol{x}$=(−1237cm,−70.7cm,+1228cm) for 7 beam momenta for LINAC data (cross) and MC simulation (histogram).

| Source position | $\Delta x$ | $\Delta y$ | $\Delta z$ |
|---|---|---|---|
| (35.3,−70.7,−1200.) | −0.3 | −2.7 | −3.0 |
| (35.3,−70.7,0.) | 0.7 | −0.5 | −1.9 |
| (35.3,−70.7,+1200.) | −1.0 | −0.7 | −1.0 |
| (35.3,−70.7,+1600.) | −0.6 | −2.8 | −10.0 |
| (35.3,−1201.,−1200.) | −3.4 | 7.0 | −7.0 |
| (35.3,−1201.,0.) | −1.1 | 16.0 | −1.1 |
| (35.3,−1201.,+1200.) | 0.6 | 10.0 | 2.0 |

Table 5.3: The vertex shift measured by the Ni-Cf source. The unit is cm.

are consistent for 8 positions, and the value is determined to be 2.4nsec, which agrees with the independently measured value [82].

It it important to know a shift of the vertex position in the vertex reconstruction, since the vertex shift causes a change of the fiducial volume size, i.e. the target number of the solar neutrinos. In order to estimate the vertex shift, the Ni-Cf calibration source is used. An advantage to use the Ni-Cf $\gamma$-ray source is that the source can emit $\gamma$-rays to almost uniform directions. The vertex shift is defined as a vector from an averaged position of the reconstructed vertex of the data to that of a corresponding MC simulation. Table 5.3 shows the vertex shift at some source positions. These values are used to obtain systematic error for the measured solar neutrino flux.

## 5.7 Energy calibration by DT

The LINAC calibration has limitations. The electrons are only moving in a downward direction when they exit the beam pipe, possibly introducing systematic errors due to direction dependences of the detector. The presence of the beam pipe in the tank while calibration data are taken is another limitation. While this is modeled in the simulation, it is still the largest source

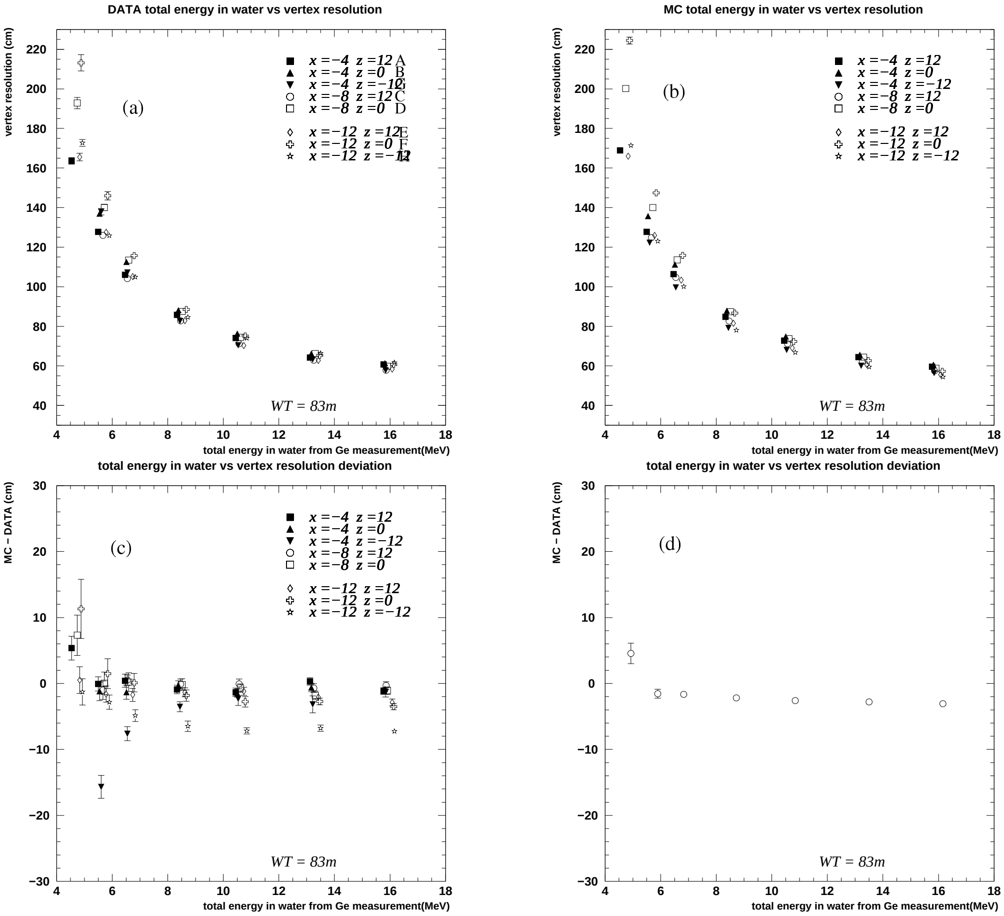

Figure 5.30: Vertex resolution as a function of the electron total energy. (a) is for LINAC data, (b) is for MC simulation, (c) is deviation between LINAC and MC at 8 positions and 7 momenta and (d) is the position combined deviation. Explanations of error bars of the figures are given in the text.

of systematic error for the calibration, especially at low energies. Additionally, the beam pipe and equipment associated with the LINAC calibration can only be operated at a restricted set of calibration ports, so the calibration must be extrapolated to the entire fiducial volume. Operating the LINAC also requires a great deal of manpower and results in significant detector down time.

The $^{16}$N used as a calibration source for SK are produced by two different mechanisms [104]. The first source results from the interaction of 14.2 MeV neutrons in the water of the detector. These neutrons are from a deuterium-tritium neutron generator (DTG), and produce a high statistics sample of $^{16}$N at a set position in the detector. The second source of $^{16}$N is the capture of stopped $\mu^-$ in the water of the detector. These events, like solar neutrinos, are uniformly distributed throughout the detector volume. For both of these data sets, the beta decay of $^{16}$N is carefully modeled, and the corresponding MC is compared to the data. Since the energy scale of the MC is set by the LINAC calibration, a comparison of $^{16}$N data to MC serves as a cross check of the energy scale.

At the center of the DTG setup is a MF Physics Model A-211 pulsed neutron generator. This neutron generator creates neutrons by the deuterium-tritium reaction,

$$^{3}\mathrm{H} + \ ^{2}\mathrm{H} \rightarrow \ ^{4}\mathrm{He} + \mathrm{n}. \tag{5.9}$$

This reaction yields isotropically distributed neutrons with an energy of 14.2 MeV.

The schematic view of the DTG generator is shown in figure 5.31.

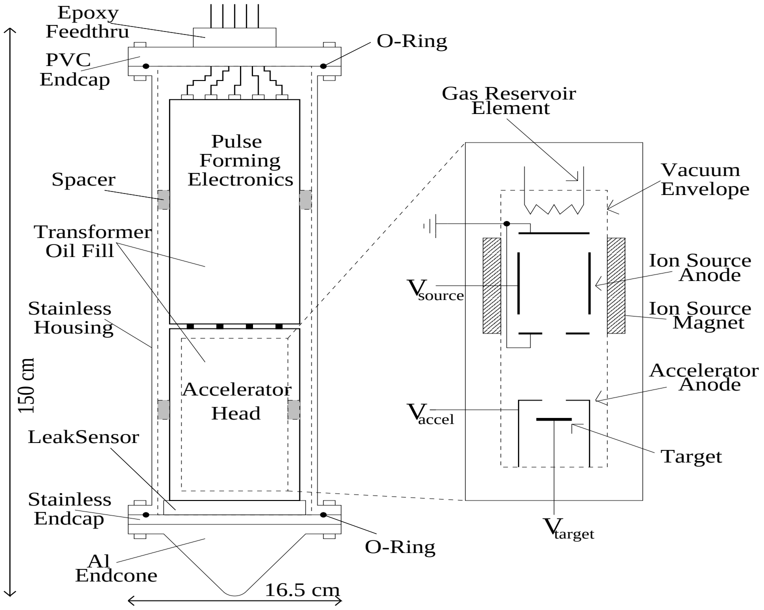

Figure 5.31: Schematic of the DTG setup including the stainless steel water-tight housing, accelerator pulse-forming electronics and accelerator head. Details of the accelerator head are also shown.

The 14.2 MeV neutrons produced by the DTG are energetic enough to produce $^{16}$N by the (n,p) reaction on $^{16}$O [83] in the water of SK, which requires neutron energies greater than $\sim$11 MeV. [84]. The (n,$\alpha$) and (n,d) reactions on $^{16}$O result in the creation of stable isotopes, while the creation of $^{15}$O by the (n,2n) reaction is energetically forbidden. The (n,p) reaction on $^{17}$O and $^{18}$O are suppressed by the low isotopic abundance and smaller reaction cross sections, which results in yields $< 1 \times 10^{-4}$ that of $^{16}$N.

When taking data at SK, the DTG is lowered to a position 2 meters above the intended $^{16}$N production point, and the data taking cycle is started (Figure 5.32). The data taking cycle is controlled by computer, directing the crane, the generator and data collection of SK. First, the crane lowers the DTG 2 meters, to the data collection position. Next, the generator is fired, creating a bubble of $^{16}$N surrounding the end of the DTG. Every time the DTG is fired, the generator is pulsed 3 times, at the maximum rate of 100 Hz, producing $\sim$3 million neutrons. Third, the DTG is raised 2 meters, removing the generator from the area containing $^{16}$N. After the DTG is fired, $\sim$10 seconds are required before the apparatus is completely withdrawn, and $\sim$60% of $^{16}$N has decayed. No data are collected while the crane is moving to prevent electrical noise generated by the crane from contaminating the data. Once the crane has stopped moving upward, data are collected in SK for 40 seconds. This cycle is repeated $\sim$25 times at a single location in the SK tank, yielding a data sample of $\sim$300,000 $^{16}$N events collected by SK.

The creation of $^{16}$N occurs naturally as a background to the solar neutrino measurement. A stopped $\mu^-$ can be captured by a $^{16}$O nucleus in the water of the detector,

$$^{16}\mathrm{O} + \mu^- \rightarrow\ ^{16}\mathrm{N} + \nu_\mu. \tag{5.10}$$

A fraction of $^{16}$N created will be in the ground state, and beta decays with a 7.13 sec half life. These events are found by collecting events that occur in the area surrounding the stopping point of a captured muon and subtracting random background events.

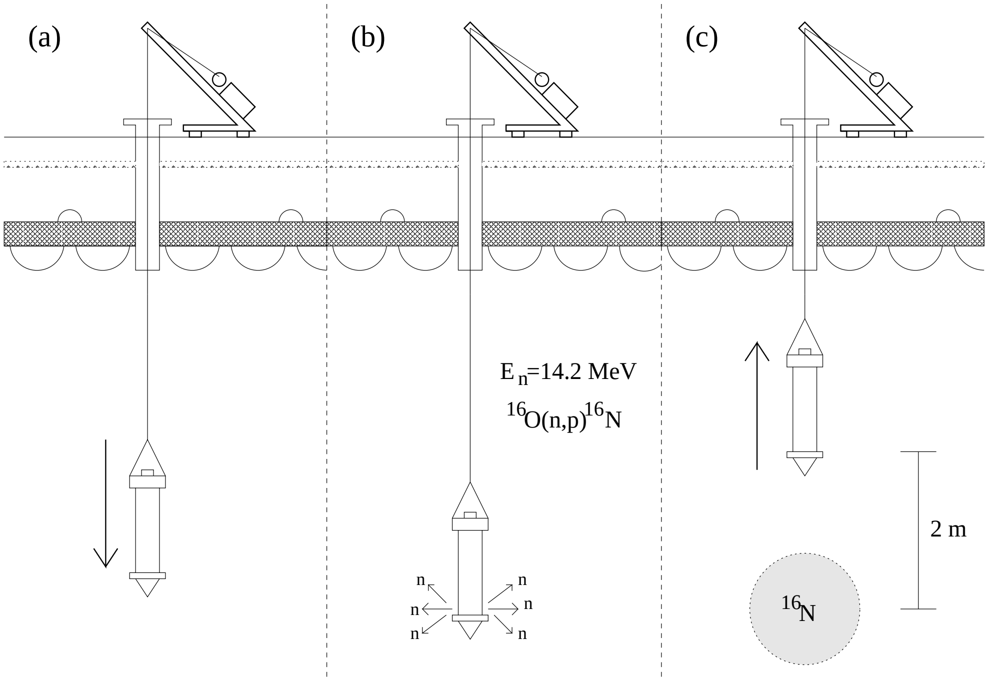

Figure 5.32: An overview of DTG data taking. In (a), the DTG is lowered to the position where data is to be taken, The DTG is fired in (b) at that location, and (c) withdrawn 2 meters and data collected.

Careful modeling of the $^{16}$N beta decay is crucial in order to perform accurate MC simulations of $^{16}$N data. All decay lines with a probability of $10^{-8}$ or greater are included. Table 5.4 contains information about the included decay lines.

The energy spectrum from a typical data taking run is presented in figure 5.33, along with the corresponding MC simulation. The peak of the energy distribution is dominated by events with a 6.1 MeV gamma ray in coincidence with an electron with a 4.3 MeV endpoint energy. 28% of the events contain an electron with an endpoint energy of 10.4 MeV and are the primary source of the observed high energy tail. This data was taken at a nominal position of (-388.9 cm, -70.7 cm, 0 cm).

The data from the DTG are also used to study the position and direction dependence of the energy scale. DTG data was taken in 6 different calibration port locations, at 7 depths per

| Fraction | $J_i^p \rightarrow J_f^p$ | ΔI | Gamma Energy (MeV) | Type |
|---|---|---|---|---|
| 66.2% | $2^- \rightarrow 3^-$ | +1 | 6.129 | GT allowed |
| 28.0% | $2^- \rightarrow 0^+$ | -2 | none | GT 1st forbidden |
| 4.8% | $2^- \rightarrow 1^-$ | +1 | 7.116 | GT allowed |
| 1.06% | $2^- \rightarrow 2^-$ | +0 | 8.872 | F+GT allowed |
| 0.012% | $2^- \rightarrow 0^+$ | -2 | 6.049 | GT 1st forbidden |
| 0.0012% | $2^- \rightarrow 1^-$ | +1 | 9.585 | GT allowed |

Table 5.4: Summary of information used in modeling the beta decay of $^{16}$N [85]. Gamma energies are also included. GT denote Gamow-Teller transitions and F denote Fermi transitions.

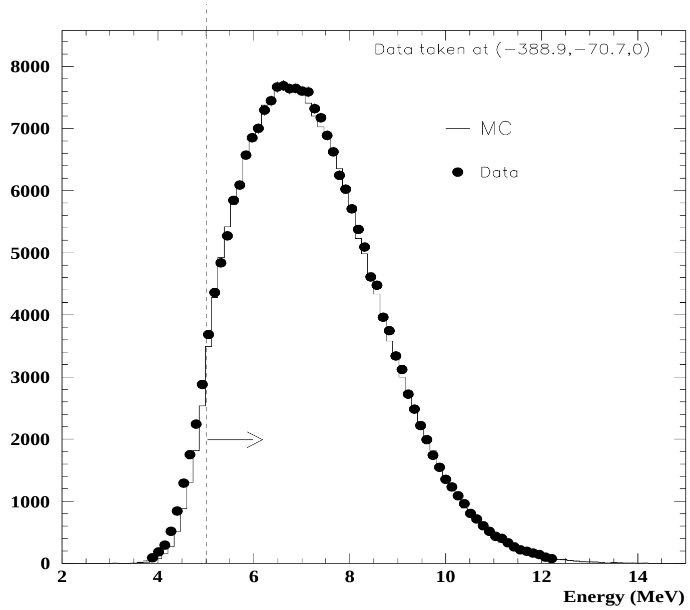

Figure 5.33: Energy spectrum for Data and MC from a typical data taking run at a single point in the SK tank. The data (points) and MC (line) are fit with a Gaussian function only above the 5.0 MeV analysis threshold.

| | |
|---|---|
| Contamination from natural background | $< 0.01\%$ |
| $^{16}$N MC decay modeling | $\pm 0.1\%$ |
| Unmodeled decay lines | $< 0.01\%$ |
| Shadowing of Čerenkov photons | $\pm 0.1\%$ |
| DTG data selection systematic | $\pm 0.1\%$ |
| DTG related radioactive background | $\pm 0.05\%$ |
| Total Systematic Error | $\pm 0.2\%$ |

Table 5.5: Summary of systematic errors from the DTG calibration.

port, providing a large sampling of the detector volume. The position dependence of the energy scale, shown in figure 5.34, is presented as a function of radial distance (r) and height (z) in the detector, by performing a position-weighted average over z and r, respectively.

The direction dependence is studied as a function of zenith angle, measured with respect to the vertical (z) axis of the detector, and as a function of azimuthal angle, measured in the x-y plane. The resulting angular dependence of the energy scale is presented in figure 5.35. In both cases, the variation in the energy scale in direction within the fiducial volume is less than 1%.

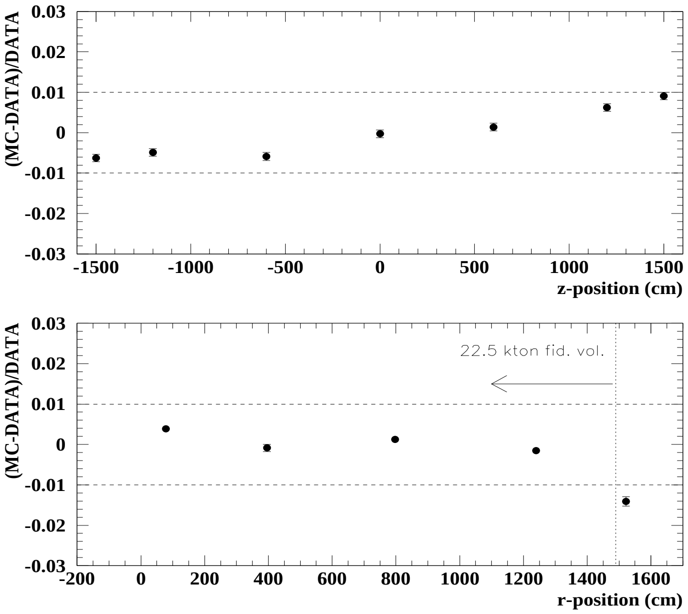

Figure 5.34: Position dependence of the energy scale from DTG data. At each r and z vertex position, a position-weighted average over all z and r positions, respectively, is performed. Only statistical errors are shown. Dashed lines indicate a deviation of ±1%.

The systematic errors for the DTG calibration for the absolute energy scale measurement are summarized in table 5.5. A simulation of neutrons in the DTG setup indicates that small amounts of background isotopes are created, including $^{24}$Na, $^{62}$Co, and $^{28}$Al. Most nuclides have long half lives and/or insufficient energy to trigger SK, but a MC simulation indicates a small amount of gamma contamination is possible, and a systematic error of ±0.1% is conservatively chosen. The DTG data selection systematic error results from a vertex position cut made to the data to remove background events occurring near the walls of the detector from the data sample.

The total position averaged energy scale deviation, $(\frac{MC-DATA}{DATA})$, measured during the July 1999 survey of the detector is found to be $-0.04\% \pm 0.04\%(stat.) \pm 0.2\%(syst.)$, indicating excellent overall agreement of the DTG data with the LINAC-based MC simulation.

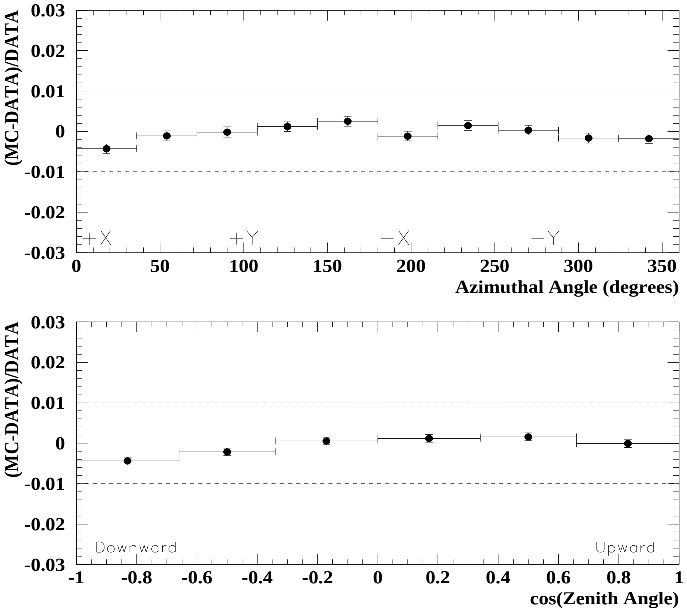

Figure 5.35: Angular dependence of energy scale from DTG data obtained from a position-weighted average over all positions in the fiducial volume. An azimuthal angle of 0 degrees corresponds to the +X axis of SK. Only statistical errors are shown. Dashed lines indicate a deviation of ±1%.

## 5.8 Trigger efficiency measurements

For the solar neutrino analysis, we use two difference triggers, as described in chapter 3: the Low Energy trigger (LE) and the Super Low Energy trigger (SLE trigger). Hence, the trigger efficiency for both has to be measured.

The trigger efficiency is measured using the Ni-Cf system and the DT generator. The low energy trigger efficiency is defined as follows.

$$Efficiency_{\text{LE trigger}} \equiv \frac{N_{\text{LE trigger}}}{N_{\text{special trigger}}} \tag{5.11}$$

$$Efficiency_{\text{SLE trigger}} \equiv \frac{N_{\text{SLE trigger}}}{N_{\text{special trigger}}} \tag{5.12}$$

where, $Efficiency_{\text{LE,SLE trigger}}$ is the trigger efficiency. $N_{\text{LE,SLE trigger}}$ is the number of events issuing both the LE, SLE trigger and a special low energy trigger with a threshold of -150 mV. $N_{special}$ is the number of events issuing the special low energy trigger. In measuring the SLE trigger efficiency, the number of event issuing the both the SLE trigger and the special low energy trigger is used instead of $N_{\text{LE,SLE trigger}}$.

The LE efficiency is 99.8% for events with energy of 6.5∼7.0 MeV, the LE trigger efficiency is 100%. The trigger efficiency is measured at a various positions in the ID and at various water transparencies to study the possible dependence on the vertex position, the event direction, and water transparency. In order to consider these dependences in the MC simulation, a trigger simulator is used. In the trigger simulator, the trigger threshold is defined by the number of effective hits. The threshold level is set to reproduce the energy and position dependence of the trigger efficiency seen in data.

The SLE trigger was installed in May 1997 and the threshold has been changed 7 times. The changes in the SLE trigger threshold are summarized in table of chapter 3

Figure 5.36 shows the energy dependence of the SLE trigger efficiency for each trigger threshold. The line shows the analysis threshold for this thesis (4.5 MeV). Above 6.0 MeV, the SLE trigger efficiency is 100% for all positions.

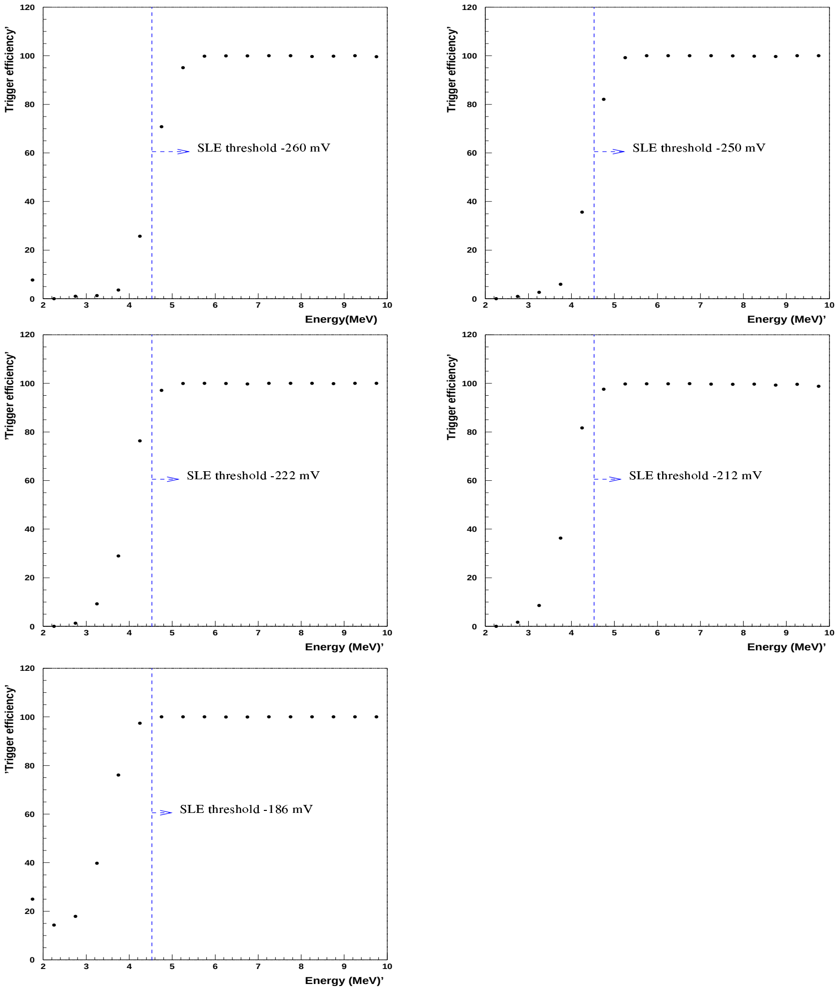

Figure 5.36: The SLE trigger efficiency as a function of energy by DT calibration.

As described in chapter 3, when the number of hit PMTs exceeds 29, a global trigger (L.E trigger) is issued. It is important for the solar neutrino observation to know how much measured energy is necessary in order to issue the trigger. In order to investigate the trigger efficiency, again the Ni-Cf source is used. As described in this chapter, the Ni-Cf source can emit sufficiently low energy $\gamma$-rays, by which the trigger efficiency as a function of measured energy can be obtained.

In the Ni-Cf source calibration, an additional trigger, whose threshold is 150mV (corresponds to about 14 hits) and called a 'Ni trigger', is provided. The trigger efficiency is obtained by calculating a ratio of the number of events which issue both the Ni trigger and the L.E. trigger to the number of events which issue the Ni trigger for several energy regions.

# Chapter 6

# General data reduction

The data set used in this analysis covers the period from May 31, 1996 to July 15, 2001 and respectively 1496 days of detector live-time (roughly ∼90% for 1678 days detector live time with high efficiency).

Background sources to the solar neutrino data sample are :

- Electronics noise and flashing PMTs
- Cosmic ray muons.
- Electrons from the decay of stopping muons.
- Muon-induced spallation products.
- Radioactivity in the detector materials and surrounding rock. (For example, external $\gamma$ ray and electron from daughter nucleus of $^{222}$Rn.)

To reduce these backgrounds, various general cuts are applied and various additional cuts are applied for 4.5 MeV bin analysis. The general and additional cuts are applied to the data in four and two stages respectively. The general cuts, we namely, are the first reduction, spallation cut, the second reduction, and the $\gamma$ cut. The additional cuts are the tight cut and the new fitting cut.

The general cut criteria for the data set is described first in this chapter and named "General data reduction" for 1496 days data set. Next, the additional cut criteria applied for 4.5 MeV energy bin analysis is described in chapter 8 and named "Tight data reduction".

## 6.1 The data set

The basic unit of the data set is a run. Each run is at most 24 hours long. Each run is divided into sub-runs, which are about 2∼10 minutes long. The length of each sub-run depends on the trigger rate.

To make the basic data set, real-time bad run (sub-runs) selection and non-real-time bad run (sub-runs) selection are applied to the all runs in order. The real-time bad run selection is automatically applied in real-time process by using some cut criteria. After this selection, the total lost time is 27.3 days. They might be related to hardware trouble. The non-real-time bad run selection is applied on all normal runs (sub-runs) after the real-time bad run selection. The quality of the runs and sub-runs remaining after real-time bad run selection are checked manually and the bad runs for LE and SLE trigger events were rejected separately. After this selection, the total lost time is 112 days. The largest rejected time is due to log book checking. The details of bad run selection is given in appendix E.

## 6.2 First data reduction

### 6.2.1 Total photo-electron cut

First of all, high energy events, such as cosmic ray muon events (deposit energy $\sim$ 8 GeV), atmospheric neutrino events (deposit energy $\sim$ 1 GeV), are eliminated. Figure 6.1 shows total photo-electron number distribution in logarithmic scale. A clear peak on the left side in figure 6.1 corresponds to the high energy events. The cut criterion is the total number of photo-electrons in the ID $\leq$ 1000p.e. This photo-electron number (i.e. 1000p.e.) corresponds to about 130 MeV for an electron event, which is sufficiently high for the solar neutrino events, and therefore the inefficiency of the cut for the solar neutrino events is negligible.

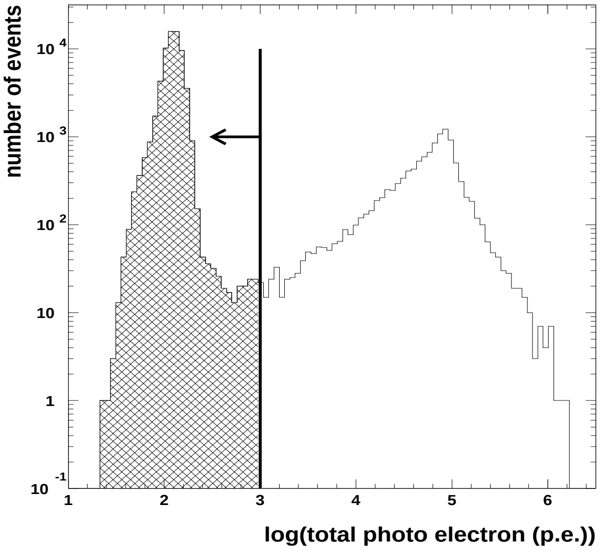

Figure 6.1: Distribution of total photo-electron number in logarithmic scale. The criterion of the total photo-electron cut is also shown.

### 6.2.2 Unfitted events cut

When the number of hit PMTs used for the vertex reconstruction is too small, it is difficult to get enough accuracy of the vertex position. Events with incomplete fitting results are removed. An incomplete fitting is defined as :

$$\text{Number of hit PMTs within 200 nsec time window} \leq 10 \tag{6.1}$$

$$\text{Number of hit PMTs within 200 nsec time window} = 0 \tag{6.2}$$

The event tagged by the above criteria is judged as incomplete fitting event and removed. This cut corresponds to an energy cut of 2 MeV threshold.

### 6.2.3 Fiducial volume cut

To reduce events caused by $\gamma$ rays coming from the surrounding rock and the materials comprising the ID wall, events that have vertex position within 2 m of the ID wall are eliminated. The fiducial general volume of SK for the solar neutrino analysis is defined by this cut to be 22.5 ktons, or 14.9 m in radius and 16.1 m $\times$ 2 in height. Figure 6.2 shows the vertex distribution from a typical data sample.

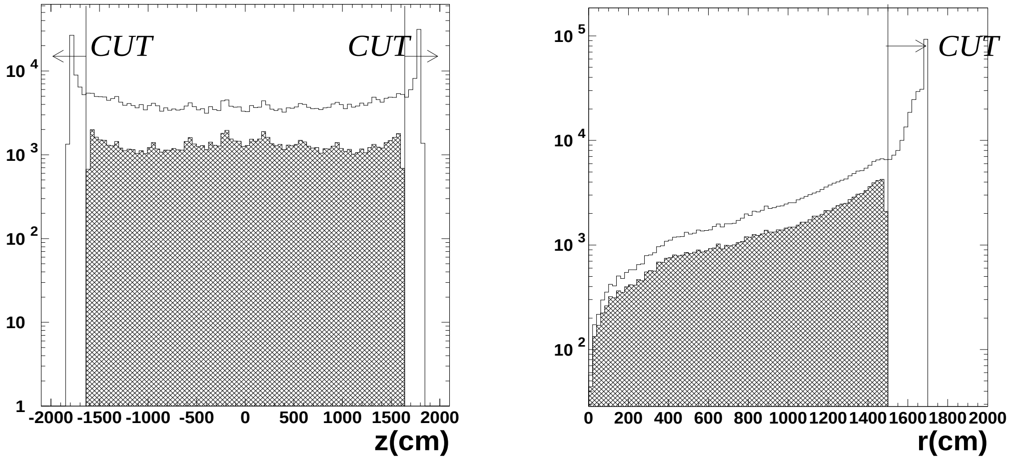

Figure 6.2: Fiducial volume cut applied to a typical data sample. The left figure shows the vertex distribution as a function z-position. The right figure shows the vertex distribution as a function of r-position. The hatched histogram shows the distributions after the fiducial volume cut.

### 6.2.4 Veto event cut

An event tagged with veto triggers which correspond to veto start and stop is removed. These online start and stop vetoes are marked as the duration of a possible online veto, which is issued if more than 64 events happen within 120 $\mu$sec.

### 6.2.5 Time difference cut

In order to eliminate $\mu$ decay electron events, after-pulse events, etc., a time difference cut is applied. Figure 6.3 shows the distribution of the time difference from a previous event. A peak around 1$\mu$sec are due to ringing events and the second peak around 15$\mu$sec is due to after-pulse events described in chapter 3. Interval events between two peaks are stopping $\mu$ decay electron events. When a high energy penetrating muon event happens, almost all PMTs of ID catch large photo-electrons. The large output signals from the PMTs are reflected on ATM side due to impedance mismatch between signal cable and the ATM input side. If the signal is sufficiently large, the reflected signals are further reflected back on the PMT side due to the same reason and the reflected signal comes back to the ATM again. The length of the cable between the PMT and the ATM is about 70m, hence the time that the signal needs to take to travel ATM-PMT-ATM is about 700nsec. However, each channel of ATM opens a 900nsec veto window after it was hit. Therefore, the first reflected signal is discarded. However the second reflected signal which comes after $\sim$1.4$\mu$sec is recorded by the ATM. These events are called ringing events.The cut criterion to reject these events is

- time difference from previous event $> 50\mu$sec

Dead time caused by the cut is $1.8\times10^{-4}$ sec, which is negligible for the solar neutrino observation.

### 6.2.6 Pedestal event cut

Events with a pedestal flag is removed. The pedestal of the ATM is measured by the 1/8 ATMs out of all ATMs every 30 minutes.

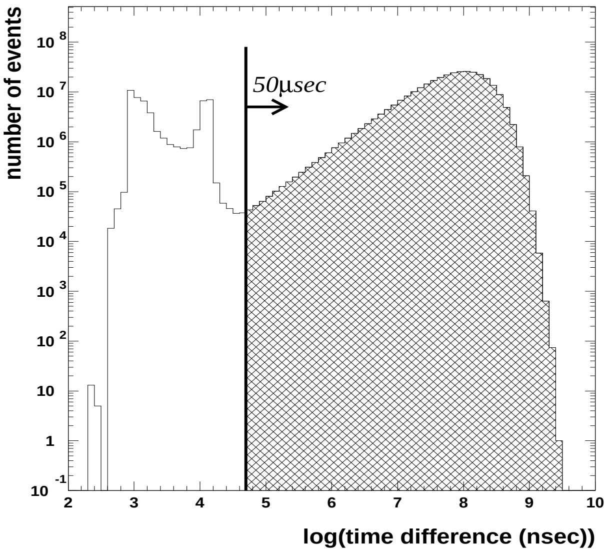

Figure 6.3: Distribution of time difference from previous event.

### 6.2.7 Incomplete event cut

Events with the incomplete flag are removed. An incomplete event could be one of the following :

- Incomplete ATM data
- Inner detector was OFF
- Outer detector was OFF

### 6.2.8 Outer detector event cut

In order to reject remaining cosmic ray muon events which hit OD PMTs, the following cut is imposed.

- OD trigger does not issue and number of hits in the OD $\leq 20$

Figure 6.4 shows the distribution of OD hits before and after the OD trigger cut on a typical data sample. The hatched area shows the distribution after the cut.

### 6.2.9 Mismatch event cut in outer detector

An event with larger than 20 OD hits is removed due to trigger mismatch. This maybe caused by OD DAQ trouble.

### 6.2.10 Noise event cut

In the electronics system used by the SK experiment, electronic noise sometimes happens. Sources of the noise are suspected to be PMT flashing, turning on-off of fluorescent lights, and so on. Figure 6.5 shows an example event display of the noise event. A characteristic point of this kind of event is that noise hit channels have small charge. Then, a following variable is defined,

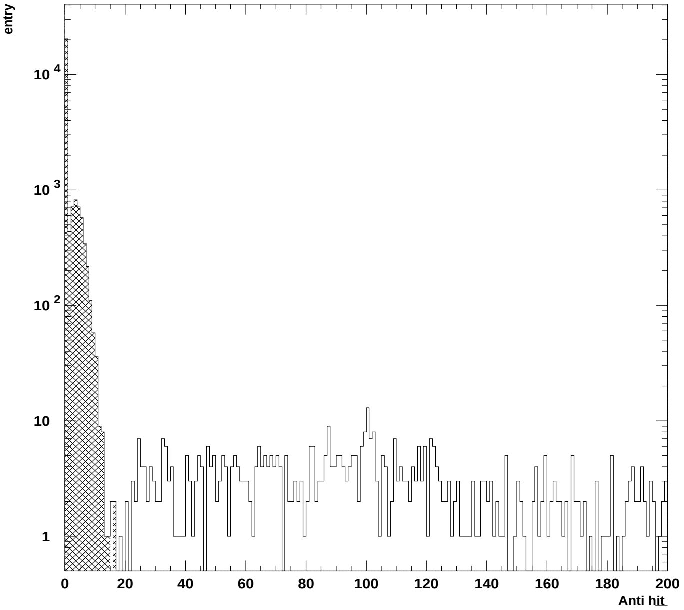

Figure 6.4: The distribution of OD hits after OD trigger cut at a typical data sample, which the number of OD hits become less 20.

$$N/S = \frac{\text{number of hit channels}(|Q_{PMT}| < 0.5\text{p.e.})}{\text{total number of hit channels}} \tag{6.3}$$

where $|Q_{PMT}|$ is the absolute charge value of the hit ATM channel. Figure 6.6(a) shows distribution of the $N/S$. A higher side peak is due to the noise events. The cut criterion of the $N/S$ cut is

- $N/S < 0.4$

### 6.2.11 Clustered ATM hits event cut

Further, these noise hit channels are often clustered in one ATM board. Then, following cut is also applied for the noise event cut,

- $ATMratio \equiv \max\left(\frac{\text{number of hit in one ATM board}}{\text{number of channel in one ATM board}}\right) < 0.95$

Distribution of the $ATMratio$ is shown in figure 6.6(b). The inefficiency of this cut for the solar neutrino events is estimated by the MC simulation as described later.

### 6.2.12 First flasher event cut

The 'flasher events' are caused by light emission from a PMT resulting from electrical discharge between dynodes. Figure 6.7 shows an event display of the typical flasher event. Most of the flashers can be found by an instantaneous increase of trigger rate (strong flasher). In this case shift crew identify the flashing PMT and high voltage of the PMT is switched off. However, in case of flashers of lower rate and lower light emission, the flasher events remain in the reduced data. They are rejected by the following criterion. When a PMT is flashing, it often detects a large pulse height and the PMTs surrounding it have signals. Figure 6.8(a) shows a scatter plot of maximum charge of one PMT ($Q_{max}$) versus number of hit PMTs surrounding that PMT which gives $Q_{max}$ ($0\leq mx \leq 24$), for a typical run including flasher events, and figure 6.8(b) shows same as (a) but for a typical normal run. The cut criterion is:

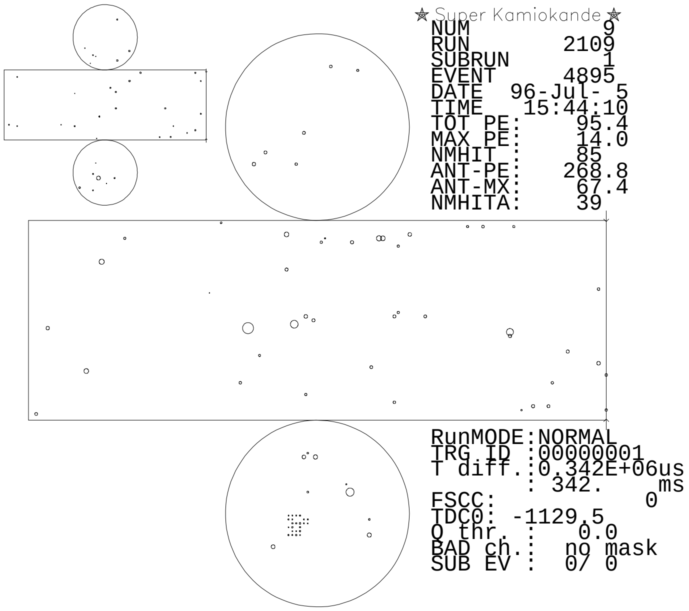

```
☆Super Kamiokande☆
NUM           9
RUN        2109
SUBRUN        1
EVENT      4895
DATE  96-Jul- 5
TIME   15:44:10
TOT PE:    95.4
MAX PE:    14.0
NMHIT :     85
ANT-PE:   268.8
ANT-MX:    67.4
NMHITA:     39

RunMODE:NORMAL
TRG ID :00000001
T diff.:0.342E+06us
       : 342.    ms
FSCC:          0
TDC0: -1129.5
Q thr. :    0.0
BAD ch.:  no mask
SUB EV :  0/ 0
```

Figure 6.5: An event display of the typical noise event.

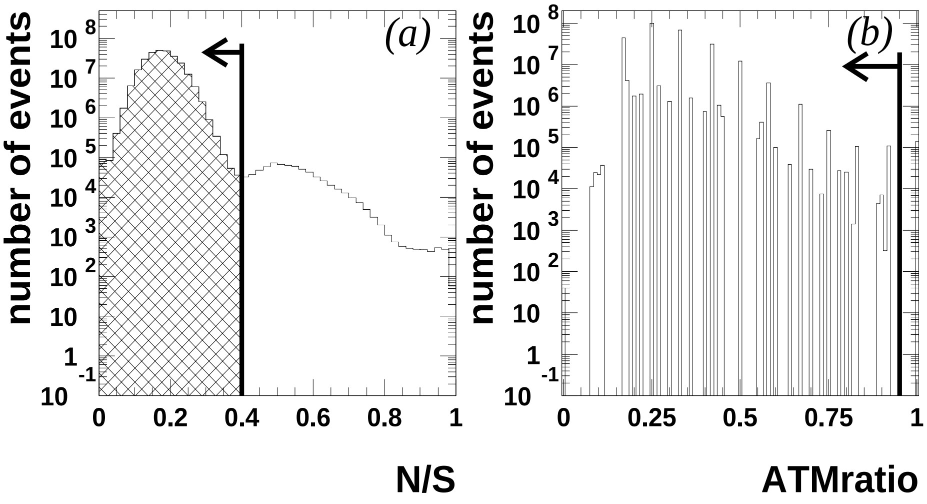

Figure 6.6: (a) shows $N/S$ distribution and (b) shows $ATMratio$ distribution.

$$\text{Number of hits around maximum charge PMT (mx24)} \geq 2 \tag{6.4}$$

$$\text{Maximum charge (Qmax)} \geq -4 \times mx24 + 75 \tag{6.5}$$

$$\text{mx24} \geq 10 \tag{6.6}$$

An event that satisfied either of the above conditions is removed. Most of Monte Carlo events that are rejected in the first reduction step are caused by this cut. In real data, most of events have so low energy that they have small charge. Flasher candidates, on the other hands, have relatively large charge compared with other background. Therefore, the reduction factor of this flasher cut in case of Monte Carlo becomes higher than that of real data. This makes a main source of systematic error in the first reduction step. The events which are in the indicated region shown in figure 6.8 are rejected.

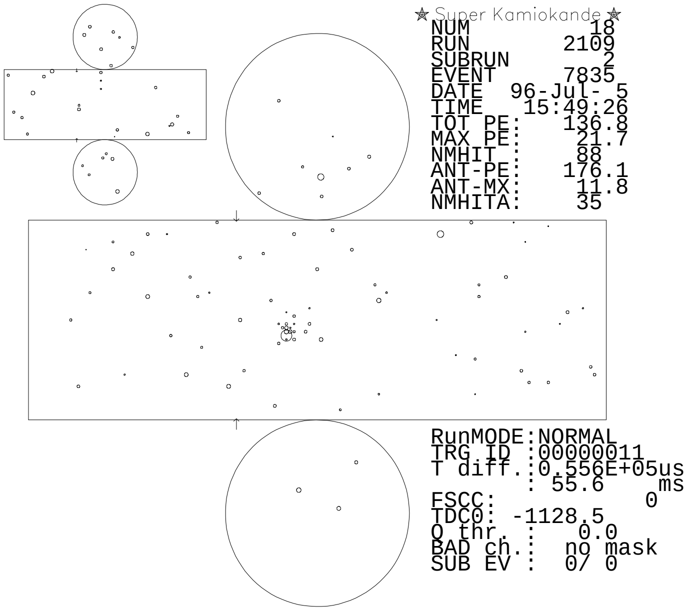

```
NUM          18
RUN        2109
SUBRUN        2
EVENT      7835
DATE  96-Jul- 5
TIME   15:49:26
TOT PE:   136.8
MAX PE:    21.7
NMHIT :    88
ANT-PE:   176.1
ANT-MX:    11.8
NMHITA:    35
```

```
RunMODE:NORMAL
TRG ID :00000011
T diff.:0.556E+05us
       : 55.6    ms
FSCC:          0
TDC0: -1128.5
Q thr. :   0.0
BAD ch.:  no mask
SUB EV :  0/ 0
```

Figure 6.7: An event display of the typical flasher event.

### 6.2.13 Goodness cut

In addition to the above "very low energy cut", a goodness cut is also applied. If a goodness $g_v$ value of an event is low, the reconstructed vertex position of the event is suspected to be wrong. Therefore, a following cut criterion is imposed:

- goodness $\geq 0.4$ (see figure 6.9)

### 6.2.14 Second flasher event cut

In addition to the vertex test, there is another re-evaluation using the reconstructed direction. If the reconstructed vertex position is near the true position, the hit PMTs distribute uniformly about the reconstructed direction. However, if the reconstructed vertex is far away from the true vertex, the PMT hit distribution is non-uniform. In order to test uniformity of the hits, a Kolmogorov-Smirnov (KS) test is applied. Figure 6.10 shows an example of the test. The left figures in figure 6.10 are for a well-reconstructed event. The lower figure shows correlation between $i$-th PMT among the $N_{50}$, which is the number of hit PMTs in 50nsec window, and an

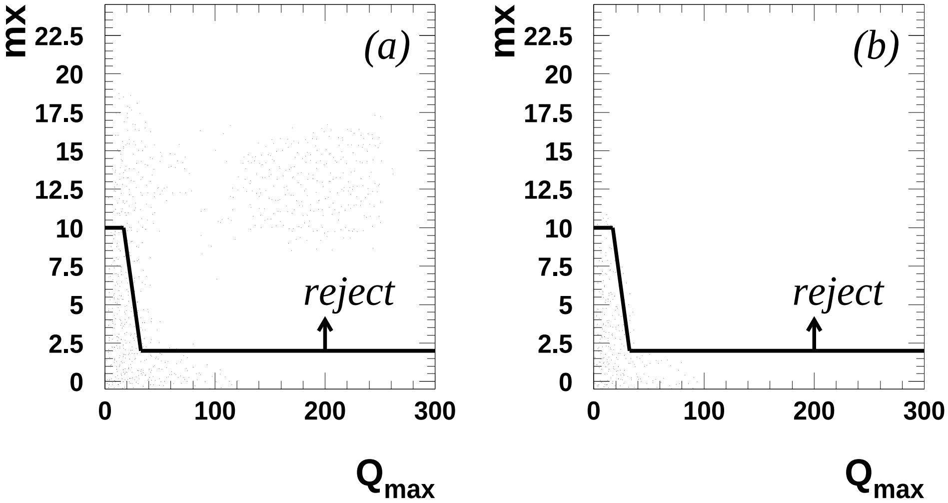

Figure 6.8: Scatter plots of $Q_{max}$ vs $mx$. The events which are in the indicated region are rejected as the flasher events.

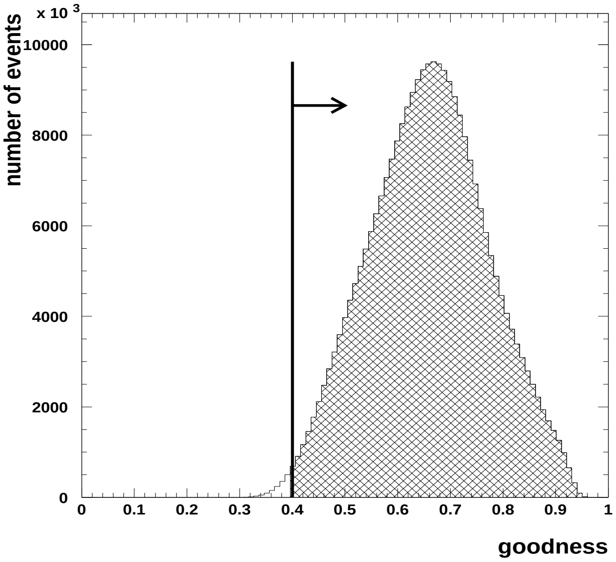

Figure 6.9: The goodness distribution. The cut criterion is also drawn.

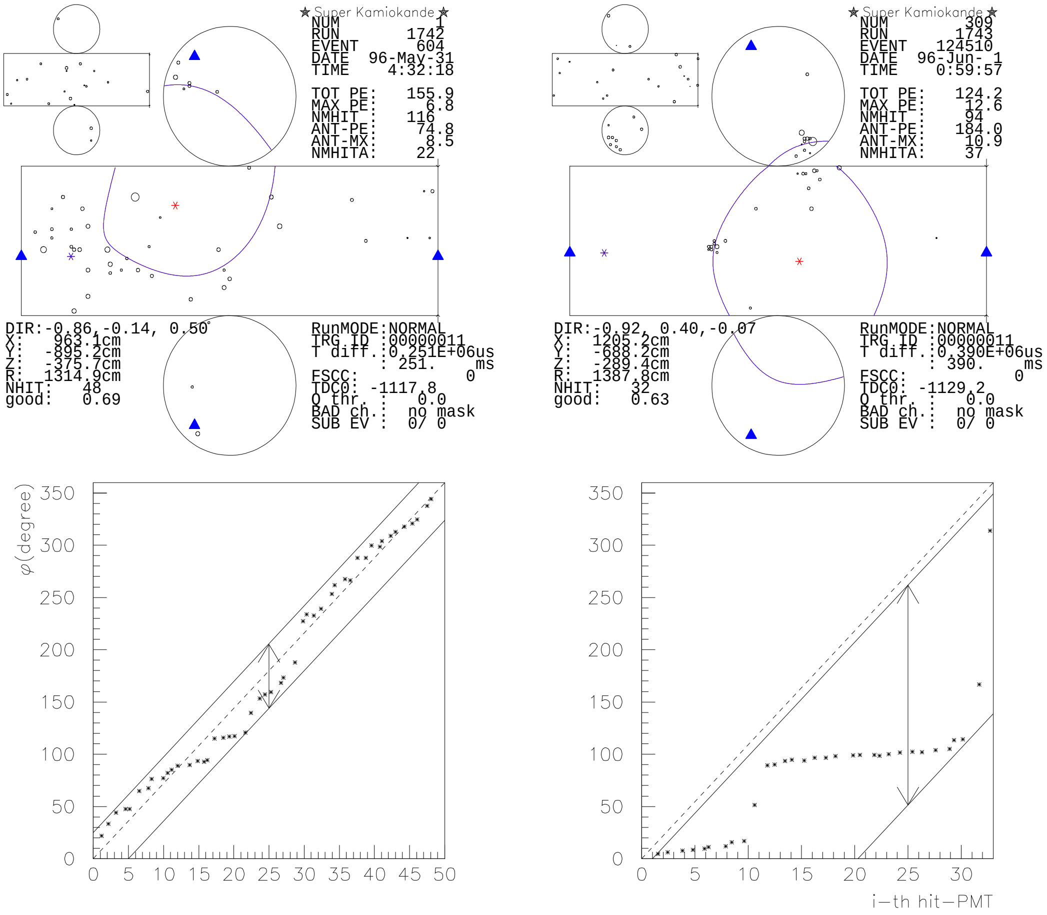

Figure 6.10: An example of the directional test. Left figures are for a well-reconstructed event and right figures are for a bad reconstructed event.

azimuth angle of the PMT with respect to the reconstructed direction. In ideal case, all PMTs should be on the broken line. Now, let us define a variable *Dirks* which is full width of azimuth angle deviation from the ideal case, divided by 360. In the bad case as with the right figures, the *Dirks* becomes large. Figure 6.11 shows correlation between *Dirks* (horizontal the axis) and $\Delta r$ (distance from a generated position in MC simulation to the reconstructed position) for solar neutrino MC events. Obviously, the events with larger *Dirks* have large $\Delta r$. Figure 6.12 shows *Dirks* distributions for the real data and the solar neutrino MC simulation in energy ranges of 6.5~7.0 MeV and 7~20 MeV, respectively. The events with $Dirks > 0.4$ are rejected. As shown in the figure, the fraction of the rejected events is larger for lower energy.

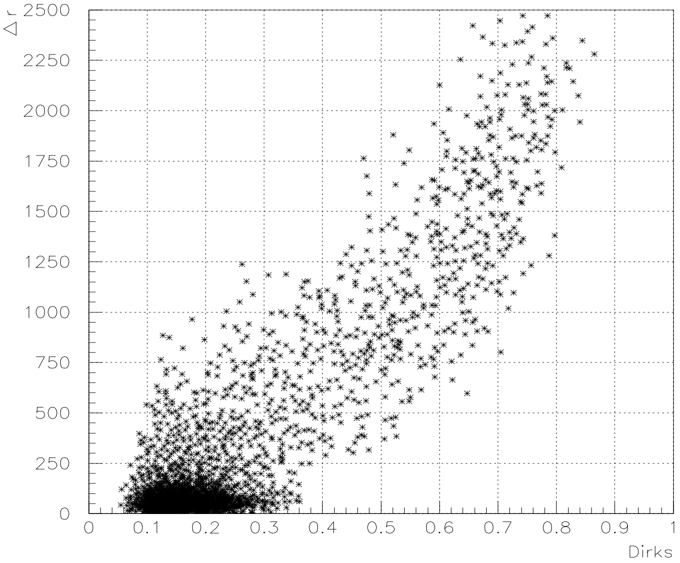

Figure 6.11: The validity check of *Dirks*. The horizontal axis is *Dirks* and the vertical axis is $\Delta r$. Points are the solar neutrino MC simulation events above measured energy of 6.5 MeV.

It is found that certain flasher events, which still remain after the above flasher cut, can be rejected using information from the goodness and the *Dirks*. These flasher events make a tiny peak in the $d_z$ distribution around $d_z \simeq -0.7$ as shown in figure 6.13(a) (blank histogram). The following cut can reject the peak:

- goodness $\geq 0.6$ and $Dirks < 0.25$

The hatched histograms in figure 6.13 are the $d_z$ distribution after applying the cut.

### 6.2.15 Bad energy cut

Event with the difference between number of hits within 50 nsec time window and effective hits for 70m case more 200 is removed due to bad energy reconstruction. However, it was never seen in the present scheme as following reduction tables.

## 6.3 Spallation cut

Some cosmic ray muons which go through the detector produce radioactive elements by breaking up an oxygen nucleus.

$$\mu + {}^{16}O \rightarrow \mu + X + ...... \tag{6.7}$$

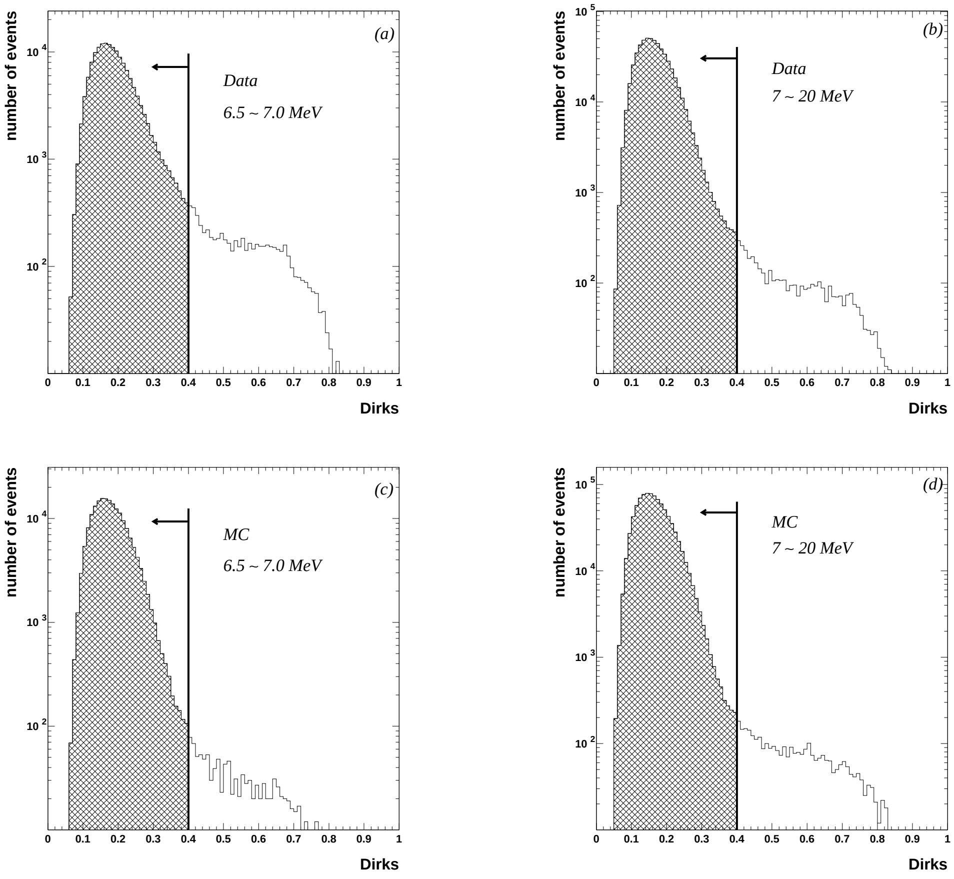

Figure 6.12: Distributions of *Dirks*. (a)real data(6.5∼7.0 MeV), (b)real data(7∼20 MeV), (c)MC data(6.5∼7.0 MeV), (d)MC data(7∼20 MeV).

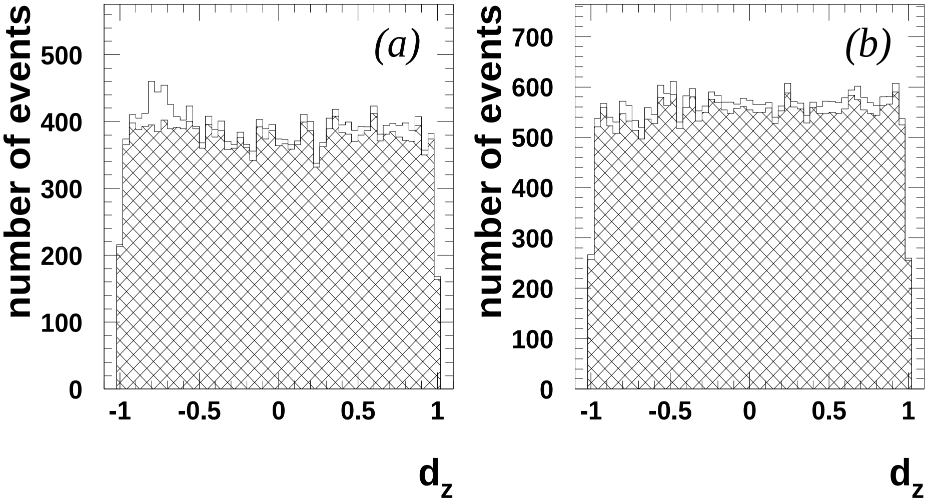

Figure 6.13: The $d_z$ distribution for runs (a) including and (b) not including the specified flasher events (blank histograms). There is a tiny peak around $d_z \simeq -0.7$ in figure (a). The hatched histograms are the resultant ones after the second flasher cut.

where X represents radioactive nuclei. The nuclei decay by $\gamma$ and $\beta$ emission with a lifetime in the range of 0.001 $\sim$ 14 sec. They are observed in SK and are called "Spallation events". The energies of the spallation events are similar to those of recoil electrons from solar neutrinos, so they are one of the major backgrounds in the solar neutrino analysis.

To identify spallation events, a likelihood method is used. The parameters for the likelihood function are:

- $\delta L$ : Distance from the low energy event to the reconstructed track of the preceding muon event.
- $\delta T$ : Time difference between the low energy event and the reconstructed track of the preceding muon event.
- $Q_{res}$ : Residual charge of the preceding muon event.

$$Q_{res} = Q_{total} - Q_{unit} \times I_{i,\mu} \tag{6.8}$$

where $Q_{total}$ is the total charge. $Q_{unit}$ is the total charge per cm and $I_{i,\mu}$ is reconstructed track length of the muon event.

If the muon track reconstruction fails, then only $\delta T$ and $Q_{total}$ are used. For spallation events, $\delta L$ and $\delta T$ are shorter, and $Q_{res}$ is larger, compared to solar neutrino events.

For the spallation cut, one calculates the likelihood values for muons in the previous 100 seconds and select a muon which gives the maximum likelihood value ($L_{max}$) Events with $L > 0.98$(for reconstructed muon events) and $L > 0.92$(for non-reconstructed muon events) are rejected as the spallation events.

Figure 6.14 shows the $L_{max}$ distribution in data and in randomly sampled events.

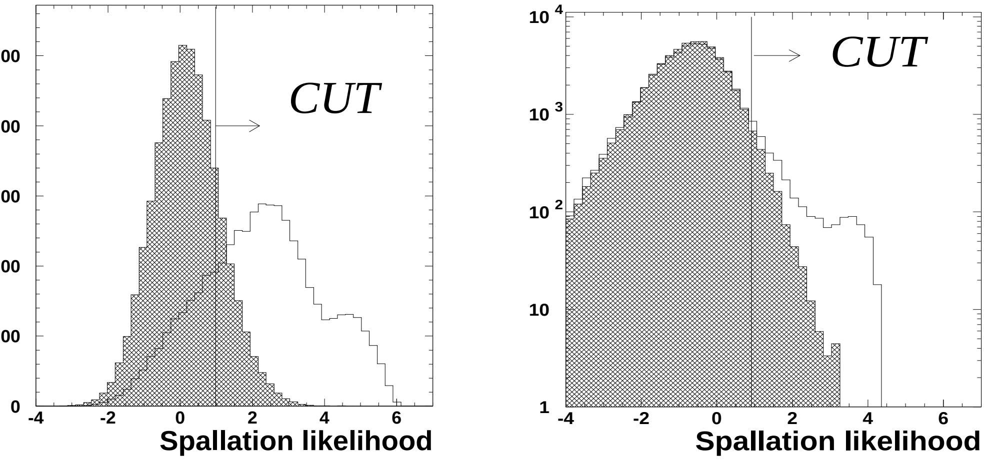

Figure 6.14: The distribution of spallation likelihood. The left figure shows the likelihood distribution for muon events with a reconstructed track. The right figure is for the case where muon reconstruction failed. The open histogram shows a typical data sample and the hatched histogram shows the randomly sampled events.

The dead time of the spallation cut is investigated using a random sample of events. The dead time is position dependent. It is estimated 21.1%, which was obtained from randomly sampled events. Figure 6.15 shows the position dependence of dead time as a function of distance from top (left figure) and barrel (right figure). Blank marks are obtained dead time at each position and lines are results of fitted polynomial functions. The position dependence is taken into account in the solar neutrino MC simulation.

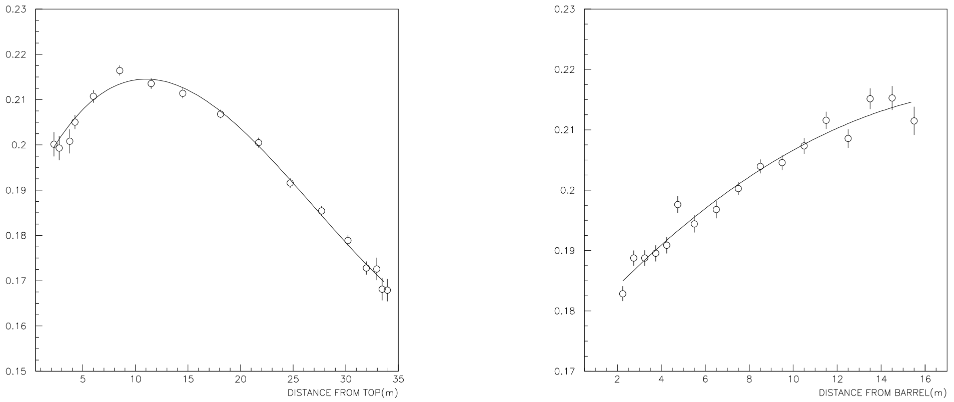

Figure 6.15: Position dependence of the dead time induced by the spallation cut. Left figure shows $z$ dependence and right figure shows $r$ dependence of the dead time (vertical axis of each figure).

## 6.4 Second data reduction

In the second reduction, further cuts were applied in order to analyze the low energy region. First of all, the vertex reconstruction is re-evaluated by goodness stability cut in order to collect clear events which occurs in the fiducial volume. Next step, the $\check{C}$erenkov ring image is tested by pattern likelihood cut comparing with the true ring image in order to reduce the remaining spallation event and $\gamma$ like event. True ring image is issued by single electron from solar neutrino MC Lastly, the vertex position is re-estimated by an other vertex reconstruction fitter which is called "Clusfit". Then, the event issued out of the fiducial volume is rejected.

### 6.4.1 Goodness stability cut

The goodness stability cut is named GRINGO (Grid Integrated New Goodness) cut from now on. The principle of the evaluations are summarized as follows :

- Evaluate vertex fit quality : compare vertex *goodness* of fit point to surroundings.
- Define hexagonal grid orthogonal to event direction.
- Require minimum fall-off of *goodness* with distance.
- From ratio of number of failed point over number of grid point.

Usually, if there are many noise hits in an event, the event is cut because of bad *goodness* from vertex reconstruction. However, some events have good *goodness* by chance by dropping local minimum chi square in the estimation. To estimate the validity of the *goodness*, the difference between the *goodness* at the original reconstructed vertex and those at test vertices around the original one are examined. For an event with many noise hits, the timing distribution of PMT hits is broader. As a result, the change in the *goodness* is small. Figure 6.16 shows the definition of the GRINGO cut. The left figure shows the definition of the grid point used in GRINGO cut. The original reconstructed vertex is situated at the center. The right figure shows the threshold of *goodness* difference as a function of the distance from the original vertex.

The stability of the *goodness* of vertex reconstruction is checked as follows.

1. Make a two dimensional grid on the plane which contains the reconstructed vertex point and normal to the reconstructed direction.

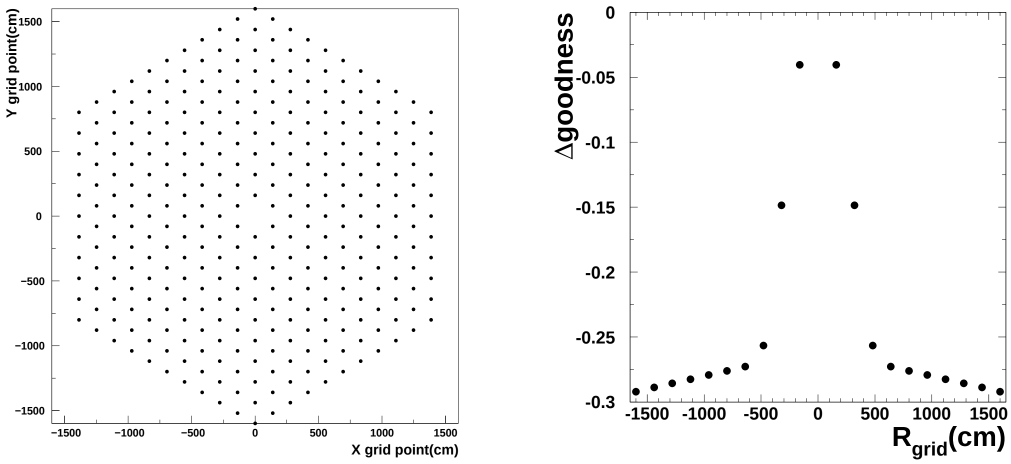

Figure 6.16: The original reconstructed vertex is situated at the center. The right figure shows the threshold of *goodness* difference as a function of the distance from the original vertex.

2. The vertex is assumed to be at each grid point and the *goodness* defined by chapter 4 is calculated at each grid point.
3. Calculate the difference between the goodness at the original vertex and at each grid point.
4. Count the number of grid points at which the deviation exceeds the threshold ($N_{bad}$).
5. Calculate the ratio of $N_{bad}$ to the total number of grid points ($R_{bad}$). If ($R_{bad}$) is larger than 0.08 then the event is cut.

The cut criterion of the GRINGO cut is determined so that the significance, (number of remaining events of solar MC)/$\sqrt{\text{(number of remaining events of DATA)}}$, becomes maximal.

Figure 6.17 shows $R_{bad}$ distribution. The hatched area shows the $R_{bad}$ distribution after GRINGO cut. Figure 6.18 shows vertex distribution before and after GRINGO cut. The hatched area shows the distribution after GRINGO cut. Figure 6.19 shows the energy distribution before and after GRINGO cut. From this figure, the GRINGO cut is a very powerful tool for SLE background rejection. This tool gives hope for 4.5 MeV project.

### 6.4.2 Pattern likelihood cut

When there are additional $\gamma$ rays in an event, for example, a spallation-like event, then the Čerenkov ring image is smeared and the direction reconstruction is not valid. To estimate the validity of the reconstructed Čerenkov ring, a likelihood function is made from a MC distribution of the angle between the reconstructed direction and the angle from reconstructed vertex to each hit PMT. Figure 6.20 shows the definition of the hit pattern of the Čerenkov ring image. $\theta_{PMT}$ is defined as an angle between the event direction and the hit PMT as seen in the figure.

The likelihood function is defined as following equation.

$$L \equiv \frac{\sum_{i=1}^{N} \log(P_i(\cos\theta_{PMT,i}, E, dis_{fromwall}))}{N} \tag{6.9}$$

where N is the number of hit PMTs within 50 nsec time window, $P_i$ is the probability of the hit pattern made from a MC distribution of the angle between the reconstructed direction and the angle from the reconstructed vertex to each hit PMT, $\cos\theta_{PMT,i}$ is the angle between the reconstructed direction and the angle from reconstructed vertex to each hit PMT, E is the energy of the event, and $dis_{fromwall}$ is the distance between the wall and the reconstructed vertex point.

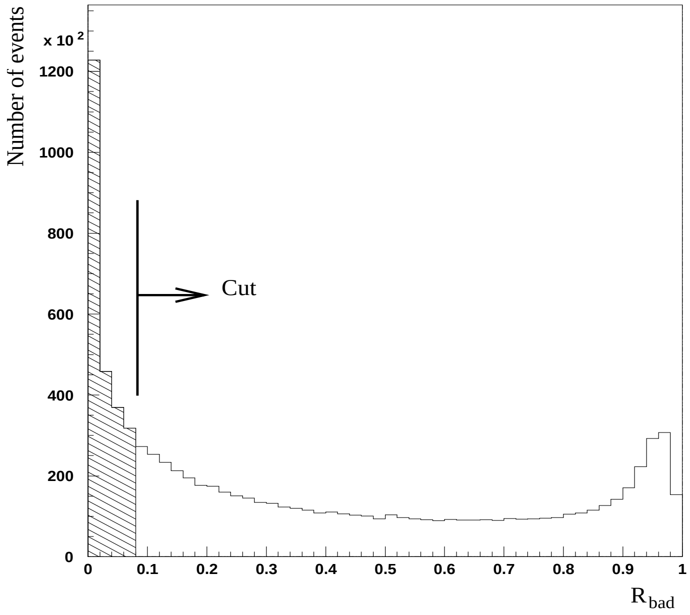

Figure 6.17: The calculated $R_{bad}$ distribution. The hatched area shows after GRINGO cut at the typical data sample.

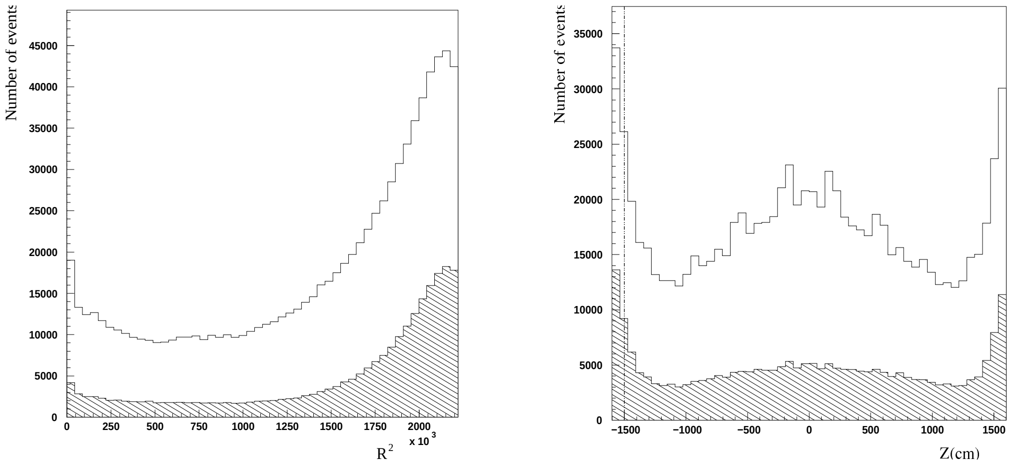

Figure 6.18: The vertex distribution before and after the GRINGO cut. The left and right figures show the radius distribution and the tank height distribution respectively. The hatched area shows the distribution after GRINGO cut at the typical data sample.

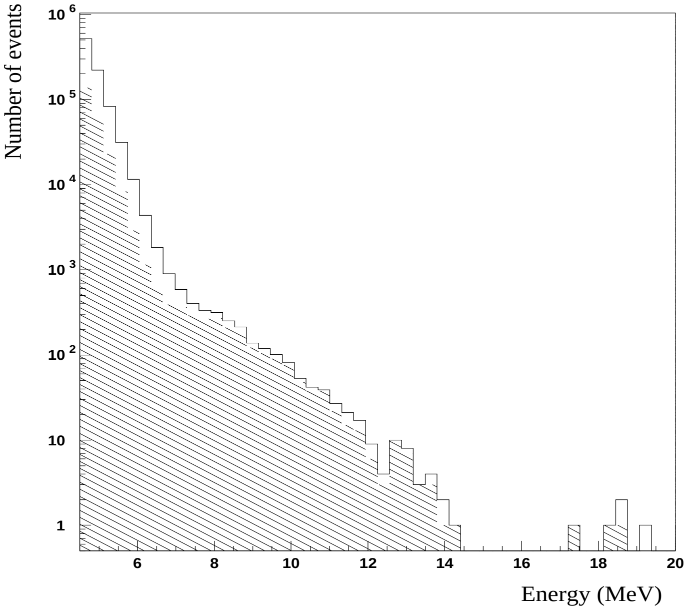

Figure 6.19: The energy distribution before and after GRINGO cut. The hatched area shows after GRINGO cut at the typical data sample.

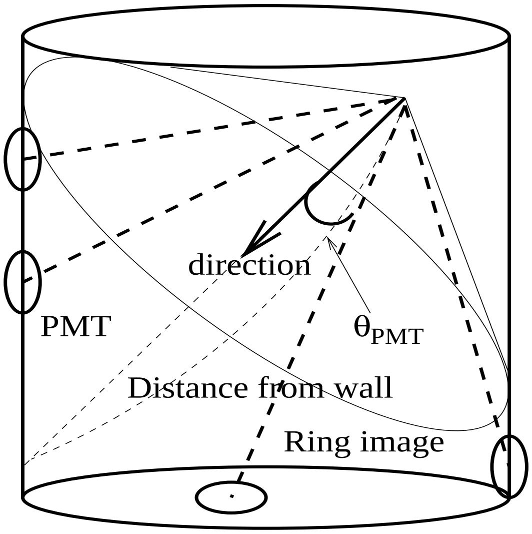

Figure 6.20: The definition of the $\theta_{PMT}$.

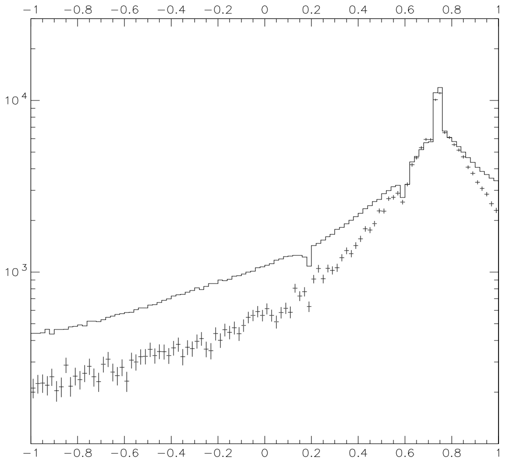

Figure 6.21: The distribution of the pattern likelihood function for the ring image at the typical energy from 8.0∼10.0 MeV.

Figure 6.21 shows the distribution of the pattern likelihood function for the ring image at the typical energy from 8.0∼10.0 MeV. The solid line is the extracted events as background events from less than 0.8 of the $\cos\theta_{sun}$ distribution (See figure 9.1, 9.2). The plots are the extracted events as solar neutrino events distributing in the $\cos\theta_{sun}$ distribution more than 0.8. $\cos\theta_{sun}$ means the the reconstructed direction correlated with the solar direction. The remaining background event is mainly the long lived spallation event with multi $\gamma$ rays. Thus, the ring image is smeared compared with the distribution of the solar neutrino like events.

The likelihood distribution for the solar neutrino like event and the background like event extracted from the typical data sample is shown figure 6.22. The top figures show the distribution using the solar neutrino like events from more than 0.8 of $\cos\theta_{sun}$ distribution. The bottom figures show the distribution using background events in less than 0.8 of the $\cos\theta_{sun}$ distribution. From the left side figure, the energy of the events are 6.5∼8.0, 8.0∼10.0, 10.0∼20.0 MeV respectively. Searching the maximum significance between the top figure and bottom figure with the change of the cut point for the likelihood function distribution, the cut point of -1.85 is decided. In the figure, the cut point is also shown. This cut is named PATLIK cut (PATtern LIKelihood cut) from now on. The cut criterion of the PATLIK cut is determined so that significance, $\frac{\text{number of remaining events of solar neutrino like data}}{\sqrt{\text{number of remaining events of background like data}}}$, becomes maximal.

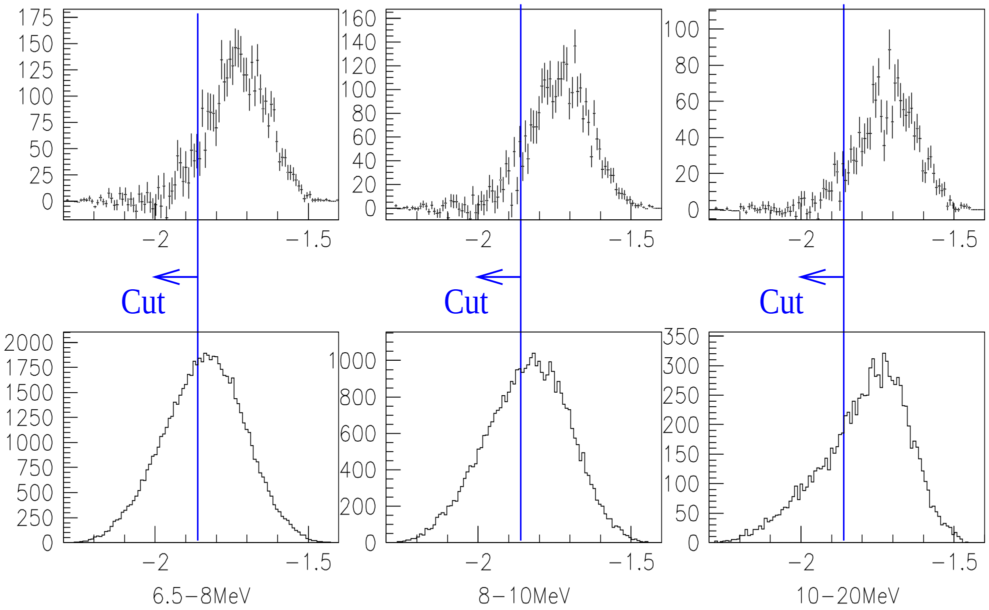

Figure 6.22: The likelihood distribution for the solar neutrino like event and the background like event extracted from the typical data sample.

In the SK, this reduction is named "PATLIK cut (PATtern LIKelihood function cut)". The likelihood distributions before and after PATLIK cut from the typical data sample is figure 6.23. The hatched area shows the distribution after the PATLIK cut.

### 6.4.3 Rejection of noise hit

In order to eliminate the noise contribution to the hit PMTs, the distance and time difference from other hit PMTs in the event are used. The conditions for noise hit PMTs are given as follows.

- The minimum distance to any other hit PMT is larger than 1250 cm.
- The minimum time difference to any other hit PMT is larger than 35 nsec.

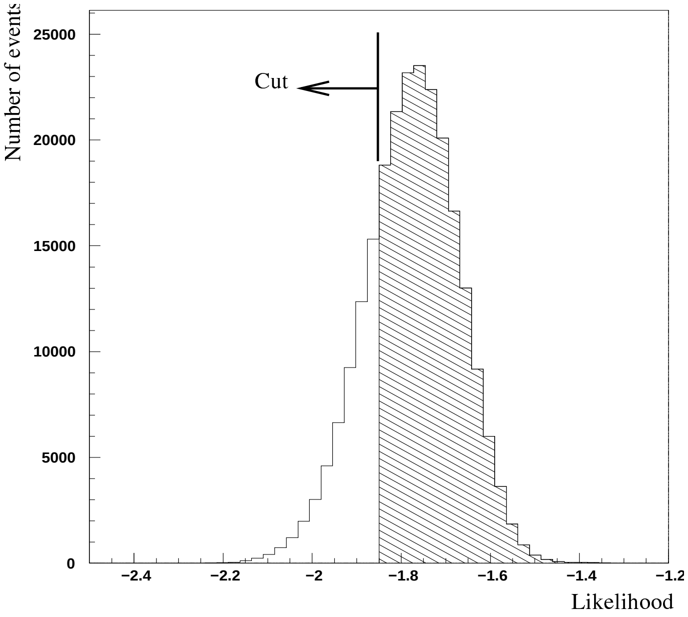

Figure 6.23: The likelihood distributions from the typical data sample.

For further removal of noise hit PMTs, the selected hit PMTs are paired which each other again. If the PMT signals are caused by Čerenkov light emitted from a point, then the time difference ($\delta t$) and the distance ($\delta r$) between a pair of hit PMTs satisfy the following relation :

$$\delta r/c > \delta t \tag{6.10}$$

A hit PMT pair which satisfies the above relation is called a "Related pair or Cluster". If the number of related pairs of a hit PMT is larger than 10, then the hit PMT is selected and used by the vertex fitter. If the distance from the new vertex to the nearest wall is smaller than 200 cm, the event is rejected. This reduction is named "Clusfit cut(Cluster fit cut)" from now on. Figure 6.25 shows the distributions of the vertex reconstructed before and after rejected noise hits.

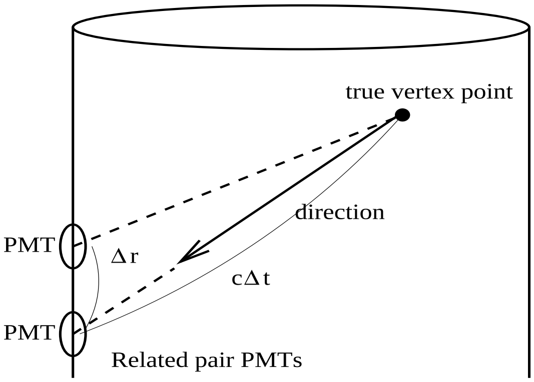

Figure 6.24: The definition of rejecting noise hits.

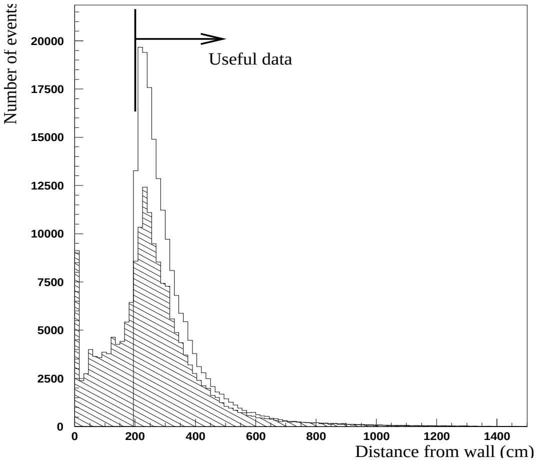

Figure 6.25: The distance distribution from the wall before and after the Clusfit cut.

## 6.5 Gamma cut

One of the major backgrounds in the solar neutrino analysis is $\gamma$ ray from the PMT glass and the surrounding rock. It is called “External $\gamma$ ray” To remove this background, the reconstructed direction of each event is projected backward and the distance from the reconstructed vertex to the detector wall $d_{eff}$. The “External $\gamma$ ray” from the surrounding rock and ID wall materials is named gamma ray from now on. Then, the reduction for $\gamma$ ray is named gamma cut from now on.

A characteristic of the $\gamma$ ray events is that they have small ’effective distance’ to the wall, $d_{eff}$, which is defined in figure 6.26.

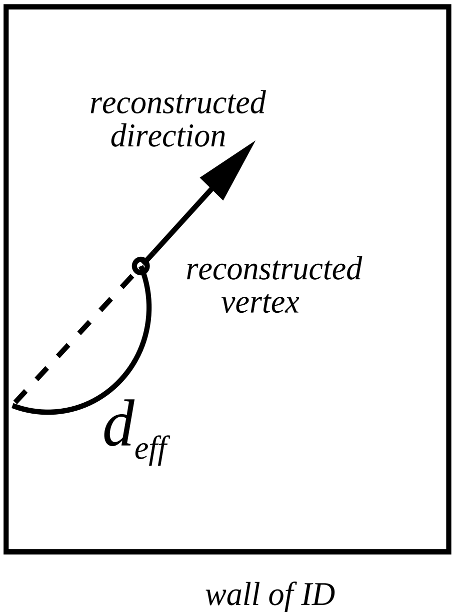

Figure 6.26: The definition of the effective distance $d_{eff}$.

The cut criterion of the $\gamma$ cut is determined so that significance, (number of remaining events of MC)/$\sqrt{\text{(number of remaining events of DATA)}}$, becomes maximal. Therefore the threshold distance is dependent on energy. It is 8 m when the energy is less than 6.5 MeV and the 4.5 m when the energy is greater than 6.5 MeV.

Figure 6.27 shows the typical vertex before and after the $\gamma$ cut for real data for the energy range of 4.5∼20.0 MeV. As shown in the figure, the application of the $\gamma$-cut makes the vertex distribution uniform.

## 6.6 Summary

Figure 6.29 and figure 6.28 show the final Z(cm) and $R^2$($cm^2$)vertex distribution by general reduction for each energy region respectively. The energy region is presented in figures. From top figure, the energy ranges are from 4.5 to 5.0 MeV, from 5.0 to 6.5 MeV, and 6.5 to 20.0 MeV respectively. Figure 6.30 and figure 6.30 shows the direction distribution after all general reduction for each energy region.

Table 6.1 shows the number of remaining events at each reduction step for the real data. Figure 6.32 shows energy spectrum of the real data after each reduction step. From the figure, the possible sources of the background are remaining spallation events, the radioactive elements originated from Rn, and remaining $\gamma$-ray events.

The origin of the spallation event remnant is attributed to an inefficiency of the muon track reconstruction. Especially, multiple muons could be mis-reconstructed.

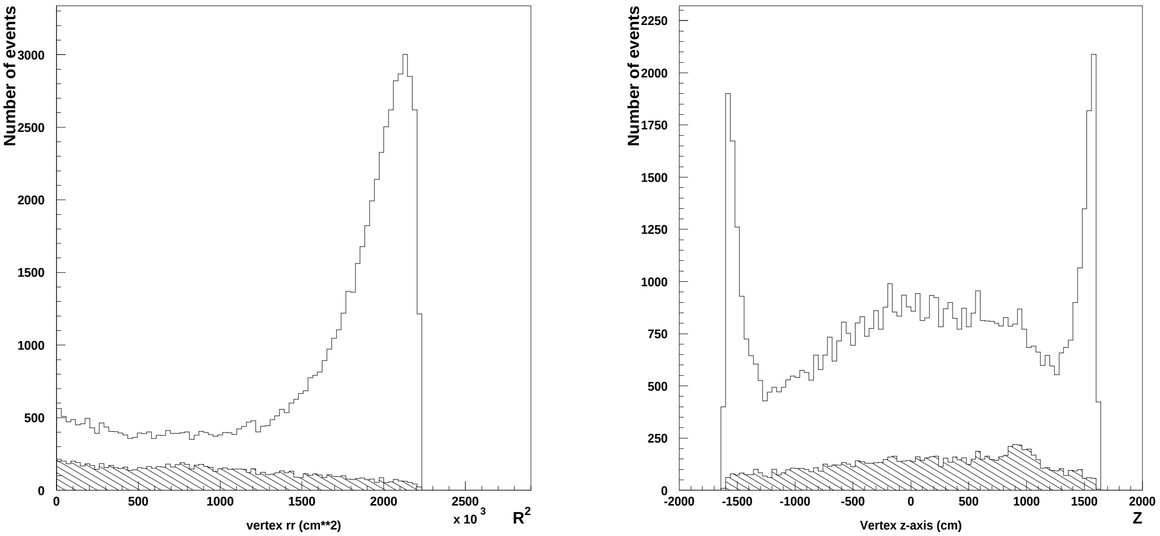

Figure 6.27: The typical vertex distribution before and after the gamma cut in energy region from 4.5 to 5.0 MeV. The hatched region is after gamma cut.

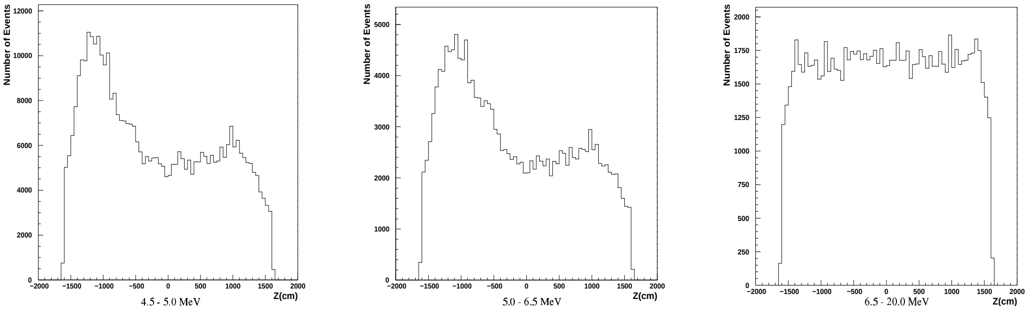

Figure 6.28: The final Z vertex distribution by general reductions for each energy region. The energy regions are presented in figures.

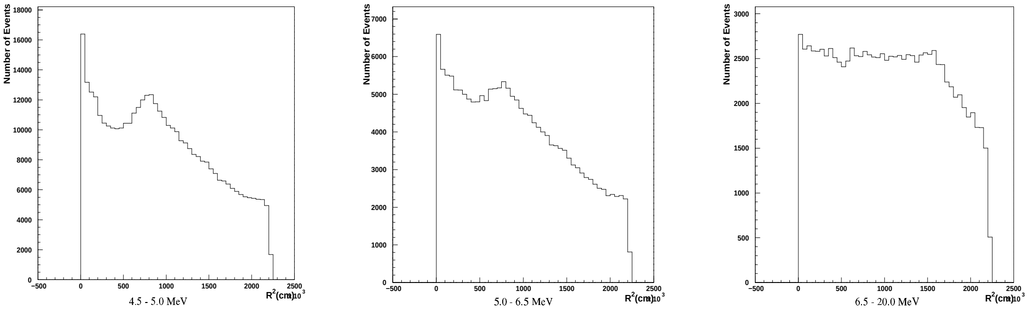

Figure 6.29: The final $R^2$ vertex distribution by general reductions for each energy region. The energy regions are presented in figures.

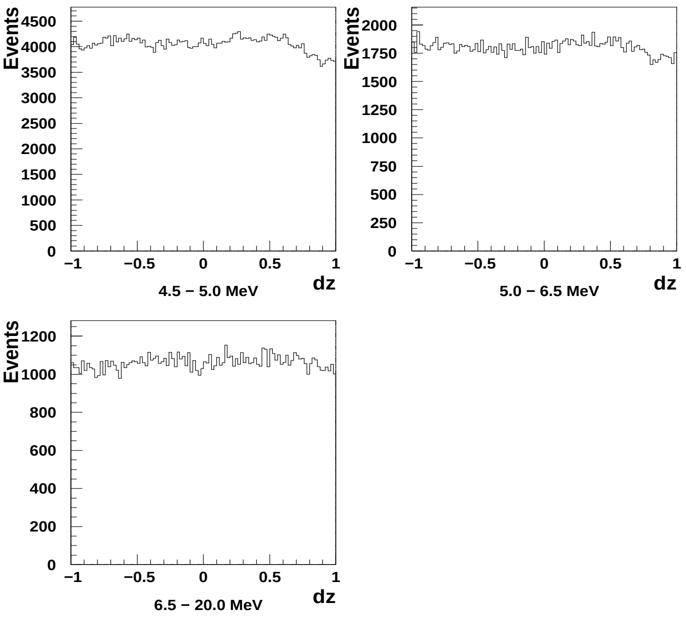

Figure 6.30: The final zenith direction distribution by general reductions for each energy region. The energy regions are presented in figures.

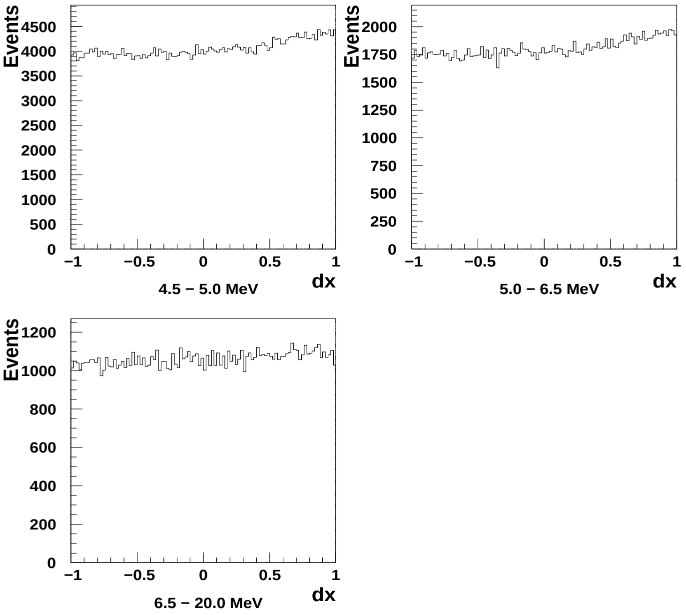

Figure 6.31: The final azimuth direction distribution by general reductions for each energy region. The energy regions are presented in figures.

These events remain as mis-fit events. These mis-fit events are accumulated in center of the tank because of characteristic of fitting tool, one can see that in figure 6.29. Mis-fitting events increases in lower energy region because the number of hit PMTs becomes small in lower energy region.

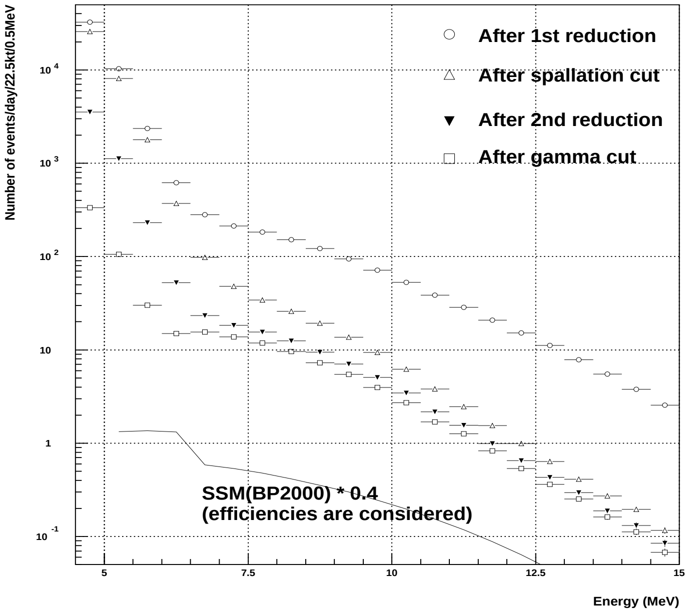

Figure 6.32: Energy spectrum after each reduction steps. See also table 6.1 for the definition of 'first', 'second', and 'third' reduction. Theoretical prediction (BP2000×0.4) is also shown (solid line).

There are two cases of radon background from the different parent nuclei. First case is $^{214}$Bi from the radon in radium series. Although the spectrum endpoint of the $^{214}$Bi, which is decay product of the $^{222}$Rn, is 3.26 MeV, due to the finite energy resolution of the detector, the $\beta$-decay events are observed from 4.5 to 6.5 MeV energy threshold. One can see the abnormal peak in the bottom region of SK tank in figure 6.28 from 4.5 to 6.5 MeV. Another possible case is due to $^{208}$Tl from the radon in thorium series. The $^{208}$Tl also decays via $\beta$-decay with 2.614 MeV gamma rays at total energy of 5.0 MeV. Therefore, in decaying, the event generates the $\check{C}$erenkov light of multi-ring with gamma ray. Figure 6.33 shows the expected energy spectrum of daughter nucleus from radon of Radium and Thorium series for each trigger threshold. The MC passed only the first data reduction.

Another possible background is $\gamma$ rays coming from the surrounding rock or material on ID wall. In the figures 6.29, 6.30, and 6.31, there is abnormal excess around $R^2$ of 750 $cm^2$ and around the direction of $\pm 0.5$ or $+1$, respectively. These are remaining external $\gamma$ rays from the wall in the low energy region.

In order to observe low energy solar neutrino flux from 4.5 to 5.0 MeV, these possible remaining backgrounds need to be reduced. The still remaining backgrounds in low energy region are radon and external $\gamma$ rays from wall materials and surrounding rocks. Figure 6.34 shows the hit pattern distribution of $\cos\theta_{PMT}$, which is described earlier in this chapter, for each MC of electron, $\gamma$, $^{214}$Bi and $^{208}$Tl from radon in energy region from 4.5 to 5.0 MeV. For the electron hit pattern, there is no remarkable difference. Therefore, it is difficult to identify the background events by analysis tool. It is necessary to reduce the radon as dominant source of the background physically.

| Reduction step | Data<br>4.5-20.0 MeV | Data<br>5.0-20.0 MeV | Data<br>6.5-20.0 MeV |
|---|---|---|---|
| Total | 564222879 | 176906705 | 23649508 |
| Unfitted event cut |  | 176906705 | 23649508 |
| Fiducial volume cut |  | 34301372 | 8373891 |
| Veto event cut |  | 34197870 | 8373638 |
| DT>50 msec cut |  | 26627697 | 2909279 |
| Pedestal event cut |  | 26413349 | 2861723 |
| Uncompleted event cut |  | 26413177 | 2861701 |
| OD triggered event cut |  | 25068589 | 2199495 |
| OD mismatch event cut |  | 25068525 | 2199452 |
| OD mismatch event cut |  | 25068525 | 2199452 |
| Noise (NS-ratio) cut |  | 25014073 | 2191202 |
| Clustered ATM cut |  | 25004524 | 1102645 |
| First Flasher cut |  | 24773119 | 2103305 |
| Goodness cut |  | 24398348 | 2076264 |
| Second flasher cut |  | 18100641 | 1956279 |
| Bad energy cut | 57729840 | 18100641 | 1956279 |
| Spallation cut | 44075188 | 12868437 | 397962 |
| GRINGO cut |  | 3614781 | 263761 |
| PATLIK cut |  | 2724267 | 169168 |
| Clusfit cut | 6160188 | 1856647 | 151666 |
| GAMMA cut | 692556 | 295922 | 113058 |

| Reduction step | MC<br>4.5-20.0 MeV |
|---|---|
| Total | 24253500 |
| Bad run cut | 22140060 |
| Trigger cut | 8176699 |
| Noise (NS-ratio) cut | 8176699 |
| Clustered ATM cut | 8174655 |
| First Flasher cut | 7833412 |
| Unfitted event cut | 7830026 |
| Goodness cut | 7829900 |
| Second flasher cut | 7753151 |
| Bad energy cut | 7753151 |
| Fiducial volume cut | 6009388 |
| GRINGO cut | 4788640 |
| Clusfit cut | 4689600 |
| PATLIK cut | 4041865 |
| Spallation cut | 3162060 |
| GAMMA cut | 2757466 |

Table 6.1: The table of the reduction steps. 'MC data' is the solar neutrino MC simulation in the energy range of 6.5∼20.0 MeV in the 22.5 kt fiducial volume.

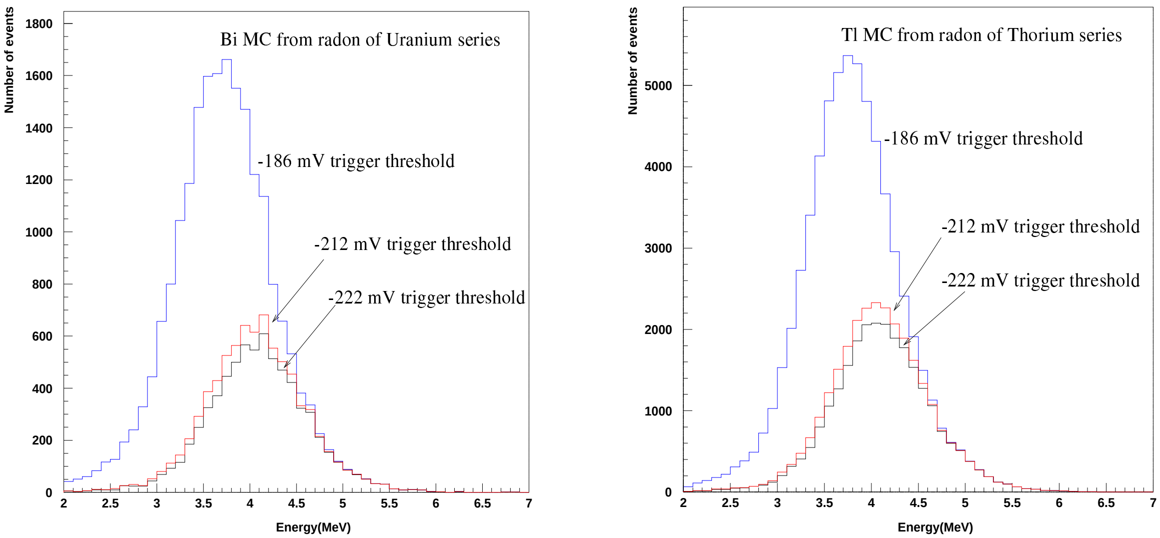

Figure 6.33: The expected energy spectrum of daughter nucleus from radon of Radium and Thorium series for each trigger threshold.

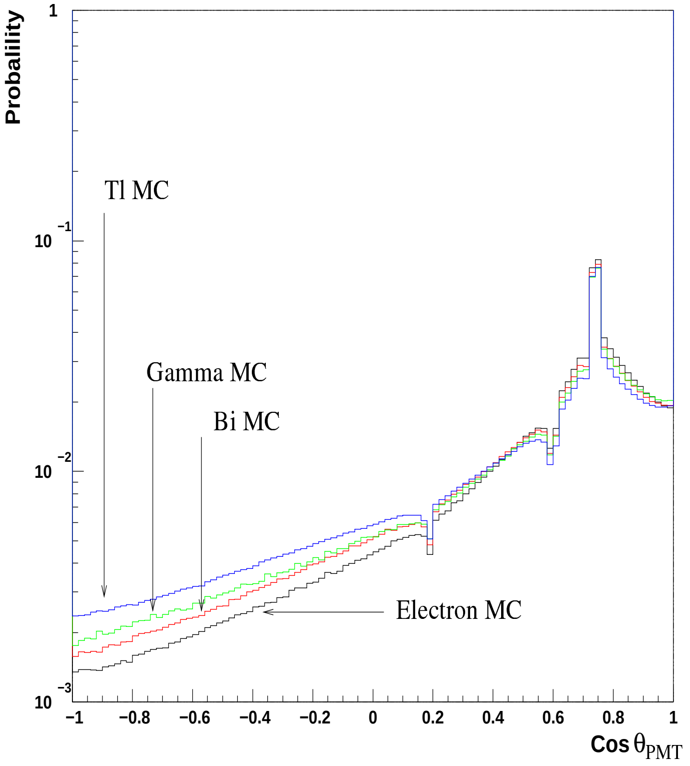

Figure 6.34: The hit pattern distribution of $\cos\theta_{PMT}$ for each MC of electron, $\gamma$, $^{214}$Bi and $^{208}$Tl from radon in energy region from 4.5 to 5.0 MeV.

# Chapter 7

# The approaches to radon reduction

The radioactivity from radon (Rn) in pure water is a major background for observing solar neutrinos at SK. After the data reduction, the Rn background is remaining in the data. Since the Rn events behave as solar events, it is difficult to reduce the Rn events by analysis tool.

Figure 7.1 shows the $\cos\theta_{sun}$ distribution for each energy thresholds in low energy region. The excess to solar direction indicates observed solar events. The flat contents for the excess to solar direction indicates Rn dominant background. As a energy threshold is lowered, the obtained peak to solar direction becomes smaller. Then, the Signal(excess)/Noise(flat) ratio becomes wrong.

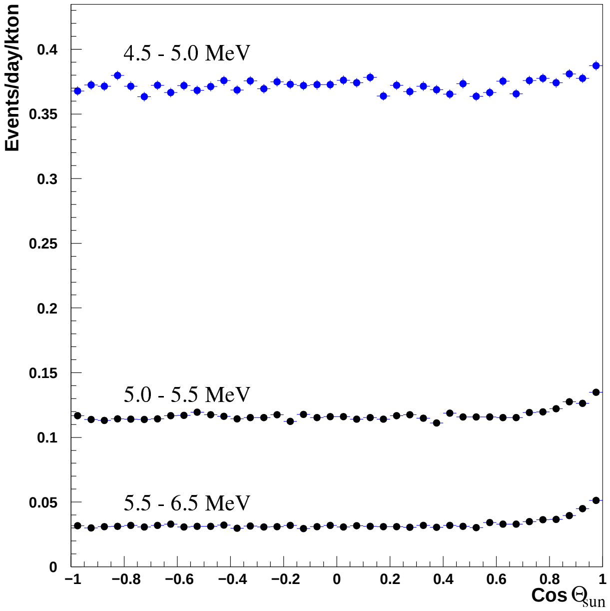

Figure 7.1: The $\cos\theta_{sun}$ distribution for each energy thresholds in low energy region.

Therefore, we have made an effort to reduce the Rn in pure water, physically, in order to observe low energy solar neutrino flux.

In this chapter, the following Rn reduction approach is described.

- The radon source in the SK water purification system was investigated and improved in Dec 2000.
- We have also studied the possibility of the Membrane Degasifier as the new radon reduction system. It was installed in the water system in February 2001.

By water system improvements, the radon concentration in the SK supply water was decreased by a factor of about 5. Basing on this result, the SK low-energy event rate analysis concluded that the current main source of the radon background is the emanation from the PMT glass, and convection is the main driving force for transporting the radon in the detector. At the last of this chapter, the current status of the radon background reduction and the future prospects are presented.

## 7.1 Solar neutrinos in Super-Kamiokande

An important task of the SK detector is to measure the energy spectrum of the recoil electrons from $^{8}$B and rare HEP solar neutrinos [5].

The energy spectrum of solar neutrino is distributed from 0 MeV up to 20 MeV. However the current analysis energy threshold is 5.0 MeV in the total recoil electron energy [5]. It is desirable to discuss the spectrums in the low-energy region in order to determine oscillation mechanism of the solar neutrinos. One of the important requirements of the solar neutrino observation in SK is to lower the energy threshold for the solar neutrino analysis as much as possible. The observation of the solar neutrino spectrums in the low-energy region is precluded by the remaining large background events after the event selection.

## 7.2 Radon background in the SK tank water

The analysis threshold is determined by the level of the background events and the event trigger threshold. The trigger threshold at 50% efficiency is 3.7 MeV and at 95% is 4.2 MeV. The dominant background sources in the low-energy region ($E \leq 6.5$ MeV) are $^{222}$Rn in the pure water, which cause a similar event to the solar neutrino events due to the beta decays of the radon daughters and external radioactivity such as gamma-rays from the PMT glass. After all reduction steps for the solar neutrino analysis, the $S/N$ is approximately 1 above 5.0 MeV in the solar direction. It is supposed from SK low-energy events that the radon concentration in the SK tank is 2.0∼3.0 mBq/m$^3$. In order to study the complete energy spectrum, it is desirable to lower the analysis energy threshold from 5.0 MeV to 4.5 MeV. This subject also means that the radon in pure water must be reduced as far as possible. For example, the radon concentration in the SK tank should be reduced down to less than 1.0 mBq/m$^3$.

For the SK detector, the following steps were done in order to achieve the needed radon reduction. Sufficient radon reduction for us means that we reduce the radon concentration in the SK supply water down to 1.0 mBq/m$^3$ which is not observed as low-energy events in the SK detector.

First of all, a super high sensitivity radon detector for water was developed to monitor the low radon concentration in the pure and degasified water before and after the radon reduction. The sensitivity of the developed radon detector is 0.7 (mBq/m$^3$)/day [102]. Secondly, the radon source was investigated in the SK water system by using the developed radon detector. Thirdly, we have also studied the utilization of the Membrane Degasifier (MD) as a more efficient radon reduction system. This new radon reduction system was also estimated by using the developed radon detector. After these steps, SK water system was improved. Finally, we concluded that the remaining background events in the low-energy region from 4.5 MeV to 6.5 MeV originated from the radon emanated from the glass of the PMTs in the SK detector.

## 7.3 The upgrades of water system in March 2000.

The total 50,000 tons of purified water in the SK is circulated through a water purification system with the flow rate of about 35 ton/hour in a closed system. The flow rate mode has started since July 1998. The water is circulated by the return pump which returns water from SK tank, and the supply pump which supplies water to the SK tank.

Figure 3.16 in chapter 3 shows a schematic view of the upgrading and improved SK water purification system in the final state of the SK-I. The SK water purification system has been improved and upgraded during the experiment basing on various studies.

In March 2000, some upgrading of the water purification system was done for following points in the figure 3.16.

First, the UF system was reinforced from 17 modules to 23 modules. Secondly, the RO system was also reinforced just before the VD system in addition to the existing RO system. These reinforcements make an effect on the removal of of the further dusts. Thirdly, the radon-free-air dissolve tank is installed before the VD system in order to increase radon removable efficiency at the VD system. In the VD system, 3600 L plastic balls like gyros were used to increase the surface area for vacuum degasification. The plastic balls were pointed out about the radon emanation from them. We actually measured the radon emanation from 100L balls of vinyl chloride and a stainless steel with an electro polished. The quality of the material was changed from a vinyl chloride to a stainless steel with an electro polished in a point of view of less radon emanation. We analyzed SK low-energy events from 4.5 MeV to 6.5 MeV before and after these upgrades. However, the effect of these upgrades was not observed.

Table 7.1 shows a summary of uranium and thorium concentration in each water. The concentration was measured with an ICP-MS device at the detection limit of 4.0 ppq. From the summary, we conclude that the SK supply water is super-high quality.

| Measuring point | Uranium concentration | Thorium concentration |
|---|---|---|
| Mine water | $3.0\times10^5$ ppq | 32.0 ppq |
| SK supply water | 0.2 ppq | 0.4 ppq |
| SK return water | 13.0 ppq | 59.0 ppq |

Table 7.1: A summary of Uranium/Thorium concentration in SK water.

## 7.4 Radon source search in the SK water purification system

First of all for radon background reduction, the radon source in the SK water purification system was investigated from Jun. 2000 to Sep. 2000 in order to reduce the radon background in the SK supply water physically. Figure 7.2 shows the flow chart of the SK water system.

In the figure 7.2, 'Point x' indicates a measuring point. We have measured the radon concentration between each components using the developed super high sensitivity radon detectors for water with 700L of collection volume (700L radon detector [102]). The radon is detected by electrostatic collection of the daughter nuclei of $^{222}$Rn and the energy measurement of the alpha decay with a PIN photodiode. The sample water was taken from these measuring points using the water pump by the flow rate of 1.0 L/min. The water was forwarded to the radon detector and measured. The flow rate is set in the same way as the calibration. The detection efficiency, used as a calibration factor, of the 700L radon detector was measured by a standard radon water source and it is $14.6\pm1.5(stat.)^{+1.6}_{-1.5}(syst.)$ (counts/day)/(mBq/m$^3$). This value is larger than the previous 70L radon detector [101] by a factor of about five [102]. The detection limits which means three standard deviation in excess of the signal above the background of the radon detector for water, is 0.7 (mBq/m$^3$)/day in one-day measurement. The details about the super high sensitivity radon detectors are reported in reference [102]. This value is smaller than the 70L radon detector by a factor of about six. The radon detectors are connected to a workstation via a network, and they are monitored in real-time.

Table 7.2 and figure 7.3 (filled circles) shows the radon concentration at each components.

The results show that the radon concentration just after the IE is about a factor of 14 higher than that of the SK supply water. Even though the radon concentration just after the IE is

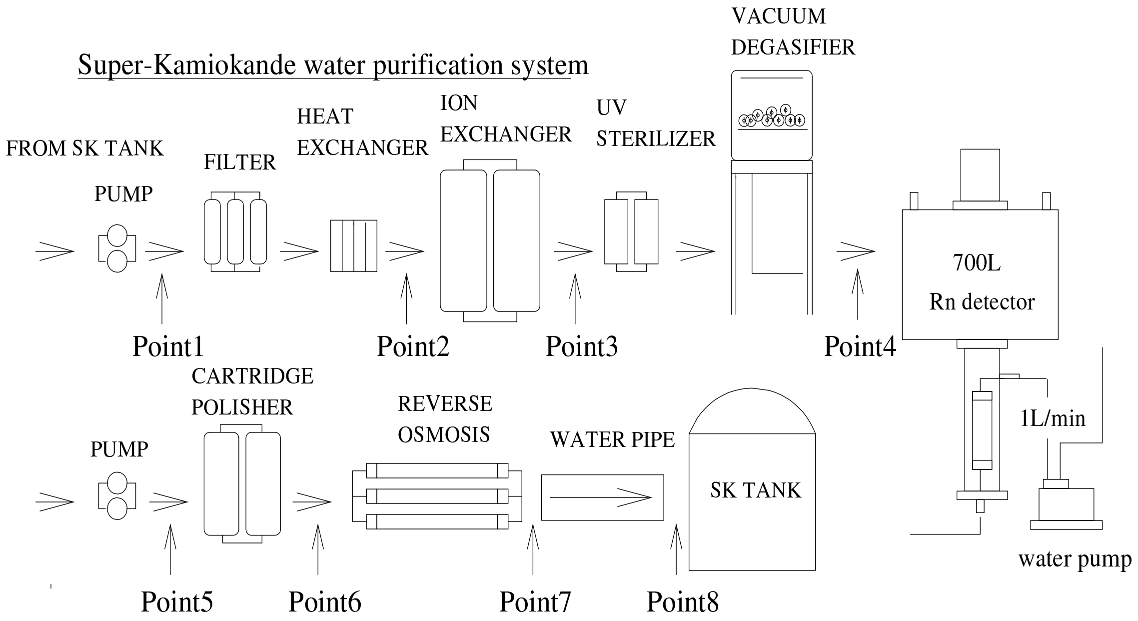

Figure 7.2: The flow chart of the SK water system and the search points of the radon source.

| Measuring point | Component | radon concentration(mBq/$m^3$) |
|---|---|---|
| Point 1 | after return pump | 13.6±1.9 |
| Point 2 | just before IE | 16.0±1.3 |
| Point 3 | just after IE | 88.0±0.6 |
| Point 4 | just after VD | 4.2±0.8 |
| Point 5 | just after supply pump | 3.7±0.7 |
| Point 6 | just after CP | 6.8±1.8 |
| Point 7 | just after UF | 5.8±0.5 |
| Point 8 | just before the SK tank | 6.5±0.2 |

Table 7.2: The radon concentration at each water system components. Error is statistical only.

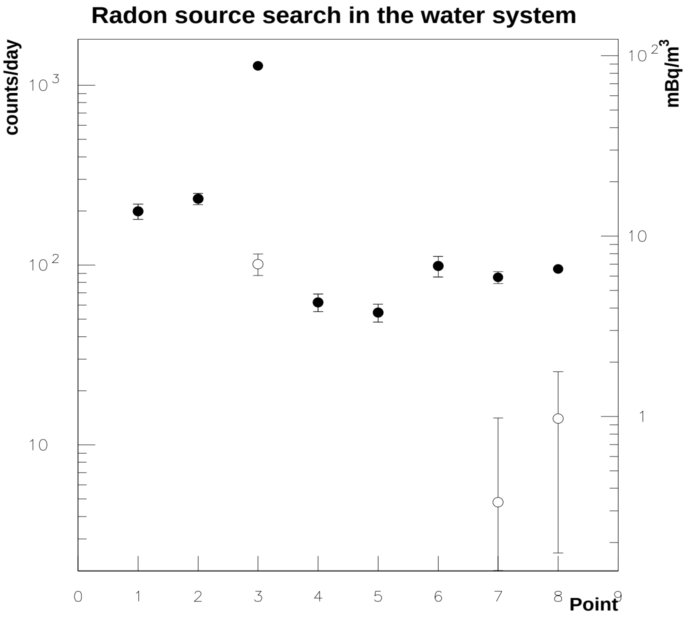

Figure 7.3: The radon concentration at each water system components. Error is *stat.* only. Points of the horizontal axis indicates component number. See table for component number.

so high, it was reduced by the VD system by a factor of about 20. This reduction efficiency (-95.0±1.0%) is almost the same level expected from the specification of the VD system.The CP produced about 46.0% of the radon concentration of the SK supply water comparing just before and just after CP system. From these results, we found two radon source points which are the IE system and CP system in the SK water purification system.

## 7.5 Membrane Degasifier as new radon reduction system

We studied the feasibility of the membrane degasifier (MD) from December 1999 to September 2000. The membrane degasifier is a hollow fiber with an outer diameter of 250 $\mu$m. The surface of this membrane has a structural feature wherein the inner surface has many small holes with a diameter of about 0.03 $\mu$m but no holes on the outer surface. The principle of the membrane degasifier is as follows. In the side separated with the membrane which let gas pass but water not pass (water phase), the water which contains gas flows. In the other side (gas phase), the pressure is reduced by the vacuum pump. Hence, the gas dissolved in the water pass through the membrane and transfered from water phase to gas phase.

In the case of the MD system installation in the SK water purification system, there are some requirements. The MD must be small, has a high radon reduction efficiency, and has a small radon emanation from itself. It is most important that radon emanation from membrane is small.

Before starting the test, we have compared the radon emanation from MD modules made by several companies and it was found that the one made by Dai-Nippon-Ink and Chemicals inc. gave the lowest radon emanation. The product is SEPAREL EF-040P. The radon concentration emanated from the membrane is 0.020±0.004(*stat.*) mBq/1module/day. Uranium and Thorium in the Poly-4Methyl-Penten1 is less than 1 ppb, a value which was estimated by the KAWATESTU TECHNOSEARCH inc. at the level of the detection limit. From these results, we have studied the radon reduction efficiency only using a Dai-Nippon-Ink module. Table 7.3 shows the specification of a membrane degasifier module(SEPAREL EF-040-P) which was studied for is the radon reduction efficiency.

This module is able to reduce gas dissolved in water down to less than 25 ppb (25 $\mu$g/L)

| Contents | Specification |
|---|---|
| Material of membrane | Poly-4Methyl-Penten1 |
| Material of housing | Vinyl chloride resin for super pure water |
| Bonding agent | Urethane and Epoxy resin |
| Endcap | Polysulfon |
| Size | 180mm$\phi\times$673mmL |
| Capacity of treatment(Max) | 2[ton/hour] |
| Active surface of membrane | $\sim$40[m$^2$] |
| Weight | $\sim$10.0[kg] |

Table 7.3: The specification of a membrane degasifier module(SEPAREL EF-040-P) whose the radon reduction efficiency was studied.

for a vacuum pressure of 20 torr and a flow rate of 2 ton/hr and water temperature of 25 degrees centigrade and air temperature of 20∼30 degrees centigrade. However, this ability is basically for oxygen dissolved in the water. In this thesis, it is reported for the first time that the radon reduction efficiency of the MD module was estimated using the super high sensitivity radon detector. Moreover, it is very important that this estimation was done under the special condition where oxygen in the water is already degasified by -96%.

A small setup was constructed on the SK tank as shown in figure 7.4 in order to estimate the radon reduction efficiency of the MD module.

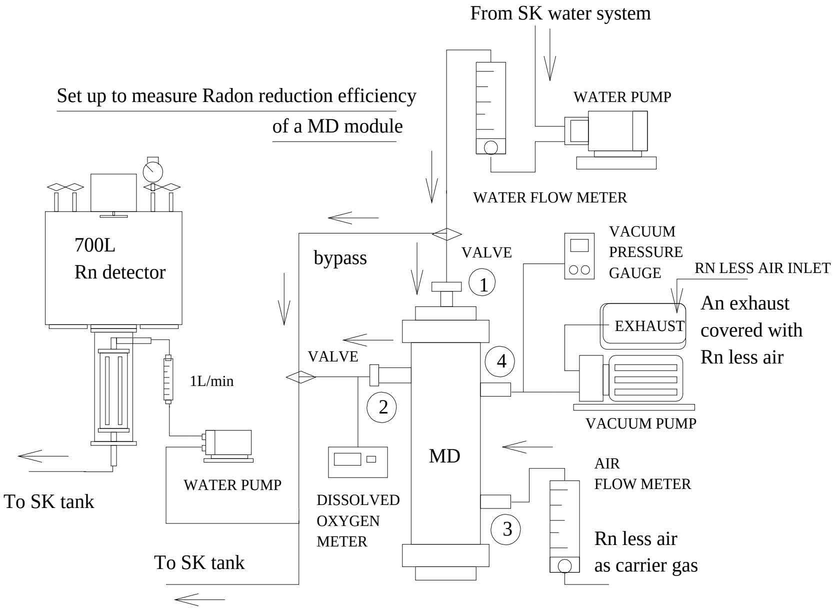

Figure 7.4: Setup to measure radon reduction efficiency of a MD module.

The setup consists of a MD module, two water pumps, a vacuum pump, a vacuum pressure gauge, a dissolving oxygen meter, and the 700L radon detector for water. In this setup, there are two routes of the water flow. In one route, the water passes through the MD module, In the other route, the water bypasses the MD module. When the radon concentration is measured by the former route, the run is called 'MD run'. The run is called 'SK water run' when the radon concentration is measured by the latter route. The water from the SK water purification system flows to one of the two routes by the manual selection. The flow rate was tuned by the flow rate meter from 0.2 tons/hour to 1.0 tons/hour. Then, a part of the water is forwarded to the radon detector to measure the radon concentration with a flow rate of 1.0 L/min and the left water is forwarded to the SK detector.

In this MD module, the water flows the outside of the hollow fiber membrane and the inside of it is reduced the pressure by the vacuum pump. The water flows from No1 nozzle to No2 nozzle through the MD module in figure 7.4. We need to inject pure air to the vacuum phase in order to increase the radon reduction efficiency by the combining radon gas with air, because the water is already degasified. We used the radon-free-air as the carrier gas. The radon-free-air is produced by the SK air purification system, the details about it are reported in chapter 3. The carrier gas was injected from the No3 nozzle. The gas separated from the water was exhausted from the No4 nozzle by the vacuum pump. A noticeable point is that the exhaust of the vacuum pump was covered with the radon-free-air to prevent the open air from flowing into the MD from this exhaust.

In the figure, the data values and the data points were fit by using the following exponential function,

$$\mathrm{N}(T) = \mathrm{N}(0) \times \exp \frac{-\ln 2.0 \cdot T}{3.8} + Constant \tag{7.1}$$

where N($T$) is the count rate at time $T$, N(0) is the obtained count rate at the injection time, and T is the elapsed time since the measurement starting in day. *Constant* indicates the value in the equilibration state of each of the measurements. We used this value in the case of the calculation of the radon reduction efficiency.

The efficiency depends on vacuum in the module, the flow rate of water through the module, and the amount of carrier gas flow into the vacuum phase of the module. We calculated the efficiency of the MD by comparing the radon concentration in 'SK water run' and it in 'MD run'. The formulation of the efficiency is given as :

$$\text{Efficiency} = \frac{\text{MD run[counts/day]-Background run[counts/day]}}{\text{SK water run[counts/day]-Background run[counts/day]}} \tag{7.2}$$

where the background run is estimated by stopping the water flow. Figure 7.5 shows a typical variation for the each runs, which are SK water run,background run, and MD run. A parenthesis(x/y) in the figure indicates a function of water(x) and carrier gas rates(y). In the figure, the MD effect was observed clearly for the SK supply water and the radon reduction succeeded almost down to the background level.

Table 7.4 shows a summary of the radon reduction efficiency of the MD module as a function of water and carrier gas. The error is statistical only.

| Vacuum pressure(kPa) | Water flow (ton/hour) | Carrier gas (L/min) | radon reduction (%) | Dissolved oxygen($\mu$g/L) |
|---|---|---|---|---|
| 6.13 | 0.2 | 0.4 | -93±4 | 525 |
| 8.50 | 0.2 | 1.0 | -90±3 | 867 |
| 0.38 | 0.4 | 0.0 | -83±3 | 5.6 |
| 0.35 | 1.0 | 0.0 | -64±12 | 3.7 |
| 0.65 | 1.0 | 1.0 | -83±5 | 235 |
| 0.93 | 1.0 | 2.0 | -90±7 | 367 |

Table 7.4: A summary of the radon reduction efficiency of the MD module as a function of water and carrier gas. Error is statistical only.

It is possible that the MD module reduce radon by about 90% in the optimum condition although the water was already degasified by the -96% efficiency. In a point of view of the installation just before SK tank, the remarkable result is that the MD module is able to reduce radon by a factor of more than about 5 for the water flow rate about 1 ton/hour. A noticeable

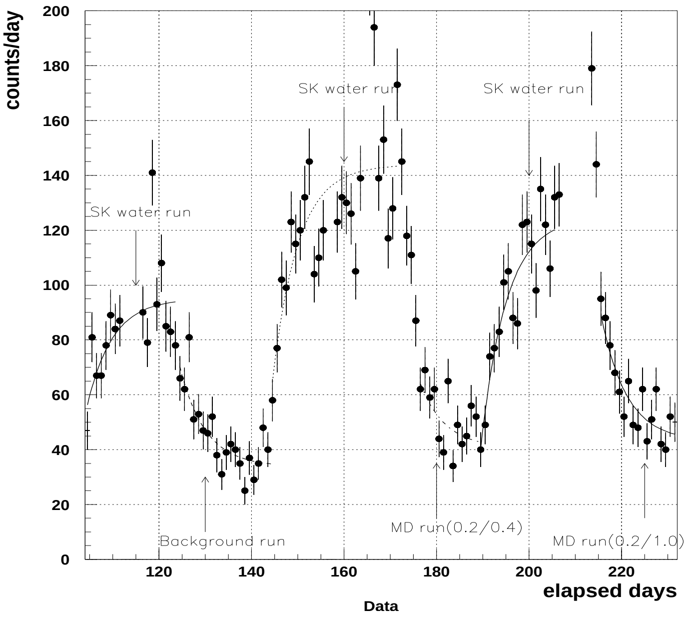

Figure 7.5: A typical variation for the each runs, which are SK water run,background run, and MD run. A parenthesis(x/y) in the figure indicates a function of water(x) and carrier gas rates(y).

point is that in this module test, the radon concentration of the SK supply water was 6.5±0.2 mBq/m$^3$ and the ability of the radon reduction was for the radon concentration in the water.

Considering a treatment of the amount of the SK supply water of 30 tons/hour, and an ability of the radon-free-air production, we decided to install a system with 30 MD modules between the water purification system and the SK tank as a final process of the SK supply water.

In the case of the installation, the optimum conditions are 1 ton/hour/module and the carrier gas of 1.0 L/min/module. A deserving special mention is that the exhaust of a vacuum pump was decided to be covered with radon-free-air because the phenomenon of the open air back-flow was observed in the experiment.

## 7.6 Improvements of water system in October 2000 and in February 2001

In the figure 3.16, the CP system and the MD system were the improvements based on the studies of the radon source search and the feasibility of the MD system.

In October 2000, improvements for the IE and the CP systems were done based on the results of the radon source search. First of all, we should explain the difference between IE and CP. Both have the functionality of removing ions. The main difference between them is that IE is re-generatable, but CP is not. The power to capture ions by IE is weaker than that of CP and that is why IE is re-generatable. When we get a "new" IE resin from the water system company, it is in most cases a re-generated one at the company. The company collected used IE resin from customers and re-generate them at once using a big plant. Hence, it is quite possible that even new IE resin has serious amount of Radium for us even though the resin is good enough for other customers. On the other hand, CP resin is made from raw materials and used only once. Therefore, it must have lower Radium concentration. The reason why we have been using both IE and CP resins in the SK water system was to prolong the life of the rather expensive CP resin. Since the quality of the SK water is quite high (resistivity is as high as 18.24 M$\Omega \cdot$m), it is possible to remove ions only using CP resin for a reasonable time period without exchange. In October 2000, we have performed the following changes.

- Empty the IE two vessels and fill CP resin in the vessels.
- Empty the CP vessels.

We monitored the radon concentration changes before and after the water system improvement by using the three super high sensitivity radon detectors for water in real time. Figure 7.6 shows a typical variation before and after water system. These data points was monitored realtimely just before SK tank. The other monitoring points were just after IE system and just after UF system. The radon concentration after the water system improvement is shown by open circle in figure 7.3 and a numerical summary is shown in table 7.5.

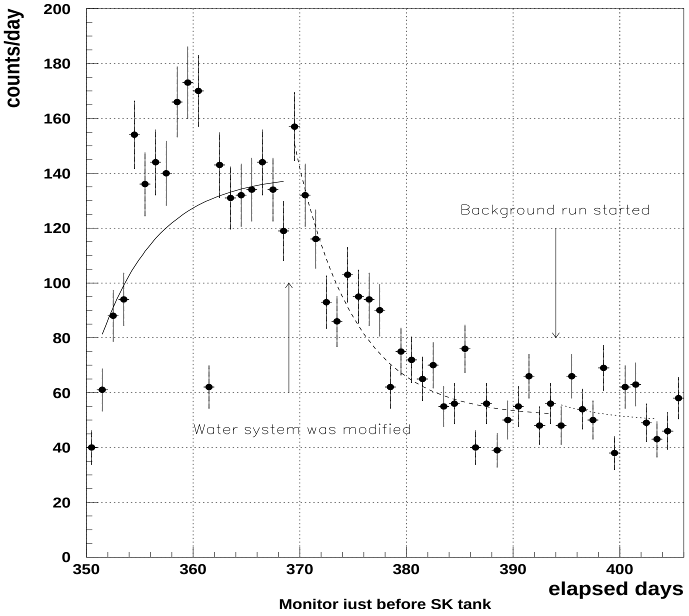

Figure 7.6: A typical variation before and after water system improvement in October 2000. These data was monitored real-timely just before SK tank.

| Component | radon concentration before October improvement | radon concentration after October improvement |
|---|---|---|
| Just after IE | 88.0±0.6 | 6.9±0.9 |
| Just after UF | 5.8±0.5 | 0.33±0.60 |
| Just before the SK tank | 6.5±0.2 | 0.96±0.74 |

Table 7.5: A comparison of the radon concentration between before and after the October 2000 improvement. Error is statistical only.

The radon concentration just after the IE vessel (now filled with CP resin) is decreased by more than a factor of 10. The detection of the limit in the radon detector for water is estimated 0.7 mBq/m$^3$/day in a one-day measurement. We did not observe clear excess of radon counts over the background level in the radon detectors at "Just after UF" and "Just before the SK tank" after the improvement. If the radon concentration in water is close to or lower than the equilibrium concentration with the background in a radon detector, no excess or negative excess should be observed. The radon concentration presented in table 7.5 is based on a simple calculation done by subtracting the background counts. The background counts in the radon detector for water is measured in the state where the water flow through the detector is stopped.

In February 2001, the MD system was installed just before the SK tank in figure 3.16. We designed a system of 30 MD modules to process SK supply water of 30 tons/hour and to inlet the radon-free-air of 1.0 L/min to each module from the module test. Moreover, we covered the exhaust of a vacuum pump by the radon-free-air. The typical pressure in the MD system is 2.6 kPa. The typical concentration of the dissolved oxygen after the MD is 290 $\mu$g/L. In this setup condition, the removal efficiency for radon is supposed about 90%. However, we could not confirm the radon reduction efficiency for the low level radon achieved by the October 2000 improvement, because the module test was done in August 2000 and the radon concentration after the October 2000 improvement was low level which was not sensitive with the radon detector for water. We monitored the radon concentration of the SK supply water just before SK tank with the radon detector for water before and after MD system installation. We could not observe a change in the radon rates, therefore the radon concentration was kept less than 1.0 mBq/m$^3$ after MD system installation. But probably the radon reduction efficiency does not strongly depend on the initial radon concentration. By these improvements, we succeeded in radon reduction in SK supply water down to less than 0.7 mBq/m$^3$.

## 7.7 SK low-energy event rate

So far in this section, we have written about success in the radon reduction in the SK water supply. Hence, the SK detector is separated from radon rich environment. However this radon reduction does not make an effect on for reducing radon background for the solar neutrino analysis. Figure 7.7 shows a history the expected radon concentration in the SK tank from January 2000 to July 2001. One data plot indicates day or night data in a day.

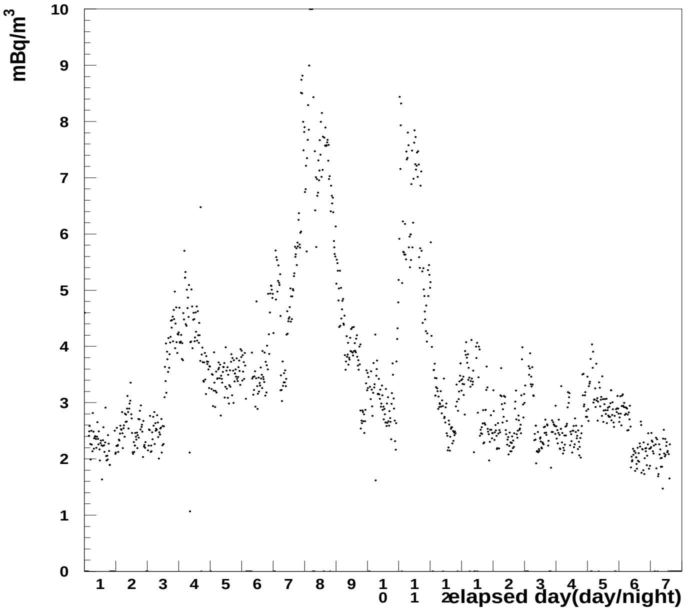

Figure 7.7: History of the expected radon concentration in SK tank calculated from the low-energy event rate between Jan. 2000 and Jul. 2001. One plot indicates radon concentration in day and night time.

The radon concentration is calculated from Super-Low-Energy event rates between 4.5 MeV and 6.5 MeV using the radon detection efficiency in the SK detector. The used events are within R<10 m, -16.1 m<Z<16.1 m (R:the radius axis of the SK tank, Z:the cylindrical axis of the SK tank). The event selection of R<10 m means that incoming gamma-ray events from the detector wall are eliminated as far as possible. In order to estimate the radon concentration in the SK water independent of the radon detector measurements, we used the SK detector to take data with a known amount of radon in December 1997. The details were reported in reference [100]. From these test run, the radon detection efficiency is defined as a following equation :

$$0.013[\text{events/day/ton}] = 1.0[\text{mBq/m}^3] \tag{7.3}$$

This correlation factor was acquired by the analysis of Super-Low-Energy (SLE) events in this run at the hardware trigger threshold of -260 mV [94]. . The SLE events have energies between 4.5 MeV and 6.5 MeV. A fast vertex reconstruction and a fiducial volume cut (32 ktons) were applied to all the events in real-time on a workstation. After these cuts, the same event selections as the SK solar neutrino analysis are applied to SLE events for this analysis. Some additional noise cuts usually are also applied using the quality of the reconstructed vertex, but for the test run and the calculation of the radon concentration, the last cuts are not applied in order to leave the raw background events. The used events were within R<10 m, -16.1 m<Z<16.1 m.

Table 7.6 shows the radon detection efficiency in the SK detector for the another hardware trigger thresholds.

| Run period | hardware trigger threshold | Radon detection efficiency for 1.0mBq/m$^3$ |
|---|---|---|
| May. 1997∼ | -260mV,-250mV | 0.013[events/day/ton] |
| Sep. 1999∼ | -222mV | 0.015[events/day/ton] |
| Dec. 1999∼ | -212mV | 0.016[events/day/ton] |
| Sep. 2000∼ | -186mV | 0.022[events/day/ton] |

Table 7.6: Radon detection efficiency in SK detector for another hardware trigger thresholds.

In the figure 7.7, the expected radon concentration in the SK tank was quite high in July∼August and November 2000. As described in last section, the radon concentration in the SK supply water is about 0.7 mBq/m$^3$ after October 2000 and February 20001 by the water system modification and MD system installation. However the radon concentration in the SK tank did not changed so much at 2∼3 mBq/m$^3$, except for the period of July∼August and November 2000. If the supplied water is uniformly diffused in the inner detector and the flow rate is 30 ton/hour, then the radon concentration at equilibrium is :

$$\frac{0.7[\text{mBq/m}^3] \cdot 720[\text{m}^3/\text{day}]}{0.182[1/\text{day}] \cdot 32000[\text{m}^3]} = 0.09[\text{mBq/m}^3] \tag{7.4}$$

The expected radon concentration in figure 7.7 is much higher than the contribution from the SK supply water. The large variations in the radon concentration of the SK tank in year 2000 is correlated with the changes of the SK supply water configuration. Table 7.7 summarizes the SK supply water configuration and the temperature of the SK supply water. figure 7.8 also shows a diagram of the SK supply water configuration.

The rise in the expected radon concentration in the SK tank in July∼August and November 2000 seems to be due to strong convection in the SK tank. Figure 7.9 shows the Z dependence of the water temperatures in the SK tank measured on August 22, 2000 and January 9,2001. The temperature measured on August 22, 2000 is uniform within 0.01 degree centigrade in the inner detector. On the other hand, the temperature profile on January 9 2001 shows that the water convection is caused only below Z=-10 m.

In this time, the radon concentration was kept at a low level. Figure 7.7 shows vertex position distribution of the low-energy data sample from 4.5 MeV to 6.5 MeV.

The event selection is the same as the stream of the radon detection efficiency. When the water temperature is not uniform, the distributions show that the radon background event rate

| Date | Supply to | Return from | Supply water temperature |
|---|---|---|---|
| Before Mar.2000 | bottom | top | ∼12.3 degree centigrade |
| Mar.-Jul.2000 | center | bottom | not measured |
| Jul.-Aug.2000 | bottom | top | ∼15.2 degree centigrade |
| Aug.-Oct.2000 | bottom | top | ∼14.3 degree centigrade |
| Oct.-Dec.2000 | center | top(1/2)bottom(1/2) | ∼14.3 degree centigrade |
| After Dec.2000 | bottom | top | ∼14.3 degree centigrade |

Table 7.7: SK supply water configuration and temperature of SK supply water.

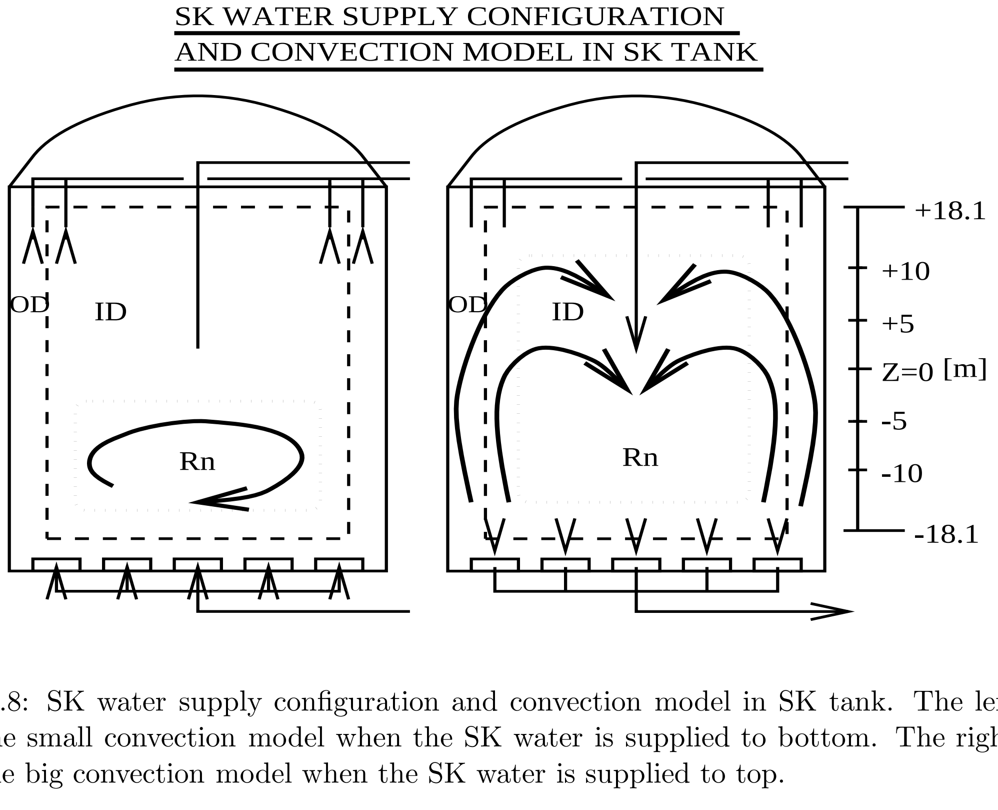

Figure 7.8: SK water supply configuration and convection model in SK tank. The left figure shows the small convection model when the SK water is supplied to bottom. The right figure shows the big convection model when the SK water is supplied to top.

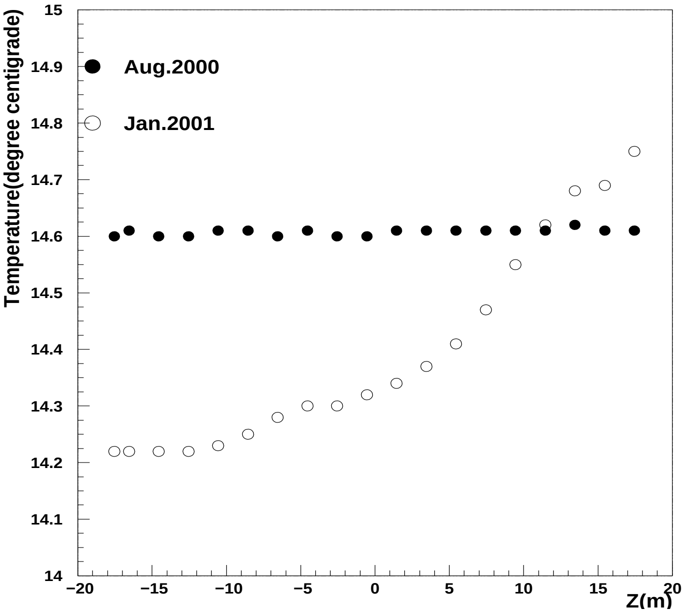

Figure 7.9: Z dependence of the SK water temperature measured on August 22 2000 and January 9 2001.

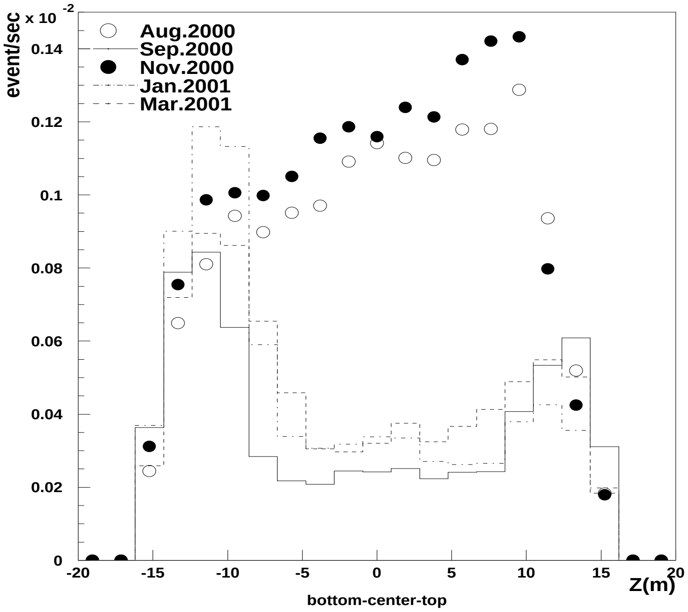

Figure 7.10: Z Vertex distribution of the low-energy events in Aug. 2000, Sep. 2000, Nov. 2000, Jan. 2001 and Mar. 2001.

is higher just in the bottom region of the SK tank and the radon concentration in figure 7.7 is low. On the other hand, when the water temperature is uniform, the distributions show that the radon background event rate is higher in the region where the water temperature is uniform and the radon concentration is high. Further, the integration of the distributions in the period when the water temperature is uniform is larger than another period when the water temperature is not uniform. Hence, we conclude that the emanation of radon from detector materials is the dominant source of radon, and the radon is transported by the convection in the SK tank. Figure 7.8 shows the our assumed convection model. The excess of vertex position distribution in the bottom region is caused by the model of the left plot in figure 7.8. The expansion of vertex position distribution in the convective period is caused by the model of the right plot in figure 7.8.

The radon emanation from various materials, namely PMTs, black plastic sheets and tyvek sheets, used in the SK tank in large quantities was measured. The measured PMTs are 20 inch PMTs used in the SK inner detector. The black plastic sheets and tyvek sheets are used in the inner and outer detector respectively. The measurement was performed by super-high sensitivity radon detector for air in which various materials were placed. The radon detector is reported about the details in reference [102]. Assuming that the radon emanated from each material is uniformly distributed over the whole SK detector (50 ktons), the equilibrium radon decay rate is given in the following equation. The 'Radon concentration in SK tank' indicates the results from the equation. Concerning the emanation from black sheets, the radon emanation is measured about the amount used around one PMT.

$$\frac{\text{Radon emanation}[\text{mBq/m}^2, \text{PMT/day}] \cdot 15000, 11146[\text{m}^2, \text{PMTs}]}{0.182[1/\text{day}] \cdot 50000[\text{m}^3]} = [\text{mBq/m}^3] \tag{7.5}$$

The results is consistent with the expected radon concentration in the SK tank during large convection periods (e.g. August and November 2000) within a factor of two.

| Material | Radon emanation | Radon concentration in SK tank |
|---|---|---|
| Black sheet | 0.08 mBq/PMT/day | 0.10 mBq/m$^3$ |
| Tyvek sheet | 1.5 mBq/m$^2$/day | 0.44 mBq/m$^3$ |
| PMT | ~4.0 mBq/PMT/day | ~ 5.0 mBq/m$^3$ |

Table 7.8: Radon emanation from various materials.

As a next step, we confirmed whether the radon expected from SK low-energy event rate in the SK tank exists or not. We actually measured the radon concentration in the SK tank with the super-high sensitivity radon detector for water (700L radon detector) in May. 2001 when the radon concentration was low and it is assumed that the no large convection happened. Figure 7.11 shows a setup to measure Z dependence of the radon concentration in the SK tank.

The sample water is taken from each Z position, which are Z=+6.5 m (Center) and Z=-15.5 m (Bottom), via a rigid nylon tube with a water pump using the bypass route in the figure 7.11. Then the radon concentration of the sample water was obtained with the radon detector. The background level in the system was measured with the measurement of the radon less water made with 'Rn less making system' (See figure 7.11), which make use of the membrane degasifier module explained in the last section. The result in the measurement is the actual background level in this system. The detection limit of the radon detector is 0.7 mBq/m$^3$. Table 7.9 summarizes Z dependence of the radon concentration in the SK tank. Figure 7.12 also shows the same results.

We calculated the expected radon concentration in the bottom region from Z=-500 m to Z=-1610 m and the center region from Z=-500 m to Z=+500 m at R=0 using the SK low-energy event rate and the radon detection efficiency in May. 2001. The expected radon concentration is 4.1 mBq/m$^3$ and 0.0mBq/m$^3$ in the bottom and center region respectively. From these results,

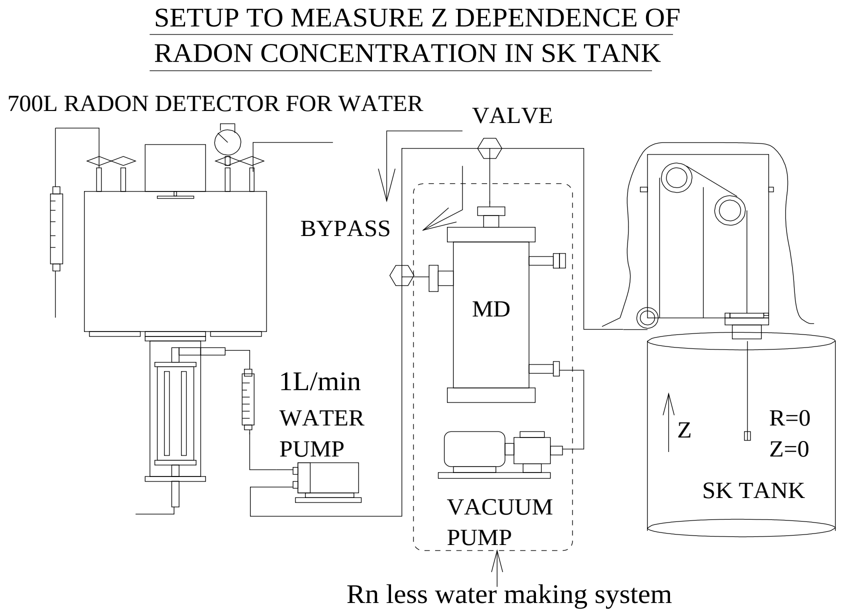

Figure 7.11: Setup to measure Z dependence of radon concentration in SK tank.

| Position(R/Z) | Radon concentration | B.G subtraction |
|---|---|---|
| Rn less water(Actual B.G) | 2.0±0.3mBq/$m^3$ | - |
| Center(0.0/+6.5) | 1.6±0.2mBq/$m^3$ | <0.7 mBq/$m^3$ |
| Bottom(0.0/-15.5) | 3.2±0.2 mBq/$m^3$ | 1.6±0.5 mBq/$m^3$ |

Table 7.9: Z dependence of the radon concentration in SK tank.

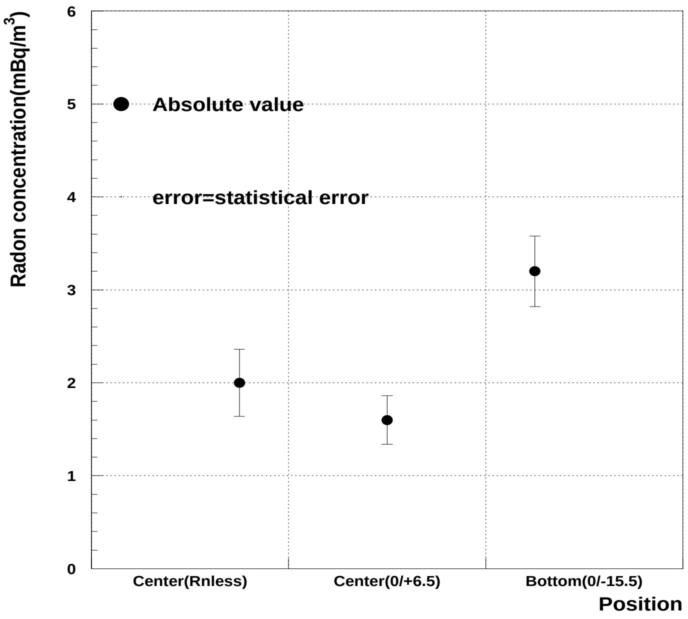

Figure 7.12: Z dependence of Radon concentration in SK tank.

we conclude that the radon concentration in the SK tank is not consistent with the expected value within a factor of 2.6, but we can confirm the radon existence in the bottom region of the SK tank in the small convection period. Moreover, when the large convection does not happen, the radon does not exist in the center region.

From the conclusions of the SK event rate analysis, we installed a new chiller system into the SK water purification system in March, 2000 in order to suppress the convection in the SK tank by lowering the SK supply water temperature to make the temperature gradient in the SK tank larger. Typical water temperatures before the 1st heat exchanger and after the 2nd heat exchanger are 14.5 degrees centigrade and 13.5 degrees centigrade, respectively in figure 3.16. The water temperature changed from 14.6 degree centigrades to 12.7 degree centigrades. However, we could not observe the effect of the installation in figure 7.7 clearly.

## 7.8 Summary

The radon concentration at various locations in the SK water purification system was measured. The radon source in the water system was investigated and improved in Dec 2000. The radon concentration in the SK supply water was decreased by a factor of about 5. We have also studied the feasibility of the Membrane Degasifier as the new radon reduction system in the water system. We found a optimum configuration of vacuum, water flow rate and radon-free-air flow rate. A system consisting of 30 Membrane Degasifier modules was installed in the SK water system in February 2001. By these improvements, the radon concentration in the SK supply water became less than 0.7 mBq/m$^3$ and the SK tank was separated from the external radon rich environment from a point of view of the radon background. After the water system improvements, the SK low-energy event rate was studied on the details. The SK event rate is much higher than the level expected from the supply water. It was concluded that the current main source of the radon background is the emanation from the PMT glass, and convection is the main driving force for transporting the radon in the detector. Even if radon moves from the surface of PMT to the inner of fiducial volume by Brownian motion, radon is able to move by about 10 cm [105]. The schematic view of estimated background contamination is like figure 7.13.

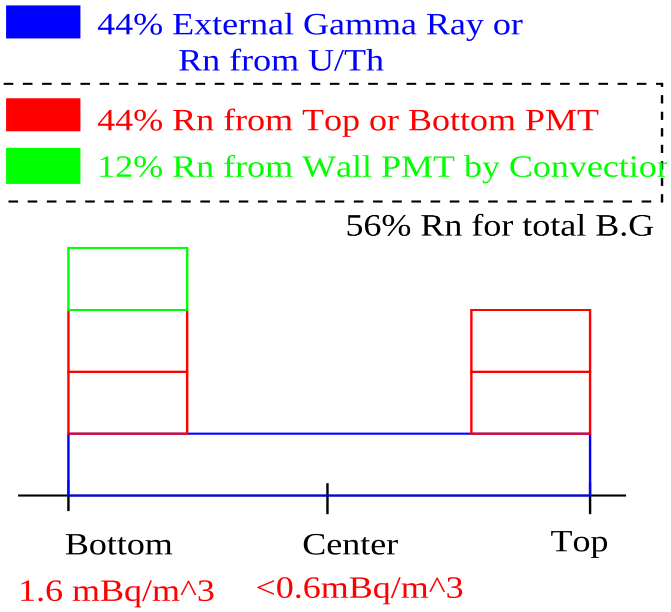

Figure 7.13: The schematic view the ratio of background contamination in SK detector.

## 7.9 Future prospects

Since the radon in the supplied water was reduced to a level acceptable for the solar neutrino analysis, we need to reduce the radon emanating from detector materials and to suppress the convection in the SK tank. We plan to do the following things for this purpose.

1. We changed the shape of the water outlet pipes in order to reduce the height of the convective zone as far as possible. We asked Mitsui-zosen Co. (SK tank company) to make a simulation program for the SK water flow. We found the optimized shape and length of the outlet pipes using the simulation. The improved pipes were replaced during the PMT replacement between July. 2001 and October. 2001 after SK-I. Figure 7.14 shows the improvement of the shape of the water outlet pipe. A new outlet pipe, which is made by transparent acrylic resin, was attached to the top of the old PVC outlet pipe. The new outlet pipe has many holes on the side of the pipe in order to let the water out in the horizontal direction.

2. We will measure radium concentration in SK tank water. As seen in the data of January. 2001 in figure 7.7, we still have background in the non-convective zone in the tank (continuum background from top to center). Is it due to radon produced from radium in water? We have installed RO system in March 2000 in order to increase the efficiency of removing radium. But, apparently the continuum background did not disappear. We need to measure radium in the SK water and understand the source of the continuum background.

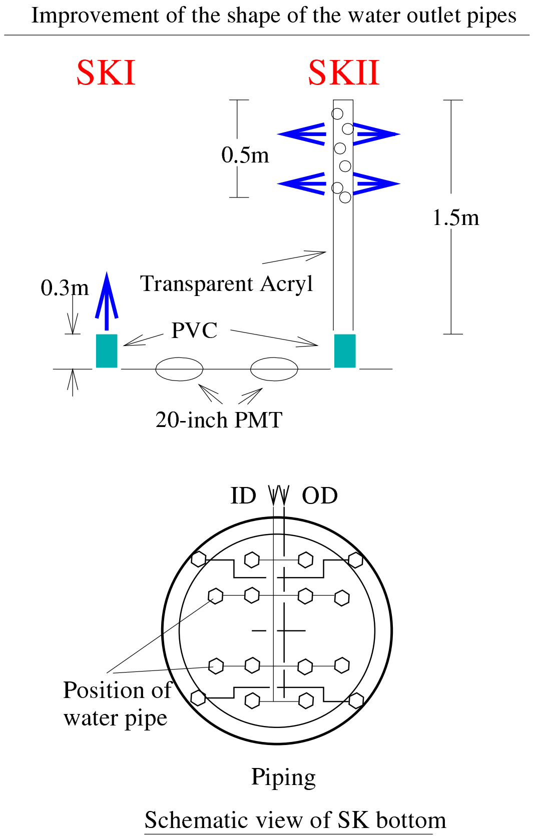

Figure 7.14: The improvement of SK water supply pipe to control water convection in SK tank.

# Chapter 8

# Tight data reduction for 4.5 MeV

In chapter 7, the Rn reduction approach to observe low energy solar neutrino was presented from hardware aspect In this chapter, the probability to lower energy threshold by the improvements of analysis tools is described from soft-ware aspect.

To lower energy threshold from 5.0 to 4.5 MeV, we need to install new reduction tools adding to general reductions, and need to improve Signal-Noise ratio. So, we applied the "Tight data reduction" to the data sample after "General data reduction which has already been described in chapter 6. First, the applied tight data reduction is explained. Then, the quality of the made data sample after tight data reduction is described in this chapter.

## 8.1 Tight Data Reduction

The tight data reduction is applied to the data sample after general data reduction in two stages. The data reduction in the first stage is named "Tight cut" from now on in this thesis. This cut is based on the "General data reduction" which is mentioned in the chapter 6. The data reduction in the second stage is called "New fitting cut" which is a developed new fitter in order to increase the efficiency of the vertex re-construction performance. Because the number of hit PMTs becomes small in low energy region, current fitting tool has no enough performance in the energy region of 4.5∼5.0 MeV. All reduction methods are optimized in order to analyze 4.5 MeV energy bin. Then, the remaining backgrounds are reduced as much as possible keeping the maximum signal significance for the background.

A special mentioned thing is that the new reduction for 4.5 MeV energy bin analysis has been developed by blind analysis in this time in order to remove the bias for the solar neutrino signal extraction. In the optimization of new reduction tool, we did not confirm the $\cos_{\theta_{sun}}$ distribution. After the all tight data reduction, we opened the data and saw the $\cos_{\theta_{sun}}$ distribution for the first time.

### 8.1.1 Tight cut

First, tight cut is applied the data sample after general data reduction. The remaining background events are removed in this stage basically. The applied reduction is based on the general data reduction optimized to 4.5 MeV analysis. First of this stage, the basic data set is made in order to collect useful 4.5∼5.0 MeV data, then applied the various reductions for remaining background.

#### Trigger efficiency cut

A trigger efficiency cut makes the basic data set for 4.5∼5.0 MeV energy region. The SLE analysis was started from May 5th in 1997. The analysis threshold is set 5.0 MeV for all SLE analysis. The trigger efficiency for 5.0 MeV data in the SLE analysis is more than 95%. However, the trigger efficiency for the 4.5 MeV data has no enough efficiency in the beginning of the SLE analysis. The trigger thresholds of SLE analysis were changed seven times during SK-I data taking. The changing periods and the thresholds are already explained in chapter 3. Therefore, the trigger threshold of 260 mV and 250 mV has no enough efficiency for 4.5 MeV data because of the high threshold. Table 8.1 explains the summary of the trigger efficiency from 4.5 to 5.0 MeV and the energy of the trigger efficiency 50% and 100% for each trigger threshold. The trigger thresholds are calculated using solar neutrino MC. Figure 8.1 shows the run progress of the trigger threshold for 50% and 95% of trigger efficiency estimated by the solar neutrino MC. The empty circle and filled circle shows the progress of the trigger threshold for SLE trigger efficiency 50% and LE trigger efficiency 50% respectively in the right figure. Otherwise, the left figure shows the run progress of the trigger efficiency 95%.

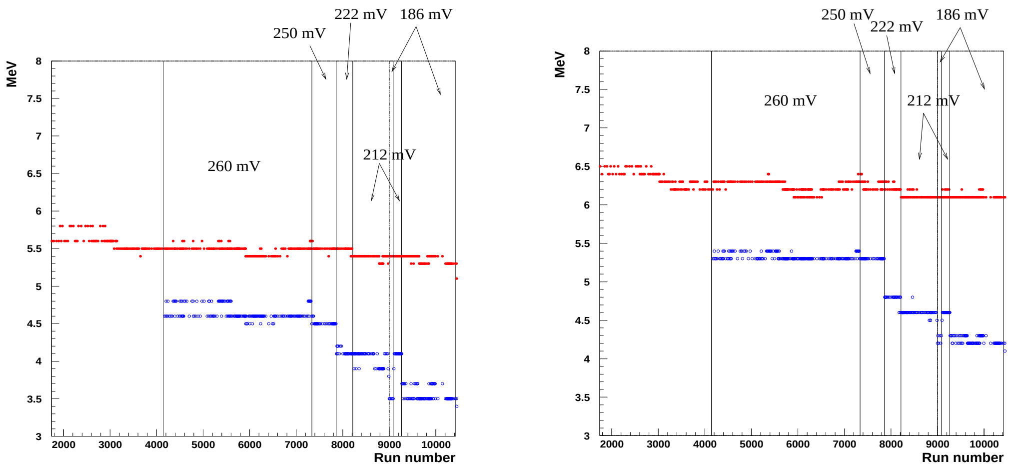

Figure 8.1: The run progress of the trigger threshold for 50% and 95% of trigger efficiency.

| SLE trigger threshold | Average of trigger efficiency from 4.5 to 5.0 MeV | Energy of trigger efficiency ( 50%/100%) |
|---|---|---|
| 260 mV | 60% | 4.7 MeV/5.5 MeV |
| 250 mV | 70% | 4.5 MeV/5.3 MeV |
| 222 mV | 95% | 4.2 MeV/4.8 MeV |
| 212 mV | 97% | 3.9 MeV/4.6 MeV |
| 186 mV | 100% | 3.5 MeV/4.3 MeV |

Table 8.1: The summary of the trigger efficiency from 4.5 to 5.0 MeV and the energy at the trigger efficiency of 50% and 100% for each trigger threshold.

Figure 8.2 shows the run progress of the trigger efficiency estimated by the solar neutrino MC. The empty circle and filled circle shows the progress of the SLE trigger efficiency and LE trigger efficiency from 4.5 to 5.0 MeV respectively. The progress sometimes fluctuates because of the fluctuation of the water transparency.

From above results, the useful 4.5 MeV data which has enough trigger efficiency more than 95% started from the SLE trigger threshold of 222 mV. The remaining live-time after this trigger efficiency cut is 566 days. This data set is the most basic data set including useful data from 4.5 to 5.0 MeV.

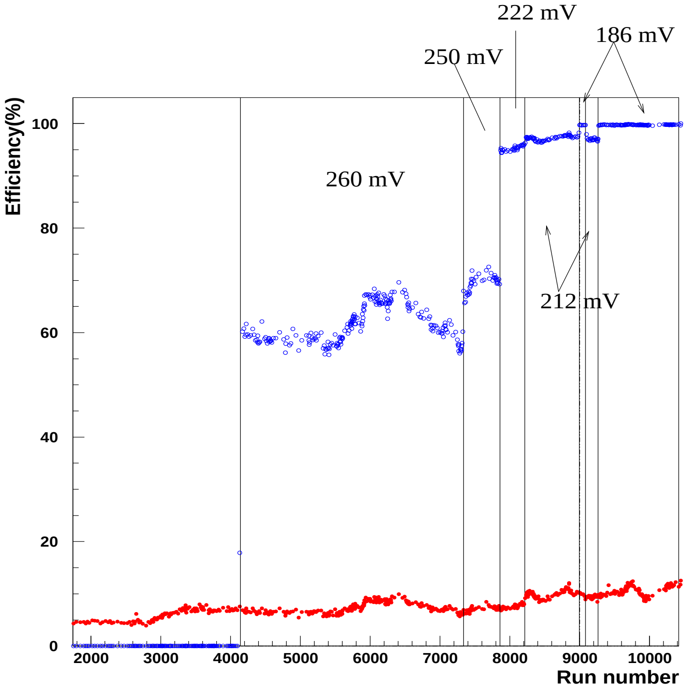

Figure 8.2: The run progress of the trigger efficiency estimated by the solar neutrino MC.

### Radon high rate run cut

After the trigger efficiency cut, the radon high rate run cut is applied to 566 days data set by a run unit. In chapter 7, the high event rate in low energy region was occurred by the large convection in the SK tank when the circulating water was supplied from the top of the tank. The data in the period is bad quality because there are many radon events in the fiducial volume coming from the wall PMT. Figure 8.3 shows the progress of the background event rate (event/day) from 4.5 to 6.5 MeV in fiducial volume of 22.5 ktons after trigger efficiency cut. The background event rate means events per day in less than 0.8 of $\cos\theta_{sun}$ distribution. The switching points of the trigger thresholds are also drawn by the solid lines. There are some jumpings of the event rate. The jumpings of the event rate from 4.5 to 6.0 MeV are due to radon background transferring from the wall PMTs by the large convection in the SK tank. Figure 8.4 shows the event rates for each energy region, which are from 4.5 to 5.0, from 5.0 to 5.5, from 5.5 to 6.5 and from 6.5 to 20.0 MeV from top figure. From this figure, the fluctuation of the event rate in low energy region from 4.5 to 5.0 MeV is mainly caused by the fluctuation in the energy region from 4.5 to 5.0 MeV which includes the dominant background source of radon.

Because the most of the events in the fluctuating periods were the radon events and it is difficult to extract the solar neutrino events in the data, the radon high rate data is removed by run unit. The rejected runs are selected by judging whether the event rate is over a event rate threshold. The event rate threshold is defined by searching the maximum significance which is

$$Significance = \frac{\text{Total solar neutrino events w/o high event rate run}}{\text{Total background events w/o high event rate run}}. \tag{8.1}$$

The background events are the events which are distributed in less than 0.8 of $\cos\theta_{sun}$ distribution. Assuming the solar neutrino event rate is constant in the all period of the data set, solar neutrino events are in proportion to the live time of a run.

$$\text{Solar neutrino events}_{run} \propto \text{Live time}_{run} \tag{8.2}$$

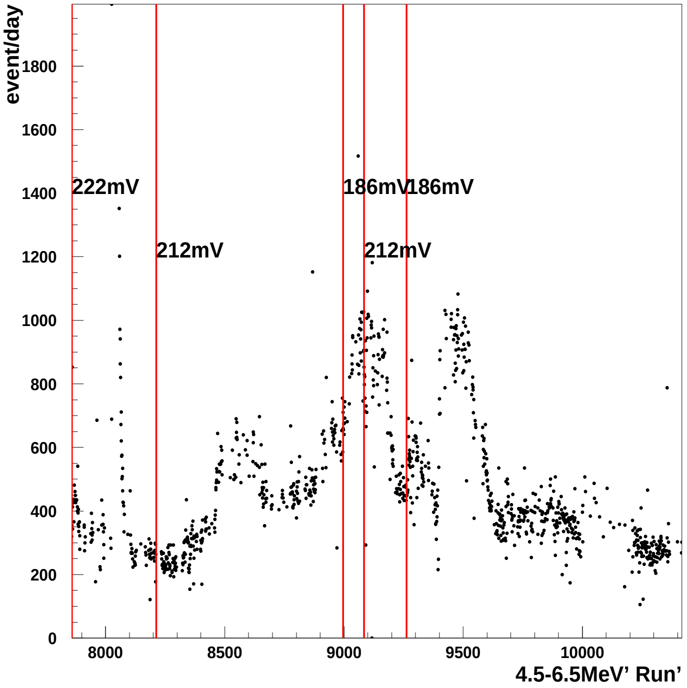

Figure 8.3: The progress of the background event rate (events/day) from 4.5 to 6.5 MeV.

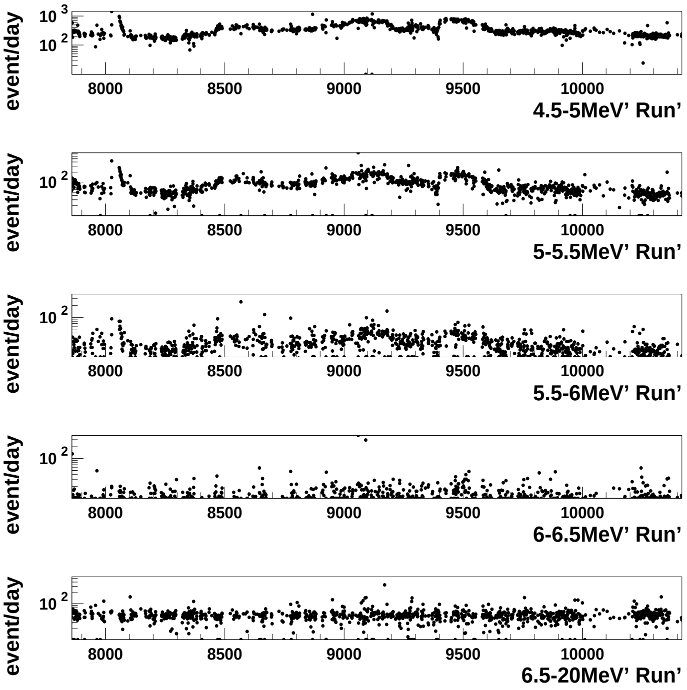

Figure 8.4: The event rates for each energy region.

$$Significance = \frac{\text{Total Live time w/o high event rate run}}{\text{Background events w/o high event rate run}}. \tag{8.3}$$

The event rate threshold is searched by maximizing the calculated significance without the high event rate run which is over the event rate threshold.

$$Significance = \frac{\sum_{i=1}^{n_{run}} T_i}{\sum_{i=1}^{n_{run}} N_i} \tag{8.4}$$

where $n$ is the number of runs whose event rate are less than the event rate threshold, $i$ is the run number, $T$ is the live time of a run, $N_i$ is the number of background events of the run whose event rate is less than a event rate threshold. The maximum significance search was applied for the energy region from 4.5 to 5.0 MeV. Figure 8.5 shows the progress of the background event rate (events/day) from 4.5 to 5.0 MeV. The decided event rate threshold of 597.0 events per day was shown by a solid line. After this radon high rate run cut, the remaining live-time is 511.5 days. In this calculation, for the all events including solar neutrino events without the bias of $\cos\theta_{sun}$ distribution, the event rate threshold is searched by the same method. The result of the event rate threshold for all events is 795.2 events per day. The remaining live-time is 511.7 days. The both results are consistent. So, in this reduction, there is no systematic bias. This data set after radon high rate run cut is the final data set for 4.5 MeV data analysis.

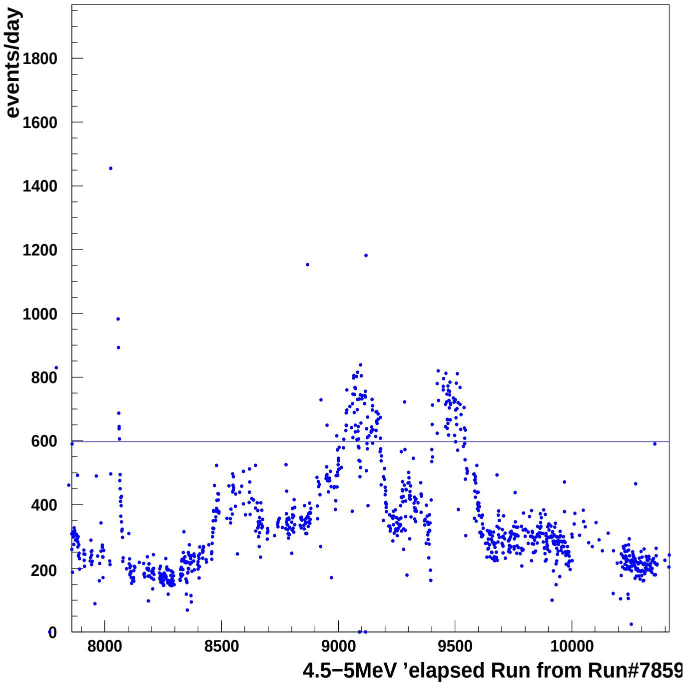

Figure 8.5: The progress of the background event rate (events/day) from 4.5 to 5.0 MeV and the decided event rate threshold of 597.0 events/day.

### Strong gamma cut

After the radon high rate run cut, the strong gamma cut is applied to the final data set. From this reduction step, the various cuts are applied by the event by event. The definition of the gamma cut is explained in chapter 6. In this section, the optimization of the strong gamma cut to the 4.5 MeV data analysis is explained. The default gamma cut is optimized to the SLE region from 5.0 to 6.5 MeV and to the LE region from 6.5 to 20.0 MeV. The distance of the gamma cut from the wall for the LE and the SLE region are 4.5 m and 8.0 m respectively.

However, the external $\gamma$ rays from the wall materials are remaining in the energy region from 4.5 to 5.0 MeV. So, the distance of the gamma cut is optimized to the energy region from 4.5 to 5.0 MeV by the maximum significance search. The significance is defined by the following formulation.

$$Significance = \frac{\text{Remaining solar neutrino events after gamma cut}}{\sqrt{\text{Remaining background events after gamma cut}}} \tag{8.5}$$

Solar MC is used as the solar neutrino events. The events distributed in less than 0.8 of $\cos\theta_{sun}$ distribution is used as the background events. The distance which make the significance maximal is the best cut point. The distance optimized to 4.5 MeV data is 9.7 m.

Figure 8.6 shows the significance result for the distance of the gamma cut. The significance for the distance from 0.0 to 8.0 m is 0 because the gamma cut is already applied by the default value. At the distance of 9.7 m, the significance becomes maximum remarkably. Figure 8.7 shows the vertex $R^2$ distribution in the energy region from 4.5 to 5.0 MeV at each distance of the gamma cut. The distances are 8.0 m, 9.0 m and 10.0 m from the top figure respectively. There is abnormal peak at the $R^2$ from $500\times10^3$ to $1000\times10^3$ for the distance of 8.0 m. However, after 10 m gamma cut, the abnormal peak is removed completely by the strong gamma cut. The strong gamma cut is applied for all energy region by this gamma cut distance.

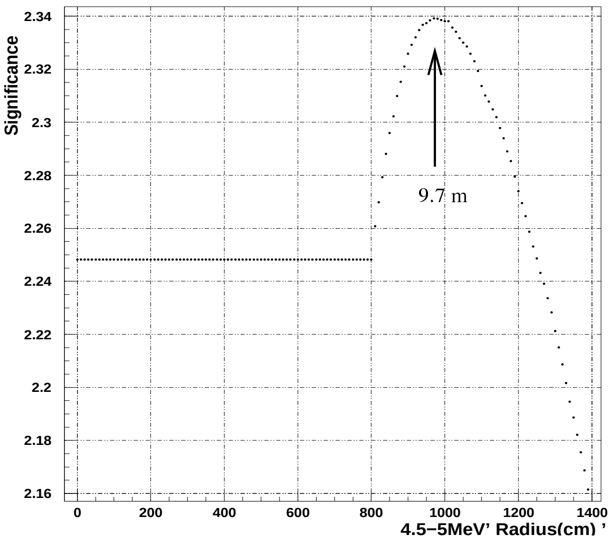

Figure 8.6: The significance results for the gamma cut distance.

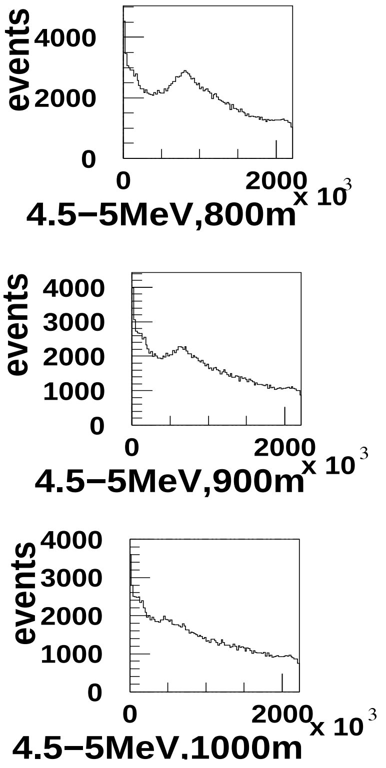

Figure 8.7: The vertex $R^2$ distribution in the energy region from 4.5 to 5.0 MeV for each gamma cut distance.

### Strong goodness stability cut

The definition of the goodness stability cut (GRINGO cut) is also already explained in chapter 6. So, in this section, the optimization to the energy region from 4.5 to 5.0 MeV data is explained. The criterion of the GRINGO cut is optimized to the energy above 5.0 MeV. The default value of the criterion is 0.08 for ratio of number of failed point over number of grid point. In the lower energy region from 4.5 to 5.0 MeV, because the number of hit PMTs is smaller than it in the energy region above 5.0 MeV, the number of mis-fit event becomes large. So, the cut criterion need to be re-optimized to the energy region from 4.5 to 5.0 MeV.

The optimization was done by searching the maximum significance after the GRINGO cut. The significance is defined by the following formulation which is same as the strong gamma cut.

$$Significance = \frac{\text{Remaining solar neutrino events after GRINGO cut}}{\sqrt{\text{Remaining background events after GRINGO cut}}} \tag{8.6}$$

Solar neutrino events are the events of the solar neutrino MC after the GRINGO cut. The background events are the events distributed in less than 0.8 of $\cos\theta_{sun}$ distribution after the GRINGO cut. Figure 8.8 shows the significance plots with the GRINGO cut value which is ratio of number of failed point over number of grid point. The horizontal axis is the GRINGO cut value. The significance becomes maximum at the GRINGO cut value of 0.031.

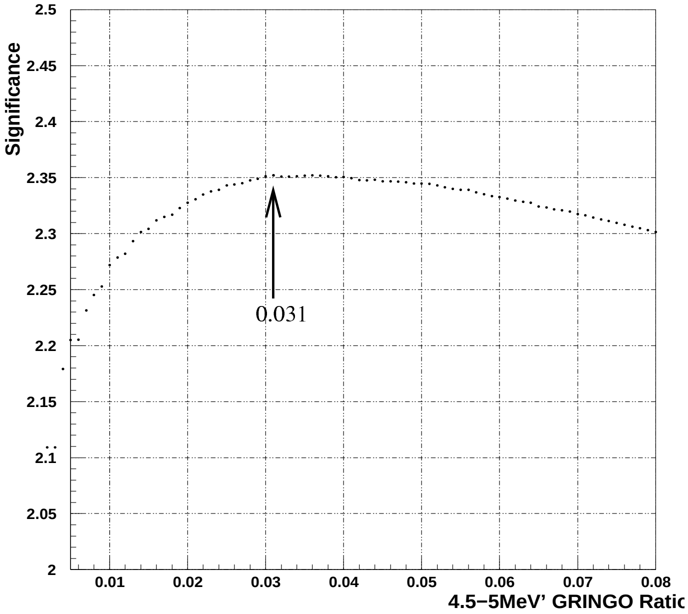

Figure 8.8: The significance plots for the GRINGO cut value.

Figure 8.9 shows the vertex distribution before and after the strong GRINGO cut of 0.031. The left figure is the $R^2$ vertex distribution and the right figure is the Z vertex distribution. The histogram is the vertex distribution before the strong GRINGO cut and the hatched region is the vertex distribution after the strong GRINGO cut. From the figures, the mis-fit events are removed for all vertex area uniformly.

### Tight Fiducial Volume cut

The fiducial volume is determined 22.5 ktons at 2 m from the wall in the general data reduction. However, the background events from the wall, for example, a external $\gamma$ ray from detector materials and radon , are remaining near the edge of the fiducial volume and the bottom region of the tank which is caused by the small convection by the water supply from the bottom. It is difficult to remove remaining events by the event by event. So, the best fiducial volume is re-estimated for the energy region from 4.5 to 5.0 MeV. The best fiducial volume is determined by the best radius and best height of the tank. The best parameter of the fiducial volume is searched by using the significance maximum after the fiducial volume cut. The best cut

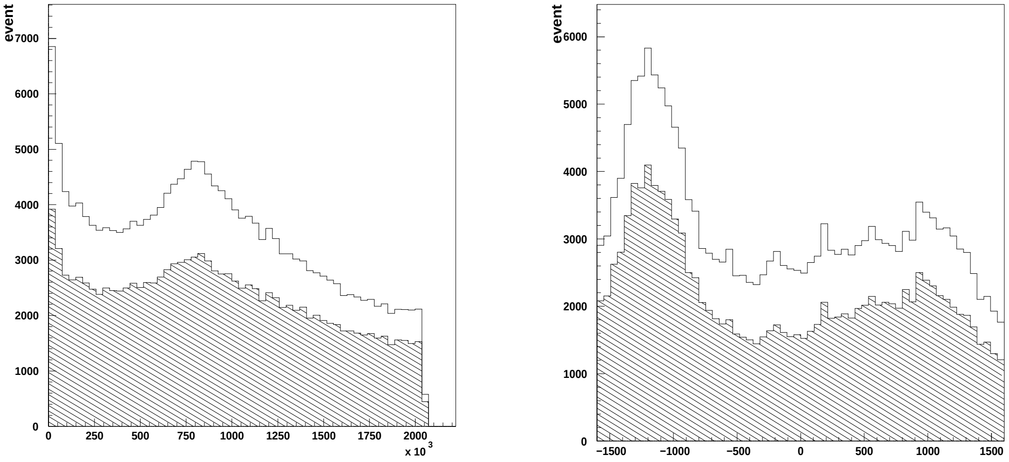

Figure 8.9: The vertex distribution before and after the strong GRINGO cut of 0.031.

parameter for the height and the radius of the tank is searched independently. Specially, for the height parameter, the height is separated with the bottom region and the top region of the tank. The significance is ratio between the solar neutrino events and the sqrt of the background events which is same definition as the gamma cut and the GRINGO cut.

The summary of the best parameters of the fiducial volume are shown in table 8.2. The values are optimized to the energy region from 4.5 to 5.0 MeV. The default value is also explained in the parenthesis of the table.

| Parameter | Region | Values(cm) |
|---|---|---|
| Radius | -1610<Z<1610 | 1430 (1490) |
| | -1619<Z<-1000 | 1490 (1490) |
| | -1000<Z<-500 | 1410 (1490) |
| | -500<Z<0 | 1380 (1490) |
| | 0<Z<500 | 1360 (1490) |
| | 500<Z<1000 | 1430 (1490) |
| | 1000<Z<1610 | 1480 (1490) |
| Height from center to bottom | 4.5<E<5.0 | 1100 (1610) |
| | 5.0<E<5.5 | 1160 (1610) |
| | 5.5<E<6.0 | 1590 (1610) |
| | 6.0<E<6.5 | 1590 (1610) |
| Height from center to top | 4.5<E<5.0 | 1580 (1610) |
| | 5.0<E<5.5 | 1590 (1610) |
| | 5.5<E<6.0 | 1590 (1610) |
| | 6.0<E<6.5 | 1590 (1610) |

Table 8.2: The summary of the best parameters of the fiducial volume cut.

From the summary, the estimated best radius is the 1430 cm for all volume in the energy from 4.5 to 5.0 MeV. As a reference, the best radiuses for each height of the SK tank are also shown in the table. Except for the center, the radius cut is not required the tight value. The center region is required the tight value because of the remaining external $\gamma$ rays from the wall, top and bottom materials. The left side of figure 8.10 shows the vertex distribution of $R^2$ and the best radius is also drawn by a solid line. The events outer of the best radius are removed.

The best heights for the energy region from 4.5 to 5.0 MeV are -1100 cm from the center in the bottom region and +1590 cm from the center in the top region. The right side of the figure 8.10 shows the vertex distribution for the tank height and the best height is also drawn by a solid line. In above 5.5 MeV, the best height is no asymmetry for the top and bottom region. However, in lower energy region, the best height produces the asymmetry because of the accumulation of the radon in bottom region. So, if the best height is optimized to the energy region from 4.5 to 5.0 MeV, the asymmetry cut is needed. In this thesis, we want to analysis day and night spectrum as possible. Therefore, the fiducial volume is not optimized to the height of the tank.

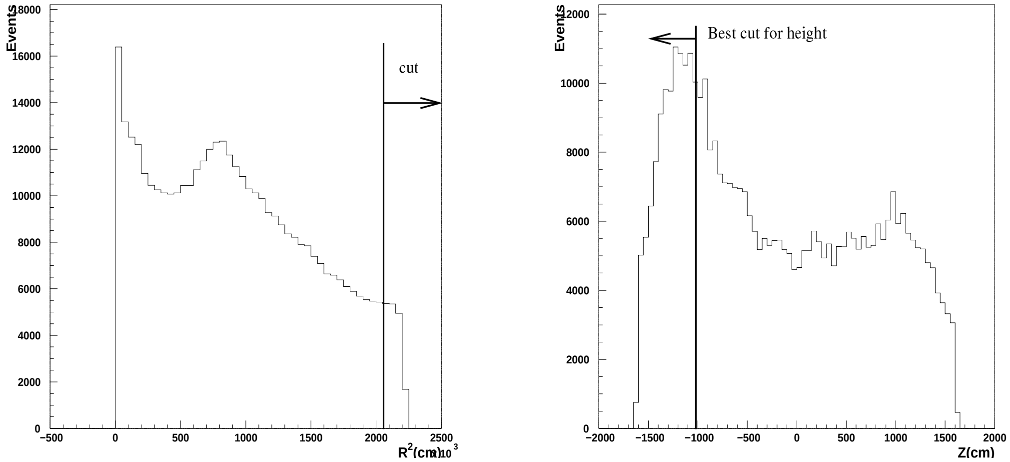

Figure 8.10: The vertex distribution of R$^2$ with the best radius cut is shown in left plot. The vertex distribution of the tank height with the best height cut is shown in right plot.

### The noise cut from the water pipe

In the background study, the abnormal event accumulation was found in the center of top of the SK tank. The energy distribution of the events are from 4.5 to 5.5 MeV. These events have a strong correlation with the position of the water pipe which was used for supplying of the water from the center of the top of the tank. So, it is supposed that the events are like $\gamma$ rays from the pipe. Figure 8.11 shows the vertex distributions in 2 dimensions (x versus y cm) from 4.5 to 5.0 MeV. The right plot is the distribution of the bottom, and the left plot is the top. The upper figures are the 3 dimensional plots, and the lower figures are plane plots. In the bottom and top distributions, the abnormal peak exists in the really center position of the tank. The mis-fit events are accumulated in the center position. But, in the top figure, in the slightly shifted position from the center around x = 100 and y = -400, there are some accumulated events. The position is almost consistent with the water pipe position (x = 50 and y = -400 cm).

Therefore, the events around the water pipe were removed. The criterion is that the events inner of the square of 3 m around the water pipe were rejected. After this cut and the best fiducial volume cut, the fiducial volume changed from 22.5 ktons to 20.5 ktons.

## 8.1.2 New fitting cut

In chapter 4, the event reconstruction methods were explained. Now, the basic principle is shown again. The vertex point is searched by the chi square testing assuming a Gaussian distribution for the true vertex point. The definition of the *goodness* function for the testing is as follows.

$$goodness = \sum_{i=1}^{N_{hit}} \exp(-\frac{\Delta t_i(x,y,z)^2}{2\sigma_i^2}) \tag{8.7}$$

$$\Delta t_i(x,y,z) = t_i - tof_i(x,y,z) - t_0 \tag{8.8}$$

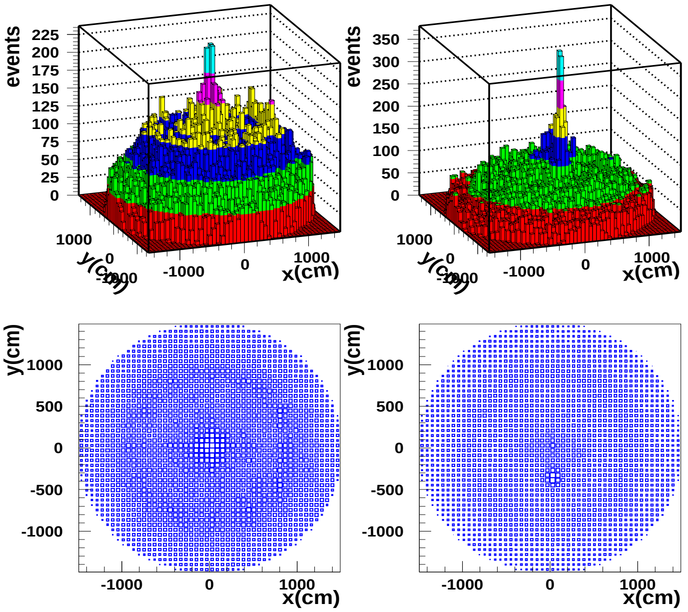

Figure 8.11: The vertex distribution in 2 dimensions (x versus y cm) from 4.5 to 5.0 MeV.

where (x,y,z) is the positions of grid points, $\Delta t_i$ is the residual time of i-th hit PMT, $t_i$ is the time of the i-th hit PMT, $tof_i$ is the time of flight of i-th hit PMT, $t_0$ is the mean time of the distribution of $\Delta t_i$.

In this vertex reconstruction, the important assumption is that the distribution of the hit PMT is the Gaussian distribution. However, in the low energy region, 5.0 MeV, the expected number of hit PMTs is about 30. So, the small number of hit PMTs in the lower energy region gives the wrong vertex point sometimes. The current vertex reconstruction does not work well in the energy region from 4.5 to 5.0 MeV (below about 25 signal hits). In SK-I data set, there are some mis-fit events in the lower energy region from 4.5 to 5.0 MeV. The most of these events are the $\gamma$ rays. So, if the corrected vertex point is given, the gamma like events can be removed combining with the general data reduction tools. In this thesis, the new vertex reconstruction method was tried for the SK-I 4.5 MeV data set in order to improve the above problems.

The new developed vertex reconstruction tool is named BONSAI (Branch Optimization Navigating Successive Annealing Iterations) fitter from now on. The hit selection of the BONSAI fitter is same as the before vertex reconstruction of the cluster fitting in chapter 6. The definition of *goodness* is different from the current vertex reconstruction in order to treat small number of hit PMTs. The *goodness* is defined by the following formulation.

$$goodness = \log(\prod_{i=1}^{N_{hit}} pdf(\Delta t_i(x,y,z)) \tag{8.9}$$

$$\Delta t_i(x,y,z) = t_i - tof_i(x,y,z) - t_0 \tag{8.10}$$

where $\Delta t_i$ is same definition as the before vertex reconstruction, *pdf* is the probability density function. The *goodness* is the log timing likelihood function for the Poisson distribution. At the maximum *goodness*, the vertex point gives the correct information.

However, sometimes, the reconstructed vertex point agrees with the local maximum point. So, the BONSAI fitter searches a tree tracing all branches for a range of the likelihood. This principle is the origin of the name. The technical order to search the starting point to search the true vertex point are as follows.

1. Hit selection using cluster fitting method.

2. Time ordering of the hit.
3. Use the four suitable combination in order to search the start position of searching true vertex position. The results of each combination gives the two or three candidates.
4. Use the best vertex point which has the maximum likelihood.

After above preparing, the search of the true vertex point starts from the starting point. In the current vertex reconstruction, the grid point is used and the fitting is applied to all $\Delta t_{i,j}$ for the pairs of the hits when the fitter searches the true vertex point. However, BONSAI fitter does not do that.

Figure 8.12 shows the performance of the BONSAI vertex reconstruction in the energy region from 4.5 to 5.0 MeV. The right side plot of the upper figures is the x vertex distribution, and left side is the y vertex distribution. In the lower figures, the right side is the z vertex distribution, and the left side is the $\mathrm{R}^2$ vertex distribution. The histograms are the results by the current vertex reconstruction. The hatched areas are the results by the BONSAI vertex reconstruction. The some events exist outer of the fiducial volume as a result of the correction of the vertex point. Especially, in the $R^2$ distribution, the mis-fit events accumulated in the center of the tank are reduced and the remaining external $\gamma$ ray at $R^2 \sim 500$ is also reduced.

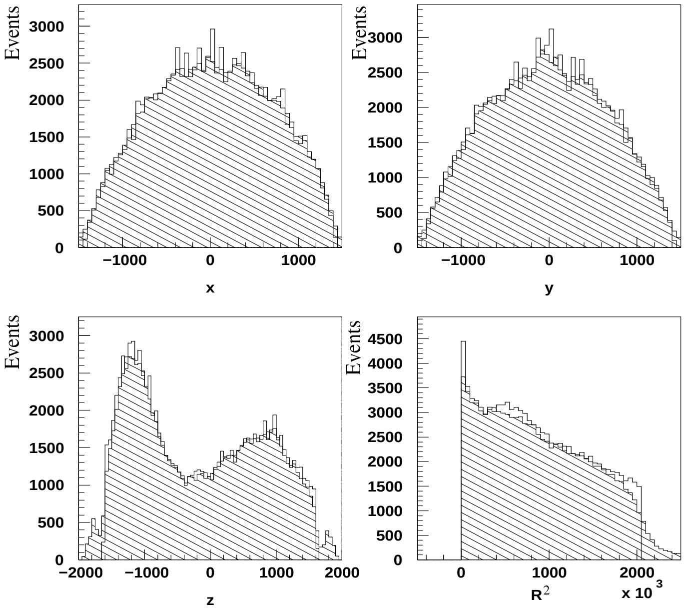

Figure 8.12: The performance of the BONSAI vertex reconstruction in the energy region from 4.5 to 5.0 MeV.

Figure 8.13 shows the difference of the vertex position between current fitter and BONSAI fitter. The number of events which has the difference less than 2.0 m are 85% for the total events.

We applied the some reduction which has an effect on the $\gamma$ ray using the new reconstructed vertex information by BONSAI fitter. The used reductions are PATLIK cut, strong gamma cut and fiducial volume cut. First of all, we searched the best combination of the cuts. Figure 8.14 shows the reduction efficiency for each reductions. The empty circles are the reduction efficiencies of the data and the filed circles are the reduction efficiencies of the solar neutrino MC. The data is extracted from less than 0.8 of the $\cos\theta_{sun}$ distribution as background events. The large difference between data and MC means that the reduction is optimized to the background reduction well. The left plot shows the reduction efficiency for the single reduction of fiducial cut (F), Gamma cut (G) and PATLIK cut (P). The right plot shows the reduction efficiency for

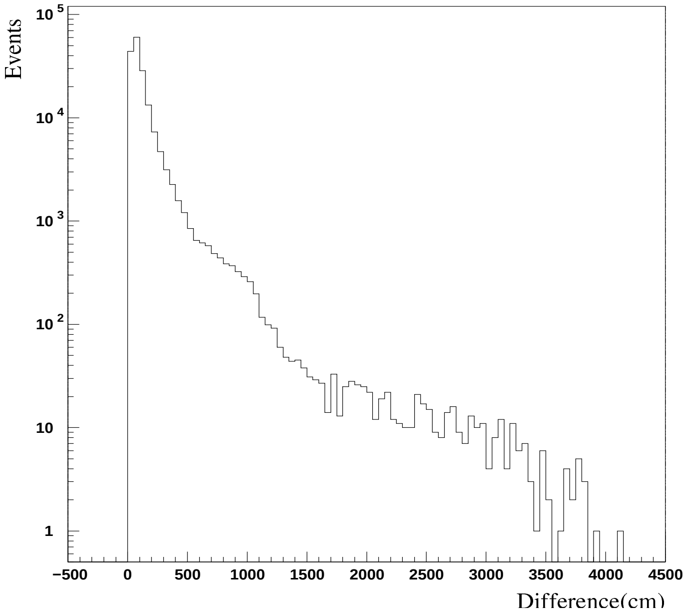

Figure 8.13: The difference of the vertex position between current fitter and BONSAI fitter.

the combination cut. The largest reduction efficiency appears when using the three combination cuts. Table 8.3 shows the summary of the reduction efficiency for the MC. Therefore, the three reductions were applied to the data set with new vertex information by BONSAI fitter.

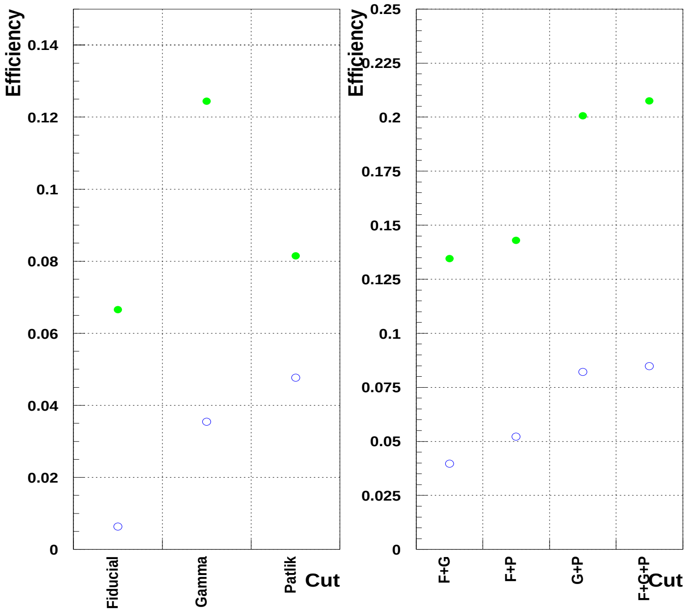

Figure 8.14: The reduction efficiencies for each reduction using BONSAI vertex.

Figure 8.15 shows the $R^2$ and Z vertex distribution before and after the three reductions using the BONSAI vertex information in energy region from 4.5 to 5.0 MeV. The hatched area shows after reductions and the histogram is before reductions. Basically, the events are uniformly reduced for all vertex area. The remarkable reduction is seen in the left figure of the $R^2$ vertex distribution. The mis-fit events accumulated in the center of the tank by current vertex reconstruction tool are reduced remarkably. Figure 8.16 shows the direction distribution before and after the three reductions using BONSAI vertex information in energy region from

| Cut | reduction efficiency for MC |
|---|---|
| Fiducial volume cut (F) | 6 % |
| Gamma cut (G) | 9.2 % |
| PATLIK cut (P) | 3.6 % |
| F+G | 9.9 % |
| F+P | 9.6 % |
| G+P | 12.9 % |
| F+G+P | 13.4 % |

Table 8.3: The summary of the reduction efficiencies for the solar neutrino events using BONSAI vertex.

4.5 to 5.0 MeV.

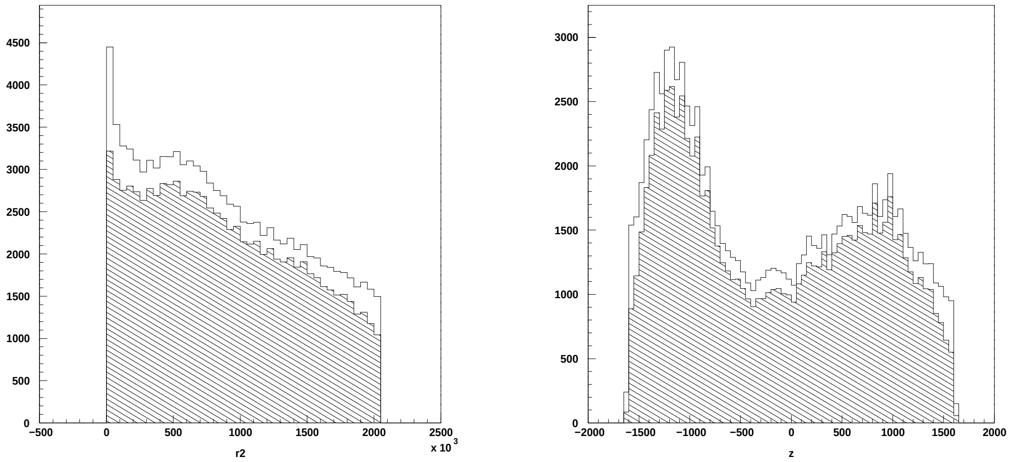

Figure 8.15: The $R^2$ and Z vertex distribution before and after the three reductions using BONSAI vertex information in energy region from 4.5 to 5.0 MeV.

## 8.2 Monte Carlo simulation of the solar neutrino events

In order to estimate the reduction efficiency of the solar neutrino signal, the whole analysis chain was applied to the solar neutrino MC events. The solar neutrino MC events are generated 10 events per minute along the solar neutrino analysis live-time for $^8$B neutrinos and hep neutrinos, which corresponds to 51 times of the event rate predicted by BP2000 (284.4 events/day), in the inner volume (32 ktons).

## 8.3 Summary and Data quality

Table 8.4 shows the summary of the reduction steps. The number is the number of the remaining events after each reduction. The reduced rate means the reduction efficiency simply calculated from the ratio between before and after each reduction. After all reductions, the remaining events are 141539 events (20% remaining for first entries).

Figure 8.17 shows the energy distribution for each reduction step, which are first entries, after the tight cut and after the new fitting cut.

Figure 8.18 shows the energy distribution of the S/N ratio for each reduction step. The S/N ratio is calculated from the ratio between the data and MC results after each reduction step for

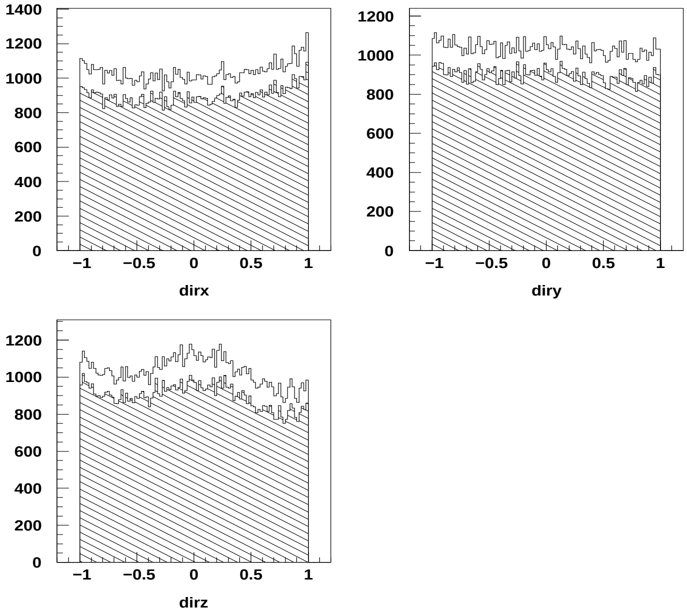

Figure 8.16: The direction distribution before and after the three reductions using BONSAI vertex information in energy region from 4.5 to 5.0 MeV.

| | Reduction step | Real Data | MC data | Reduced rate of Data |
|---|---|---|---|---|
| first | all events | 692556 | 3544686 | |
| Tight cut | Trigger efficiency cut | 385640 | 1413144 | 44% |
| | Radon high rate run cut | 313406 | 1277429 | 19% |
| | Strong GAMMA cut | 298099 | 1235504 | 5% |
| | Strong GRINGO cut | 226988 | 995836 | 24% |
| | Best F.V R cut | 175758 | 917912 | 23% |
| | Water Pipe cut | 173012 | 908809 | 1.5% |
| | final number of events | 173012 | 908809 | 75% |
| New fitting cut | F.V cut | 163953 | 895709 | 12% |
| | PATLIK cut | 151432 | 854918 | 8% |
| | Strong GAMMA cut | 141539 | 819050 | 7% |
| | final number of events | 141539 | 819050 | 80% |

Table 8.4: The table of the reduction steps. 'MC data' is the solar neutrino MC simulation in the energy range of 4.5∼20.0 MeV in the 20.5kt fiducial volume.

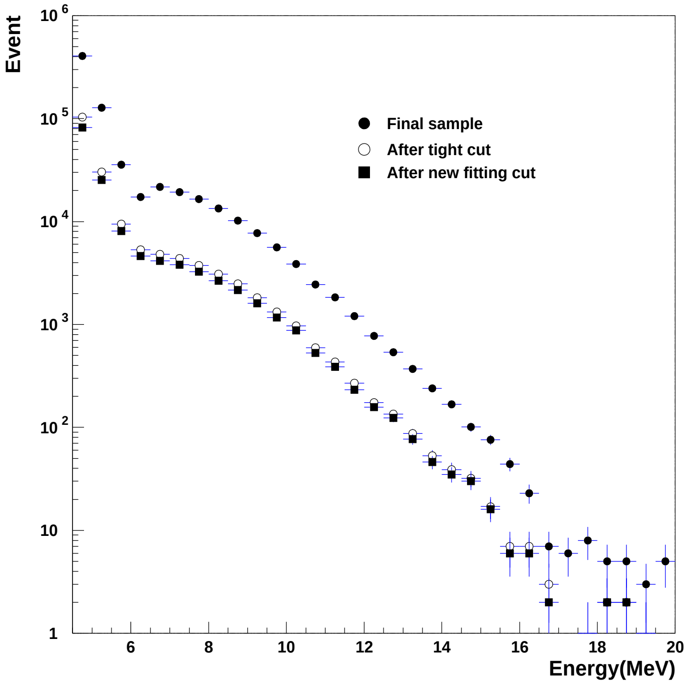

Figure 8.17: The energy distribution for summarized reduction steps of first entries, after the tight cut and after the new fitting cut.

the second entries which is after the trigger efficiency cut. The S/N ratio from 4.5 to 5.0 MeV increased by a factor of about 1.9 for the second entries. Since the S/N ratio was improved remarkably in the low energy region, the optimization to reduce the background events in the low energy region is done well. The improvement of the data quality for the second entries is +53% (the background events are reduced by 53%).

We estimated the improvement of the data quality for the first entries from the following calculation of the S/N ratio and the Significance values.

$$\text{S/N ratio} = \frac{\text{Signal(Solar MC after all reductions)} \times \text{Oscillation factor}}{\text{Data(Data } \cos\theta_{sun} < -0.8 \text{ after all reductions)}} \tag{8.11}$$

$$\text{Significance} = \frac{\text{Signal(Solar MC after all reductions)} \times \text{Oscillation factor}}{\sqrt{\text{Data(Data } \cos\theta_{sun} < 0.8 \text{ after all reductions)}}} \tag{8.12}$$

where the oscillation factor is the following equation.

$$\text{Oscillation factor} = \frac{284.4\text{[events/day]}}{24. \times 60. \times 10.} \times 0.465 \tag{8.13}$$

The value of 0.465 is the official number of the data over SSM in SK-I. Table 8.5 shows the summary of the calculation results in the energy region from 4.5 to 5.0 MeV. If it is assumed the only background events are reduced after all reductions, the improvement of the data quality for the first entries is +25% (the background events are reduced by 25%).

Figure 8.19 shows the vertex distribution in the energy region from 4.5 to 5.0 MeV after all reductions. Figure 8.20 shows the direction distribution in same energy region as vertex distribution. The histogram means before the tight data reduction, and the hatched area means the after all reductions. The tight data reduction reduced the events uniformly. Especially, in the $R^2$ distribution, the reductions have an effect on the mis-fit events in the center of the

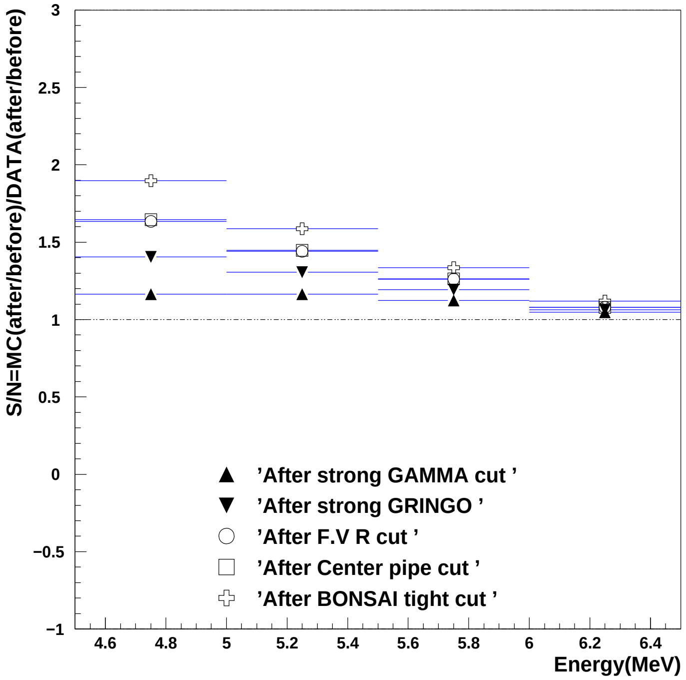

Figure 8.18: The energy distribution of the S/N ratio for each reduction step.

| Cut | SK-I 1496 days data | 511 days data |
|---|---|---|
| S/N | 0.06 | 0.08 |
| Significance | 2.70 | 2.74 |

Table 8.5: The summary of the calculation results for the S/N ratio and the significance in the energy region from 4.5 to 5.0 MeV.

tank and the remaining $\gamma$ ray around the $R^2 = 500 \sim 1000$. This reduction performance for $\gamma$ ray is appeared in the direction distributions. The events from wall materials were reduced remarkably.

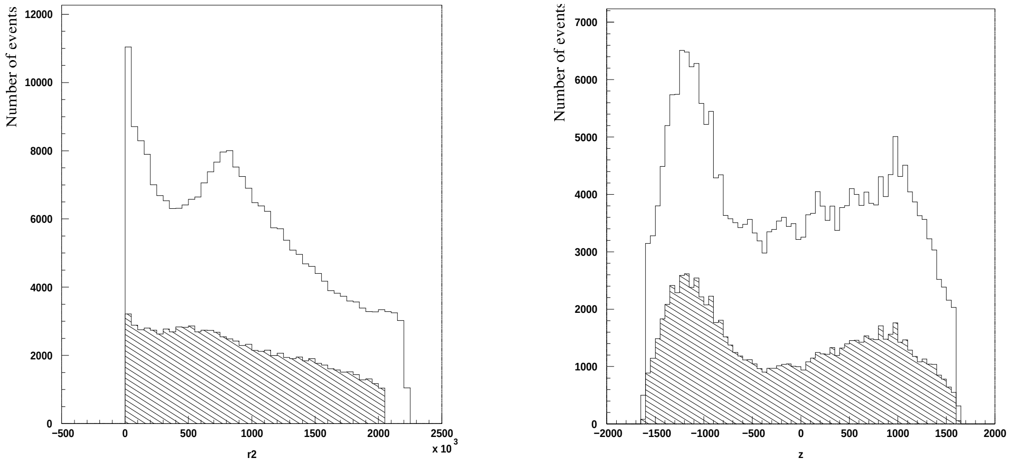

Figure 8.19: The vertex distribution in the energy region 4.5 to 5.0 MeV after all reductions.

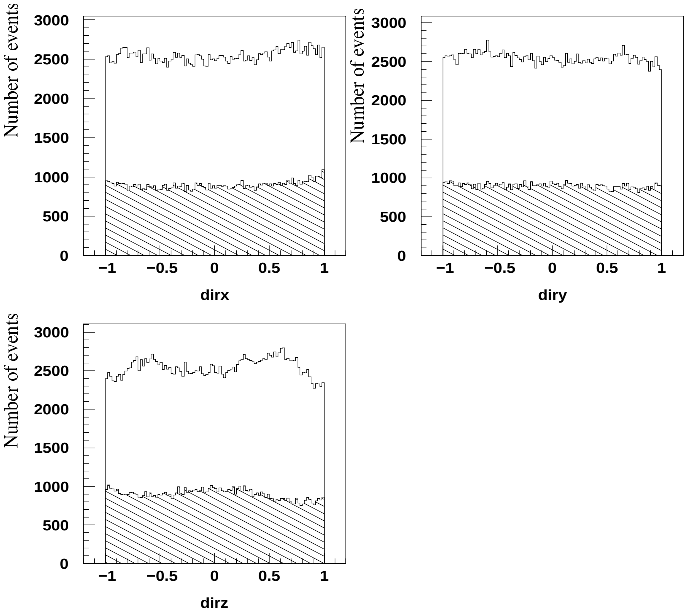

Figure 8.20: The direction distribution in the energy region 4.5 to 5.0 MeV after all reductions.

## 8.4 Remaining background

In Z distribution, there are remaining radon events transported from bottom PMTs by the convection of water supply. This is exactly the pure radon background after all reductions. However, if it is assumed that the distribution of the top region is applicable to the bottom region, the ratio for background contamination looks like small. In the future, one can hope these events will be reduced by the controller system of the water convection.

The final estimation of the radon concentration in bottom region is shown in table 8.6 based on above assumption. The calculation is done as follows.

$$\text{Radon concentration} = \frac{\mathrm{N_{bottom}[events]} - \mathrm{N_{top}[events]}}{\mathrm{F.V./2[ton]} \times \text{Live Time[day]} \times \text{Rn detection efficiency}[\frac{\mathrm{mBq/m^2}}{\mathrm{events/day/ton}}]} \quad (8.14)$$

where $\mathrm{N_{bottom}}$ is the remaining events in the bottom region under the center of the tank. $\mathrm{N_{top}}$ is the remaining events in the top region above the center of the tank. F.V. means the fiducial volume which is 20.5 ktons in this analysis. Rn detection efficiency which is the radon observed rate in the SK tank is estimated as follows.

$$1.0[\mathrm{mBq/m^3}] = 0.0074[\mathrm{events/day/ton}] \quad (8.15)$$

The radon detection efficiency depends on the trigger threshold. The estimated value is the averaged number by weighting the live time of each trigger threshold for each radon detection efficiency in each trigger threshold. The radon detection efficiencies for another hardware trigger thresholds without the tight data reduction in all volume of the SK tank are shown in table 8.7.

| Data set | F.V. | Live-time | Efficiency | Radon conc. |
|---|---|---|---|---|
| SK-I 566 days data<br>(only trigger efficiency cut) | 22.5 ktons | 566 days | 0.0074 | - |
| SK-I 511 days data<br>(after all reduction) | 20.5 ktons | 511 days | 0.0027<br>(0.0074×0.37) | 1.52±0.03 $\mathrm{mBq/m^3}$ |

Table 8.6: The summary of the expected radon concentration in the bottom region of the SK tank in the energy region from 4.5 to 5.0 MeV. The value of 0.37 is the reduction efficiency of the tight data reduction.

| Run period | Hardware trigger threshold | Radon detection efficiency for 1.0$\mathrm{mBq/m^3}$ |
|---|---|---|
| May. 1997∼ | -260mV,-250mV | 0.0050[events/day/ton] |
| Sep. 1999∼ | -222mV | 0.0057[events/day/ton] |
| Dec. 1999∼ | -212mV | 0.0065[events/day/ton] |
| Sep. 2000∼ | -186mV | 0.0086[events/day/ton] |

Table 8.7: The radon detection efficiency after the general data reduction for each hardware trigger threshold.

The final expected radon concentration of 1.52±0.03 $\mathrm{mBq/m^3}$ is consistent with the absolute measurements of the radon concentration in the SK tank (1.6±0.5 $\mathrm{mBq/m^3}$).

# Chapter 9

# Results

Solar neutrino events are detected by recoil electrons via $\nu - e$ scattering. The strong angular correlation between the incident neutrino direction and the scattered electron direction is used to extract the solar neutrino flux.

Figure 9.2 shows the distribution of $\cos\theta_{sun}$ for all events passing the reduction cuts described in chapter 6, 8. $\theta_{sun}$ is defined as the angle reconstructed momentum and the radius vector from the Sun. It is shown in figure 9.1. The energy range of the event is $4.5 \sim 20.0$ MeV in the figure. The filled circles show data, and the histogram shows MC normalized to data. The dotted line shows the background shape which is used in extracting the neutrino signal.

A clear peak due to solar neutrinos is seen, as described above. The flat component in the $\cos\theta_{sun}$ distribution is due to radon background in the water, radioactive spallation products and $\gamma$ rays from the surrounding rock and materials comprising the ID wall.

In this chapter, the method used to extract the solar neutrino signal is explained. The flux measurement and the observed recoil electron energy spectrum of new data above 4.5 MeV is described. The day and night time energy spectrum is presented in appendix G.

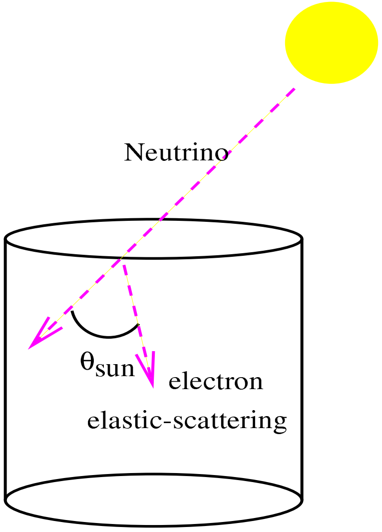

Figure 9.1: The definition of $\cos\theta_{sun}$.

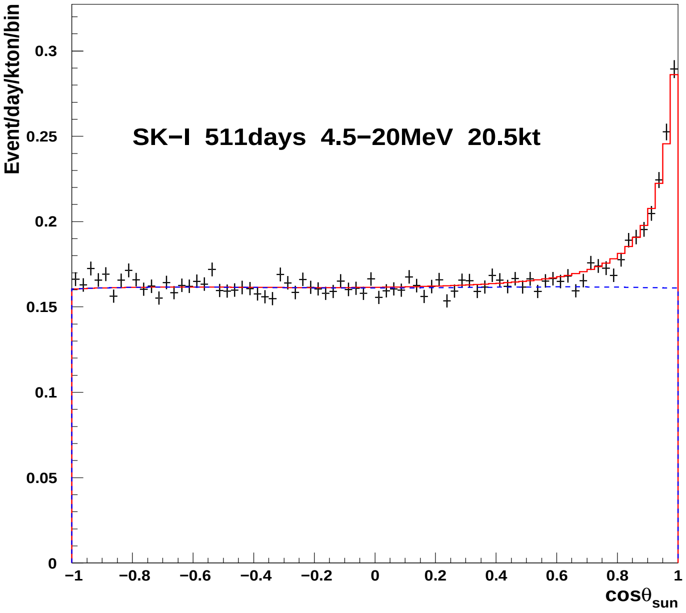

Figure 9.2: The $\cos\theta_{sun}$ distribution of all events($E = 4.5 \sim 20.0$MeV)

## 9.1 Solar neutrino signal extraction

In order to obtain the measured flux relative to the SSM, a extended maximum likelihood method (EMLM) is used. In old solar neutrino extraction, the simple maximum likelihood method had been used. But, in the most recent analysis, the EMLM has been used. The details of the reasons is explained later.

The probability function for the likelihood consists of signal and background components in old method:

$$P(E_e, \cos\theta_{sun}, x) = P_{bg} \times (1-x) + P_{sig} \times x \tag{9.1}$$

where $E_e$ is the recoil electron energy and $x$ is the fraction of the solar neutrino signals relative to the observed total number of events.

The probability function for the signal ($P_{sig}$) is obtained by the solar neutrino MC simulation at various energy regions. Figure 9.3 shows the distributions of $P_{sig}$ at 4.5, 8, 10, 14 MeV. The distribution is named XANG. The XANG is made by the smoothed probability function for the signal distribution of MC by the smoothing functions. The details is described in appendix F. In this thesis, the smoothing function is different from current analysis. The smoothing functions are changed from the sorting method to the function fitting method. It was problem that the old smoothing function created a artificial shape for original MC $\cos\theta_{sun}$ distribution. So, the new smoothing method was developed. It has a small artificial effect.

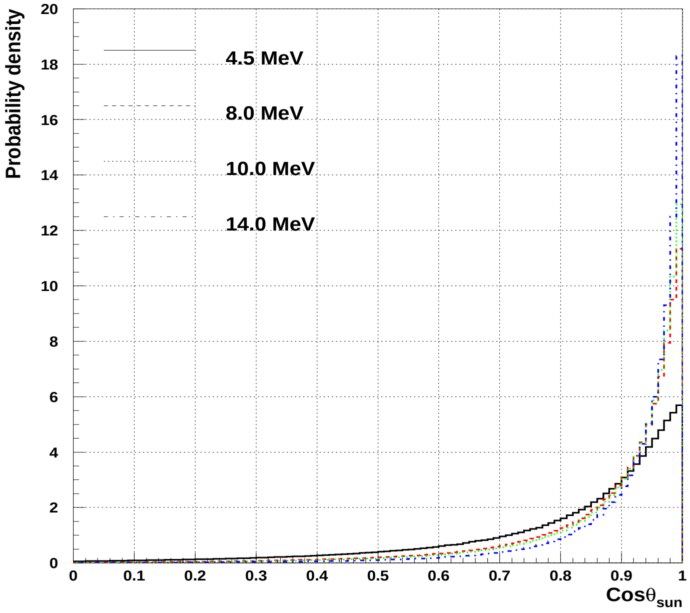

Figure 9.3: The probability density function for signal, $P_{sig}$ at various energy.

The background shape is almost flat. But, asymmetries in the $\gamma$ ray background from the surrounding rocks and PMT gain variations may slightly distort the background shape. Especially, the effect is most important factor for extracting solar signals in low energy region, for example, 4.5 ~ 5.0 MeV. Small deviations from a flat background shape are taken into account by simulating the background distribution. In order to obtain the background shape, the zenith angle ($\cos\theta_z$) distribution of the events is fit with 8-th degree polynomial. The background probability function ($P_{bg}$) is obtained by transforming this fit function into a function $\cos\theta_{sun}$. The fitting function was weighted by the $\cos\theta_{sun}$ distribution of the real data. Then, it was distributed $\cos\theta_{sun}$ with $\cos\theta_{x,y}$ of the random number. By this method, the background which has enough statistics is simulated. Here, it is assumed that the background shape does not dependent on the azimuth angle. Possible azimuth dependence ($\phi$ asymmetry of the background) is discussed in the systematic errors. Figure 9.4 shows the distributions of $P_{bg}$ at 4.5,8.0,10.0, and 14.0 MeV.

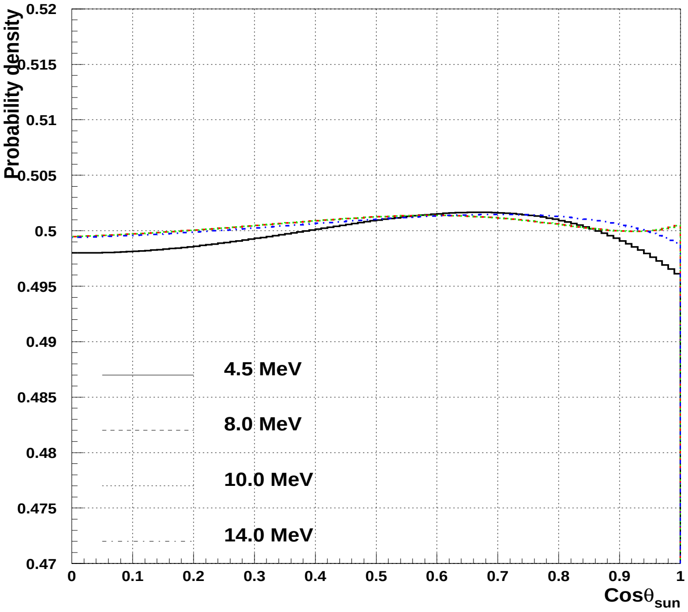

Figure 9.4: The probability density function for background, $P_{bg}$ at various energy.

The fraction of signal $x$ differs between energy regions. In order to get this fraction at various energy regions separately, the probability function is defined as follows:

$$P(E_e, \cos\theta_{sun}, x_i(x)) = P_{bg}(E_e, cos\theta_{sun}) \times (1 - x_i(x)) + P_{sig}(E_e, \cos\theta_{sun}) \times x_i(x) \tag{9.2}$$

where $x_i(x)$ of a scale factor is defined by following steps.

1. Assuming $^8$B spectrum and no spectrum distortion, the following equation is defined.

$$\frac{S_{all}^{data}}{N_{all}^{SSM}} = \frac{S_i^{data}}{N_i^{SSM}} \tag{9.3}$$

2. From probability function fitting, one can obtain

$$x = \frac{S_i^{data}}{N_i^{data}}. \tag{9.4}$$

3. Therefore, one can obtain $x_i(x)$ by following equation.

$$x_i(x) = \frac{N_i^{SSM}}{N_{all}^{SSM}} \frac{N_{all}^{data}}{N_i^{data}} \times x. \tag{9.5}$$

   where $i$ is the index of the energy region. $N_{all}$ and $N_i$ are the total number of events and the number of events in each energy region respectively. $S_{all}$ and $S_i$ are the extracted total solar neutrino signals and the number of solar neutrino signals in each energy region.

From the probability function, the traditional likelihood function is defined as follows.

$$L(x) = \prod_{i=1}^{N_{ene}} \prod_{j=1}^{N_i} P_{ij}(E_e, \cos\theta_{sun}, x_i(x)) \tag{9.6}$$

where $N_{ene}$ is the number of the energy regions and $N_i$ is the number of events in i-th energy region. In this function, there was a problem. The problems was the total number of events is fixed. The problems produced the harmful effect as following lists.

- Fitted results using the likelihood function is just a number of signal events in our particular data sample. (and it does not correspond to the absolute value of the true number of signal rate)
- For small $N_i$ bin, the scale factor $x_i$ tend to fluctuate largely and make many negative likelihood values.

To avoid these harmful effect, we improved the smoothing technique for scale factor ($x_i$) and used the extended maximum likelihood function [90] [5]. The extended maximum likelihood function is as follows:

$$L_E(x) = \frac{e^{-T} \cdot T^N}{N!} \cdot L_T(x) \tag{9.7}$$

where $L_E$ and $L_T$ are the extended maximum likelihood function and the traditional maximum likelihood function respectively. $T$ is the extracted true all number of events which is total number of true extracted signals adding to total number of true fitted background events. $N$ is the total observed number of events. Therefore, the extended likelihood function is transfered as follows.

$$L(x) = \prod_{i=1}^{N_{ene}} \frac{B_i + x_i \cdot S}{N!} \prod_{j=1}^{N_i} P_{ij}(E_e, \cos\theta_{sun}, x_i) \tag{9.8}$$

$x_i$ is the new scale factor for the signal. $B_i$ is the number of true fitted background events in i-the energy bin. $S$ is the total number of the true extracted signals. The probability function with new scale factor is as follows.

$$P(E_e, \cos\theta_{sun}, x_i) = P_{bg,i}(E_e, cos\theta_{sun}) \times B_i + P_{sig,i}(E_e, \cos\theta_{sun}) \times S \cdot x_i \tag{9.9}$$

where

$$S_{MC,i} = x_i \times S_{MC}. \tag{9.10}$$

$S_{MC,i}$ is the number of the expected signal events in i-th bin for total expected signal events of $S_{MC}$. In this analysis, the data are divided into 20 energy regions. From 4.5 to 14.0 MeV, data are divided into regions 0.5 MeV width. The last region is from 14.0 to 20.0 MeV.

## 9.2 Results of the flux measurement

In this section, the flux measurement is summarized. For the flux measurement, the events with reconstructed recoil electron from 4.5 to 20.0 MeV is used. In this thesis, the flux measurement is done for three data sets. The data set I (dsI) is the full 1496 days data set of SK-I. The data set II (dsII) is the periodical 566 days data set of SK-I, which is same period as the data set of the 4.5∼5.0 MeV analysis but without tight data reduction. The data set III (dsIII) is the final 511 days data set of SK-I with 4.5∼5.0 MeV data.

### 9.2.1 The results of total $^8$B neutrino flux

First of all, the total number of recoil electron events by the solar neutrino is shown for each data set. The total systematic error is given +3.5% and -3.2% for data set I,II. The total systematic error is given +5.8% and -5.3% for data set III.

$$\mathrm{N_{signal,dsI}} = 222967^{+226}_{-225}(\mathrm{stat.})^{+780}_{-713}(\mathrm{syst.}) \tag{9.11}$$

$$\mathrm{N_{signal,dsII}} = 8920^{+146}_{-145}(\mathrm{stat.})^{+312}_{-285}(\mathrm{syst.}) \tag{9.12}$$

$$\mathrm{N_{signal,dsIII}} = 5823^{+120}_{-119}(\mathrm{stat.})^{+338}_{-309}(\mathrm{syst.}) \tag{9.13}$$

The expected number of solar neutrino events in total, $N_{expect}$ is obtained as follows.

$$N_{expect} = \sum_{i=1}^{N_{thr}} \frac{N_{red,i}}{N_{MC,i}} \times T_{livetime,i} \times N_{ssm} \tag{9.14}$$

The expected number of solar neutrino events in j-th energy bin, $N_{expect,j}$ is obtained as follows.

$$N_{expect,j} = \sum_{i=1}^{N_{thr}} \frac{N_{red,i,j}}{N_{MC,i,j}} \times T_{livetime,i,j} \times N_{ssm} \tag{9.15}$$

where $N_{thr}$ is the number of trigger thresholds. As described in chapter 3, there are 7 different trigger thresholds. $N_{MC}$ is the number of the solar neutrino MC events in i-th run period of each trigger threshold. $N_{red,i}$ is the number of solar neutrino MC events after the reduction steps in i-th run period. $T_{livetime,i}$ is the live-time of i-th run period. $N_{SSM}$ is the SSM prediction of the number of solar neutrino recoil electrons in SK, which is 284.4 events/day. The live-time is summarized in table 9.1 for the data set I,II and in table 9.2 for the data set III.

| trigger | LE/SLE | run number | live time(day/night time) |
|---|---|---|---|
| LE | -320mV | R1742-4141 | 280.026(135.29/144.73) day |
| LE+SLE | -320mV -260mV | R4142-7333 | 548.375(270.77/277.61) day |
| LE+SLE | -320mV -250mV | R7334-7858 | 101.701(56.96/44.74) day |
| LE+SLE | -320mV -222mV | R7859-8233 | 78.072(33.84/44.23) day |
| LE+SLE | -302mV -212mV | R8234-8995 | 173.492(84.41/89.08) day |
| LE+SLE | -302mV -186mV | R8996-9093 | 17.147(10.02/7.13) day |
| LE+SLE | -302mV -212mV | R9094-9267 | 50.610(26.4/24.25) day |
| LE+SLE | -302mV -186mV | R9268-10417 | 246.693(115.49/131.20) day |
| total(dsII) | | R7859-10417 | 566.01(270.13/295.88) day |
| total(dsI) | | R1742-10417 | 1496.12(733.15/762.97) day |

Table 9.1: The live-time summary for each trigger threshold in the data set I,II.

Figure 9.5 shows the SSM prediction of the number of solar neutrino recoil electrons in SK. The expected numbers of events for the flux analysis are:

$$\mathrm{N_{expect,SSM_{BP2000},dsI}} = 48173 \text{ events} \tag{9.16}$$

$$\mathrm{N_{expect,SSM_{BP2000},dsII}} = 19316 \text{ events} \tag{9.17}$$

$$\mathrm{N_{expect,SSM_{BP2000},dsIII}} = 12209 \text{ events} \tag{9.18}$$

| trigger | LE/SLE | run number | live time(day/night time) |
|---|---|---|---|
| LE+SLE | -320mV -222mV | R7859-8233 | 72.95(31.78/41.16) day |
| LE+SLE | -302mV -212mV | R8234-8995 | 173.408(84.33/89.08) day |
| LE+SLE | -302mV -186mV | R8996-9093 | 7.72(4.49/3.23) day |
| LE+SLE | -302mV -212mV | R9094-9267 | 31.83(15.90/15.93) day |
| LE+SLE | -302mV -186mV | R9268-10417 | 225.58(107.36/118.22) day |
| total(dsIII) | | R7859-10417 | 511.48(243.86/267.62) day |

Table 9.2: The live-time summary for each trigger threshold in the data set III.

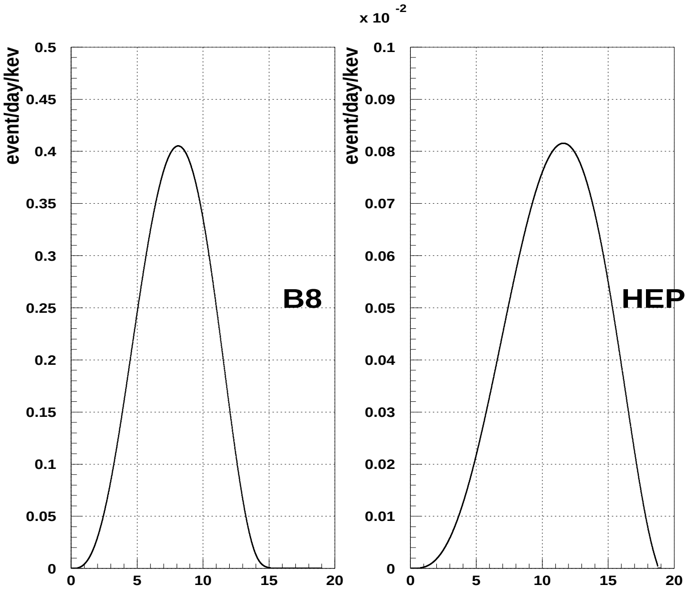

Figure 9.5: The SSM prediction of the number of solar neutrino recoil electrons in SK detector.

Therefore, the ratios Data/$\mathrm{SSM_{BP2000}}$ are obtained as:

$$\mathrm{Data/SSM}(\mathrm{SSM_{BP2000}}, \mathrm{dsI}) = 0.462^{+0.005}_{-0.005}(\mathrm{stat.})^{+0.016}_{-0.015}(\mathrm{syst.}) \quad (9.19)$$
$$\mathrm{Data/SSM}(\mathrm{SSM_{BP2000}}, \mathrm{dsII}) = 0.463^{+0.008}_{-0.007}(\mathrm{stat.})^{+0.016}_{-0.015}(\mathrm{syst.}) \quad (9.20)$$
$$\mathrm{Data/SSM}(\mathrm{SSM_{BP2000}}, \mathrm{dsIII}) = 0.478^{+0.01}_{-0.01}(\mathrm{stat.})^{+0.028}_{-0.025}(\mathrm{syst.}) \quad (9.21)$$

The solar neutrino flux $\Phi_\nu$ is obtained for each data set by multiplying this ratio by the $\mathrm{SSM_{BP200,v2}}$ flux prediction.

$$\Phi_\nu(\mathrm{SSM_{BP2000}}, \mathrm{dsI}) = 2.34^{+0.02}_{-0.02}(\mathrm{stat.})^{+0.08}_{-0.08}(\mathrm{syst.})(\times 10^6/\mathrm{cm}^2/\mathrm{sec}) \quad (9.22)$$
$$\Phi_\nu(\mathrm{SSM_{BP2000}}, \mathrm{dsII}) = 2.33^{+0.04}_{-0.04}(\mathrm{stat.})^{+0.08}_{-0.08}(\mathrm{syst.})(\times 10^6/\mathrm{cm}^2/\mathrm{sec}) \quad (9.23)$$
$$\Phi_\nu(\mathrm{SSM_{BP2000}}, \mathrm{dsIII}) = 2.41^{+0.05}_{-0.05}(\mathrm{stat.})^{+0.14}_{-0.13}(\mathrm{syst.})(\times 10^6/\mathrm{cm}^2/\mathrm{sec}) \quad (9.24)$$

The result of the data set III is used in this thesis for energy spectrum analysis. The Data/SSM result is consistent with the another results within 1.3 sigma. Therefore, the result from new analysis including 4.5~5.0 MeV data has no systematic bias.

### 9.2.2 The results of $^8$B neutrino flux from 4.5 to 5.0 MeV

The details of the 4.5~5.0 MeV data is described in this section. The event rates as shown in table 9.3 can be observed for each energy region in the SK detector by SSM prediction.

| Energy | Event rate (events/day) |
|---|---|
| $^8$B | |
| 4.5-5.0 | 11.18 |
| 5.0-5.5 | 13.29 |
| 5.5-6.0 | 15.27 |
| 6.0-6.5 | 17.02 |
| 6.5-7.0 | 18.45 |
| 7.0-7.5 | 19.50 |
| 4.5-6.5 | 56.75 |
| 6.5-20.0 | 199.56 |
| *hep* | |
| 4.5-5.0 | 0.0096 |
| 5.0-5.5 | 0.0122 |
| 5.5-6.0 | 0.0150 |
| 6.0-6.5 | 0.0179 |
| 6.5-7.0 | 0.0210 |
| 7.0-7.5 | 0.0240 |
| 4.5-6.5 | 0.0548 |
| 6.5-20.0 | 0.6767 |

Table 9.3: The expected event rates in the SK detector by prediction.

Figure 9.6 shows the $\cos\theta_{sun}$ distribution of the data set III with 4.5~5.0 MeV data. In the figure, the $\cos\theta_{sun}$ distributions for 5.5~6.0 and 5.0~5.5 MeV energy regions are also drawn. Figure 9.7 shows the expanded plot of the $\cos\theta_{sun}$ distribution for 4.5~5.0 MeV energy region. We can see the clear solar neutrino peak to the solar direction in this energy region. The histogram shows the result of the likelihood fits. The dashed line shows the background shape. The black circles show the data with statistical error.

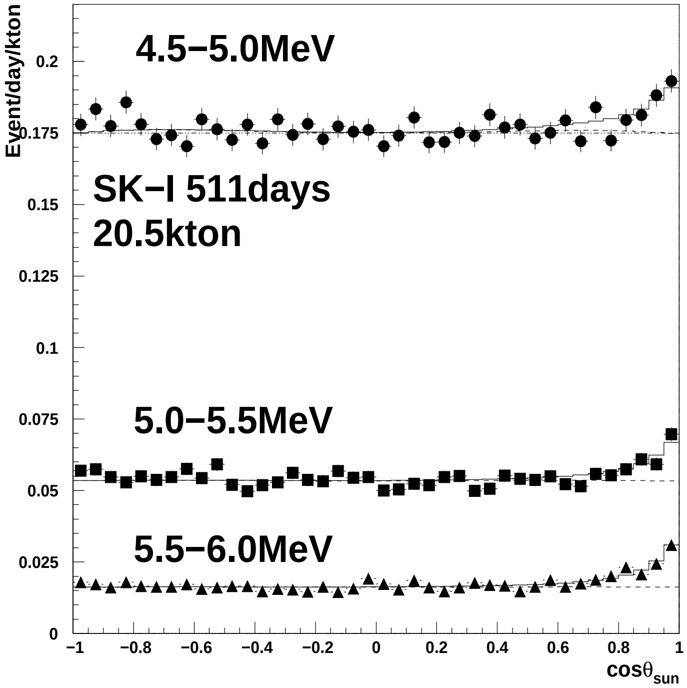

Figure 9.6: The $\cos\theta_{sun}$ distribution for 5.5∼6.0, 5.0∼5.5 and 4.5∼5.0 MeV energy regions of the data set III.

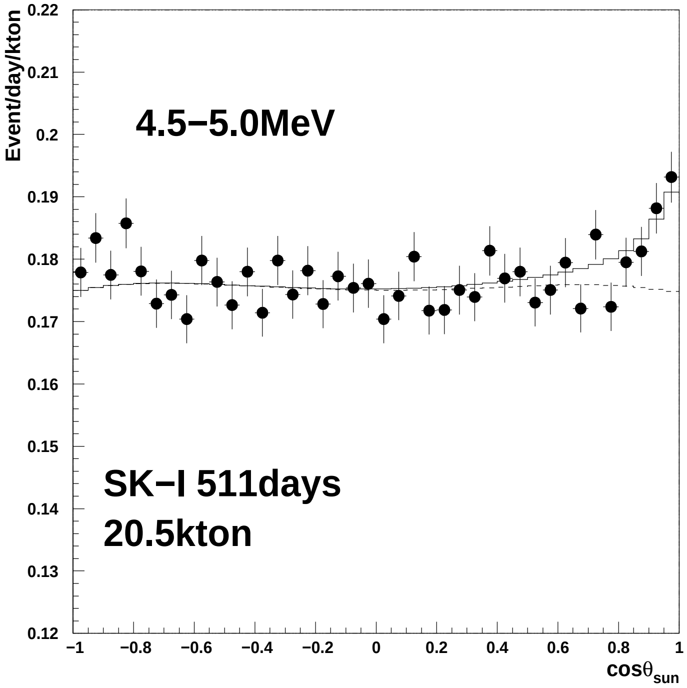

Figure 9.7: The expanded plot of the $\cos\theta_{sun}$ distribution for 4.5∼5.0 MeV energy region.

The number of the extracted solar neutrino signals in this energy region with a systematic error of ±5.9% is as follows:

$$\mathrm{N}_{\mathrm{signal},4.5-5.0} = 722^{+139}_{-137}(\mathrm{stat.})^{+43}_{-43}(\mathrm{syst.}) \tag{9.25}$$

The expected solar neutrino events in this energy region is as follows:

$$\mathrm{N}_{\mathrm{expect,SSM_{BP2000}},4.5-5.0} = 1109 \text{ events} \tag{9.26}$$

We obtained the solar neutrino flux in this energy region for the first time in the world as follows:

$$\Phi_\nu(\mathrm{SSM_{BP2000}}, 4.5-5.0) = 3.28^{+0.63}_{-0.62}(\mathrm{stat.})^{+0.19}_{-0.19}(\mathrm{syst.})(\times 10^6/\mathrm{cm}^2/\mathrm{sec}) \tag{9.27}$$

The Data/SSM in this energy region is as follows:

$$\mathrm{Data/SSM}(\mathrm{SSM_{BP2000}}, 4.5-5.0) = 0.651^{+0.13}_{-0.12}(\mathrm{stat.})^{+0.038}_{-0.038}(\mathrm{syst.}) \tag{9.28}$$

In this energy region, the observed solar neutrino events are also deficits by the solar neutrino oscillation comparing with the SSM prediction.

## 9.3 Results of the energy spectrum measurement

Figure 9.8, figure 9.9, figure 9.10 present the $\cos\theta_{sun}$ distribution in various energy bins. The filled circles show the data with statistical error, the histograms show the result of the likelihood fit, and the dashed lines show the background shape used to extract the solar neutrino signals.

The width of each energy bin is divided as follows:

- 4.5∼14.0 : 0.5 MeV for each bin
- 14.0∼20.0 : combined into one bin

As described in figure 9.5, $^8$B neutrino energy spectrum endpoint is about 15 MeV. The hep flux is predicted to be 0.04% of the expected $^8$B neutrino flux, although the end point energy is 18.77 MeV. Therefore, the number of solar neutrino events with recoil electron energy above 14 MeV is expected to be much smaller than that below 14 MeV. This is the reason for the large width of the last bin.

Figure 9.11 shows the measured solar neutrino recoil electron energy spectrum and the expected spectrum from the SSM prediction. This figure is result of the data set III which includes the 4.5 MeV data. We can see the deficit of the observed solar neutrino flux in all over the energy region.

Figure 9.12 shows the ratio of the measured recoil electron energy spectrum to the predicted spectrum. This figure is the result of the data set III which includes the 4.5 MeV data. Figure 9.13 also shows the ratio of the measured recoil electron energy spectrum to the predicted spectrum for the results of data set I and II. In the right side plot, the result of the data set III is overlaid with the result of the data set II. The data set I is the SK-I full data. The data set II is the periodical data which has same time period as data set III but no any tight data reduction. Comparing these three figures, although the fluctuation of the data by the poor statistics, the tendency is consistent in all energy region. It is concluded that the new made data set III with 4.5∼5.0 MeV data has no systematic bias. In table 9.4, the numerical summary of the recoil electron energy spectrum is represents. The error is statistical only.

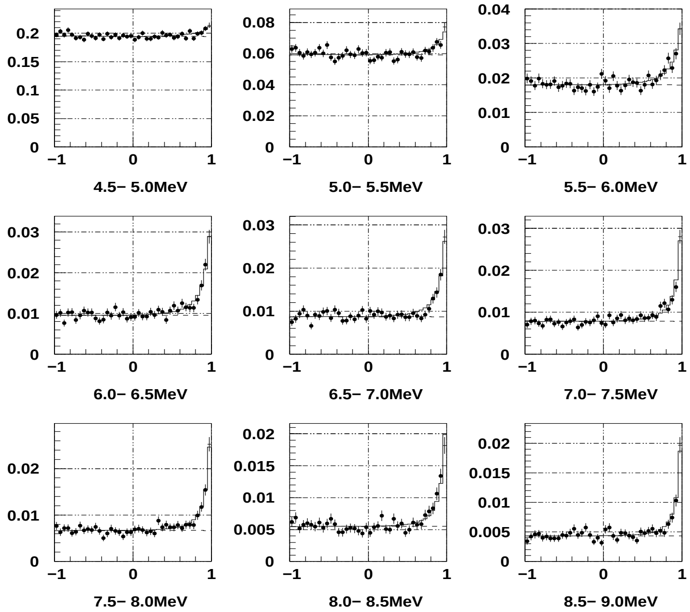

Figure 9.8: The $\cos\theta_{sun}$ distribution in each energy bin from 4.5 to 9.0 MeV. The unit of the vertical axis is events/day/kton/bin.

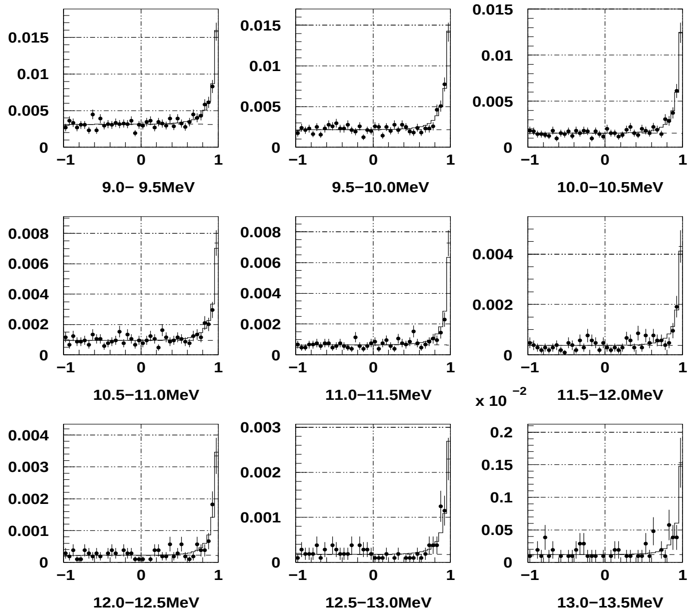

Figure 9.9: The $\cos\theta_{sun}$ distribution in each energy bin from 9.0 to 13.5 MeV. The unit of the vertical axis is events/day/kton/bin.

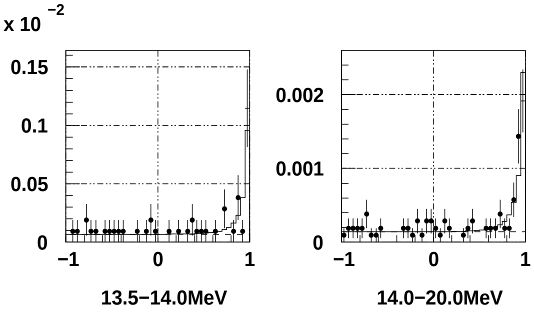

Figure 9.10: The $\cos\theta_{sun}$ distribution in each energy bin from 13.5 to 20.0 MeV. The unit of the vertical axis is events/day/kton/bin.

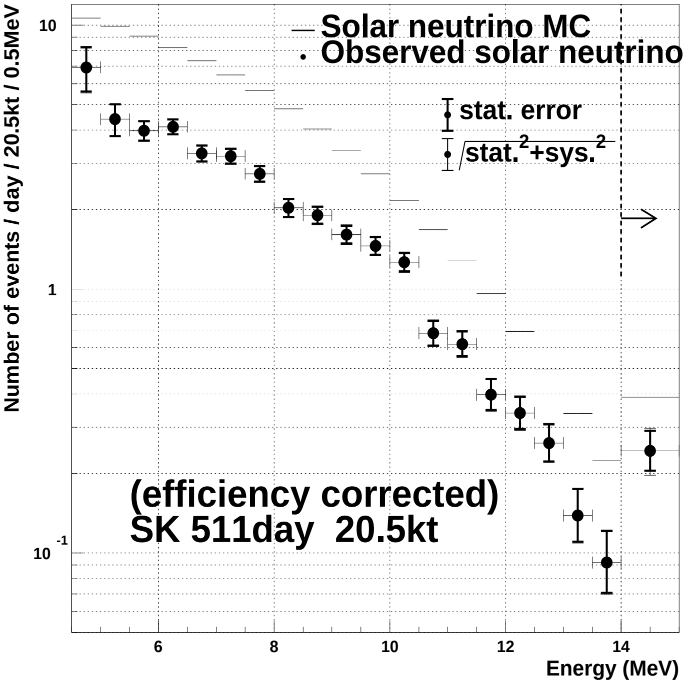

Figure 9.11: The measured solar neutrino recoil electron energy spectrum. The expected spectrum from SSM is also shown. The thick error bar shows the statistical error only. The thin error bar shows the total error including systematic error.

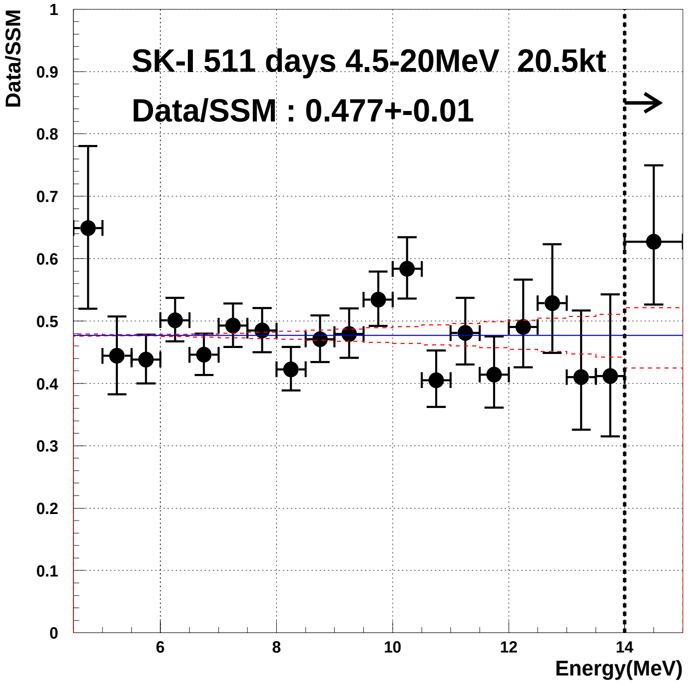

Figure 9.12: The ratio of the measured recoil electron energy spectrum to the predicted spectrum. The error bars shows total errors including systematic error and statistical errors. The center value of the best fit for the total recoil electron is shown by the solid center line. The dashed line shows the systematic errors for the predicted $^8$B spectrum including energy resolution, energy scale resolution and uncertainty for the $^8$B spectrum.

| Energy | Data/SSM | Statistical error | Flux($\times 10^6$/cm/s) | Statistical error |
|---|---|---|---|---|
| 4.5- 5.0 | 0.649 | +0.125-0.123 | 3.27 | +0.63-0.62 |
| 5.0- 5.5 | 0.444 | +0.061-0.060 | 2.24 | +0.31-0.30 |
| 5.5- 6.0 | 0.438 | +0.037-0.036 | 2.21 | +0.19-0.18 |
| 6.0- 6.5 | 0.501 | +0.032-0.031 | 2.53 | +0.16-0.15 |
| 6.5- 7.0 | 0.445 | +0.031-0.029 | 2.25 | +0.15-0.15 |
| 7.0- 7.5 | 0.492 | +0.033-0.031 | 2.48 | +0.16-0.15 |
| 7.5- 8.0 | 0.484 | +0.033-0.031 | 2.44 | +0.16-0.16 |
| 8.0- 8.5 | 0.422 | +0.034-0.032 | 2.13 | +0.17-0.16 |
| 8.5- 9.0 | 0.470 | +0.035-0.033 | 2.37 | +0.18-0.17 |
| 9.0- 9.5 | 0.479 | +0.038-0.036 | 2.42 | +0.19-0.18 |
| 9.5-10.0 | 0.534 | +0.042-0.039 | 2.69 | +0.21-0.19 |
| 10.0-10.5 | 0.583 | +0.048-0.044 | 2.94 | +0.24-0.22 |
| 10.5-11.0 | 0.405 | +0.046-0.041 | 2.04 | +0.23-0.21 |
| 11.0-11.5 | 0.480 | +0.054-0.048 | 2.42 | +0.27-0.24 |
| 11.5-12.0 | 0.414 | +0.059-0.051 | 2.09 | +0.30-0.26 |
| 12.0-12.5 | 0.490 | +0.074-0.063 | 2.47 | +0.37-0.32 |
| 12.5-13.0 | 0.528 | +0.093-0.078 | 2.66 | +0.47-0.39 |
| 13.0-13.5 | 0.410 | +0.106-0.083 | 2.07 | +0.53-0.42 |
| 13.5-14.0 | 0.411 | +0.130-0.096 | 2.08 | +0.65-0.48 |
| 14.0-20.0 | 0.627 | +0.120-0.099 | 3.16 | +0.60-0.50 |

Table 9.4: The numerical summary of the recoil electron energy spectrum.

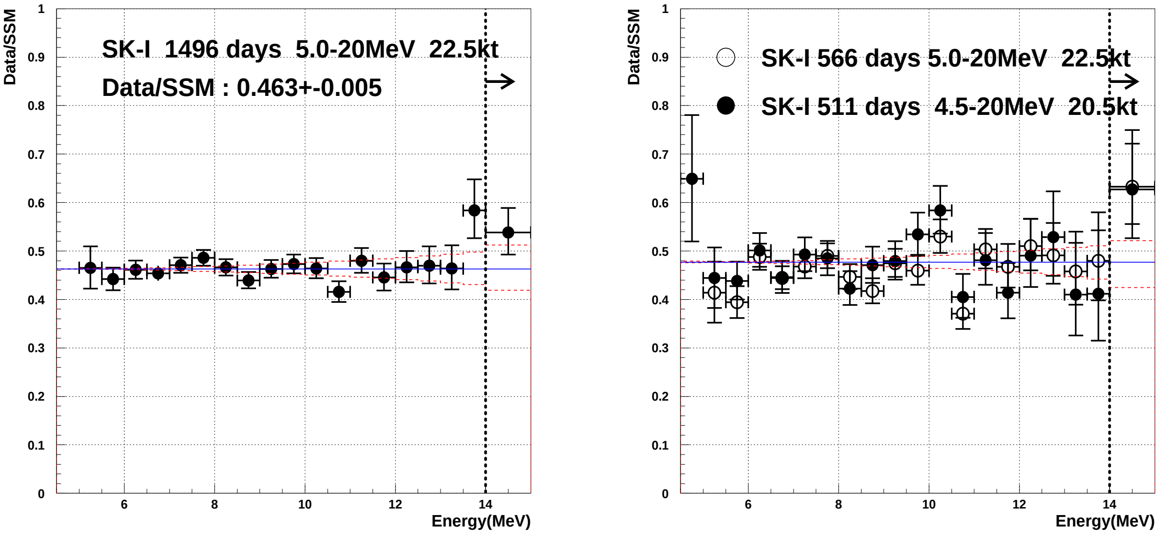

Figure 9.13: The definition in the figure is same as Figure 9.12. The left figure is the result of the data set I (1496 days). The right figure shows the result of the data set II (566 days, no tight data reduction) with empty circles and data set III (511 days) with filled circles.

## 9.4 systematic uncertainties

Systematic uncertainties in the energy spectrum measurement are classified into two categories. The one are errors that are correlated with energy. And they are called correlated errors. The other are errors that are not correlated error basically, and they are called uncorrelated errors. In the uncorrelated errors, some error has the correlation with energy, In this case, the error is called uncorrelated-correlated error. In this section, the correlated errors and the uncorrelated errors are explained separately. The all uncertainties is updated in order to analyze the new data set III which includes 4.5∼5.0 MeV data in this thesis. Especially, the main factor for the uncertainties of 4.5∼5.0 MeV data is described in detail.

### 9.4.1 Correlated errors

Uncertainties in the absolute energy scale and the energy resolution directly affect the shape of the observed energy spectrum. Moreover, the effect in each energy bin is the independent. So the correlation between each energy bin should be considered in evaluating the systematic error of each bin.

The uncertainty in the energy scale and the energy resolution are summarized here.

- Position dependence of the energy scale deviation, (Data-MC)/MC, is measured to be within ±0.5 % by LINAC calibration. For the energy resolution, it is within ±2.0 %.
- Energy dependence of the energy scale deviation is also studied using LINAC calibration data and it is obtained to be within ± 2.0 %
- The systematic uncertainty due to the LINAC system itself is 0.33 % for electron energy of 8.9 MeV.
- Directional dependence of the energy scale deviation measured using spallation data is found to be within ± 0.5 %.
- The uncertainty due to the water transparency measurement is ± 0.22 %.

The effect of above uncertainties are obtained are evaluated as follows. In order to simulate the observed energy spectrum $f(E_{obs})$ given the original spectrum $f_o(E_e)$ which uses SSM $_{\mathrm{BP2000}}$ and $^8$B spectrum by Ortiz, the following function is defined:

$$f(E_{obs}) = \int_0^\infty f_0(E_0)R(E_{obs}, E_e)P(E_e)dE_e, \tag{9.29}$$

where $R(E_{obs}, E_e)$ is a function to simulate the energy resolution, and $P(E_e)$ is a function for the detection efficiency.

By varying $R(E_{obs}, E_e)$ and $P(E_e)$, one can simulate the expected results that include the uncertainties. Then the effects of the uncertainties can be estimated by comparing the simulated results with the observed results. The effect of the theoretical uncertainty in the $^8$B neutrino energy spectrum is estimated in the same way. The estimated systematic errors are given in table 9.5. Figure 9.14 shows the total correlated errors for each energy bin.

| Energy | Total error(%) | Error with Res. + Scal.(%) | Error with $^8$B(%) |
|---|---|---|---|
| 4.5-5.0 | +0.39 -0.20 | +0.35 -0.19 | +0.17 -0.08 |
| 5.0-5.5 | +0.25 -0.16 | +0.24 -0.16 | +0.08 -0.01 |
| 5.5-6.0 | +0.21 -0.16 | +0.20 -0.16 | +0.05 -0.01 |
| 6.0-6.5 | +0.32 -0.33 | +0.29 -0.30 | +0.14 -0.13 |
| 6.5-7.0 | +0.51 -0.56 | +0.45 -0.50 | +0.24 -0.25 |
| 7.0-7.5 | +0.75 -0.81 | +0.66 -0.71 | +0.37 -0.39 |
| 7.5-8.0 | +1.03 -1.07 | +0.89 -0.93 | +0.52 -0.54 |
| 8.0-8.5 | +1.35 -1.35 | +1.16 -1.16 | +0.70 -0.69 |
| 8.5-9.0 | +1.70 -1.65 | +1.44 -1.40 | +0.90 -0.87 |
| 9.0-9.5 | +2.09 -1.97 | +1.75 -1.65 | +1.14 -1.06 |
| 9.5-10.0 | +2.51 -2.32 | +2.09 -1.93 | +1.39 -1.27 |
| 10.0-10.5 | +2.97 -2.71 | +2.45 -2.24 | +1.68 -1.51 |
| 10.5-11.0 | +3.46 -3.15 | +2.84 -2.60 | +1.98 -1.78 |
| 11.0-11.5 | +3.98 -3.64 | +3.26 -3.00 | +2.29 -2.07 |
| 11.5-12.0 | +4.54 -4.20 | +3.71 -3.45 | +2.62 -2.39 |
| 12.0-12.5 | +5.13 -4.81 | +4.19 -3.96 | +2.96 -2.73 |
| 12.5-13.0 | +5.75 -5.47 | +4.70 -4.52 | +3.30 -3.09 |
| 13.0-13.5 | +6.39 -6.18 | +5.24 -5.12 | +3.64 -3.45 |
| 13.5-14.0 | +7.04 -6.90 | +5.81 -5.75 | +3.98 -3.81 |
| 14.0-20.0 | +10.85 -9.45 | +9.05 -8.32 | +5.99 -4.49 |

Table 9.5: The numerical results for the correlated error.

### 9.4.2 Uncorrelated error

#### Trigger efficiency

The trigger efficiency dependents on the vertex position and water transparency. These dependences are considered in the solar neutrino MC simulation. The systematic error with the trigger efficiency is estimated by comparing the measured trigger efficiency with the trigger simulation of the solar neutrino MC. The estimation of systematic uncertainty with it is a important factor of all uncertainties in low energy region, specially 4.5∼5.0 MeV, because the trigger efficiency is exactly relative to the number of hit PMTs. By comparing the measured trigger efficiency with the trigger efficiency of the solar neutrino MC, the precision of the solar neutrino MC simulation is evaluated.

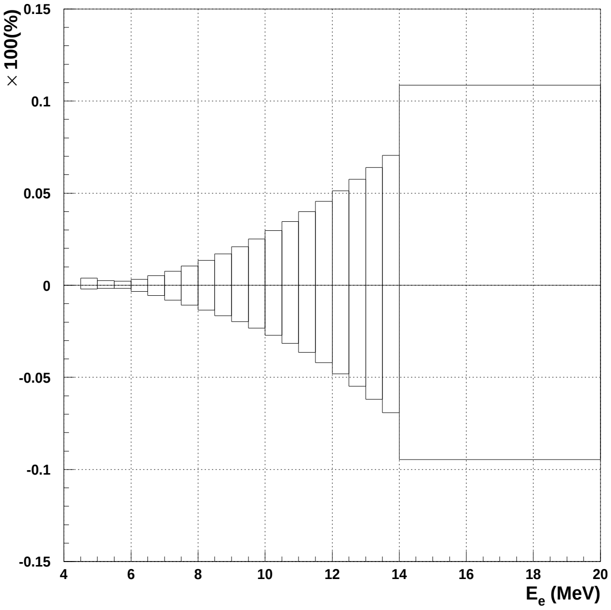

Figure 9.14: The total correlated errors for each energy bin.

For the LE trigger, the efficiency is almost 100% above 6.5 MeV. The summary of LE trigger efficiency is presented in table 9.6. In the energy region from 6.5 to 7.0 MeV and from 7.0 to 7.5 MeV, the uncertainties with the trigger efficiencies are ±0.3% and ±0.1% respectively. The result is obtained by the maximum deviation between the DT calibration data and solar neutrino MC considering the live time in the period of each trigger threshold.

| LE threshold | Energy (50%/95% trigger efficiency) | Live time |
|---|---|---|
| Data set I | | |
| -320 mV(R1742-R8239) | 5.5 MeV/6.3 MeV | 1013.8 days (for 1496 days) |
| -302 mV(R8239-R10417) | 5.4 MeV/6.1 MeV | 483.3 days (for 1496 days) |
| Data set II | | |
| -320 mV(R7859-R8239) | 5.5 MeV/6.3 MeV | 83.7 days (for 566 days) |
| -302 mV(R8239-R10417) | 5.4 MeV/6.1 MeV | 483.3 days (for 566 days) |
| Data set III | | |
| -320 mV(R7859-R8239) | 5.5 MeV/6.3 MeV | 78.6 days (for 511 days) |
| -302 mV(R8239-R10417) | 5.4 MeV/6.1 MeV | 433.9 days (for 511 days) |

Table 9.6: The summary of the LE trigger efficiency.

The details of the SLE trigger efficiency is already described in chapter 8. For the SLE trigger, the trigger efficiency varies with the hardware threshold change. The trigger efficiency is measured for every SLE trigger threshold by DT calibration described in chapter 5. The result is obtained by the maximum deviation between the DT calibration data and solar neutrino MC considering the live time in the period of each trigger threshold. Table 9.7 shows the summary of the live time average of SLE trigger efficiency by DT calibration in 4.5∼5.0 MeV.

Figure 9.15 shows the progress of the simulated trigger efficiency by solar neutrino MC and the live time average of the trigger efficiency by the DT calibration. The solid lines in the figure present the DT calibration in each trigger threshold. The dot points present the simulated trigger efficiency by the solar neutrino MC.

Figure 9.16 shows the summary of the live time average of the trigger efficiency for the solar neutrino MC and DT calibration in each trigger threshold. The MC is almost consistent with

| SLE threshold | Trigger efficiency |
|---|---|
| -260 mV | 70.8 % |
| -250 mV | 82.1 % |
| -222 mV | 97.7 % |
| -212 mV | 87.2 % |
| -186 mV | 99.9 % |

Table 9.7: The summary of the live time average of the SLE trigger efficiency by the DT calibration in 4.5~5.0 MeV.

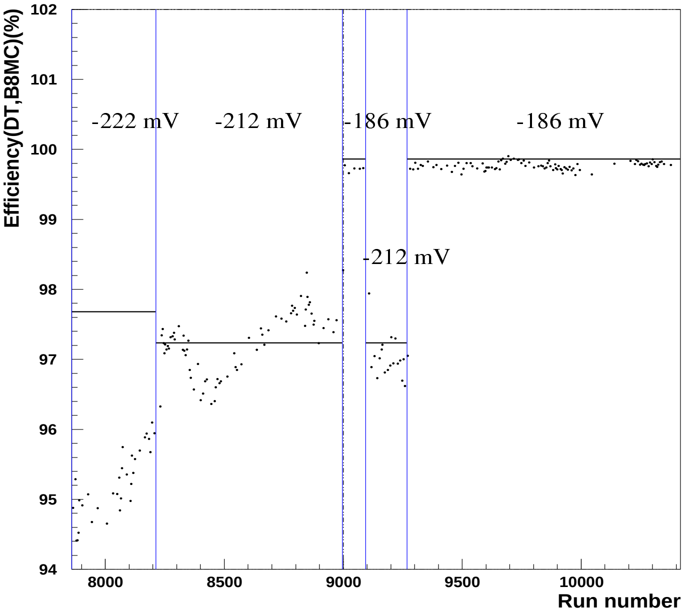

Figure 9.15: The progress of the simulated trigger efficiency by solar neutrino MC and the live time average of the trigger efficiency by the DT calibration.

DT data.

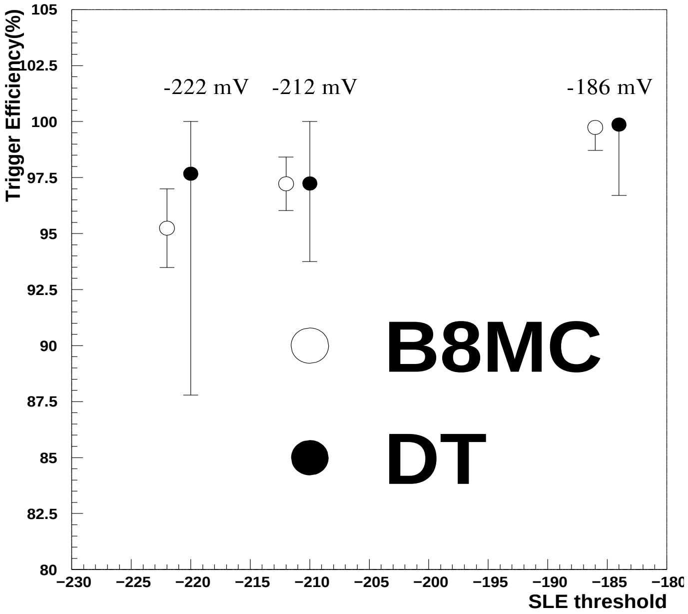

Figure 9.16: The summary of the trigger efficiency for the solar neutrino MC and the DT calibration in each trigger threshold.

Table 9.8 shows the numerical results of uncertainties with the trigger efficiency for each energy region.

| Energy region | Uncertainty (Data set III) | Uncertainty (Data set I,II) |
|---|---|---|
| 4.5 - 5.0 | ±1.1% | - |
| 5.0 - 5.5 | ±0.4% | +2.2 -1.0 % |
| 5.5 - 6.0 | ±0.7% | +0.6 -0.3 % |
| 6.0 - 6.5 | ±0.4% | +0.0 -0.0 % |
| 6.5 - 7.0 | ±0.3% | +0.2 -0.2 % |
| 7.0 - 7.5 | ±0.1% | +0.0 -0.0 % |
| 7.5 - 20.0 | ±0.0% | +0.0 -0.0 % |

Table 9.8: The numerical results of uncertainties with the trigger efficiency for each energy region.

### IT trigger efficiency

The systematic error due to the IT is studied using the Ni-Cf source. The deviation between the reduction efficiency of the IT data and that for Ni-Cf MC simulation is calculated at various positions in the ID. The volume average of those deviations in each energy bin is obtained in table 9.9.

### 1st reduction

The systematic error due to reduction comes from the reduction efficiency between data and MC simulation. In 1st reduction, the relatively largest systematic errors come from flasher cuts. The reduction efficiency of the flasher cut is obtained by comparing the reduction efficiency is spallation event data with that in $^8$B The deviation (Data-MC)/MC is less than ± 0.3%. Table 9.10 shows the summary.

| Energy region | Uncertainty (Data set III) | Uncertainty (Data set I,II) |
|---|---|---|
| 4.5 - 5.0 | ±1.1% | - |
| 5.0 - 5.5 | ±1.1% | ±1.1% |
| 5.5 - 6.0 | ±0.5% | ±0.5% |
| 6.0 - 6.5 | ±0.1% | ±0.1% |
| 6.5 - 7.0 | ±0.0% | ±0.0% |
| 7.0 - 20.0 | ±0.0% | ±0.0% |

Table 9.9: The uncertainty with the IT trigger efficiency.

| Energy region | Uncertainty (Data set III) | Uncertainty (Data set I,II) |
|---|---|---|
| 4.5 - 5.0 | ±0.3% | - |
| 5.0 - 20.0 | ±0.3% | ±0.3% |

Table 9.10: The uncertainty with the 1st reduction.

### Spallation cut

The uncertainty with the spallation cut is due to spallation dead time. The position dependents of the spallation dead time is presented in the figure of chapter 6, and it is used to simulate the spallation cut in MC simulation. The systematic error due to this position dependence of the dead time is estimated to be 0.05% by comparing the dead time calculated in MC with the dead time calculated from data. This uncertainty is considered only for flux measurement.

| Flux | Uncertainty (Data set III) | Uncertainty (Data set I,II) |
|---|---|---|
| Total flux | ±0.3% | ±0.2% |

Table 9.11: The uncertainty with the spallation cut.

### 2nd reduction

The systematic uncertainty with the GRINGO cut is obtained using the LINAC (or Ni-Cf) calibration data at various positions and the LINAC (or Ni-Cf) MC at each corresponding position. In order to obtain the energy dependence of the uncertainty, a volume average is calculated. In 4.5∼5.0 energy region, the deviation (Data-MC)/MC is calculated using the LINAC calibration. Above 5.0 MeV data, the deviation (Data-MC)/MC is calculated using the Ni-Cf calibration.

The systematic uncertainty with the Cluster fit cut is estimated using Ni-Cf calibration data at various positions.

The systematic uncertainty caused by PATLIK cut is estimated using LINAC data and LINAC MC in 4.5∼5.0 energy region. The deviation (Data-MC)/MC is calculated using the LINAC calibration. In SK-I full data set, the systematic error is estimated using spallation products with short time (∼30 msec). The reduction efficiency for the spallation events is compared with that in solar neutrino MC simulation.

### Gamma cut

The gamma cut uses the reconstructed vertex and direction in events. So the differences of vertex and angular resolution between data and MC simulation introduce systematic uncertainties. To estimate the influence of these differences, the following method is adopted.

| Cut | Uncertainty (Data set III) | Uncertainty (Data set I,II) |
|---|---|---|
| GRINGO cut | ±1.2% (<5.0 MeV) | ±0.2% (>5.0 MeV) |
| Cluster cut | ±0.3% (<5.0 MeV) | ±0.3% (>5.0 MeV) |
| PATLIK cut | ±1.9% (<5.0 MeV) | ±0.7% (>5.0 MeV) |

| Energy region | Total error (Data set III) | Total error (Data set I,II) |
|---|---|---|
| 4.5 - 5.0 | ±2.3% | - |
| 5.0 - 20.0 | ±0.8% | ±0.8% |

Table 9.12: The uncertainty with the 2nd reduction.

1. Shift the reconstructed vertices and direction of events within the differences in the vertex and angular resolution between data and MC.
2. Apply the gamma cut to the modified data and compare the reduction efficiency with the result of original data.

The used differences in the vertex and angular resolution are measured with LINAC as described in chapter 5.

| Energy region | Uncertainty (Data set III) | Uncertainty (Data set I,II) |
|---|---|---|
| 4.5 - 5.0 | ±0.1% | - |
| 5.0 - 20.0 | ±0.1% | ±0.1% |

Table 9.13: The uncertainty with the gamma cut.

### Tight data reduction for 4.5$sim$5.0 MeV data

The systematic uncertainties for new installed tight data reduction is also estimated in this time. The systematic errors for strong GRINGO cut, fiducial volume cut, and PATLIK cut with BONSAI reconstructed vertex information is calculated using the LINAC calibration data. The errors are estimated the deviation (Data-MC)/MC of the LINAC calibration for each reduction. The systematic errors for the strong gamma cut and strong gamma cut with BONSAI reconstructed vertex information is estimated by above described method.

| Cut | Uncertainty (Data set III) | Uncertainty (Data set I,II) |
|---|---|---|
| Strong GAMMA cut | ±0.2% (4.5 - 20.0 MeV) | - |
| Strong GRINGO cut | ±1.3% | - |
| F.V cut with BONSAI vertex | ±0.2% (4.5 - 20.0 MeV) | - |
| GAMMA cut with BONSAI vertex | ±0.4% (4.5 - 20.0 MeV) | - |
| PATLIK cut with BONSAI vertex | ±2.0% (4.5 - 20.0 MeV) | - |

| Energy region | Uncertainty (Data set III) | Uncertainty (Data set I,II) |
|---|---|---|
| 4.5 - 5.0 | ±2.4% | - |
| 5.0 - 20.0 | ±2.4% | - |

Table 9.14: The uncertainty with the tight data reduction for the 4.5∼5.0 MeV data analysis.

### Vertex shift

Systematic shifts in the reconstructed vertex relative to the original vertex is studied with Ni-Cf calibration at various positions.

| Energy region | Uncertainty (Data set III) | Uncertainty (Data set I,II) |
|---|---|---|
| 4.5 - 5.0 | ±0.2% | - |
| 5.0 - 20.0 | ±0.2% | ±0.2% |

Table 9.15: The uncertainty with the vertex-shift.

### Non-flat Background

Non-flat background shape is the largest systematic uncertainty in all systematic uncertainties for the energy spectrum analysis above 4.5 MeV, because the fluctuation of background becomes large in lower energy region by the remaining radon and gamma rays background.

In order to obtain the background shape used in the solar neutrino signal extraction, it is assumed that the background is independent of azimuth angle $\phi$. So, the asymmetry is considered about $\theta$. But, the $\phi$ asymmetry in the energy scale and background sources with possible asymmetric $\phi$ distribution may introduce deviations from flatness in the background $\cos\theta_{sun}$ distribution.

So the difference between the originally measured signal events and the obtained using the background shape considering energy scale $\phi$ asymmetry and flatness background is treated as the systematic error.

Figure 9.17 shows the background shapes for each asymmetries and flatness in energy region from 4.5 to 5.0 MeV. The solid flat line indicates the flatness background. The solid waving line indicates the $\theta$ asymmetry background. The dashed line indicates the background shape considering about $\phi$ asymmetry.

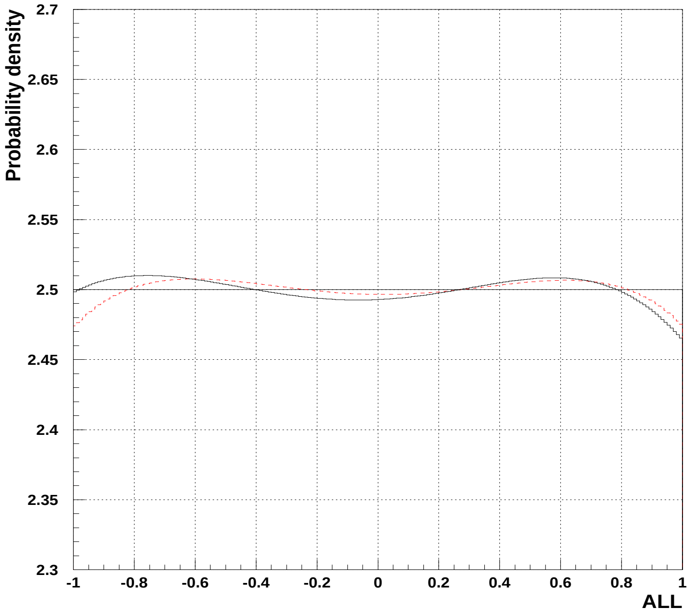

Figure 9.17: The fluctuation of probability function of $P_{bg}$ as $\cos\theta_{sun}$ function.

### Angular resolution

The measured angular resolution in MC simulation is slightly worse than in data as described in chapter 5. In solar neutrino signal extraction, the MC angular resolution is corrected so that it agrees with data. The systematic uncertainty due to angular resolution is the difference between the number of the obtained signal events using the MC angular resolution and using the corrected angular resolution.

| Energy region | Uncertainty (Data set III) | Uncertainty (Data set I,II) |
|---|---|---|
| 4.5 - 5.0 | ±4.5% | - |
| 5.0 - 5.5 | ±0.5% | ±0.6% |
| 5.5 - 6.0 | ±0.5% | ±0.5% |
| 6.0 - 6.5 | ±0.3% | ±0.1% |
| 6.5 - 7.0 | ±0.3% | ±0.1% |
| 7.0 - 20.0 | ±0.1% | ±0.1% |

Table 9.16: The uncertainty with the non-flat background.

| Energy region | Uncertainty (Data set III) | Uncertainty (Data set I,II) |
|---|---|---|
| 4.5 - 5.0 | ±1.0% | - |
| 5.0 - 20.0 | ±1.0% | ±1.0% |

Table 9.17: The uncertainty with the angular resolution.

### Likelihood fit resolution

The solar signal extraction is done by the likelihood function fit. Therefore, the signal extraction is dependent on the numerical method exactly. The systematic uncertainty with likelihood function fit is estimated as following steps.

1. The background events and the background shape is extracted from the final data sample ($\cos\theta_{sun} < 0$).
2. Using the energy distribution and $\cos\theta_{sun}$ distribution of the solar neutrino MC, the signal is generated by random number basing on Poisson function. This number of signals is true number.
3. Simulated data is made by combining the extracted background events and the generated signals. Then, the likelihood fit is applied to this simulated data.
4. The true number of signals is compared with the results from the likelihood fit. The difference of them is the uncertainty by the numerical method of the solar signal extraction.

| Energy region | Uncertainty (Data set III) | Uncertainty (Data set I,II) |
|---|---|---|
| 4.5 - 5.0 | ±0.5% | - |
| 5.0 - 20.0 | ±0.5% | ±1.0% |

Table 9.18: The uncertainty with the likelihood fit.

### Cross section

The uncertainty with the cross section between neutrino-electron elastic scattering is 0.2% all over energy region.

### Live time

The systematic uncertainty due to live-time calculation is evaluated from the difference between calculations using several different data samples (raw data, muon data or low energy triggered

| Energy region | Uncertainty (Data set III) | Uncertainty (Data set I,II) |
|---|---|---|
| 4.5 - 5.0 | ±0.2% | - |
| 5.0 - 20.0 | ±0.2% | ±0.2% |

Table 9.19: The uncertainty with the cross section.

| Flux | Uncertainty (Data set III) | Uncertainty (Data set I,II) |
|---|---|---|
| Total flux | ±0.1% | ±0.1% |

Table 9.20: The uncertainty with the live time calculation.

data). The systematic error has an effect on the flux measurement and Day/Night flux measurement.

Figure 9.18 shows the summary of the error for each energy bin. The empty circle means the error with data set I,II. The filled circle means the error with data set III which include 4.5 MeV data. Table 9.21 is a numerical summary of the figure.

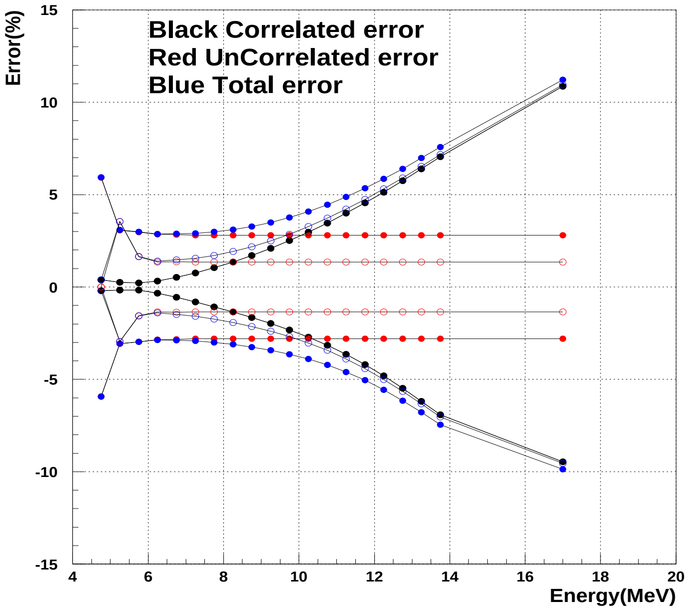

Figure 9.18: The total uncertainty with the energy spectrum.

| Energy | Total error(%) for dsIII | Total error(%) for dsI,II |
|---|---|---|
| 4.5 5.0 | +5.94 -5.93 | - |
| 5.0 5.5 | +3.07 -3.06 | +3.54 -2.95 |
| 5.5 6.0 | +2.97 -2.97 | +1.65 -1.56 |
| 6.0 6.5 | +2.86 -2.86 | +1.39 -1.39 |
| 6.5 7.0 | +2.87 -2.88 | +1.46 -1.47 |
| 7.0 7.5 | +2.90 -2.91 | +1.55 -1.57 |
| 7.5 8.0 | +2.98 -3.00 | +1.70 -1.73 |
| 8.0 8.5 | +3.11 -3.11 | +1.91 -1.91 |
| 8.5 9.0 | +3.28 -3.25 | +2.17 -2.13 |
| 9.0 9.5 | +3.49 -3.42 | +2.49 -2.39 |
| 9.5 10.0 | +3.76 -3.66 | +2.85 -2.68 |
| 10.0 10.5 | +4.08 -3.89 | +3.26 -3.03 |
| 10.5 11.0 | +4.45 -4.21 | +3.71 -3.43 |
| 11.0 11.5 | +4.87 -4.59 | +4.21 -3.89 |
| 11.5 12.0 | +5.34 -5.05 | +4.74 -4.41 |
| 12.0 12.5 | +5.84 -5.57 | +5.31 -5.00 |
| 12.5 13.0 | +6.39 -6.15 | +5.90 -5.64 |
| 13.0 13.5 | +6.97 -6.78 | +6.53 -6.33 |
| 13.5 14.0 | +7.58 -7.45 | +7.17 -7.04 |
| 14.0 20.0 | +11.21 -9.86 | 10.94 -9.55 |

Table 9.21: The numerical results for the total error ($\sqrt{\mathrm{Corr}_{\mathrm{err}}^2 + \mathrm{Uncorr}_{\mathrm{err}}^2}$).

# Chapter 10

# Discussions

In this chapter, the distortion of the solar neutrino energy spectrum and the effect of 4.5∼5.0 MeV bin for the constraints on the solar neutrino oscillation is discussed basing on the results of chapter 9. First, the distortion of the solar neutrino energy spectrum is inspected. After that, the effect of 4.5∼5.0 MeV bin for the constraints on the oscillation parameter decision is discussed.

## 10.1 The distortion of solar neutrino energy spectrum

In order to compare the shape of the observed energy spectrum with the expectation of SSM, the ratio of observed and expected numbers of events for each energy bin is taken; These ratios are plotted in chapter 9 as Data/SSM.

In order to inspect the distortion caused by solar neutrino oscillation, the observed energy spectrum is examined using the following $\chi^2$ definition [7]:

$$\chi^2 = \sum_{i=1}^{n_{ene}} \left\{ \frac{ (\frac{Data}{SSM})_i - \alpha \cdot \frac{1}{f_i^{corr}(\epsilon_{scl},\epsilon_{res},\epsilon_{b8})} }{\sigma_i} \right\}^2 + \epsilon_{scl}^2 + \epsilon_{res}^2 + \epsilon_{b8}^2 \tag{10.1}$$

where $\sigma_i$ is a $1\sigma$ error for each i-th energy bin defined as a sum of statistical error and uncorrelated errors added quadratically, and $\alpha$ is a free parameter which normalizes the measured $^8$B solar neutrino flux relative to the expected flux, and $f_i^{corr}$ is the response function and defined as follow:

$$f_i^{corr} = (1 + \sigma_{i,res} \times \epsilon_{res})(1 + \sigma_{i,scl} \times \epsilon_{scl})(1 + \sigma_{i,b8} \times \epsilon_{b8}) \tag{10.2}$$

where $\sigma_{i,res}, \sigma_{i,scl}, \sigma_{i,b8}$ are $1\sigma$ errors of the absolute energy scale, the energy resolution, and the expected solar neutrino spectrum shape. $\epsilon_{res}, \epsilon_{scl}, \epsilon_{b8}$ are also free parameters used for constraining the variation of correlated systematic errors.

The minimum value of this $\chi^2$ is obtained by numerically varying the free parameters. Table 10.1 shows the summary of the numerical results for the examination.

The resulting minimum $\chi^2$ corresponds to an agreement of the measured energy shape with the expected energy shape at the 51.0 % confidence level, for example, data set I. The rather poor fit of $\chi^2$ for the data set II is due mainly to fluctuation in the observed energy spectrum at lower energy region unless the statistics is almost enough. This fluctuation comes from the wrongness of S/N ratio without any tight data reduction unless the statistics is smaller than full data set I. Comparing the $\chi^2$ result of data set III with data set I, the result is almost consistent. This means the data quality of the data set III is good unless the statistics is poorer than the data set I.

| Data set | Energy region (d.o.f) | $\chi^2$ | $\alpha$ | C.L. |
|---|---|---|---|---|
| Data set I(1496d) | 5.0 - 20.0 (19-1=18) | 17.19 | 0.457 | 51.0% |
| Data set II(566d) | 5.0 - 20.0 (19-1=18) | 27.23 | 0.453 | 7.5% |
| Data set III(511d) | 5.0 - 20.0 (19-1=18) | 18.29 | 0.471 | 43.7% |
| Data set IV(511d) | 4.5 - 20.0 (20-1=19) | 20.11 | 0.472 | 38.8% |

Table 10.1: The minimum value of this $\chi^2$ is obtained by numerically varying the free parameters for energy spectrum distortion.

The data set IV indicates the distortion of the solar neutrino energy spectrum. This poorer fit of $\chi^2$ than the $\chi^2$ of data set I comes from the rise of the first 4.5∼5.0 energy bin in the observed spectrum. So, a comparison of the observed recoil electron energy spectrum from solar neutrino with the expectation exhibits a poorer agreement at the 38.8 % confidence level than the energy spectrum of 19 bins. By including the 4.5∼5.0 energy bin, the distortion of the energy spectrum becomes more certain.

## 10.2 Constraints on neutrino oscillation from energy spectrum

### 10.2.1 The allowed solutions from flux measurements

The observed flux in SK is 46.2% for the SSM prediction in full data set I, as described in chapter 9. The Chlorine experiments and Gallium experiments, which sensitive to lower energy neutrino, also show flux deficits in chapter 2. SNO experiment confirmed flux deficits as well. From these flux measurement results, 5 solutions resulted from local minimum $\chi^2$ is indicated by the parameter of two-flavor neutrino oscillation. In order to fit the observed flux from four experiments, a standard $\chi^2$ method is adopted. The definition on $\chi^2$ is as follows:

$$\chi^2 = \sum_{i,j=1}^{N_{exp}} (R_i^{data} - R_i^{osc}) V_{i,j}^{-1} (R_j^{data} - R_j^{osc}) \tag{10.3}$$

$N_{exp}$ is the number of the flux measurements, which is 4 in this analysis. $R_i^{data}$ is the ratio of the measured solar neutrino flux to the SSM predicted flux for each experiment. $R_i^{osc}$ is the ratio of the solar neutrino flux calculated assuming neutrino oscillations to the SSM prediction. $V_{i,j}$ is the error matrix which includes errors from the theoretical uncertainty in the solar neutrino flux. The definition in $V_{i,j}$ is as follows :

$$V_{i,j} = (\sigma_{i,j}^{cs})^2 + (\sigma_{i,j}^{ssm})^2 + (\sigma_{i,j}^{exp})^2 \tag{10.4}$$

where $\sigma_{i,j}^{cs}$ is an error matrix which includes the uncertainty in the neutrino cross sections. $\sigma_{i,j}^{exp}$ is an error matrix for each experiment. $\sigma_{i,j}^{ssm}$ is an error matrix for the uncertainty in the SSM. The uncertainties in the SSM are as follows :

- Uncertainty in the interaction cross section for reactions in the PP-chain and the CNO-cycle.
- Uncertainty in the solar luminosity.
- Uncertainty in the abundances of heavy elements.
- Uncertainty in the radiative opacity of the Sun.

| Mechanism | Solution | $\Delta m^2$ | $\tan^2\theta$ |
|---|---|---|---|
| Vacuum Oscillation | Vacuum solution | $7.9\times10^{-11}$ | 0.26/3.8 |
| | Quasi vacuum solution | $6.7\times10^{-10}$ | 1.50 |
| MSW effect | SMA | $4.6\times10^{-6}$ | 0.0016 |
| | LMA | $6.6\times10^{-5}$ | 0.42 |
| | LOW | $7.2\times10^{-8}$ | 0.63 |
| Global minimum | LMA | $6.0\times10^{-5}$ | 0.42 |

Table 10.2: The local minimum of $\chi^2$ for global analysis of all solar neutrino experiments. (Ga, Cl, SK, and SNO(CC))

- Uncertainty in the element diffusion in the Sun.

The local minimum of $\chi^2$ is shown in table 10.2. Figure 2.17 shows the iso-$\chi^2$ contours of $\chi^2 - \chi^2_{globalmin}$ corresponding to an allowed region at 95% C.L.. As shown in figure 2.17, there are several allowed regions.

### 10.2.2 Constraints from energy spectrum measurements

In this section, the distortion of the energy spectrum is inspected which solution is most flavored by comparing the observed energy spectrum with the expected energy spectrum by each solution. The solutions by each allowed regions are described above section.

When the distortion is examined for the expected energy spectrum, in the analysis, $\chi^2$ is defined as follows.

$$\chi^2 = \sum_{i=1}^{n_{ene}} \left\{ \frac{(\frac{Data}{SSM})_i^{data} - \frac{(\frac{Data}{SSM})_i^{exp}}{f_i^{corr}(\epsilon_{scl},\epsilon_{res},\epsilon_{b8})}}{\sigma_i} \right\}^2 + \epsilon_{scl}^2 + \epsilon_{res}^2 + \epsilon_{b8}^2 \tag{10.5}$$

The definitions of the parameters in above equation is same as previous section. $(\frac{Data}{SSM})_i^{exp}$ is the ratio of the flux calculated assuming neutrino oscillations to the SSM prediction and defined as follows.

$$(\frac{Data}{SSM})_i^{exp} = \frac{\alpha \times P_{i,osc}(^8B)\phi_i(^8B) + \beta \times P_{i,osc}(hep)\phi_i(hep)}{\phi_i(^8B) + \phi_i(hep)} \tag{10.6}$$

where $P_{i,osc}(^8\mathrm{B}, \mathrm{hep})$ is the oscillation probability function in i-th energy bin for $^8$B and *hep* flux, $\phi_i(^8\mathrm{B}, \mathrm{hep})$ is the each flux predicted by SSM. $\alpha$ and $\beta$ are free parameters so that one can perform a solar model independent analysis of neutrino oscillation parameters. Since the SSM prediction of the hep neutrino flux has large uncertainty, the hep contribution to the recoil electron spectrum can be treated as an additional free parameter.

Figure 10.1, figure 10.2, and figure 10.3 show the results of comparison between the observed energy spectrum and expected energy spectrum for each solution. The right plot in the figures is the results of data set III including 4.5∼5.0 MeV data. The left plot in the figures is the results of full data set I without 4.5∼5.0 MeV data. Figure 10.1, figure 10.2, and figure 10.3 are the comparisons for the vacuum oscillation solutions, the MSW solutions, and the global minimum $\chi^2$ of all solar neutrino experiments respectively. In table 10.3, the summary of the numerical results for the $\chi^2$ examination is presented.

The energy spectrum with 4.5∼5.0 MeV data does not favor the VO and the SMA solutions. It favors the LMA, the LOW, the Quasi VO solutions at almost same C.L.. However, the full data set favor LMA and Quasi VO solutions. The dominant factor of this difference is due to

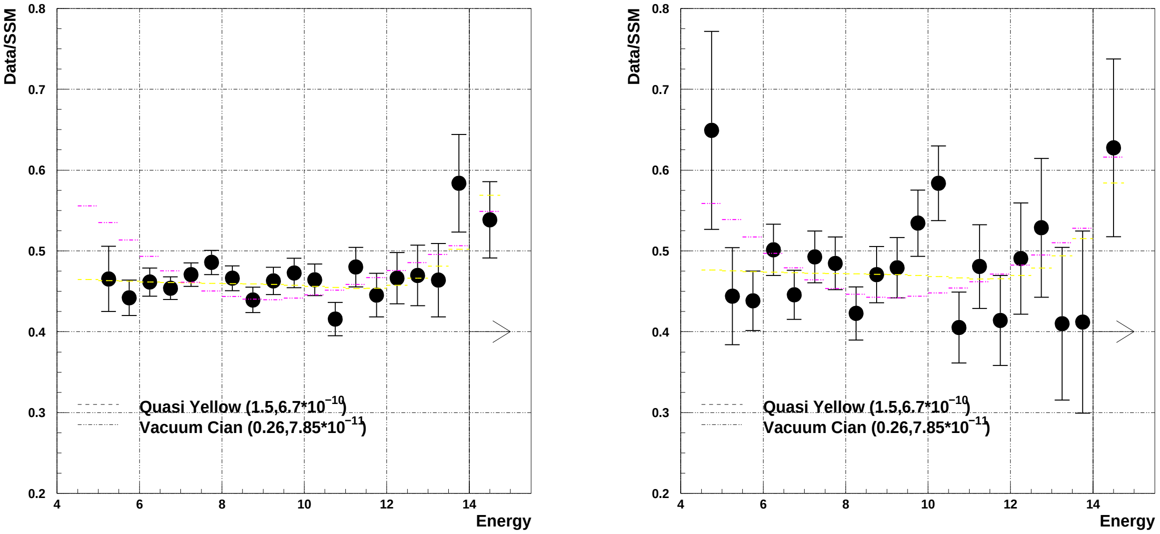

Figure 10.1: The comparison between the energy spectrum and the expected energy spectrum for the vacuum oscillation solutions.

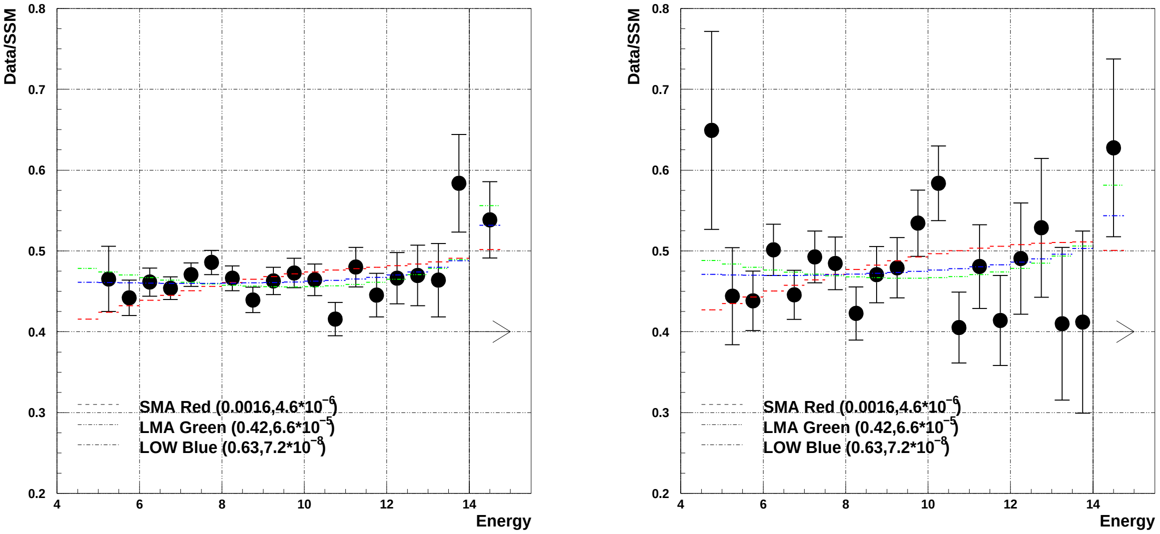

Figure 10.2: The comparison between the energy spectrum and the expected energy spectrum for the MSW solutions.

| Data set | Energy region (d.o.f) | $\chi^2$ | $\alpha$ | $\beta$ | C.L. |
|---|---|---|---|---|---|
| VO | | | | | |
| Data set I(1496d) | 5.0 - 20.0 (19-1=18) | 36.86 | 0.91 | 1.04 | 0.5% |
| Data set II(566d) | 5.0 - 20.0 (19-1=18) | 37.53 | 0.88 | 5.36 | 0.4% |
| Data set III(511d) | 5.0 - 20.0 (19-1=18) | 27.34 | 0.91 | 4.30 | 7.3% |
| Data set IV(511d) | 4.5 - 20.0 (20-1=19) | 28.15 | 0.91 | 4.31 | 8.1% |
| Quasi VO | | | | | |
| Data set I(1496d) | 5.0 - 20.0 (19-1=18) | 13.24 | 0.77 | 2.50 | 77.7% |
| Data set II(566d) | 5.0 - 20.0 (19-1=18) | 24.5 | 0.75 | 6.27 | 13.9% |
| Data set III(511d) | 5.0 - 20.0 (19-1=18) | 17.51 | 0.79 | 2.30 | 48.8% |
| Data set IV(511d) | 4.5 - 20.0 (20-1=19) | 19.37 | 0.79 | 2.49 | 43.3% |
| SMA | | | | | |
| Data set I(1496d) | 5.0 - 20.0 (19-1=18) | 28.84 | 0.98 | 3.88 | 5.0% |
| Data set II(566d) | 5.0 - 20.0 (19-1=18) | 29.79 | 0.96 | 3.62 | 4.0% |
| Data set III(511d) | 5.0 - 20.0 (19-1=18) | 21.27 | 0.99 | 1.01 | 26.6% |
| Data set IV(511d) | 4.5 - 20.0 (20-1=19) | 24.4 | 1.01 | 1.01 | 18.1% |
| LMA | | | | | |
| Data set I(1496d) | 5.0 - 20.0 (19-1=18) | 14.82 | 1.03 | 6.42 | 67.4% |
| Data set II(566d) | 5.0 - 20.0 (19-1=18) | 25.04 | 1.01 | 9.00 | 12.4% |
| Data set III(511d) | 5.0 - 20.0 (19-1=18) | 18.14 | 1.05 | 6.75 | 44.6% |
| Data set IV(511d) | 4.5 - 20.0 (20-1=19) | 19.78 | 1.05 | 6.88 | 40.8% |
| LOW | | | | | |
| Data set I(1496d) | 5.0 - 20.0 (19-1=18) | 14.92 | 0.90 | 4.91 | 66.7% |
| Data set II(566d) | 5.0 - 20.0 (19-1=18) | 24.33 | 0.87 | 7.56 | 14.4% |
| Data set III(511d) | 5.0 - 20.0 (19-1=18) | 17.63 | 0.91 | 4.59 | 48.0% |
| Data set IV(511d) | 4.5 - 20.0 (20-1=19) | 19.62 | 0.92 | 3.90 | 41.8% |
| Solar best | | | | | |
| Data set I(1496d) | 5.0 - 20.0 (19-1=18) | 14.69 | 1.04 | 6.29 | 68.3% |
| Data set II(566d) | 5.0 - 20.0 (19-1=18) | 24.84 | 1.01 | 10.45 | 12.9% |
| Data set III(511d) | 5.0 - 20.0 (19-1=18) | 18.05 | 1.06 | 6.72 | 45.2% |
| Data set IV(511d) | 4.5 - 20.0 (20-1=19) | 19.72 | 1.06 | 6.85 | 41.1% |

Table 10.3: The summary of the numerical results for $\chi^2$ examination for each oscillation solution.

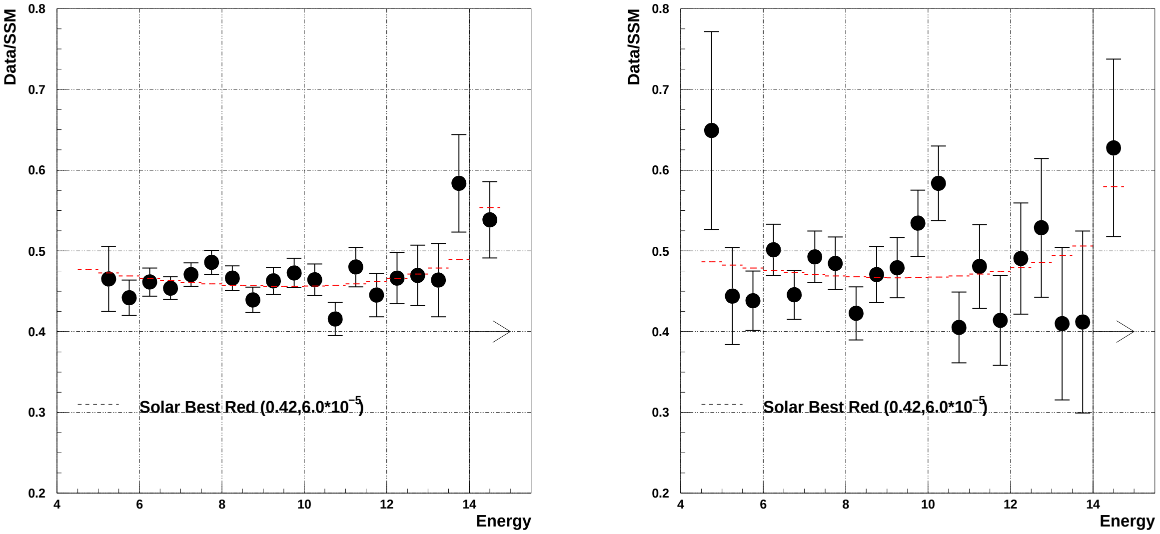

Figure 10.3: The comparison between the energy spectrum and the expected energy spectrum for the global minimum $\chi^2$ of all solar neutrino experiments.

the statistical uncertainty with the data set III. The comparison between data set III without 4.5∼5.0 data and data set IV with 4.5∼5.0 data means the 4.5∼5.0 data has no strong effect to the decision of oscillation solution, because the 4.5∼5.0 has large uncertainty in this analysis. Although the results of $\chi^2$ for 4.5∼5.0 data can not give a impact, one can understand in visual that the bin of 4.5∼5.0 MeV is key to decide the oscillation parameter.

## 10.3 Combined constraints on neutrino oscillation

Using the measured flux from the Chlorine and Gallium experiments, SK, SNO, and SK recoil electron energy spectrum, the allowed regions obtained.

The combinations of the analysis are as follows:

- Energy spectrum analysis
  - Constraints from the flux measurements of all solar neutrino experiments (Chlorine, Gallium, SK, and SNO). : make allowed region (Green area in the contour plot).
  - Constraints from the energy spectrum measurements by SSM independent analysis (flux(rate) not constrained). : make excluded region (Orange area in the contour plot).

$$\begin{aligned}\chi^2 &= \sum_{i,j=1}^{N_{exp}} (R_i^{data} - R_i^{osc}) V_{i,j}^{-1} (R_j^{data} - R_j^{osc}) \\ &+ \sum_{i=1}^{n_{ene}} \left\{ \frac{(\frac{Data}{SSM})_i^{data} - \frac{(\frac{Data}{SSM})_i^{exp}}{f_i^{corr}(\epsilon_{scl},\epsilon_{res},\epsilon_{b8})}}{\sigma_i} \right\}^2 + \epsilon_{scl}^2 + \epsilon_{res}^2 + \epsilon_{b8}^2 \end{aligned} \tag{10.7}$$

where $\alpha$ and $\beta$ are free parameters.

- Energy spectrum and global analysis
  - Constraints from the flux measurements of all solar neutrino experiments (Chlorine, Gallium, SK, and SNO). : make allowed region (Green area in the contour plot).

  - Constraints from the energy spectrum measurements by SSM independent analysis (flux(rate) not constrained). : make excluded region (Orange area in the contour plot).
  - Constraints from the energy spectrum measurements by SSM dependent analysis (flux(rate) constrained). : make allowed region. (Sky blue area in the contour plot).

$$\begin{aligned}
\chi^2 &= \sum_{i,j=1}^{N_{exp}} (R_i^{data} - R_i^{osc}) V_{i,j}^{-1} (R_j^{data} - R_j^{osc}) \\
&+ \sum_{i=1}^{n_{ene}} \Big\{ \frac{(\frac{Data}{SSM})_i^{data} - \frac{(\frac{Data}{SSM})_i^{exp}}{f_i^{corr}(\epsilon_{scl},\epsilon_{res},\epsilon_{b8})}}{\sigma_i} \Big\}^2 + \epsilon_{scl}^2 + \epsilon_{res}^2 + \epsilon_{b8}^2 \\
&+ \sum_{i=1}^{n_{ene}} \Big\{ \frac{(\frac{Data}{SSM})_i^{data} - \gamma \cdot \frac{(\frac{Data}{SSM})_i^{exp}}{f_i^{corr}(\epsilon_{scl},\epsilon_{res},\epsilon_{b8})}}{\sigma_i} \Big\}^2 + \epsilon_{scl}^2 + \epsilon_{res}^2 + \epsilon_{b8}^2 + \epsilon_{\gamma}^2 \qquad (10.8)
\end{aligned}$$

where $\gamma$ is a free parameter which is constrained by the SSM flux. The uncertainty in $\gamma$ comes from the uncertainty in the $^8$B neutrino flux. The $\epsilon_\gamma$ is the error factor due to the uncertainty in the $^8$B neutrino flux.

- Energy spectrum and global analysis with SNO(CC) flux constraints
  - Constraints from the flux measurements of all solar neutrino experiments (Chlorine, Gallium, SK, and SNO). : make allowed region (Green area in the contour plot).
  - Constraints from the energy spectrum measurements by SSM independent analysis (flux(rate) not constrained). : make excluded region (Orange area in the contour plot).
  - Constraints from the energy spectrum measurements by SSM dependent analysis (flux(rate) constrained by SNO(CC) result). : make allowed region (Sky blue area in the contour plot).

$$\begin{aligned}
\chi^2 &= \sum_{i,j=1}^{N_{exp}} (R_i^{data} - R_i^{osc}) V_{i,j}^{-1} (R_j^{data} - R_j^{osc}) \\
&+ \sum_{i=1}^{n_{ene}} \Big\{ \frac{(\frac{Data}{SSM})_i^{data} - \frac{(\frac{Data}{SSM})_i^{exp}}{f_i^{corr}(\epsilon_{scl},\epsilon_{res},\epsilon_{b8})}}{\sigma_i} \Big\}^2 + \epsilon_{scl}^2 + \epsilon_{res}^2 + \epsilon_{b8}^2 \\
&+ \sum_{i=1}^{n_{ene}} \Big\{ \frac{(\frac{Data}{SSM})_i^{data} - \gamma \cdot \frac{(\frac{Data}{SSM})_i^{exp}}{f_i^{corr}(\epsilon_{scl},\epsilon_{res},\epsilon_{b8})}}{\sigma_i} \Big\}^2 + \epsilon_{scl}^2 + \epsilon_{res}^2 + \epsilon_{b8}^2 + \epsilon_{\gamma}^2 \qquad (10.9)
\end{aligned}$$

where $\gamma$ is a free parameter which is constrained by the SNO(CC) flux measurement. The uncertainty in $\gamma$ comes from the uncertainty in the result of $^8$B neutrino flux measurement by SNO(CC) flux measurement. The $\epsilon_\gamma$ is the error factor due to the uncertainty of the $^8$B neutrino flux by SNO(CC) flux measurement.

Figure 10.4, figure 10.5 and figure 10.6 shows the allowed and excluded regions in " Energy spectrum analysis", "Energy spectrum and global analysis" and "Energy spectrum and global analysis with SNO(CC) flux constraints" respectively. In the figure 10.4, the distortion of recoil electron energy spectrum excluded the solutions of the Vacuum, the Quasi Vacuum oscillation and almost all of the SMA just by itself. In the global analysis with the SNO(CC) flux constraint, the LOW and a part of the LMA solution is favored by the distortion of the energy spectrum.

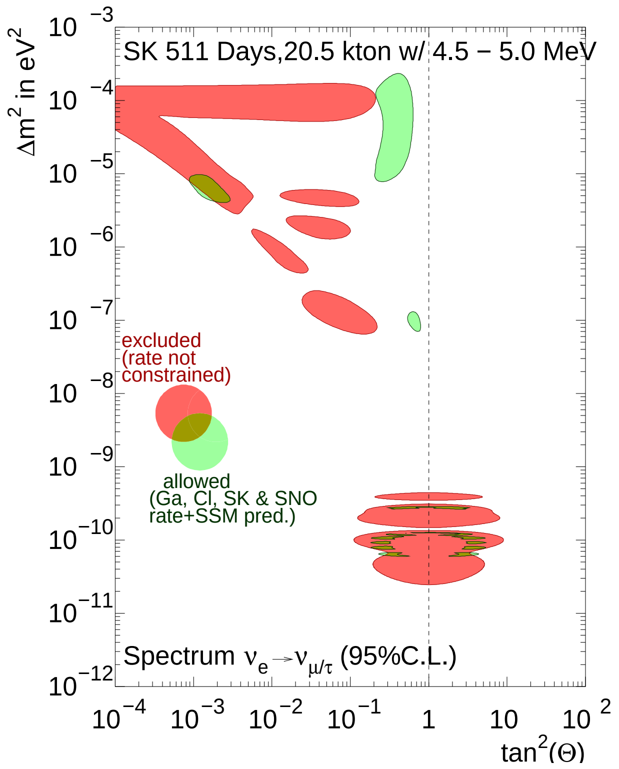

Figure 10.4: The allowed and excluded region in “ Energy spectrum analysis”.

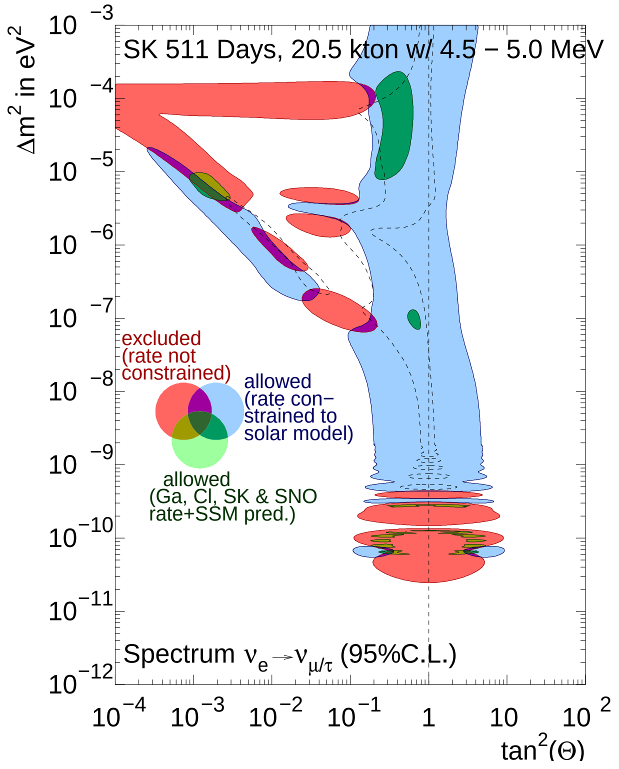

Figure 10.5: The allowed and excluded region in “ Energy spectrum and global analysis”

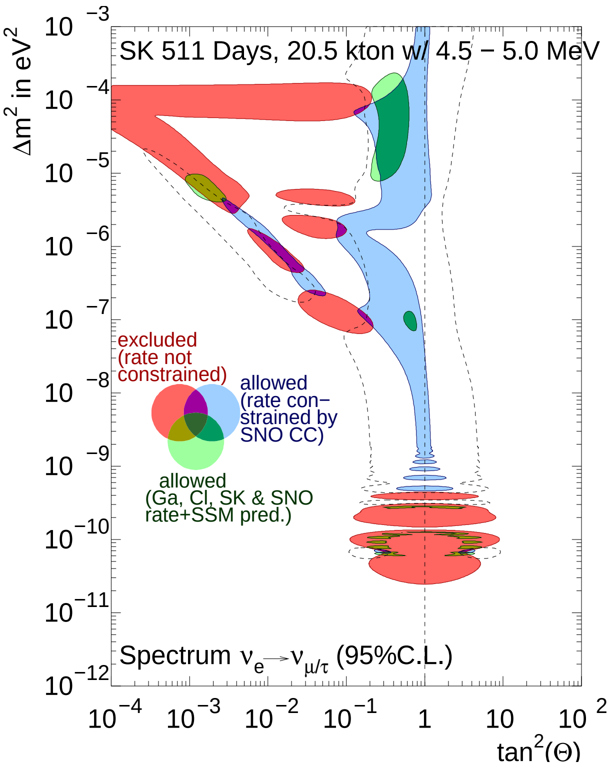

Figure 10.6: The allowed and excluded region in "Energy spectrum and global analysis with SNO(CC) constrain".

Figure 10.7 shows the comparison of the global analysis with the SNO(CC) flux constraint between the data set II without 4.5∼5.0 MeV data and the data set IV with 4.5∼5.0 MeV data. The excluded region becomes large in the SMA allowed region and the allowed region becomes small in the LMA region. The dominant factor for the changes are the new added bin (4.5∼5.0 MeV) in spite of the low statistics of the data set IV.

Figure 10.8 shows the comparison of the global analysis with SNO(CC) flux constraints between the data set III without 4.5∼5.0 MeV data and the data set IV with 4.5∼5.0 MeV data. The difference is just number of bins. The excluded region in the SMA solution becomes slightly large. But, the energy bin from 4.5 to 5.0 MeV has no effect on the LMA allowed region in this analysis. This is why the statistical uncertainty is still large for the decision for the LMA solution.

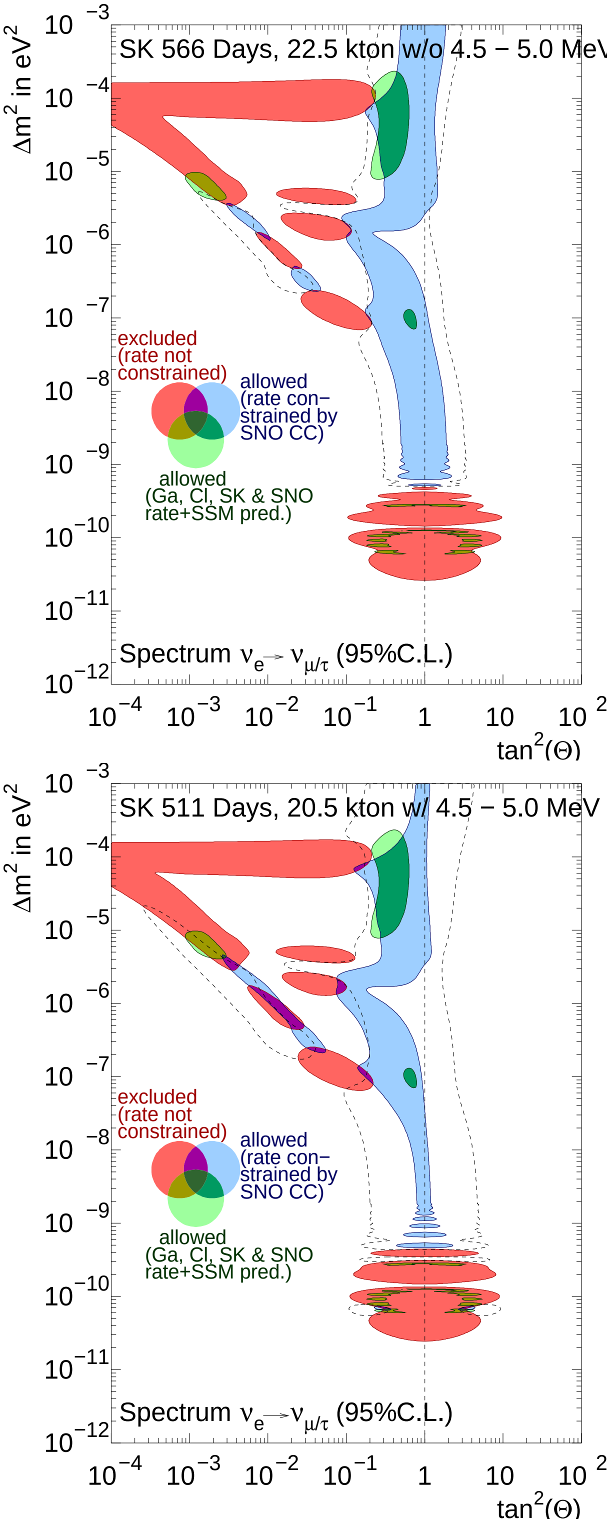

Figure 10.7: The comparison of the global analysis with the SNO(CC) flux constraint between the data set II without 4.5∼5.0 MeV data and the data set IV with 4.5∼5.0 MeV data.

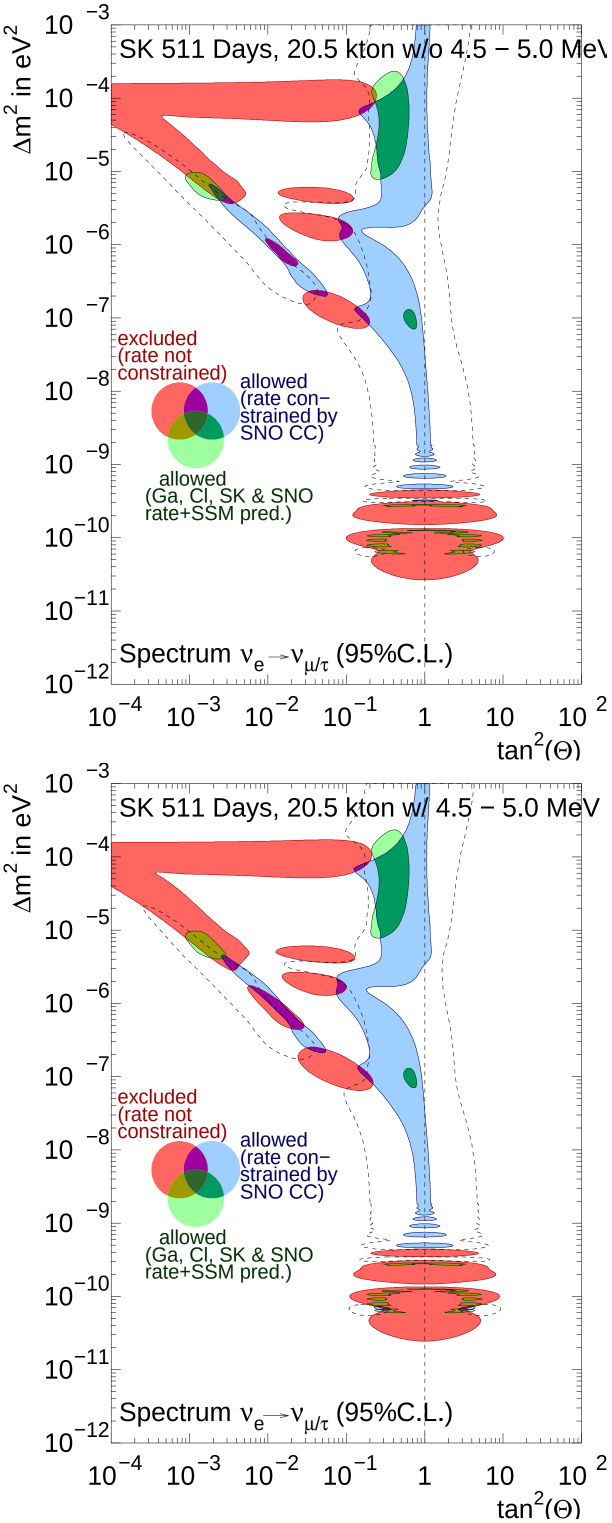

Figure 10.8: The comparison of the global analysis with the SNO(CC) flux constraint between the data set III without 4.5∼5.0 MeV data and the data set IV with 4.5∼5.0 MeV data.

# Chapter 11

# Conclusions and future prospect

## 11.1 Conclusions

SK-I observed the flux of the energy region from 4.5 to 5.0 MeV for the first time basing on 511 days new data set from the collection from May 31, 1996 to July 15, 2001. SK-I get a clear solar neutrino peak in the $\cos\theta_{sun}$ distribution of this energy region. The number of signals in this energy region is :

$$\mathrm{N}_{\mathrm{signal},4.5-5.0} = 722^{+139}_{-137}(\mathrm{stat.})^{+43}_{-43}(\mathrm{syst.}). \tag{11.1}$$

The $^{8}$B solar neutrino flux in the energy region from 4.5 to 5.0 MeV is obtained to be :

$$\Phi_{\nu}(\mathrm{SSM}_{\mathrm{BP2000}}, 4.5-5.0) = 3.28^{+0.63}_{-0.62}(\mathrm{stat.})^{+0.19}_{-0.19}(\mathrm{syst.})(\times 10^{6}/\mathrm{cm}^{2}/\mathrm{sec}) \tag{11.2}$$

The ratio to the SSM prediction is :

$$\mathrm{Data/SSM}(\mathrm{SSM}_{\mathrm{BP2000}}, 4.5-5.0) = 0.651^{+0.13}_{-0.12}(\mathrm{stat.})^{+0.038}_{-0.038}(\mathrm{syst.}) \tag{11.3}$$

In this energy region, the deficit of the solar neutrino to the SSM prediction is confirmed by about 3 sigma.

For the total flux, the ratio to the SSM prediction is obtained to be :

$$\mathrm{Data/SSM}(\mathrm{SSM}_{\mathrm{BP2000}}) = 0.479^{+0.014}_{-0.013}(\mathrm{stat.})^{+0.028}_{-0.025}(\mathrm{syst.}) \tag{11.4}$$

This ratio is consistent with the ratio for the 1496 days full data set within 1.3 sigma. It is concluded that the new data set to analyze 4.5∼5.0 MeV data has no systematic bias. The new results give the strong credit to the various SK-I results gathered up to now from different aspect.

The measured recoil electron energy spectrum from 4.5 to 5.0 MeV is presented. The energy spectrum is examined the distortion to the predicted SSM energy spectrum without the neutrino oscillation. The probability of the distortion is higher than full data analysis by including 4.5∼5.0 energy bin.

The energy spectrum is inspected which neutrino oscillation solution is most flavored by comparing with the expected energy spectrum of each solution in the SSM independent analysis. It is confirmed the 4.5∼5.0 MeV bin indicates the tendency of the LMA solution energy spectrum.

In combined constraints on neutrino oscillation, the excluded and allowed regions were obtained by the energy spectrum with 4.5∼5.0 MeV data. Almost of the SMA, all of vacuum solution and quasi vacuum solution is excluded at 95% C.L. only by SK energy spectrum measurements. By combined global analysis, a part of the LMA solution were also excluded at 95% C.L.. From the various comparisons between with 4.5~5.0 MeV data and without 4.5~5.0 MeV data, it is found that the allowed region around the LMA solution becomes slightly small and excluded regions around the SMA solution becomes slightly large. The 4.5~5.0 MeV data has an effect on the decision of the oscillation parameter.

However, the statistical uncertainty of the 4.5~5.0 MeV data is too large to discuss the decision of the oscillation parameter. In order to make this energy bin effective, we need more statistics of this energy bin with the smaller background.

## 11.2 Future prospect

Figure 11.1 shows the result of KamLAND (Kamioka Liquid scintillator Anti Neutrino Detector) experiment which has observe the disappearance of the anti-electron neutrino coming from the reactor [20]. The allowed region for neutrino two flavor oscillation by KamLAND is shown with the result of the global analysis for solar neutrino experiments (Chlorine, Gallium, SK, SNO). KamLAND also confirmed LMA solution as a most favored neutrino oscillation mechanism from a different point of view. The following equations are the oscillation probability and the best fit values for oscillation parameters in KamLAND Nails Neutrino Oscillations.

$$\begin{aligned} P_{\nu_e \rightarrow \nu_e} &= 0.611 \pm 0.085 \pm 0.041 \\ \Delta m^2 &= 6.9 \times 10^{-5} \mathrm{eV}^2, \tan^2\theta = 0.0 \end{aligned} \tag{11.5}$$

Figure 11.2 shows the result of this thesis including 4.5~5.0 MeV data overlaid with the expected spectrum of KamLAND result.

So, now, solar neutrino observation is shifting new phase. So far, it is searched whether the solar neutrino oscillation is correct or not and which oscillation solution is true. Now, we can search what parameter number of LMA solution is. In the figure 11.1, the green line shows the expected constraints by the asymmetry between day and night time flux.

To determine the oscillation parameter,

- We need more statistics, (the statistical uncertainty with asymmetry between day and night time flux is 2 times larger than the systematic uncertainty.)
- We need to observe the lower energy spectrum with high statistics.

It is important to improve the S/N ratio in the low energy region as much as possible in order to satisfy above requirements in the future. All solar neutrino experiments locate in underground. Radon is the most dominant source of the background for the solar neutrino observation. So, primary subjects is to reduce radon background in all solar neutrino experiments. Our development of the technique to lower energy threshold will be useful in the future.

In SK detector, the dominant background source is the radon transported by the water convection from PMTs. In SK-II, PMTs are covered with acrylic case. And, the controller system of the water convection is installed in the tank of the SK-II detector. We confirmed the zone of the water convection becomes smaller than SK-I by measuring the temperature in the SK-II tank. Figure 11.3 shows the water temperature with height of the SK-I tank and the SK-II tank.

The zone of the water convection in the SK-II becomes smaller than the SK-I by the effect of controller system. In the future, we can hope to lower the energy threshold and improve the S/N ratio in the solar neutrino observation.

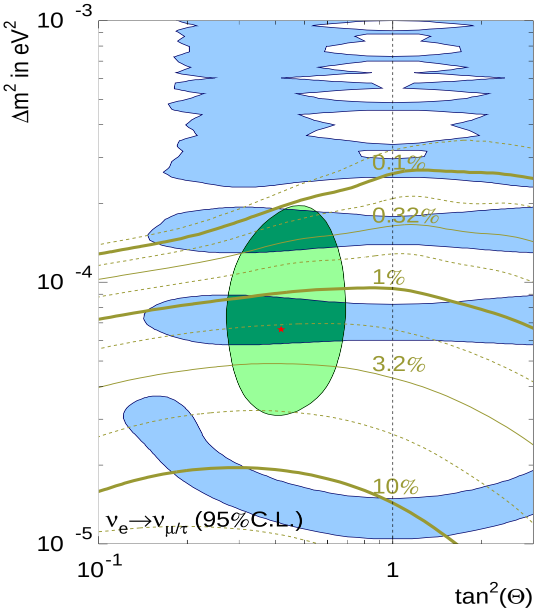

Figure 11.1: The KamLAND result is overlaid with the results of global analysis for solar neutrino experiments (Chlorine, Gallium, SK, SNO). [2]

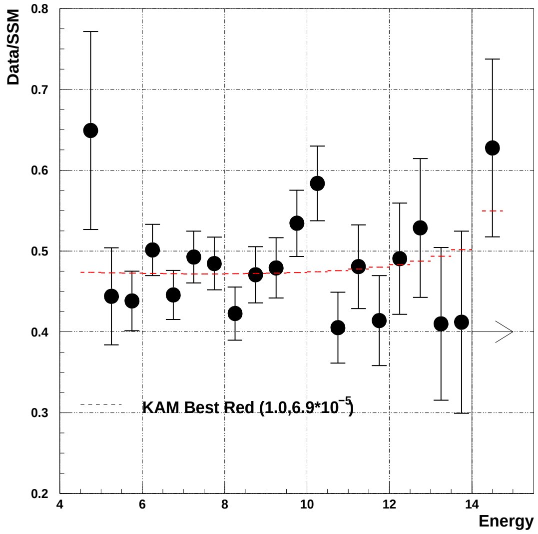

Figure 11.2: The expected spectrum from KamLAND result and the energy spectrum of this thesis with 4.5∼5.0 MeV data.

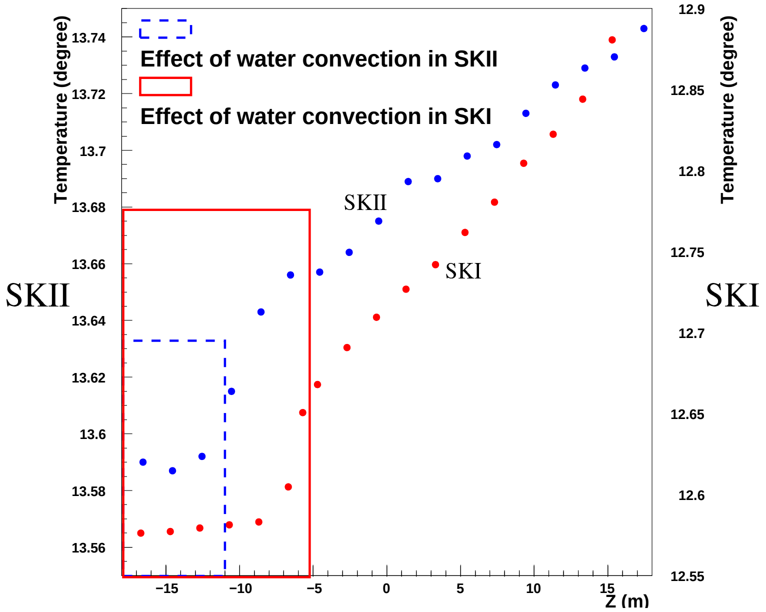

Figure 11.3: The water temperature with the height of the tank in SK-I and SK-II. The box with solid line and dashed line shows the SK-I and SK-II convection zone in the bottom region respectively.

# Appendix A

# The $^7$Be and *hep* neutrino flux

The most important nuclear physics experiment for solar neutrino research is an accurate measurement of the low energy proton capture rate on $^7$Be. The largest astrophysical uncertainties in the calculation of the $^8$B neutrino flux are about 5% [60]. Therefore, the low energy cross section for the production of $^8$B by proton capture on $^7$Be must be measured to an accuracy of 5 % in order to prevent this nuclear physics measurement from dominating the error budget in inferring astrophysical and neutrino properties from solar neutrino experiments.

The flux of the higher energy neutrinos (from $^8$B beta-decay) that is measured in the Kamiokande, Super-Kamiokande, and SNO solar neutrino experiments is proportional to the low energy value for the proton capture cross section. According to the combined standard model (standard solar model and standard electroweak theory), the rate measured in the chlorine solar neutrino experiment is also proportional to this cross section. The rate at which $^8$B is produced in the Sun is so slow that the value of the proton capture cross section on $^7$Be that is assumed in the solar model calculations has no perceptible effect on the solar models. This is the reason for the linear dependence of the $^8$B neutrino flux on the $^8$B production cross section.

$$^7\mathrm{Be(beam)} + \mathrm{H(target)} \rightarrow \ ^8\mathrm{B} + \gamma \tag{A.1}$$

The $^3\mathrm{He} +^4\mathrm{He}$ fusion cross section must also be measured more precisely. The uncertainties in this cross section dominate the uncertainties in the prediction of the $^7$Be neutrino flux and are also an important source of uncertainty in the prediction of the $^8$B neutrino flux.

## A.1 The $^7$Be neutrino flux

T he flux of $^7$Be solar neutrinos is relatively accurately determined by standard solar models, but-if one assumes nothing happens to solar neutrinos after they are created-the $^7$Be neutrinos appear to be almost entirely absent in the gallium and chlorine solar neutrino experiments. This is one of the most severe aspects of the "solar neutrino problem." This viewgraph shows that the flux of $^7$Be solar neutrinos is independent of the rate at which $^8$B neutrinos are produced by the relatively less certain cross section for proton capture on $^7$Be. The reason is that the proton capture, which gives rise to $^8$B neutrinos, is very much slower than the electron capture that gives rise to $^7$Be neutrinos.

$$\phi(^7Be) \propto \frac{R(e)}{R(e) + R(p)} \tag{A.2}$$

$$R(p) \approx 0.001 R(e) \tag{A.3}$$

The figure A.1 shows the fractional differences between the calculated sound speeds for the standard model and what may e the most accurate available sound speeds measured by helioseismology, the LOWL1 + BiSON measurements presented in Basu *et al.* (1997) [62]. These sound speeds are derived from a combination of the data obtained by the Birmigham Solar Oscillation Network(BiSON) and the Low-$\ell$ instrument (LOWL). The rms fractional difference between the calculated and the measured sound speeds is $10.4 \times 10^{-4}$ over the entire region in which the sound speeds are well measured, $0.05 \leq r \leq 0.95 R_\odot$. In the solar core, $0.05 \leq r \leq 0.25 R_\odot$ (in which about 95%of the solar energy and neutrino flux are produced in a standard solar model), the rms fractional difference $6.3 \times 10^{-4}$. The standard model sound speeds agree with the measured sound speeds to 0.1% whether or not one limits the comparison to the solar interior or averages over the entire Sun. Systematic uncertainties $\sim 3 \times 10^{-4}$ are contributes to the sound speed profile by each of three sources: the assumed reference model, the width of the inversion kernel, and the measurement errors(BPB00 [62]). The vertical scale of the figure was chosen so as to include the arrow marked "$^7$Be lowered ($\sigma$ off Ga)". This arrow indicates the typical difference between solar model speeds and helioseismological measurements that would be expected if the discrepancy between the gallium solar neutrino measurements and the predictions were due to errors in the solar physic of the standard solar model (BBP98 [63]).

The figure shows the excellent agreement between the calculated sound speeds for the Standard solar model (BP2000) and the helioseismologically measured (Sun) sound speeds. The horizontal line at 0.0 represents the hypothetical case in which the calculated sound speeds and the measured sound speeds agree exactly everywhere in the Sun. The rms fractional difference between the calculated and the measured sound speeds is 0.10% for all solar radii between between 0.05 $R_\odot$ and 0.95 $R_\odot$ and is 0.08% for the deep interior region, r 0.25 $R_\odot$, in which neutrinos are produced. Taken from figure A.2 of "Solar Models: current epoch and time dependences of normalized luminosity".

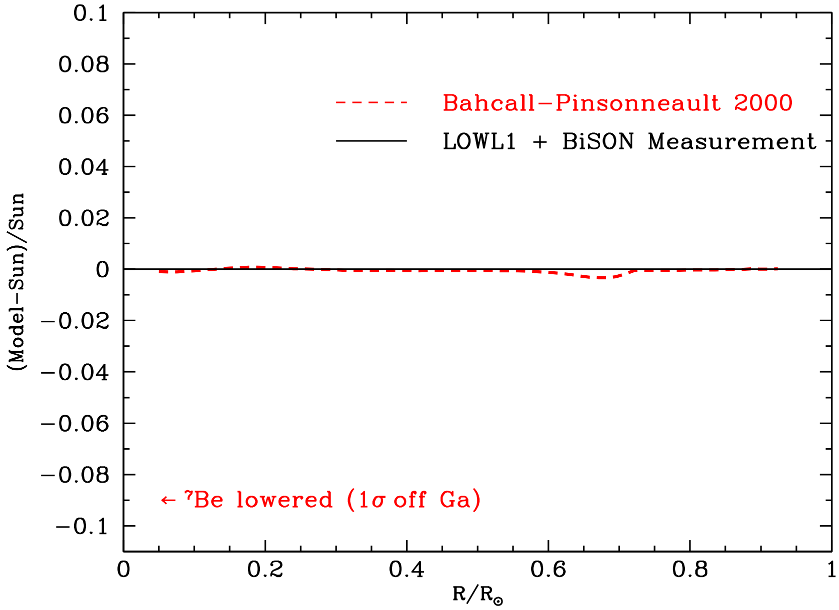

Figure A.1: Predicted versus measured sound speeds. (http://www.sns.ias.edu/j̃nb/)

## A.2 The hep neutrino flux

In the *hep* neutrino flux calculation of the BP2000, the most recent and detailed calculation (Marcucci *et al.* 2000a [64]) is used for the $S_0$-factor for the $^3\mathrm{He}(\mathrm{p}, \mathrm{e}^+ + \nu_\mathrm{e})^4\mathrm{He}$ reaction:$S_0(hep) = 10.1 \times 10^{-20}$keVb, which is a factor of 4.4 times larger than the previous best estimate. For values of $S_0(hep)$ in the range of current estimates, the assumed rate of the *hep*-reaction only affects in a noticeable way the calculation flux of *hep* neutrinos and does not affect the calculated

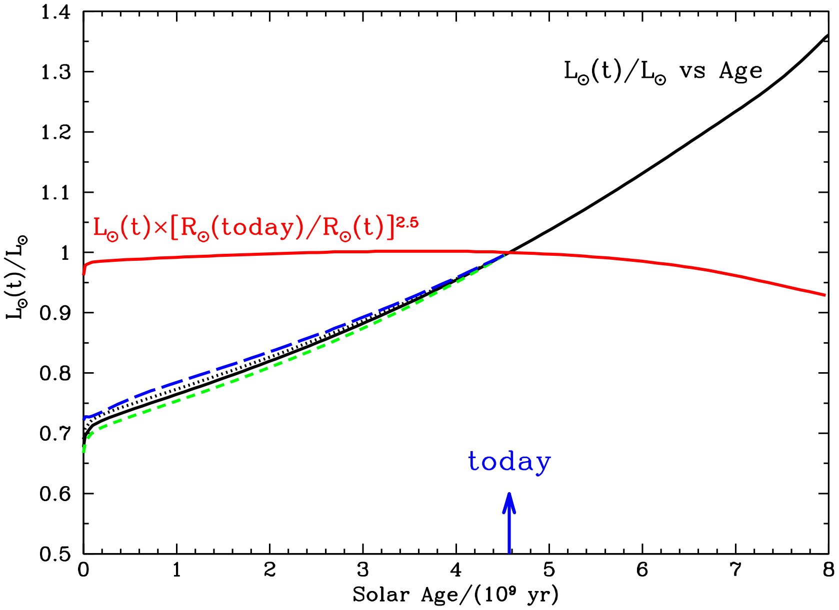

Figure A.2: Normalized solar luminosity vs. solar age for the standard solar model (solid curve) and for three "deficient" solar models: the No Diffusion model (dotted curve), the $S_{34} = 0$ model (short-dashed curve), and the Mixed model (long-dashed curve). (http://www.sns.ias.edu/$\tilde{\text{j}}$nb/)

flux fluxes of other neutrinos, helioseismological characteristics, or other physical properties of the Sun.

An estimated uncertainty for the *hep* flux is not quoted. The difficulty of calculating from first principles the nuclear cross section factor $S_0(hep)$ is an uncertainty in the *hep* flux. The *hep*-reaction is uniquely difficult to calculate among the light-element fusion reactions since the one-body and two-body contributions to the reaction rate are comparable in magnitude but opposite in sign, so that the net results is sensitive to a delicate cancellation. Also two-body axial currents from excitations of $\delta$ isobars are model dependent. In addition, the calculated rate is sensitive to a small components in the wave function, particularly $D - state$ admixture generated by tensor interactions. These complications have been discussed most recently and most throughly by Marcucci *et al.* (2000b).

From the analysis using the recoil electron energy spectrum from 18 MeV to 25 MeV in 1496 days of data, the preliminary upper limit of the *hep* neutrino is obtained to be 7.9 times the *hep* flux predicted by the SSM (BP2000).

# Appendix B

# Detector simulation

In order to investigate solar neutrino physics, the detector response for solar neutrino events has to be known. In order to understand the detector response, a Monte Carol (MC) simulation of the detector is carried out. The simulation program is based on GEANT [91] which is developed at CERN (European laboratory for particle physics). The program reproduces the behavior of electrons and photons in materials faithfully with the consideration of physical processes such as Coulomb multiple scattering, ionization loss, bremsstrahlung, etc. for electrons, and Compton scattering, pair creation, etc. for photons in energy range of a few keV to a few TeV.

In the SK detector simulation, the production and propagation of Čerenkov photons generated by recoil electrons have to be considered also [99]. The production of these is based on equation (3.2). The propagation of these is slightly complicated. When the Čerenkov photons travel in water, they suffer Rayleigh scattering and absorption. Rayleigh scattering is dominated for short wavelength ($\lambda \leq$400nm) due to wavelength dependence of $\propto 1/\lambda^4$, and the absorption effect is dominant for long wavelength ($\lambda \geq$ 400nm). These effects are related to the water attenuation length. The theoretical wavelength dependence of Rayleigh scattering and absorption are calculated [80] separately, however, the magnitude of these effects is not known since these factors depend on the purity of water. Therefore, these parameters are tuned in the MC. These parameters with a collection factor (described later) are turned so that the simulation of the LINAC calibration (see chapter 5) reproduces the real data. In figure B.1, the wavelength dependence of attenuation coefficient for light in the water in SK, which is calculated from the tuned parameters, is shown together with the results of a direct measurement (A description of this direct measurement is given in chapter 5.).

The speed of Čerenkov light in water depends on the wavelength. The speed is the group velocity $v_g$ which is given by:

$$v_g = \frac{c}{n(\lambda) - \lambda \dfrac{dn(\lambda)}{d\lambda}} \tag{B.1}$$

where $n(\lambda)$ is index of refraction as a function of wavelength $\lambda$ and is parameterized as [81]:

$$n(\lambda) = \sqrt{\frac{a_1}{\lambda^2 - \lambda_a^2} + a_2 + a_3\lambda^2 + a_4\lambda^4 + a_5\lambda^6} \tag{B.2}$$

The unit of $\lambda$ is $\mu$m and the parameters are tabulated in table B.1. These values were obtained by fitting equation (B.2) to the results of measurements. This index of refraction and group velocity is also put into the detector simulation.

The Čerenkov photons are reflected by the surface of PMTs and black sheet. The reflectivities of PMT and black sheet are calculated under the law of optics (The structure of the surface of a PMT is composed of 4mm thickness glass ($n$ = 1.47) and 20nm thickness bi-alkali ($n$ = 3.50)and the layer of bi-alkali is inside of the glass layer. The index of refraction of black sheet (polyethylene) is 1.6.) and the results are again put into the simulation. The polarization of

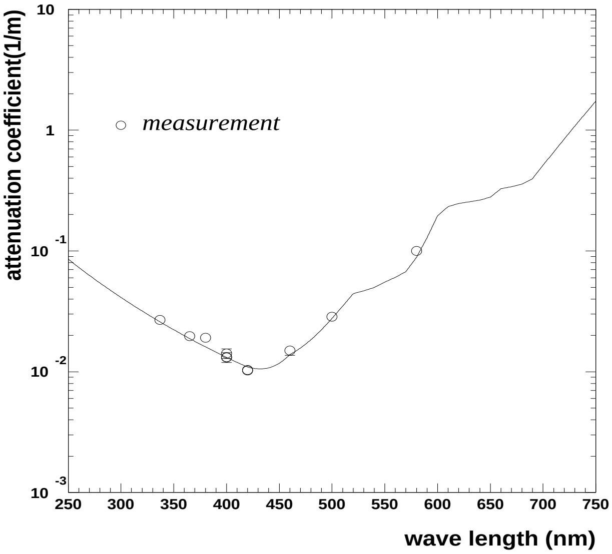

Figure B.1: The water attenuation coefficient for the water in SK tank which is calculated from the tuned parameter. Open marks are the measured value (see chapter 5).

| parameter | value |
|---|---|
| $\lambda_a^2$ | 0.018085 |
| $a_1$ | $5.743534\times10^{-3}$ |
| $a_2$ | 1.769238 |
| $a_3$ | $-2.797222\times10^{-2}$ |
| $a_4$ | $8.715348\times10^{-3}$ |
| $a_5$ | $-1.413942\times10^{-3}$ |

Table B.1: The values of parameters in equation (B.2).

Čerenkov photon is considered at the reflection step. The reflectivities of the PMT and black sheet are shown in figure B.2 for $p$-wave and $s$-wave and the average of both polarization.

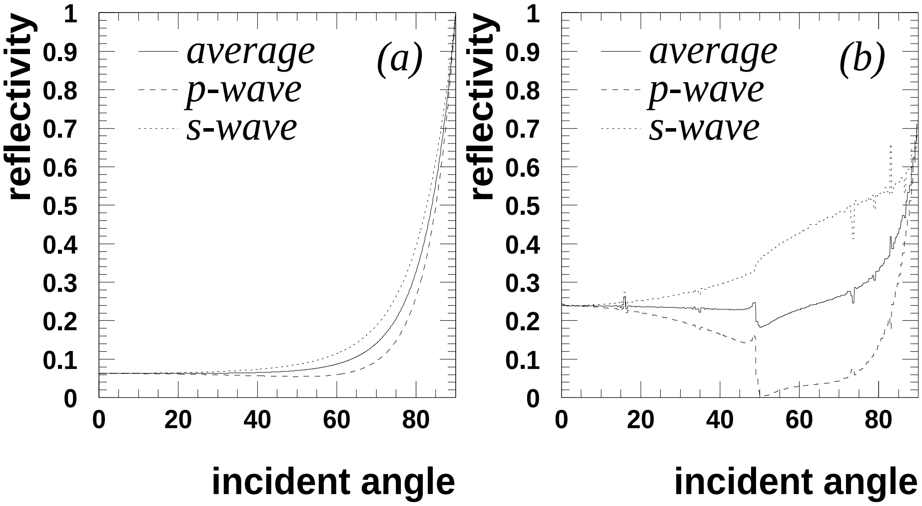

Figure B.2: The reflectivity of the PMT and black sheet. Figure(a) is for black sheet and (b) for the PMT. The horizontal axis of each figure is the incident angle (degree) and the vertical axis is reflectivity.

The PMT response to Čerenkov photons has to be considered. To begin with, the wavelength dependence of the quantum efficiency (see figure 3.12), which was measured by HAMAMATSU, is taken into account. For a solar neutrino event, most PMTs are given only 1 photo-electron, therefore it is important to know the output charge distribution of a PMT which is given by a single photo-electron, in order to choose the threshold on the analog signals at the ATM. This distribution is measured using the Ni-Cf source. A typical distribution of output charges in response to single photo-electron hits is shown in figure B.3. The output charge in the MC simulation is determined by random number distribution of figure B.3. The time resolution of a PMT is also taken into account. The resolution is calibrated using the vertex resolution of LINAC data.

Finally, the contribution of the dark noise is taken into account. PMT dark noise is simulated by distributing random hits according to the observed average dark rate of the ID PMTs. The charge for these hits is distributed according to the single photo-electron distribution. The dynode collection efficiency, which is the probability that an electron generated by the photoelectric effect reaches the dynode, is not known. Accordingly, this factor is also tuned in the MC simulation.

The ID-PMTs have two kinds of after-pulses. One after-pulse arrives about 15$\mu$sec after the signal. This kind of after-pulse happens when a large amount of Čerenkov photons (greater than 400p.e.) hit the PMT. The reason is that the many electrons generated by the photons ionize the remaining gas in the PMT on their way from cathode to dynode. The ions move to the cathode with a smaller velocity due to their large mass, and many electrons are generated again when the ions hit the cathode. Another after-pulse, which is more serious for solar neutrino observation, arrives about 100nsec after signal. This after-pulse is caused by an electron which is scattered by the first dynode elastically and goes back to the dynode with a time lag. As a result, the timing response of the PMT can be delayed by about 100nsec. In the detector simulation, this after-pulse is generated with 2% probability, which is measured by LINAC and Ni-Cf calibration, and a time delay which is distributed in a Gaussian of 10nsec width and a

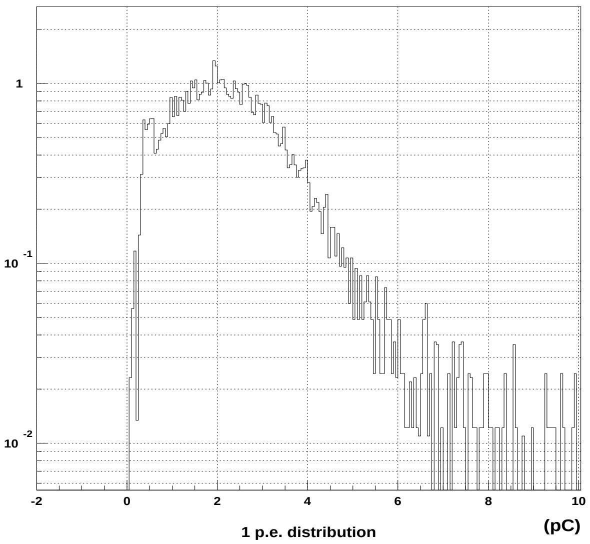

Figure B.3: The charge distribution of a PMT after a single photo-electron hit.

mean of 100nsec.

The result of the detector simulation is recorded in the same format as real data, and the same analysis is applied.

# Appendix C

# Reconstruction of cosmic ray muons

Cosmic ray muons are generated by the interactions of the primary cosmic ray particles high in the atmosphere. They penetrate 1000m rock and reach the ID at a rate of about 2Hz. The energetic muons often break $^{16}$O nuclei and produce radioactive elements, which decay by emitting electrons or positrons or $\gamma$-rays with energies ranging up to about 20 MeV. Since the energy of these events is similar to that of the recoil electrons from solar neutrinos, these events (spallation events) become a serious background. In order to reject spallation events, precise reconstruction of the muon tracks is crucial, because the vertex position of spallation events is strongly correlated with the track of the parent muon. In this section, brief explanations of muon fitting and quality of the reconstruction are given.

A muon event is defined as an event where the total number of photo-electrons is greater than 6000p.e. (For reference, note that if a muon travels 1m in the ID, about 2300p.e. are observed.) and one PMT exists which recorded a charge greater than 200p.e.. Reconstruction of the muon event proceeds in two steps. The first step is called 'fast reconstruction'. This method finds the entrance point and the exit point of the muon as follows. The entrance position is defined as the position of the PMT which is hit earliest and has more than 2 neighboring hits within 5nsec. The exit point is defined as the center of gravity of the PMTs which detect more than 231p.e. (from now on these PMTs are called 'charge-saturated PMTs'). The track of the muon is the line connecting the entrance and exit points. The success or failure of the first reconstruction method is tested as follows. Two variables are defined: $L_{ent}$, which is the minimum distance between each charge-saturated PMT position and the entrance point, and $L_{exit}$, which is the maximum distance between each charge-saturated PMT position and the exit point. If $L_{ent} > 300$cm and $L_{exit} < 300$cm, the reconstruction is regarded as success. This required condition rejects stopping muons (the muons which stop in the ID) and multiple muon events (more than 2 muons enter the ID at the same time). The events whose reconstruction fails go to the second reconstruction step.

When the number of the charge-saturated PMTs is large, the first reconstruction may have failed. Therefore, events with a residual charge $Q_{res}$ greater than 25,000p.e. are always sent to the second reconstruction step even though the requirements on $L_{ent}$ and $L_{exit}$ in the first step are met. $Q_{res}$ is defined by:

$$Q_{res} = Q_{total} - pL \tag{C.1}$$

and $Q_{total}$ is the total photo-electrons observed in the event, $L$(cm) is the track length, and $p$ = 23p.e./cm is the average number of observed photo-electrons per unit track length for muons.

The second step reconstruction is based on the vertex reconstruction method of solar neutrino events. The difference is that the track of a muon is not point-like. In this reconstruction method, the entrance point is same as that used by the fast reconstruction method and the exit point is searched for so as to maximize the goodness $g_\mu$ defined by:

$$g_\mu = \frac{\sum_i \frac{1}{\sigma_i^2} \exp\left\{ -\frac{1}{2}\left(\frac{t_i - T}{1.5\sigma_i}\right)^2 \right\}}{\sum_i \frac{1}{\sigma_i^2}} \tag{C.2}$$

$$t_i = T_i(\boldsymbol{x}_i) - \frac{l_\mu(\boldsymbol{x}_{exit})}{c} - \frac{l_{photon}(\boldsymbol{x}_{exit})}{c'} \tag{C.3}$$

where $\boldsymbol{x}_{exit}$ is the exit point and $T$ is the arrival time of the muon. $l_\mu(\boldsymbol{x}_{exit})$ and $l_{photon}(\boldsymbol{x}_{exit})$ are defined in figure C.1. If $L_{ent} > 300$cm, $L_{exit} < 300$cm and $g_\mu > 0.88$, this muon fit is regarded as successful. Events which do not satisfy this condition are regarded as unfitted.

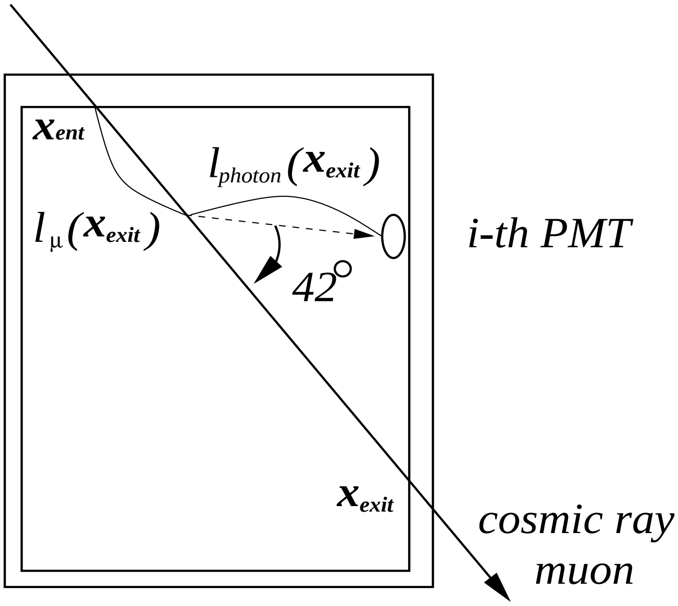

Figure C.1: The definition of the variables used by the second muon reconstruction.

The efficiency of the muon event reconstruction is checked by visual inspection for 1000 muon events. For this purpose, muon events are classified as follows

- single muon events : events which contain only a single muon track
- stopping muon events : muon events stopping in the ID
- hard interaction events : events with $Q_{res} \geq$25000p.e.
- edge clipping events : muons with track length less than 5m
- multiple muon events : events which contain more than or equal to 2 muon tracks

Table C.1 summarizes the fitting efficiency. About 6% of the muon events are not fit.

The precision of the muon track reconstruction is evaluated by comparing the results of above fitting and manual fitting, which is carried out by visual scan. This comparison is performed in the following way: (1) calculate the distance between the entrance points obtained by both program and manual fits ($d_{ent}$), (2) calculate the distance between exit points obtained by both fits ($d_{exit}$), (3) define the average distance between them ($(d_{ent} + d_{exit})/2 \equiv \overline{d}$). The distribution of $\overline{d}$ is shown in figure C.2. The track resolution is defined as shown in figure C.2; i.e. it is the distance which 68% of all entries fill below. It is evaluated to be 67cm.

| muon type | number of events | number of unfitted events |
|---|---|---|
| single muon | 835 | 5 |
| stopping muon | 10 | 8 |
| hard interaction | 41 | 2 |
| edge clipping | 58 | 19 |
| multiple muon | 56 | 28 |
| total | 1000 | 62 |

Table C.1: The fitting efficiency for the classified muon events.

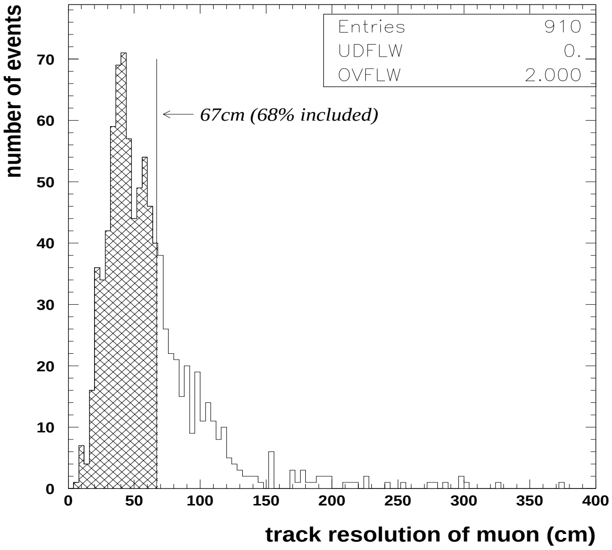

Figure C.2: The track resolution. The resolution is evaluated to be 67cm.

# Appendix D

# Systematic uncertainties with LINAC calibration

## D.1 LINAC beam energy calibration

In order to calibrate the SK detector within 1% accuracy, the precise beam energy has to be known. The beam energy is measured by a Ge detector. The Ge detector has a germanium crystal of 57.5mm diameter and 66.4mm length. Energy resolution of the detector is 1.92 keV for the 1.33 MeV $\gamma$-rays of $^{60}$Co. Reading out the output charge of the Ge detector and digitization of it is done by a Multi-Channel-Analyzer. After pulling up the vertical pipe in figure 5.13 and disconnecting the D3 magnet, the end-cap with the trigger counter is connected horizontally just before the D3 magnet. The Ge detector is located just after the end-cap. Relation between deposit energy in the crystal and digital counts is calibrated using $\gamma$-rays in energy range from 0.662 MeV of $^{137}$Cs to 9.000 MeV of Ni(n,$\gamma$)Ni reaction. Linearity is kept within 0.03% error in the energy range.

The primary purpose of using a Ge detector is to measure energy of not electrons but $\gamma$-rays. In a case of electrons, they go through a thin beryllium window, which is the entrance window of it, and inactive region surrounding the Ge crystal before they reach the active region. As a result, the electrons lose some of their energy before being detected. In order to measure the energy loss, the Ge detector was calibrated using an air-core beta spectrometer at the Tanashi-branch of KEK. A view of the spectrometer is shown in figure D.1. A radioactive element of $\beta$-rays used for that purpose is $^{207}$Bi. A $^{207}$Bi emits a monochromatic electron by internal conversion process with a half life of 38 years. Ratio of momentum spread to momentum $\Delta p/p$ at focus place is about 0.01% [72]. The 975.7 and 1682.2 keV electrons are used to calibrate. Figure D.2 shows comparisons between background subtracted data and MC simulation, where the depth of the inactive layer and the thickness of the beryllium window are tuned to be 41$\mu$m and 500$\mu$m respectively.

With the knowledge of the energy loss at the Ge detector, energies of the electron beam injected into the water tank are measured for various D1 magnet electric current. Table D.1 lists correlation of the D1 magnet current and the measured energy by the Ge detector. The beam energies in the beam pipe are evaluated by taking into account energy losses of the trigger counter, the Ti window, the Be window and the inactive region by MC simulation. The total energy in SK tank is calculated from the evaluated beam momentum and the energy loss of the trigger counter and the Ti window.

Figure D.3 shows the energy spectrum measured by the Ge detector for various beam momentum with MC simulation. The measurements were done five times for three $x$ positions. The uncertainty of the beam energy is evaluated by comparing different measurements and estimated to be ±20 keV for full width.

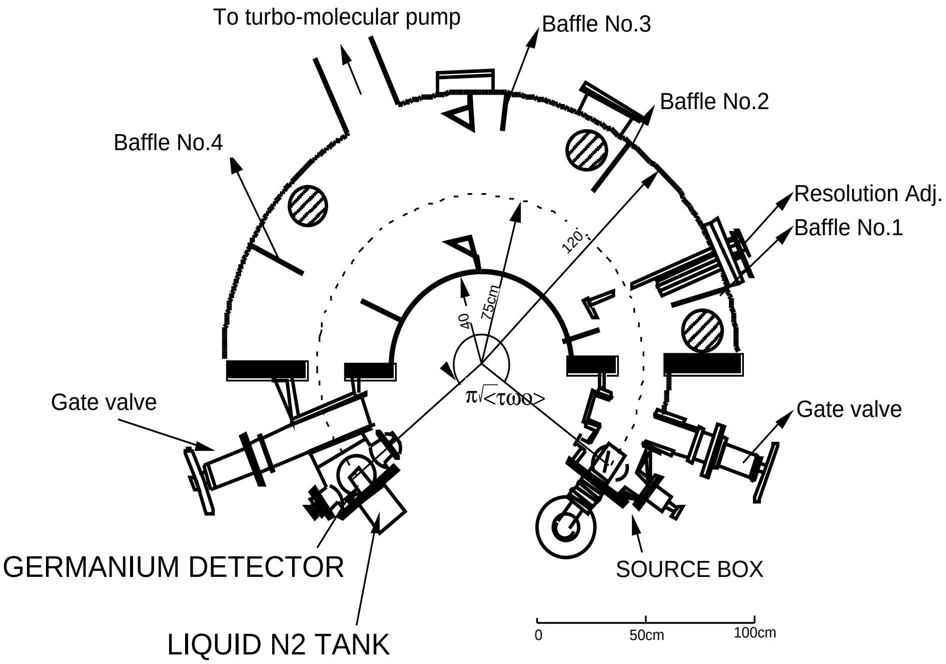

Figure D.1: A view of the air-core beta spectrometer.

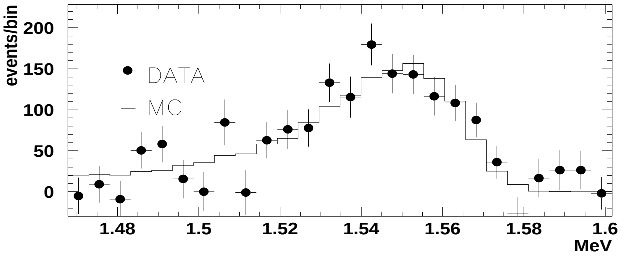

Figure D.2: The results of the Ge detector calibration using the air-core beta spectrometer with the monochromatic internal conversion electron ray from $^{207}$Bi. The upper figure is for 975 keV and lower figure is for 1682.2 keV electrons.

| D1 magnet current (A) | Ge energy (MeV) | beam momentum (MeV/c) | energy in-tank (MeV) |
|---|---|---|---|
| 6.0 | 16.31 | 15.44 | 16.09 |
| 5.0 | 13.65 | 12.80 | 13.44 |
| 4.0 | 10.99 | 10.14 | 10.78 |
| 3.2 | 8.86 | 8.03 | 8.67 |
| 2.5 | 7.00 | 6.17 | 6.79 |
| 2.15 | 6.03 | 5.21 | 5.84 |
| 1.8 | 5.08 | 4.25 | 4.89 |

Table D.1: The correlation between the D1 magnet current and the measured energy by the Ge detector, the beam momentum in the beam pipe and the total energy in SK water tank.

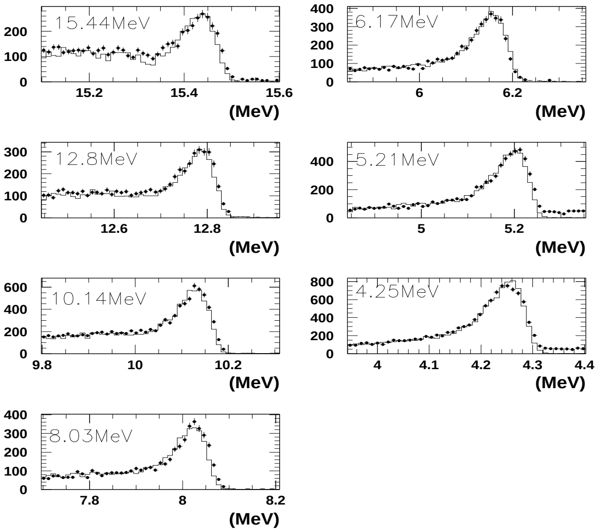

Figure D.3: The measurement of the beam momentum by the Ge detector. The cross marks are data and histograms are MC simulation.

## D.2 Systematic uncertainty with the LINAC system

In order to confirm that the absolute energy is determined within 1%, systematic uncertainty of the LINAC calibration system have to be considered. The source of the systematic error is classified as follows.

### D.2.1 Uncertainty of the beam energy determination

This value is determined by measuring the beam energy five times and taking full width of the distribution for each D1 magnet current, and it is estimated to be ±20 keV for all 7 momenta.

### D.2.2 Beam correlated background

When the electron beam is injected to the tank, there is a possibility that beam correlated background exists. The source of the background is thought to be the $\gamma$-rays produced by the run off electrons, which hit the collimator before the D2 magnet or the vertical beam pipe between the D3 magnet and the end point of the beam pipe. In order to evaluate level of the background, data taking with "empty" (microwave) trigger and "random" (clock) trigger was done. The trigger logic of these trigger modes is shown in figure 5.15. As described above, since the injection rate of single electron is 0.1 per microwave, 90% microwave triggered data are empty with possible background. By comparing the background level of the empty trigger data and the random trigger data, the background level is estimated. Differences between the background level fluctuate around zero, and conservative estimation is done, i.e. averaging over the absolute values of these differences, and the systematic uncertainty of the beam correlated background is evaluated to be ±0.16%.

### D.2.3 Reflectivity of the end point of the beam pipe

The most serious uncertainty of the LINAC system is reflectivity of the end point cap of the beam pipe. In the MC simulation, it is found that about 5% Čerenkov photons hit the end point at the electron momentum of 5 MeV/c. Although the reflectivity of the end point was measured, it is found that there is a possibility that an air bubble is trapped in a hollow space enclosing the Ti window and the unknown size of the bubble changes the reflectivity of the end point. In order to estimate the effect, two set of MC simulations for the extreme case of no air and maximum bubble size are carried out. And conservative uncertainty of this is estimated. The results are given in table D.2.

### D.2.4 Summary

Energy dependence of combined systematic uncertainty (the sum of square of all uncertainties) is also shown in table D.2. The uncertainty is large for small beam momentum due to the larger fraction of Čerenkov photons that hit the end point. The systematic uncertainty is shown as outside error bars in figure 5.24(a).

## D.3 The time and directional uniformity of the energy scale

There are two other important aspects for the energy calibration, i.e. the time and directional uniformity of the energy scale. The former is checked by the spallation events, the Ni-Cf $\gamma$-ray source, and the $\mu$ decay electron events. The latter is checked by only the spallation events. In this section, a description of these two aspects of the energy calibration is given.

| beam momentum (MeV/c) | fraction hitting beam pipe | error due to reflectivity | total systematic error |
|---|---|---|---|
| 16.31 | 0.51% | ±0.06% | ±0.21% |
| 13.65 | 0.67% | ±0.08% | ±0.24% |
| 10.99 | 0.88% | ±0.11% | ±0.27% |
| 8.86 | 1.3% | ±0.18% | ±0.33% |
| 7.00 | 2.2% | ±0.28% | ±0.44% |
| 6.03 | 3.3% | ±0.40% | ±0.55% |
| 5.08 | 4.7% | ±0.68% | ±0.81% |

Table D.2: The list of the LINAC systematic error.

### D.3.1 The time uniformity

As mentioned in section 5.3, the water transparency have been changing since the beginning of data taking of SK. The time variation of the water transparency affects the energy scale of the detector strongly. In order to correct for the variation, the water transparency obtained by the $\mu$ decay electron events is substituted for the equation (4.7) event by event. In order to check the validity of the method, radioactive sources, such as the spallation events, the Ni-Cf $\gamma$-ray events and the $\mu$ decay electron events, are used.

These products emit $\beta$-rays whose energy are similar to that of the recoil electrons scattered by the solar neutrinos. Further, the elements are produced almost uniformly in space and time in the ID and emit $\beta$-rays with uniform direction. Hence, the spallation products are good calibrator to investigate the directional and time uniformity of the energy scale of ID. However, branching ratio of the spallation products generated by the interaction is not known in detail, therefore it is difficult to use these radioactive elements as a calibrator for the absolute energy determination. Figure D.4 shows energy spectrum of the spallation events. In order to study the time variation of the energy scale using the spallation events, the following manipulation is done. At first, the total spallation sample is separated into time periods. For each period, the energy scale is changed artificially by multiplying a factor and the energy spectrum of the each

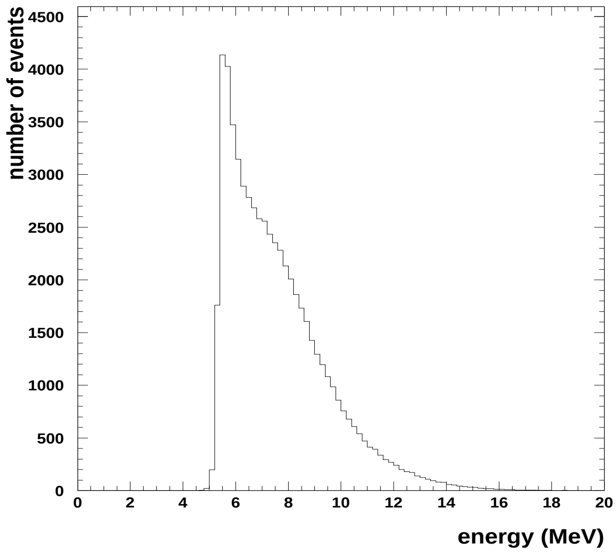

Figure D.4: Energy spectrum of the spallation events.

period is compared with that of the whole sample. Comparison is done by a $\chi^2$ test in a energy range of 6.5∼15 MeV. The lower bound of 6.5 MeV is determined by taking into account the trigger efficiency and Rn event contamination. The upper bound is set to 15 MeV, because, above 15 MeV, statistics of the spallation events become poor. Figure D.5(a) shows the time variation of the factor. The figure shows that the energy scale is consistent within ±0.5%.

Though the Ni-Cf source has large systematic uncertainty by itself, this source is useful for this purpose, since only the relative energy scale is important. Unfortunately, the data taking with this source is not carried out frequently, therefore this source is used for an additional check. Figure D.5(b) shows the time variation of averaged energy of recoil electrons scattered by the Ni-Cf $\gamma$-rays. This figure shows also that the energy scale is consistent within ±0.5%.

Third radioactive source is the $\mu$ decay electron events. The $\mu$ decay electron events used here are the same as those used for the calculation of the water transparency. Advantages to using the events for this purpose are that statistics of the events are large and background contamination is almost negligible. Figure D.5(c) shows the time variation of energy of the events. One point corresponds to two weeks. The figure also shows that the energy scale is stable within ±0.5%.

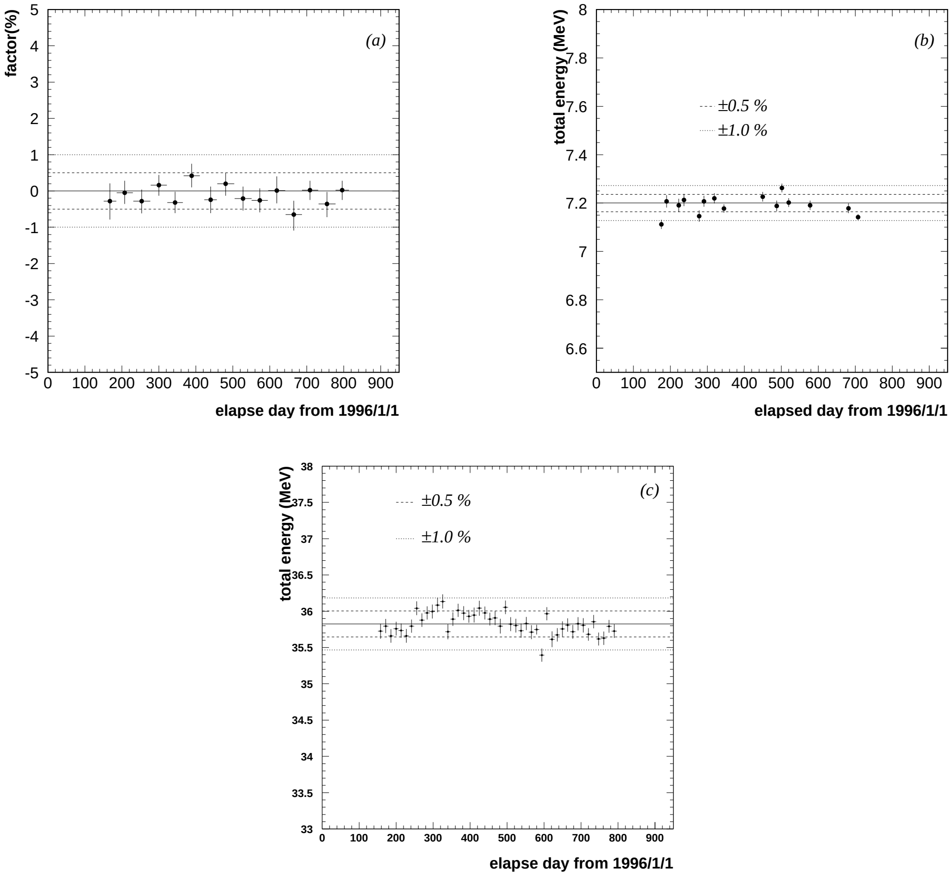

Figure D.5: The time variation of the energy scale for three calibration sources. (a) the spallation events, (b) the Ni-Cf source, (c) the $\mu$ decay electron events.

In summary, three radioactive sources indicate that the time variation of the energy scale for long time period (∼2 years) is stable within ±0.5%.

### D.3.2 The directional uniformity

To know the directional uniformity of the energy scale and to extrapolate the precise energy calibration achieved by the LINAC calibration to all directions are quit important when studying the energy spectrum distortion and the day/night effect caused by the MSW effect. Unfortunately, the only reliable source to check the uniformity is the spallation events. The Ni-Cf calibration source has directional asymmetry caused by asymmetrical configuration of the Ni wire and material such a pulling stainless steel wire, a signal cable, etc. The $\mu$ decay electron events have direction dependent energy spectrum due to polarization of the parent stopping muon.

Figure D.6 shows zenith angle dependence of the energy scale for the spallation events. The way of estimating the factor is the same as that used for the time variation investigation. The figure indicates that the directional dependence of the energy scale is consistent within ±0.5%.

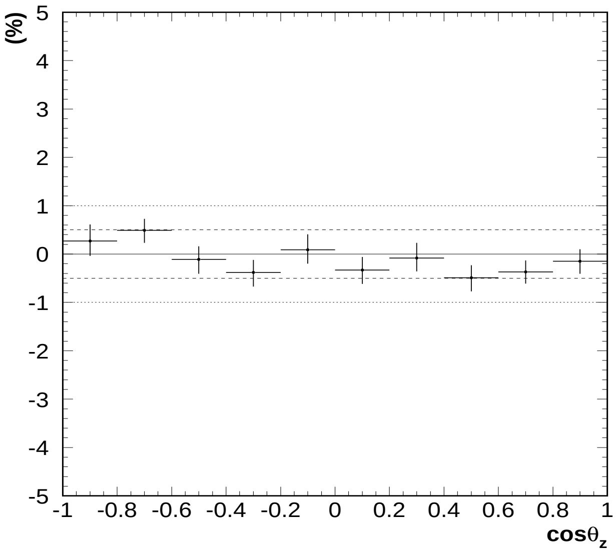

Figure D.6: The directional dependence of the energy scale.

# Appendix E

# Bad run selection to make data set

The basic unit of the data set is a run. Each run is at most 24 hours long. Each run is divided into sub-runs, which are about 2∼10 minutes long. The length of each sub-run depends on the trigger rate.

To make the basic data set, real-time bad run (sub-runs) selection and non-real-time bad run (sub-runs) selection are applied to the all runs in order. The bad run selections are applied by the unit of Run and Sub-run.

## E.1 Real-time bad run selection

First of all, the real-time bad run selection is applied to the all normal runs. At the online real-time reduction process, obvious bad sub-runs are automatically selected as bad sub-runs. In this real-time bad run selection, there are 12 categories for bad run selection. So, real-time bad run selection is done by the following criteria.

1. Run-time with less than 30 seconds (short sub-run)
2. Live-time is less than 0 seconds (abnormal dead-time)
3. Total-run time is less than 300 seconds (short run)
4. Abnormal flasher event rates

$$\text{rate of flasher events} > 0.5Hz \tag{E.1}$$

5. Abnormal NS-ratio (Noise/Signal ratio) events rates

$$\frac{\text{Number of events with NS-ratio}<0.4}{\text{Total number of events}} > 0.01 \tag{E.2}$$

6. Abnormal incomplete event rates

$$\frac{\text{Number of events with incomplete flag}}{\text{Total number of events}} > 0.1 \tag{E.3}$$

7. Abnormal anti mis-match event rates

$$\frac{\text{Number of events with the number of antihit}>20}{\text{Total number of events}} > 0.01 \tag{E.4}$$

8. Abnormal Low-goodness event rates

$$\frac{\text{Number of events with } goodness<0.4}{\text{Total number of events}} > 0.05 \tag{E.5}$$

9. Abnormal number of bad channel

$$\text{Number of bad PMTs} > 500 \tag{E.6}$$

10. Time difference between TQ(Time and Charge)-real information and muon information file is greater than 20 %

11. Muon rate is less than 1 Hz

12. No muon information table file

| Criterion number | Rejected unit (Run or Sub-run) | Number of rejected Sub-runs | Lost time (days) |
|---|---|---|---|
| 1 | Sub-runs | 3270 | 0.1 |
| 2 | Sub-runs | 1593 | 1.2 |
| 3 | Sub-runs | 1566 | 1.8 |
| 4 | Sub-runs | 2956 | 4.6 |
| 5 | Sub-runs | 1977 | 7.1 |
| 6 | Sub-runs | 3795 | 6.8 |
| 7 | Sub-runs | 3325 | 4.1 |
| 8 | Sub-runs | 210 | 0.5 |
| 9 | Sub-runs | 274 | 0.4 |
| 10 | Sub-runs | 2872 | 0.7 |
| 11 | Sub-runs | 1131 | 2.2 |
| 12 | Sub-runs | 121 | 0.5 |
| | Total Lost time | | 27.3 |

Table E.1: The summary of number of the rejected sub-runs by the real-time bad run selection.

The summary of number of the rejected sub-runs by real-time bad run selection is presented in table E.1 The most largest bad run was selected by Abnormal NS-ratio rates or abnormal incomplete flag rates. They might be related to the hardware trouble.

## E.2 Non-real-time bad run selection

The non-real-time bad run selection is applied all normal Runs after the Real-time bad run selection. People checked the quality of the runs and sub-runs remaining after real-time bad run selection manually and reject the bad runs.

The manual bad run selection is applied by the following of selection steps.

### E.2.1 Bad run selection

- Log book check
  Looking the log book and run summary, the useless run is rejected by several persons. Figure E.1 shows the rejected time by the log book check. The left figure shows the rejected time versus the categorized reason. The right figure shows the rejected time by the log book check for each run number from 1742 to 10417.

- Dark rate
  The dark rates are calculated for each run by using the hits before muon events. The current criteria is 3.2∼3.7 kHz.

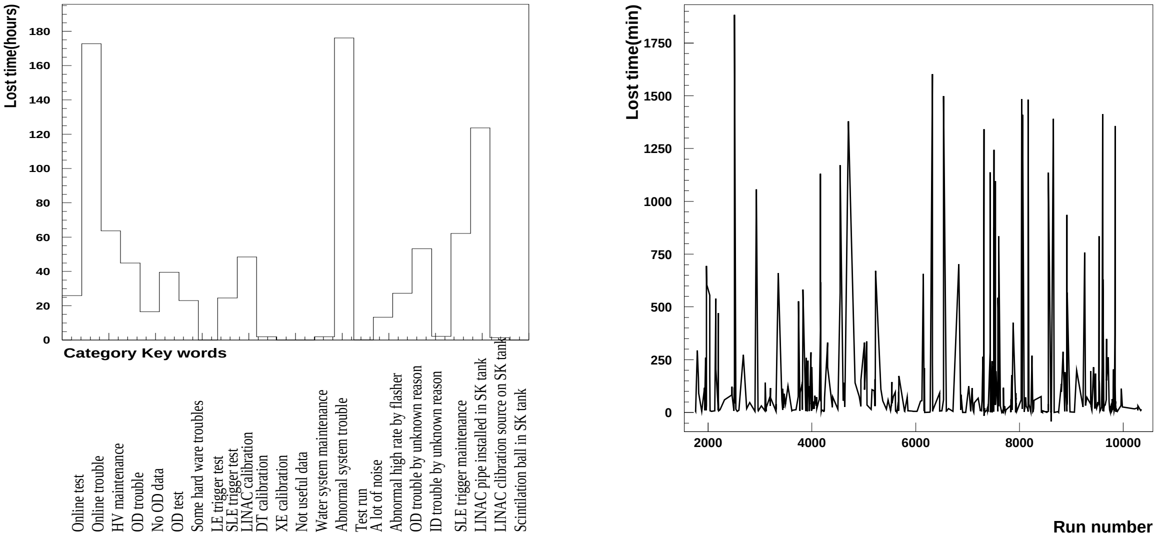

Figure E.1: The rejected time by the log book check. The left figure shows the rejected time versus the categorized reason. The right figure shows the rejected time by the log book check for each run number from 1742 to 10417.

- Number of ID/OD bad channels
  The run with too many bad channels are removed because there may exist some anisotropy. The run with too small bad channels are also removed because the bad run selection may fail.

- Muon event rate
  Checking muon files for spallation cut, if muon rate is too small (most case, it becomes 0), there are something wrong in the muon analysis or file. So, spallation cut is wrong for the run. The sub-runs with too large muon event rate is also removed because muon analysis has something wrong.

- Delta-T cut event rate
  If run is very noisy, the number of event cut by delta-T is increase. The sub-run with too large event rate cut by delta-T (this cut is called "delta-T cut event rate") is removed because the quality of the data may differ from the run with usual delta-T cut event rate.

- Pedestal event rate
  If there are some hardware trouble around trigger flags, dead-time calculation may become incorrect. Pedestal event rate is used to monitor whether trigger flag system is working well or not. We can not judge easily if the pedestal event is too small or not. Therefore, only the sub-run with too many pedestal events is removed.

- Incomplete event rate
  To check hardware trouble around trigger flags, this selection is used. If there are something wrong about hardware, incomplete event rate becomes too large.

- Strong flasher event rate
  We have some good flasher cut tools. But if the flasher is extremely strong, some amount of flasher events remain in the final sample.Flasher event has strong directional correlations. So, if it overlaps with the direction of the sun, it could make some amount of fake solar neutrino flux.

- External flush event rate
  If the following list of event rate are extremely high, there are something wrong. External flush event happens under the following condition of high event rate.

  - OD triggered event rate
  - OD mismatch event rate
  - NS ratio cut event rate
  - ATM ratio cut event rate
  - Unfitted event rate

- Live run list in tqreal summary files and in data file
  The live time is calculated from tqreal summary files. The final data sample is of course made from data files. They are independently generated. So, the list of sub runs in both tqreal summary and data files after the 1st reductions are compared to make sure that we are using the same run list. The trouble found here is a bunch of "no data files". This means real-time process may have some trouble at some step. So, usually re-process is needed for these sub runs. There is only a small afraid. If the run time is very short (the current shortest sub run time is 30 sec), all the events are really removed at the 1st reductions.

- Others

  - Gamma source on the SK tank for LINAC calibration
  - High radon rate for Radon calibration
  - Bad trigger level at hard-ware trigger threshold changing.

### E.2.2 Summary

The following table E.2 shows the manual bad run selection summary of the total lost time from the rejected run as bad run.

Thus, we see that 112 days of live-time can be accounted for by the LE manual bad run selection cuts. In figure E.2, the detector live time after bad run selection is plotted as a function of elapsed run number from May 5, 1996. The highest plot, middle plot and the lowest plot shows total detector live time, solar neutrino analysis live time after real-time bad run rejection and solar neutrino analysis live time after non-real-time bad run rejection respectively.

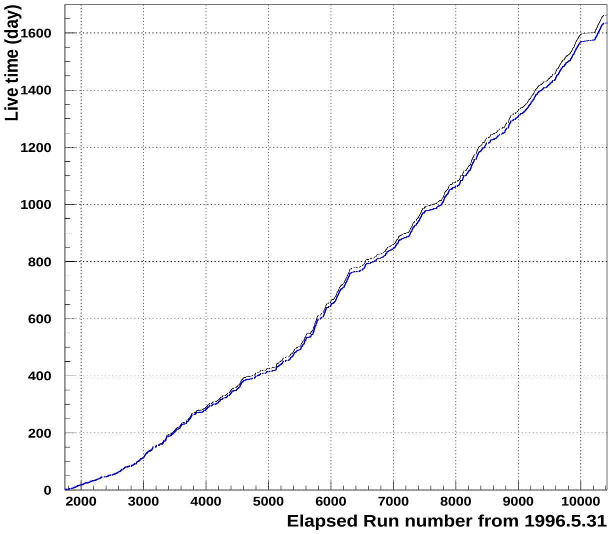

Figure E.2: The detector live time after bad run selection for elapsed run number from May 5, 1996. The highest plot, middle plot and the lowest plot shows total detector live time, after real-time bad run rejection and after non-real-time bad run rejection respectively.

| Step<br>number | Cut criteria | Rejected unit<br>(Run or Sub-run) | Rejected Runs<br>or Sub-runs | Lost time<br>(days) |
|---|---|---|---|---|
| | Log book checking | | | |
| 1 | Log book check(Bad run) | Runs | 553 | 49.4 |
| 2 | Log book check(Bad run end) | Sub-runs | 2912 | 2.2 |
| 3 | Gamma source on the top of the tank | Runs | 52 | 20.2 |
| 4 | Radon water injection for radon calibration | Runs | 31 | 13.1 |
| 5 | Bad trigger level | Runs | 22 | 2.0 |
| 6 | Dark rate | Runs | 148 | 18.0 |
| 7 | Number of OD bad channels | Sub-runs | 1345 | 2.5 |
| 8 | Number of ID bad channels | Sub-runs | 276 | 1.2 |
| 9 | Abnormal muon rate | Sub-runs | 222 | 0.2 |
| 10 | Muon event rate | Sub-runs | 116 | 0.00 |
| 11 | Delta cut event rate | Sub-runs | 453 | 0.9 |
| 12 | Pedestal event rate | Sub-runs | 52 | 0.1 |
| 13 | Incomplete event rate | Sub-runs | 212 | 0.6 |
| 14 | Strong flasher event rate | Sub-runs | 4 | 0.0 |
| 15 | OD triggered event rate | Sub-runs | 85 | 0.2 |
| 16 | OD mismatch event rate | Sub-runs | 14 | 0.0 |
| 17 | NS ratio event rate | Sub-runs | 33 | 0.1 |
| 18 | ATM ratio cut event rate | Sub-runs | 64 | 0.1 |
| 19 | External flasher event rate | Sub-runs | 41 | 0.3 |
| 20 | Live runs list | Sub-runs | 223 | 0.8 |
| 21 | Low goodness | Sub-runs | 41 | 0.0 |
| 20 | Data problem | Sub-runs | 107 | 0.0 |
| | Total Lost time | | | 112 |

Table E.2: The manual bad run selection summary of the total lost time.

# Appendix F

# The probability function of solar signal for solar signal extraction

The probability function for the signal ($P_{sig}$) is obtained by the solar neutrino MC simulation at various energy regions. The distribution is named XANG. The XANG is made by smoothing the probability function of the MC by smoothing functions. In this thesis, the smoothing function is different from current analysis. The smoothing function is changed from sorting method to function fitting method. It was problem that the old smoothing function created a artificial shape for the $\cos\theta_{sun}$ distribution of the original MC. So, the new smoothing method which has small artificial effect was developed.

## F.1 Old way to make the signal probability function

The $\cos\theta_{sun}$ distribution made from the signals of solar neutrino MC is applied following smoothing method in order to smooth because it has some fluctuation due to statistics. If the fluctuation is large, the extraction of the solar neutrino signal from real data is not done correctly. The $\cos\theta_{sun}$ distribution of the signal before smoothing is called original XANG from now on. Figure F.2 shows the original XANG in 8.0∼9.0 MeV energy region. After smoothing, it is called smoothing XANG from now on. Figure F.3 shows the smoothing XANG for each smoothing step in 8.0∼9.0 MeV energy region. The original XANG is made for 12 energy regions (4.5∼5.0, 5.0∼5.5, 5.5∼6.0...12.5∼100.0 MeV) and 7 zenith angles (All-time, Day-time, Night-time:Mantle1... Mantle5, Core) as shown in figure F.1. The region is given in table F.1.

| Zenith angle | region |
|---|---|
| MANTLE1 | $0.00 < \cos\theta_z \leq 0.16$ |
| MANTLE2 | $0.16 < \cos\theta_z \leq 0.33$ |
| MANTLE3 | $0.33 < \cos\theta_z \leq 0.50$ |
| MANTLE4 | $0.50 < \cos\theta_z \leq 0.67$ |
| MANTLE5 | $0.67 < \cos\theta_z \leq 0.84$ |
| CORE | $0.84 < \cos\theta_z \leq 1.00$ |

Table F.1: The region of the zenith angle division.

1. Tail fitting
   In small statistical region of the $\cos\theta_{sun} < 0.0$, the distribution is replaced with the exponential function.

2. Sorting
   In the $\cos\theta_{sun} > 0.0$, the fluctuation due to statistics appears. Some bins which is near

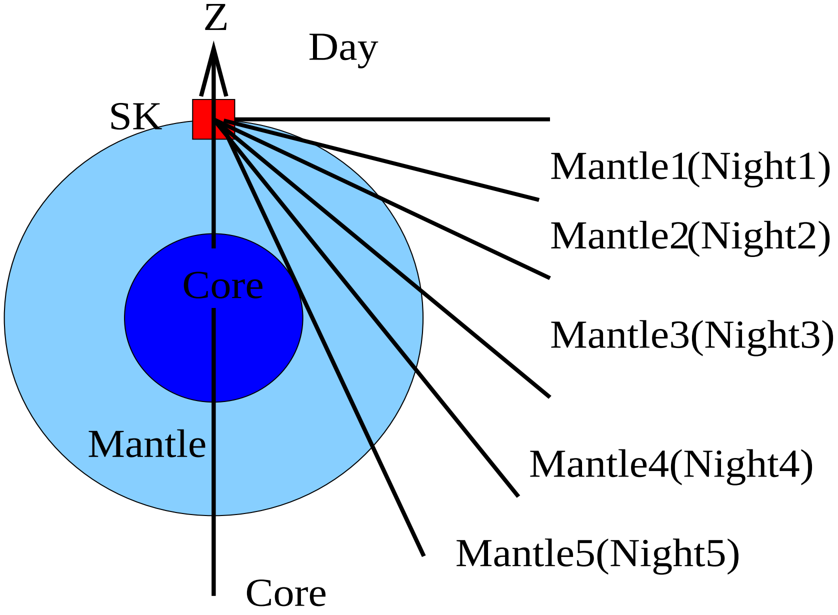

Figure F.1: The definition of the zenith angle division.

to the solar direction have smaller statistics than some bins farther from solar direction. This fluctuation is improved by the sorting method. It means a smaller statistical bin is exchanged a higher statistical bin for each bin.

3. Spline
   The numerical method of Spline [92] is applied to smooth.
4. Secondary sorting
   Above sorting is applied again.
5. Running average of first differential
   The running average of first differential is applied to the $\cos\theta_{sun} < 0.99$.
6. Normalization
   The distribution is transfered to the probability function.

These smoothing methods have an large effect on small statistical distribution, for example, in energy region from 12.5 to 100.0 MeV and zenith angle of Mantle 1 from 0.00 to 0.16. Figure F.4 shows the bad example due to smoothing method.

## F.2 The effect of smoothing for spectrum analysis

The original XANG has some fluctuations. It is not smooth because of low statistics of the MC. So, the high statistics MC which has 10 times larger statistics than usual MC is generated in order to skip the smoothing. Comparing the observed solar neutrino flux for SK-I full data of 1496 days between the result by using the smoothing XANG and by using the original XANG which can skip the smoothing by the high statistics MC, the smoothing effect is estimated. The original XANG which can skip the smoothing is called no smoothing XANG from now on.

Figure F.5 shows the ratio between the energy spectrum result by using smoothing XANG and by using no smoothing XANG.

The energy spectrum by using no smoothing XANG is slightly down uniformly by 0.5%. This result is due to the running average effect in the smoothing.

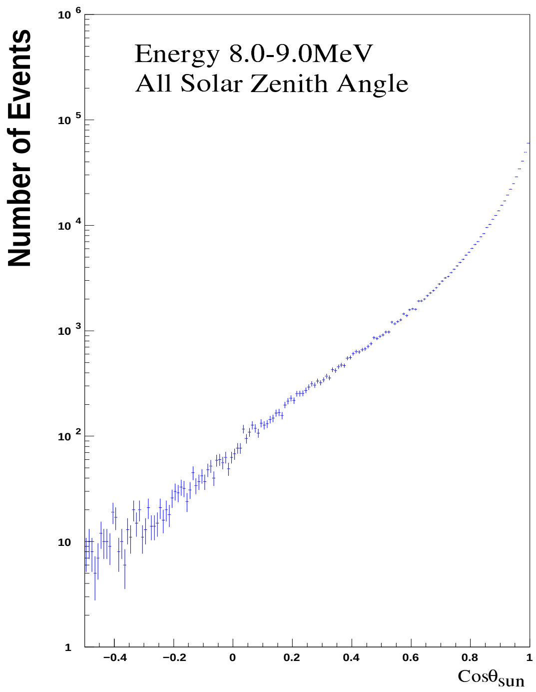

Figure F.2: The original XANG of $\cos\theta_{sun}$ distribution of all events(E = 8.0 $\sim$ 9.0MeV).

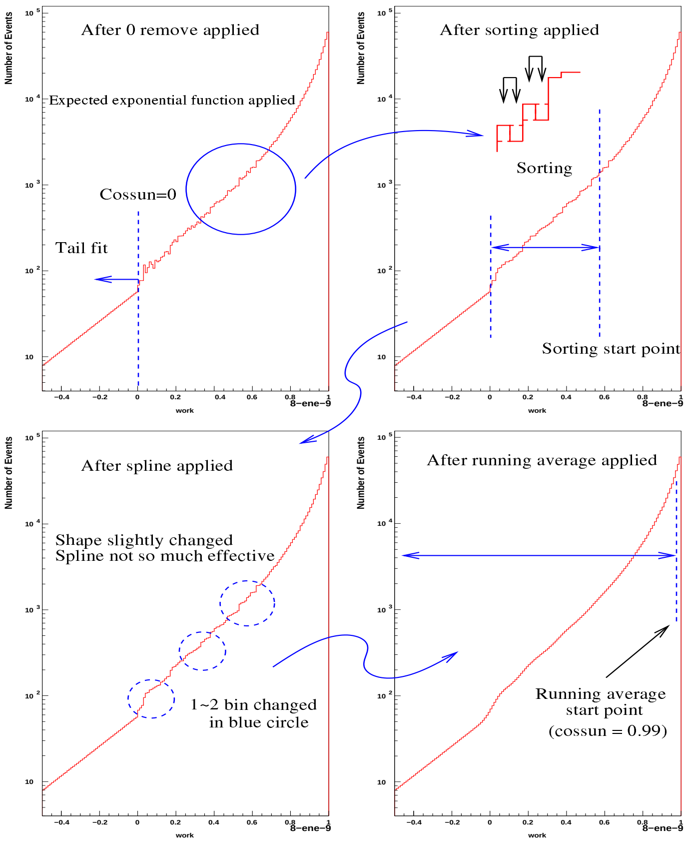

Figure F.3: The smoothing XANG of $\cos\theta_{sun}$ distribution of all events(E = 8.0 $\sim$ 9.0MeV).

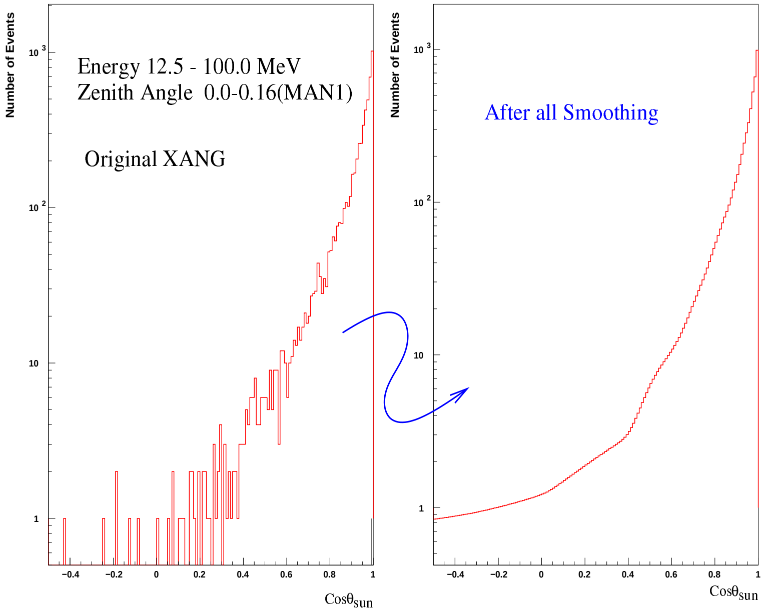

Figure F.4: The bad example of the smoothing XANG for $\cos\theta_{sun}$ distribution.

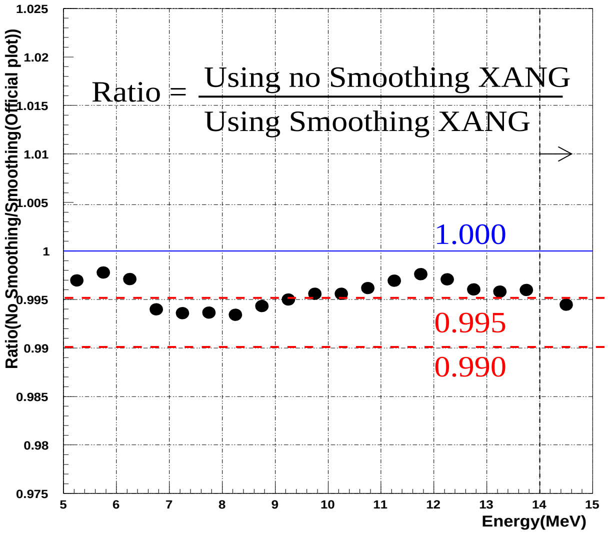

Figure F.5: The ratio between the energy spectrum result by using smoothing XANG and it by using no smoothing XANG.

Figure F.6 shows the ratio between the zenith energy spectrum result by using smoothing XANG and by using no smoothing XANG. The zenith energy spectrum is obtained by dividing the energy spectrum into each zenith angles region as shown in figure F.1.

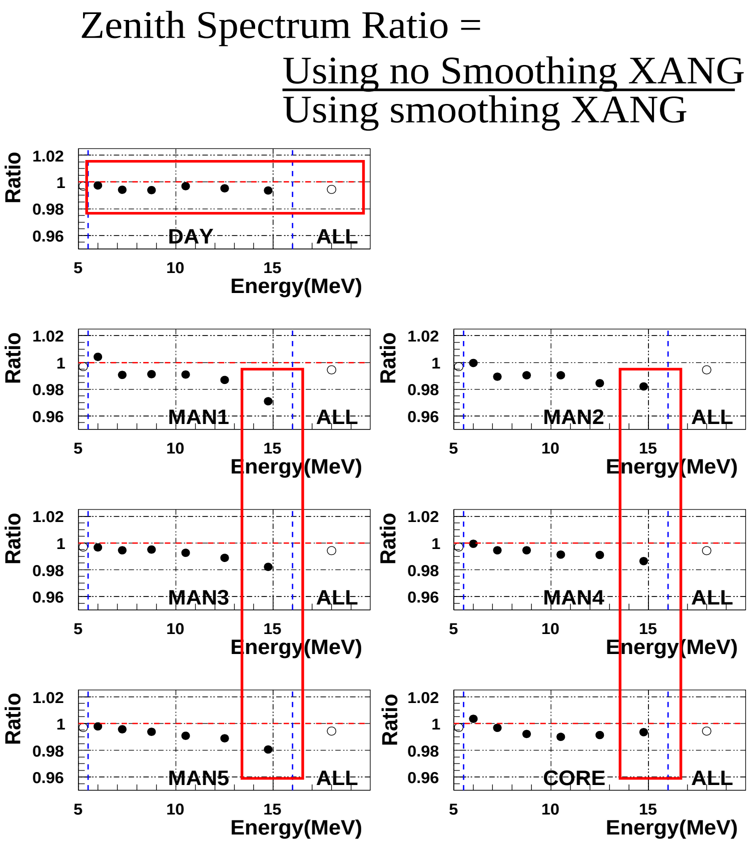

Figure F.6: The ratio between the zenith energy spectrum result by using smoothing XANG and it by using no smoothing XANG.

In the high energy region, the spectrum is down largely by 2∼3%. This result is due to the tail fitting effect in the smoothing because the tail fitting changes the normalization factor for original XANG.

In the estimation of the smoothing effect, the largest change is 2∼3 % in zenith energy spectrum. Figure F.7 shows the results of the oscillation analysis by using the zenith energy spectrum. The left figure is the result by using smoothing XANG, and the right figure is the result by using no smoothing XANG. It is concluded that the oscillation analysis results did not change.

## F.3 New way to make the signal probability function

The smoothing method has some wrong effects on the original shape of XANG. So, this method need to be improved. In this improvement, the following contents is required.

- The shape of original xang is not changed.
- The fluctuation in the low statistical region is improved.

From above requirements, the new smoothing method is developed. The developed smoothing method is a high order exponential function fitting with polynomial function. The original xang is replaced with the fitting result in the small statistical region.

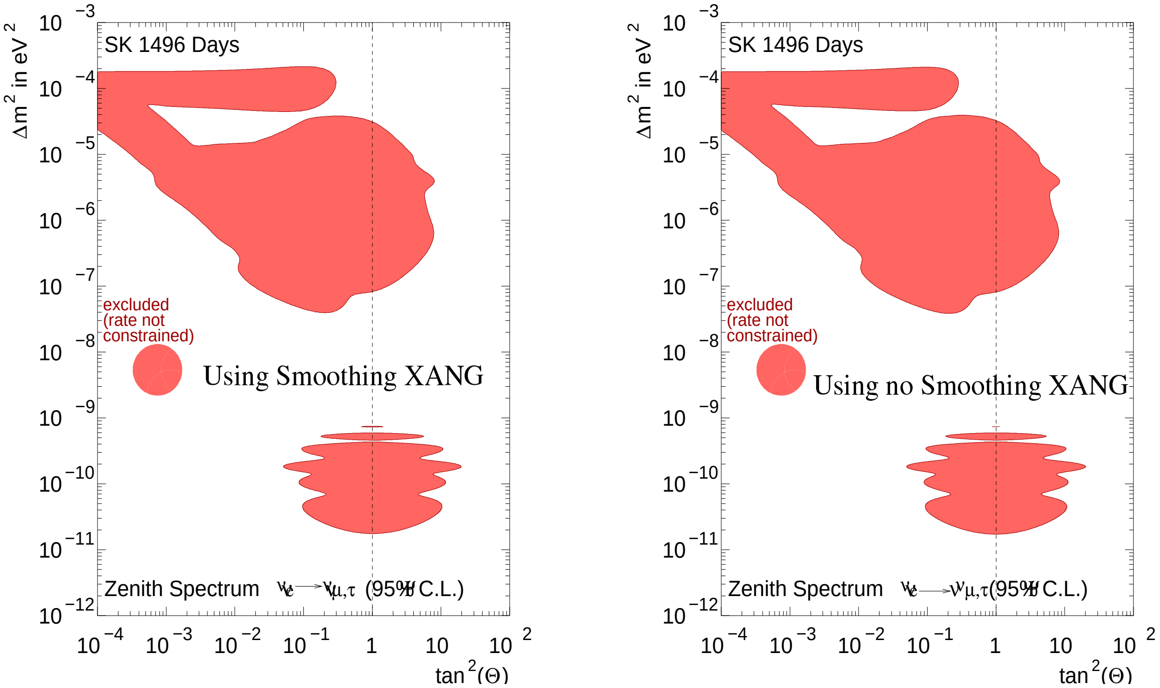

Figure F.7: The results of oscillation analysis by using zenith energy spectrum. The left figure is the result by using smoothing XANG, and the right figure is the result by using no smoothing XANG.

Figure F.8 shows the outline of the new method. The way to fit polynomial function is as follows:

1. The original xang is divided into three regions as figure F.8.
2. In the peak region, the shape of original XANG is used as it is, because the statistics in this region is enough. The fluctuation does not appear.
3. In the region from middle to tail, the exponential function with polynomial function is applied. The function is as following equation.

$$\begin{aligned} f(x) &= exp(P_n(x)) \\ P_n &= p_1 \cdot x + p_2 \cdot x^2 \cdots + p_n \cdot x^n \\ x &= \cos\theta_{sun} \end{aligned} \tag{F.1}$$

   where $f(x)$ is the fitting function, $n$ is the order of polynomial function which has 4,6,12 or 16 in this method, $p_n$ is fitting free parameter.

   The various combined order for $n$ is used in this fitting. For example, in the middle region, $n = 12$ is used, and in the tail region, $n = 8$ is used. Or, the single function with $n = 16$ or $n = 12$ is used in all over the region from middle to tail. These combinations is selected from a point of view of the best agreement with the original XANG by $\chi^2$ testing.

Figure F.9 shows the agreement between the fitting results and the original XANG in the energy region from 8.0 to 9.0 MeV and the zenith angle from 0.00 to 0.16. In the top and left figure, the fitting result (solid line) is overlaid on the original XANG (histogram). The another figures show the ratios between the fitting result and the original XANG for each $\cos\theta_{sun}$ region with the statistical uncertainties of $1\sigma$ of solid line. The difference is suppressed within statistical uncertainties in all regions.

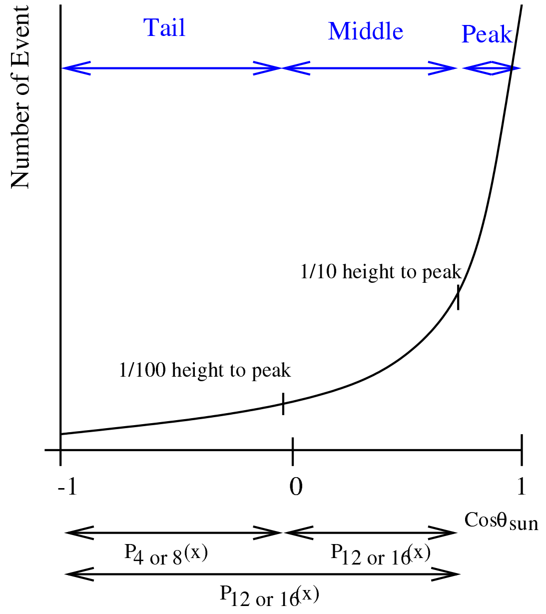

Figure F.8: The outline of the new method.

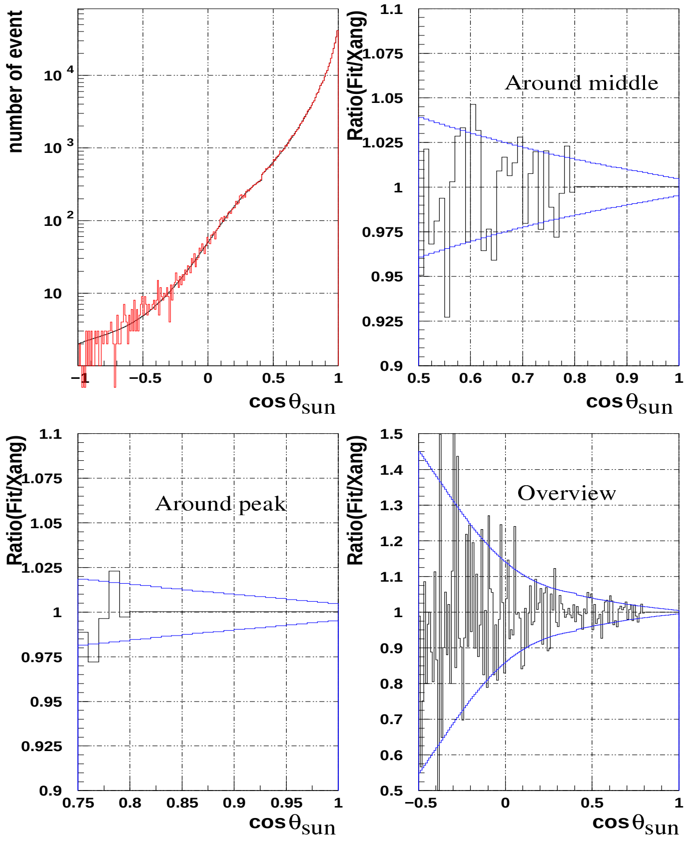

Figure F.9: The agreement between the fitting results and the original XANG in the energy region from 8.0 to 9.0 MeV and the zenith angle from 0.00 to 0.16.

# Appendix G

# Day and Night flux with 4.5∼5.0 MeV data

SK can measure the $^8$B neutrino flux in real time, so one can compare the day time flux with night time flux. For certain values of $\Delta m^2$ and $\sin^2 2\theta$, these fluxes are different because of re-generation in the earth.

The data sample is divided into day time and night time samples defined by the zenith angle of the direction of the sun as shown in figure 2.16 and the region is given in table G.2. The systematic uncertainties for day and night time flux are same as energy spectrum measurement except for the live-time uncertainty.

## G.1 Flux measurements

The day time flux is obtained as follows.

$$\Phi_\nu(\mathrm{day}, \mathrm{SSM_{BP2000}}, \mathrm{dsI}) = 2.31^{+0.03}_{-0.03}(\mathrm{stat.})^{+0.08}_{-0.08}(\mathrm{syst.})(\times 10^6/\mathrm{cm}^2/\mathrm{sec}) \tag{G.1}$$
$$\Phi_\nu(\mathrm{day}, \mathrm{SSM_{BP2000}}, \mathrm{dsII}) = 2.34^{+0.06}_{-0.05}(\mathrm{stat.})^{+0.08}_{-0.08}(\mathrm{syst.})(\times 10^6/\mathrm{cm}^2/\mathrm{sec}) \tag{G.2}$$
$$\Phi_\nu(\mathrm{day}, \mathrm{SSM_{BP2000}}, \mathrm{dsIII}) = 2.40^{+0.07}_{-0.07}(\mathrm{stat.})^{+0.14}_{-0.13}(\mathrm{syst.})(\times 10^6/\mathrm{cm}^2/\mathrm{sec}) \tag{G.3}$$

The night time flux is obtained as follows.

$$\Phi_\nu(\mathrm{night}, \mathrm{SSM_{BP2000}}, \mathrm{dsI}) = 2.36^{+0.03}_{-0.03}(\mathrm{stat.})^{+0.08}_{-0.08}(\mathrm{syst.})(\times 10^6/\mathrm{cm}^2/\mathrm{sec}) \tag{G.4}$$
$$\Phi_\nu(\mathrm{night}, \mathrm{SSM_{BP2000}}, \mathrm{dsII}) = 2.33^{+0.05}_{-0.05}(\mathrm{stat.})^{+0.08}_{-0.08}(\mathrm{syst.})(\times 10^6/\mathrm{cm}^2/\mathrm{sec}) \tag{G.5}$$
$$\Phi_\nu(\mathrm{night}, \mathrm{SSM_{BP2000}}, \mathrm{dsIII}) = 2.42^{+0.07}_{-0.07}(\mathrm{stat.})^{+0.14}_{-0.13}(\mathrm{syst.})(\times 10^6/\mathrm{cm}^2/\mathrm{sec}) \tag{G.6}$$

The mean distance between the sun and the earth is summarized in table G.1. The measured flux is correlated for the eccentricity of the earth's orbit at 1 AU.

| Data set | All | Day | Night |
|---|---|---|---|
| I | 1.001 | 1.004 | 0.998 |
| II | 0.998 | 1.001 | 0.995 |
| III | 0.997 | 1.000 | 0.994 |

Table G.1: The mean distance between the sun and the earth in this analysis.

The ratios of the measured flux to the SSM prediction for day and night time fluxes are as follows:

$$\mathrm{Data/SSM(day, SSM_{BP2000}, dsI)} = 0.458^{+0.007}_{-0.007}(\mathrm{stat.})^{+0.016}_{-0.015}(\mathrm{syst.}) \quad (G.7)$$

$$\mathrm{Data/SSM(day, SSM_{BP2000}, dsII)} = 0.463^{+0.011}_{-0.011}(\mathrm{stat.})^{+0.016}_{-0.015}(\mathrm{syst.}) \quad (G.8)$$

$$\mathrm{Data/SSM(day, SSM_{BP2000}, dsIII)} = 0.475^{+0.014}_{-0.014}(\mathrm{stat.})^{+0.028}_{-0.025}(\mathrm{syst.}) \quad (G.9)$$

$$\mathrm{Data/SSM(night, SSM_{BP2000}, dsI)} = 0.468^{+0.007}_{-0.007}(\mathrm{stat.})^{+0.016}_{-0.015}(\mathrm{syst.}) \quad (G.10)$$

$$\mathrm{Data/SSM(night, SSM_{BP2000}, dsII)} = 0.461^{+0.011}_{-0.010}(\mathrm{stat.})^{+0.016}_{-0.015}(\mathrm{syst.}) \quad (G.11)$$

$$\mathrm{Data/SSM(night, SSM_{BP2000}, dsIII)} = 0.479^{+0.014}_{-0.013}(\mathrm{stat.})^{+0.028}_{-0.025}(\mathrm{syst.}) \quad (G.12)$$

The difference ($\mathrm{R}_{\frac{\mathrm{day}}{\mathrm{night}}}$) between the day time flux and night time flux is calculated as follows:

$$\mathrm{R}_{\frac{\mathrm{day}}{\mathrm{night}}} = \frac{\Phi_{\mathrm{day}} - \Phi_{\mathrm{night}}}{(\Phi_{\mathrm{day}}0 + \Phi_{\mathrm{night}})/2} \quad (G.13)$$

Therefore, some neutrino oscillation parameters predict a non-zero difference for $\mathrm{R}_{\frac{\mathrm{day}}{\mathrm{night}}}$ due to the matter effect in the earth's mantle and core [86].

$$\mathrm{R}_{\frac{\mathrm{day}}{\mathrm{night}},\mathrm{dsI}} = -0.021^{+0.020}_{-0.020}(\mathrm{stat.})^{+0.013}_{-0.012}(\mathrm{syst.}) \quad (G.14)$$

$$\mathrm{R}_{\frac{\mathrm{day}}{\mathrm{night}},\mathrm{dsII}} = 0.004^{+0.095}_{-0.095}(\mathrm{stat.})^{+0.013}_{-0.012}(\mathrm{syst.}) \quad (G.15)$$

$$\mathrm{R}_{\frac{\mathrm{day}}{\mathrm{night}},\mathrm{dsIII}} = -0.008^{+0.098}_{-0.098}(\mathrm{stat.})^{+0.022}_{-0.020}(\mathrm{syst.}) \quad (G.16)$$

Figure G.1 shows the fluxes for day time and night time. The night time period is divided into 5 bins. Numerical results for each data set are given in table G.2. The error is statistical error only. In the figure, the left plot shows the result of the data set I, and the right plot shows the results of the data set II, III. The black circle indicates the result of the data set III. The white circle indicates the result of the data set II.

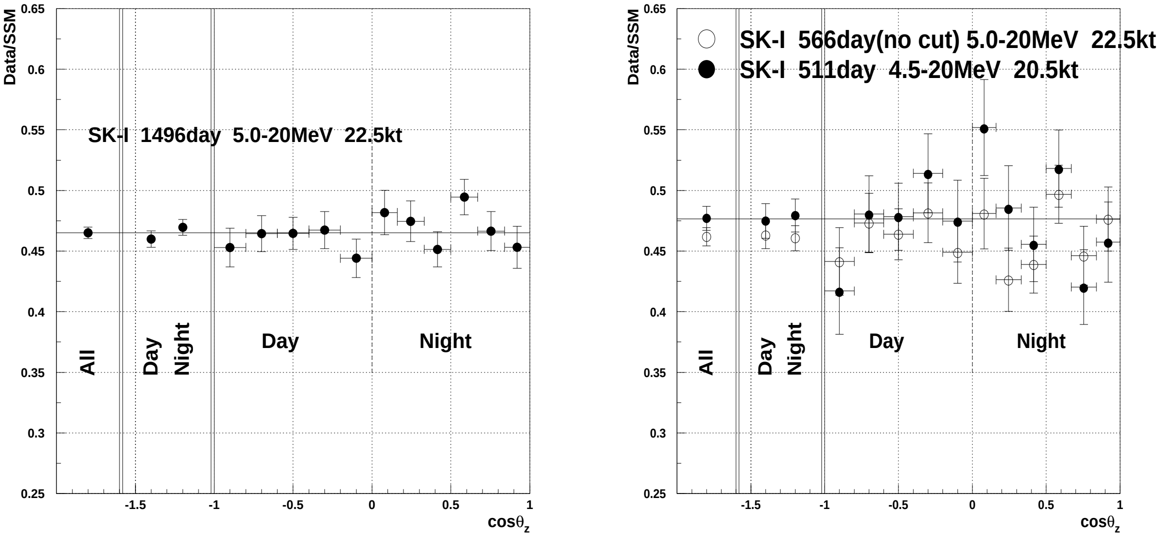

Figure G.1: The time variation of the ratio of the measured flux to the SSM prediction.

The Data/SSM of 4.5∼5.0 MeV data analysis (data set III) is almost consistent with the another data sets within ∼ 1.0 sigma. It is shows the data set for the energy spectrum with

| Time bin | $\cos\theta_z$ | Data/SSM | Observed flux($\times 10^6\mathrm{cm}^{-2}\mathrm{s}^{-1}$) |
|---|---|---|---|
| Data set I | | | |
| N1 | 0.0∼-0.2 | 0.474+0.016-0.016 | 2.394+0.083-0.080 |
| N2 | -0.2∼-0.4 | 0.458+0.015-0.015 | 2.312+0.076-0.074 |
| N3 | -0.4∼-0.6 | 0.474+0.013-0.013 | 2.393+0.066-0.064 |
| N4 | -0.6∼-0.8 | 0.469+0.015-0.015 | 2.368+0.075-0.073 |
| N5 | -0.8∼-1.0 | 0.459+0.016-0.015 | 2.318+0.078-0.076 |
| Data set II | | | |
| N1 | 0.0∼-0.2 | 0.458+0.026-0.025 | 2.310+0.132-0.126 |
| N2 | -0.2∼-0.4 | 0.438+0.024-0.023 | 2.210+0.122-0.117 |
| N3 | -0.4∼-0.6 | 0.476+0.022-0.021 | 2.402+0.109-0.105 |
| N4 | -0.6∼-0.8 | 0.452+0.023-0.022 | 2.284+0.117-0.113 |
| N5 | -0.8∼-1.0 | 0.473+0.024-0.023 | 2.388+0.120-0.115 |
| Data set III | | | |
| N1 | 0.0∼-0.2 | 0.525+0.036-0.034 | 2.650+0.180-0.171 |
| N2 | -0.2∼-0.4 | -0.494+0.032-0.031 | 2.496+0.164-0.156 |
| N3 | -0.4∼-0.6 | 0.474+0.028-0.027 | 2.393+0.142-0.136 |
| N4 | -0.6∼-0.8 | 0.466+0.031-0.029 | 2.354+0.154-0.147 |
| N5 | -0.8∼-1.0 | 0.442+0.030-0.028 | 2.231+0.150-0.142 |

Table G.2: Numerical results of the flux of night time divided into 5 for each data set.

4.5∼5.0 MeV has no systematic bias in the time variation. However, the fluctuation and statistical error is very large in the data set III because of the poor statistics. So, the time variation analysis is not described in this thesis.

Figure G.2 shows the ratio of the measured recoil electron day time and night time energy spectrum to the predicted spectrum. The numerical summary of the day time and the night time recoil electron energy spectrum is given in table G.3. Figure G.2 is the result of the data set III, and figure G.3 is the the results of the data set I,II.

## G.2 Oscillation analysis

Figure G.4 shows the comparison between day-night energy spectrum and the expected day-night spectrum for each allowed solution. The right figure is night time energy spectrum, and the left figure is day time energy spectrum.

When the combined constraints on neutrino oscillation is examined by the expected energy spectrum, $\chi^2$ is defined as follows:

$$\begin{aligned}
\chi^2 &= \sum_{i,j=1}^{N_{exp}} (R_i^{data} - R_i^{osc}) V_{i,j}^{-1} (R_j^{data} - R_j^{osc}) \\
&+ \sum_{i=1}^{n_{dn}} \sum_{i=1}^{n_{ene}} \Bigg\{ \frac{(\frac{Data}{SSM})_i^{data} - \frac{(\frac{Data}{SSM})_i^{exp}}{f_i^{corr}(\epsilon_{scl},\epsilon_{res},\epsilon_{b8})}}{\sigma_i} \Bigg\}^2 + \epsilon_{scl}^2 + \epsilon_{res}^2 + \epsilon_{b8}^2 \\
&+ \sum_{i=1}^{n_{ene}} \Bigg\{ \frac{(\frac{Data}{SSM})_i^{data} - \gamma \cdot \frac{(\frac{Data}{SSM})_i^{exp}}{f_i^{corr}(\epsilon_{scl},\epsilon_{res},\epsilon_{b8})}}{\sigma_i} \Bigg\}^2 + \epsilon_{scl}^2 + \epsilon_{res}^2 + \epsilon_{b8}^2 + \epsilon_{\gamma}^2 \qquad \text{(G.17)}
\end{aligned}$$

where $n_{dn}$ is the number of day and night bins, which is 2 in this analysis. Figure G.5 shows the comparison of the result for global analysis with SNO(CC) flux constraints between

| Energy | Data/SSM | Statistical error | Flux($\times 10^6/cm/s$) | Statistical error |
|---|---|---|---|---|
| Day | | | | |
| 4.5- 5.0 | 0.563 | +0.186-0.182 | 2.84 | +0.94-0.92 |
| 5.0- 5.5 | 0.448 | +0.091-0.088 | 2.26 | +0.46-0.44 |
| 5.5- 6.0 | 0.405 | +0.054-0.051 | 2.05 | +0.27-0.25 |
| 6.0- 6.5 | 0.519 | +0.048-0.045 | 2.62 | +0.24-0.22 |
| 6.5- 7.0 | 0.438 | +0.045-0.042 | 2.21 | +0.22-0.21 |
| 7.0- 7.5 | 0.462 | +0.048-0.045 | 2.33 | +0.24-0.22 |
| 7.5- 8.0 | 0.481 | +0.049-0.045 | 2.42 | +0.24-0.23 |
| 8.0- 8.5 | 0.424 | +0.050-0.046 | 2.14 | +0.25-0.23 |
| 8.5- 9.0 | 0.432 | +0.051-0.046 | 2.18 | +0.26-0.23 |
| 9.0- 9.5 | 0.440 | +0.055-0.050 | 2.22 | +0.28-0.25 |
| 9.5-10.0 | 0.531 | +0.062-0.055 | 2.68 | +0.31-0.28 |
| 10.0-10.5 | 0.683 | +0.075-0.067 | 3.45 | +0.38-0.34 |
| 10.5-11.0 | 0.428 | +0.069-0.059 | 2.16 | +0.34-0.29 |
| 11.0-11.5 | 0.576 | +0.087-0.074 | 2.91 | +0.44-0.37 |
| 11.5-12.0 | 0.424 | +0.091-0.074 | 2.14 | +0.46-0.37 |
| 12.0-12.5 | 0.516 | +0.112-0.090 | 2.60 | +0.56-0.45 |
| 12.5-13.0 | 0.567 | +0.147-0.115 | 2.86 | +0.74-0.58 |
| 13.0-13.5 | 0.251 | +0.144-0.094 | 1.27 | +0.72-0.47 |
| 13.5-14.0 | 0.379 | +0.192-0.122 | 1.91 | +0.97-0.61 |
| 14.0-20.0 | 0.531 | +0.175-0.128 | 2.68 | +0.88-0.65 |
| Night | | | | |
| 4.5- 5.0 | 0.726 | +0.169-0.166 | 3.66 | +0.85-0.84 |
| 5.0- 5.5 | 0.440 | +0.084-0.081 | 2.22 | +0.42-0.41 |
| 5.5- 6.0 | 0.468 | +0.053-0.050 | 2.36 | +0.26-0.25 |
| 6.0- 6.5 | 0.484 | +0.044-0.042 | 2.44 | +0.22-0.21 |
| 6.5- 7.0 | 0.452 | +0.044-0.041 | 2.28 | +0.22-0.20 |
| 7.0- 7.5 | 0.517 | +0.045-0.042 | 2.61 | +0.23-0.21 |
| 7.5- 8.0 | 0.487 | +0.046-0.043 | 2.46 | +0.23-0.21 |
| 8.0- 8.5 | 0.420 | +0.047-0.043 | 2.12 | +0.23-0.22 |
| 8.5- 9.0 | 0.504 | +0.051-0.047 | 2.54 | +0.25-0.23 |
| 9.0- 9.5 | 0.512 | +0.054-0.050 | 2.58 | +0.27-0.25 |
| 9.5-10.0 | 0.536 | +0.059-0.053 | 2.70 | +0.30-0.27 |
| 10.0-10.5 | 0.494 | +0.063-0.056 | 2.49 | +0.32-0.28 |
| 10.5-11.0 | 0.381 | +0.064-0.056 | 1.92 | +0.32-0.28 |
| 11.0-11.5 | 0.403 | +0.072-0.061 | 2.03 | +0.36-0.30 |
| 11.5-12.0 | 0.406 | +0.082-0.067 | 2.05 | +0.41-0.34 |
| 12.0-12.5 | 0.466 | +0.104-0.083 | 2.35 | +0.52-0.42 |
| 12.5-13.0 | 0.499 | +0.127-0.100 | 2.51 | +0.64-0.50 |
| 13.0-13.5 | 0.552 | +0.166-0.124 | 2.78 | +0.84-0.62 |
| 13.5-14.0 | 0.444 | +0.196-0.130 | 2.24 | +0.98-0.65 |
| 14.0-20.0 | 0.709 | +0.176-0.138 | 3.58 | +0.89-0.69 |

Table G.3: The numerical summary of the day time and the night time recoil electron energy spectrum.

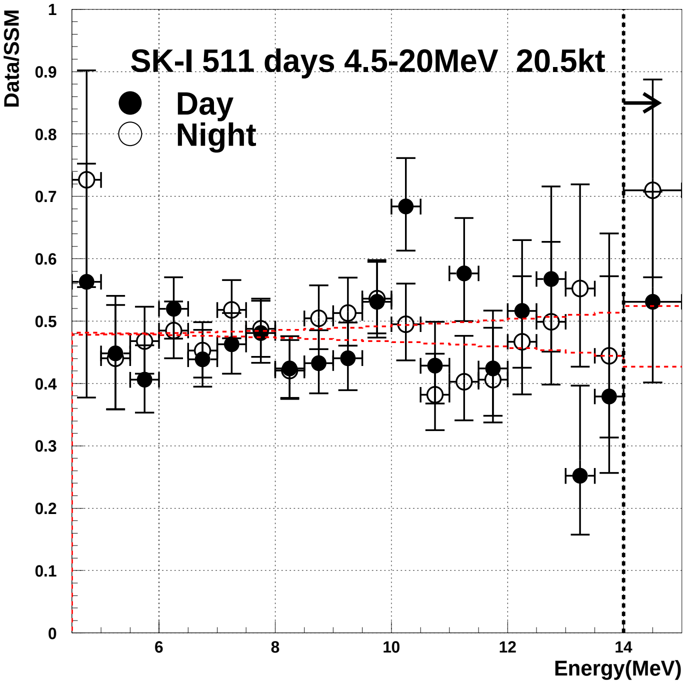

Figure G.2: The ratio of the measured day time and night time energy spectrum to the predicted spectrum. The error bars shows the total errors including systematic error and statistical errors. The dashed line shows the systematic errors for the predicted $^8$B spectrum including energy resolution, energy scale resolution and uncertainty for $^8$B spectrum.

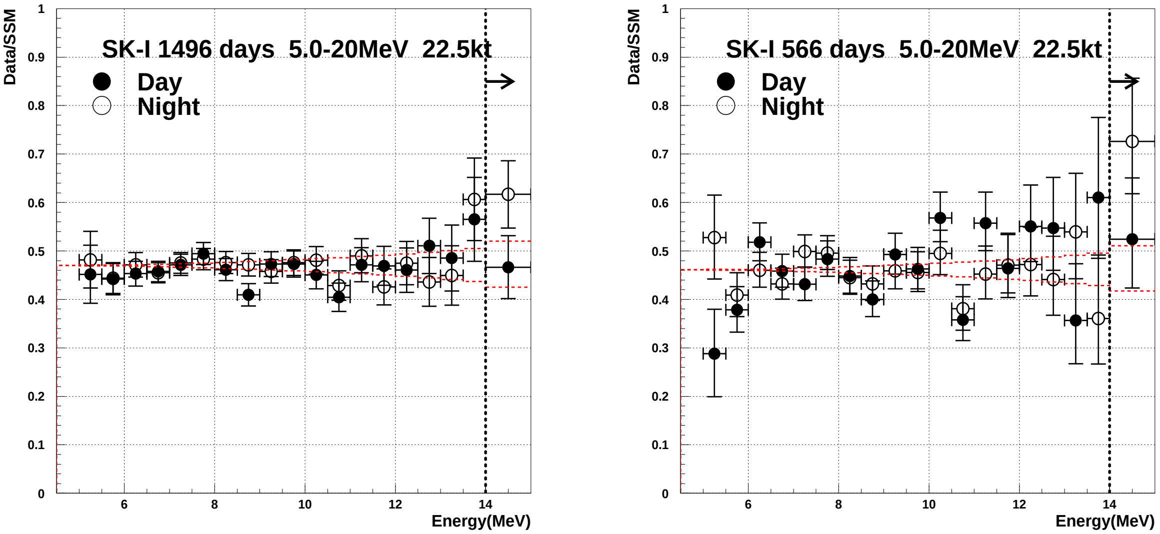

Figure G.3: The definition in the figure is same as figure G.2. The left plot is the result of the data set I (1496 days). The right plot shows the results of the data set II (566 days, no tight data reduction).

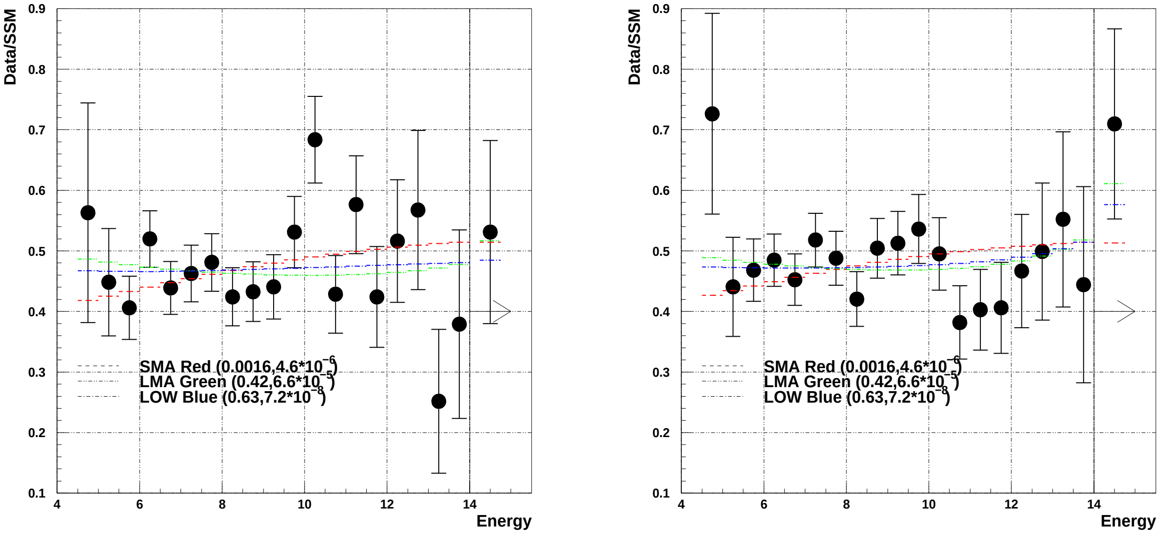

Figure G.4: The comparison between day-night energy spectrum and the expected day-night spectrum for each allowed solution.

the data set III without 4.5∼5.0 MeV data and the data set IV with 4.5∼5.0 MeV data using day-night energy spectrum. The difference is just number of bins Green area in the contour plot indicates allowed area by constraints from the flux measurements of all solar neutrino experiments. Orange area in the contour plot indicates allowed area by constraints from the energy spectrum measurements by SSM independent analysis. Sky blue area in the contour plot indicates allowed area by constraints from the energy spectrum measurements by SSM dependent analysis (flux(rate) constrained by SNO(CC) result).

The allowed region in SMA solution becomes small by 4.5∼5.0 MeV data. Then, the allowed region by day-night energy spectrum with SSM independent analysis disappeared by 4.5∼5.0 MeV data. It also became small in LMA region.

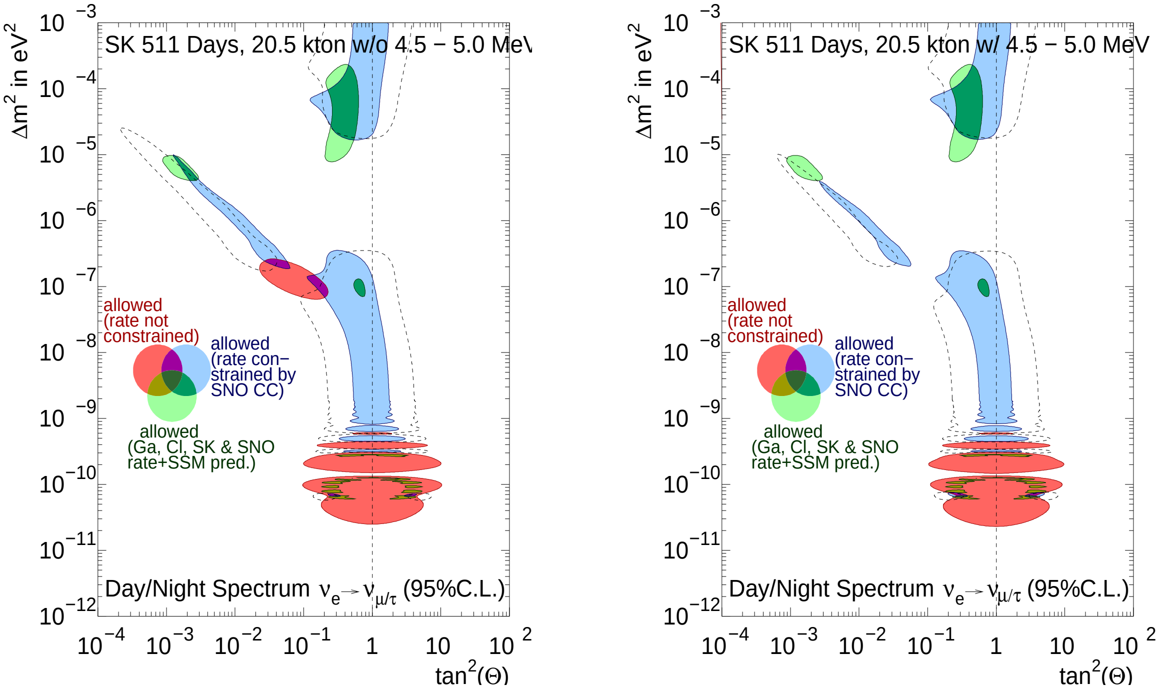

Figure G.5: The comparison of result for global analysis with SNO(CC) flux constraints between the data set III without 4.5∼5.0 MeV data and the data set IV with 4.5∼5.0 MeV data.

# Bibliography

[1] Y. Fukuda, *et al.*, (The Super-Kamiokande Collaboration), Nucl. Instr. & Meth. A 501 418-462 (2003)

[2] Y. Fukuda, *et al.*, (The Super-Kamiokande Collaboration), Phys. Lett. B539 (2002) 179-187

[3] Y. Fukuda, *et al.*, (The Super-Kamiokande Collaboration), Phys. Rev. Lett. 77 (1996) 1683

[4] K. Hirata, *et al.* (Kamiokande-II Collaboration), Phys. Rev. Lett. 63 (1989) 16

[5] Y. Fukuda, *et al.*, (The Super-Kamiokande Collaboration), Phys. Rev. Lett. 86 (2001) 5651-5655

[6] Y. Fukuda, *et al.*, (The Super-Kamiokande Collaboration), Phys. Rev. Lett. 86 5656-5660 (2001)

[7] Y. Fukuda, *et al.*, (The Super-Kamiokande Collaboration), Phys. Rev. Lett. 82 (1999) 2430-2434

[8] Davis, R., Phys. Rev. Lett. 12 (1964) 303-305

[9] Davis, Raymond, Jr., Harmer, Don S., Hoffman, Kenneth C., Phys. Rev. Lett. 20 (1968) 1205-1209

[10] Davis, R., Prog. Part. Nucl. Phys. 32 (1994) 13-32

[11] Cleveland, Bruce T., *et al.*, Astrophys. J. 496 (1998) 505-526

[12] M. Altmann, *et al.*, (GNO-Collaboration), Physics Letters B 490(1-2) (2000) 16-26

[13] E. Bellotti, Nuclear Physics B (Procceedings Supplements) 91(1-3) (2000) 44-49

[14] Hampel, W. *et al.* (GALLEX Collaboration), Phys. Lett. B447 (1999) 127-133.

[15] Hampel, W. *et al.* (GALLEX Collaboration), Phys. Lett. B388 (1996) 384-396.

[16] Anselmann, P. *et al.* (GALLEX Collaboration), Phys. Lett. B357 (1995) 237-247.

[17] Anselmann, P. *et al.* (GALLEX Collaboration), Phys. Lett. B314 (1993) 445-458.

[18] Anselmann, P. *et al.* (GALLEX Collaboration), Phys. Lett. B285 (1992) 376-389.

[19] W. Hampel *et al.* Physics Letters B 420(1-2) (1998) 114-126

[20] K. Eguchi *et al.* (KamLAND Collaboration), Phys. Rev. Lett. 90 (2003) 021802

[21] Abdurashitov, J. N. *et al.* (SAGE Collaboration), Phys. Rev. C60 (1999) 055801

[22] Abazov, A. I. *et al.*, Phys. Rev. Lett. 67 (1991) 3332-3335.

[23] Abdurashitov, J. N. *et al.* (SAGE Collaboration), Phys. Rev. C59 (1999) 2246-2263

[24] Abdurashitov, Dzh. N. *et al.*, Phys. Rev. Lett. 77 (1996) 4708-4711.

[25] Ahmad, Q. R. *et al.* (SNO Collaboration), Phys. Rev. Lett. 89 (2002) 011302

[26] Ahmad, Q. R. *et al.* (SNO Collaboration), Phys. Rev. Lett. 89 (2002) 011301

[27] Ahmad, Q. R. *et al.* (SNO Collaboration), Phys. Rev. Lett. 87 (2001) 071301

[28] Dick, R.H., J.R. Kuhn, and K.G. Libbrecht Nature, 316, (1985) 687

[29] J.N Bahcall, M.H. Pinosonneault, and S. Basu, Astrophys.J. 555, (2001) 990 (BP2000)

[30] S. Turck-Chieze *et al.*, Astrophys. J. 555, (2001) L69

[31] A.R. Junghans *et al.*, Phys. Rev. Lett. 88, (2002) 041101

[32] J.N Bahcall, M.C. Gonzalez-Garcia, and C. Pena-Garay, JHEP 0204, 007 (2002).

[33] C.A Iglesias and F.J. Rogers, Astrophys.J. 371 (1991) 408

[34] Frohlich, C., Lean, J., Geophysical Research Letters 25, (1998) 4377

[35] Frohlich, C., Crommelynck et al. Solar Phys., 162 (1995) 101

[36] J.N.Bahcall and M.H.Pinsonneault 1992, Rev. Mod. Physics, 64, 885.

[37] Adelberger EG, *et al.*, Rev. Mod. Phys. 70, (1998) 1265

[38] Gruzinov, J.N. Bahcall, Astrophys.J. 504 (1998) 996-1001

[39] Salpeter, E.E., Australian Journal of Physics 7, (1954) 373

[40] Thoul, A. A., Bahcall, J. N., and Loeb, A.: ApJ 421, (1994) 828

[41] Bahcall J.N., Pinsonneault M.H., Rev. Mod. Phys. 67, (1995) 781

[42] Turcotte S., Richer J., Michaud G., ApJ 504, (1998) 559 NASA ADS

[43] Grevesse, N. & Suaval, A. J., Space Sci Rev, 85, (1998) 161

[44] Bahcall J.N., Pinsonneault M.H., Rev. Mod. Phys. 67, (1995) 781

[45] J.N. Bahcall Phys. Rev. D, 49, No. 8, (1994) 3923

[46] J.N. Bahcall Phys. Rev. C, 56, No. 6, (1997) 3391

[47] J.N. Bahcall, L. Lisi, D.E. Alburger, *et al.* Phys. Rev. C, 54, (1996) 411

[48] Bahcall, J. N., & Pinsonneault, M. H. Rev. Mod. Phys., 67, (1995) 781

[49] Thoul, A. A., Bahcall, J. N., & Loeb, A. ApJ, 421, (1994) 828

[50] Bahcall, J. N., & Pinsonneault, M. H. Rev. Mod. Phys., 64, (1992) 885

[51] Grevesse, N. Phys. Scripta, T8, (1984) 49

[52] Grevesse N., & Noels A. 1993, in Origin and Evolution of the Elements, ed. N. Prantzos, E. Vangioni-Flam, & M. Cass (Cambridge: Cambridge University Press)

[53] Grevesse, N., & Sauval, A. J. Space Sci. Rev., 85, (1998) 161

[54] Bahcall, J. N., & Ulrich, R. K. Rev. Mod. Phys., 60, (1988) 297

[55] J. Napolitano, S.J. Freedman, and J. Camp, Phys. Rev. C 36 (1987) 298

[56] D.H. Wilkinson and D.E. Alburger, Phys. Rev. Lett. 26, (1971) 1127

[57] B.J. Farmer and C.M. Class, Nucl. Phys. 15. (1960) 626

[58] L. De Braeckeleer and D. Wright (unpablished data), as quated in L. De Braeckeleer *et al.*, Phys. Rev. C 51, (1995) 2778

[59] J.N. Bachall and M.H.Pinsonneault, Rev. Mod. Phys. 67, (1995) 781

[60] J.N Bahcall, S. Basu, MH Pinsonneaul Phys. Lett. B, 433, (1998) 1-8

[61] Basu, S., *et al.*, MNRAS, 292, (1997) 243

[62] Basu, S., Pinsonneault, M.H., & Bahcall, J.N. ApJ, 529, (2000) 1084 (BPB00)

[63] J. Bahcall, S. Basu and M. Pinsonneault, Phys. Lett. B433, (1998) 1

[64] Marcucci, L. E., Schiavilla, R., Viviani, M., Kievsky, A., & Rosati, S. Phys. Rev. Lett., 84, (2000a) 5959

[65] W. Hamptel and L. P. Remsberg, Phys. Rev. C31, (1985) 666

[66] W. Hamptel et al., Phys. Lett. B420, (1998) 114

[67] J.N. Bachall. and U.K. Urrich, Rev. Mod. Phys. 60, (1988) 297

[68] W. Hamptel et al., Phys. Lett. B447, (1999) 127

[69] J.N. Bachall, Phys. Rev. C56, (1997) 3391

[70] T.Kajita, talk at *"XVIII International Conference on Neutrino Physics and Astrophysics"* (1998)

[71] Felix Boehm and Petr Vogel "*Physics of Massive Neutrinos*" (Cambridge 1987) p146

[72] M.Fukugita and A.Suzuki, "*Physics and Astrophysics of Neutrinos*", (Springer-Verlag, 1994)

[73] D.L.Anderson, "*Theory of the Earth*" (Blackwell scientific publication, 1989)

[74] J.N Bachall, P.I. Krastev, and Ayu. Smirnov, JHEP05, 015, (2001)

[75] "Physicas and Astrophysics of Neutrinos", edited by M.Fkukugita and A. Suzuki, Springer-Verlag.

[76] Eric G. Adelberger *et al.*, Rev. Mod. Phys., 70, (1998) 1265-1292

[77] J.N.Bahcall, M.Kamionkowski, and A.Sirlin, Phys.Rev.D 51 (1995) 6146

[78] H.Ikeda,*et.al*, Nucl.Instr.and.Meth.,A320 (1992) 310

[79] T.Tanimori, *et.al*, IEEE Tran.on.Nucl.Sci 36 (1989) 497

[80] A.Morel, *et.al*, Limnology and Oceanography 22 (1977) 709

[81] I.Thorm äheln, K.Scheffler, and J.Scaub, in *Water and Steam*, Proceedings of the 9th ICPS (Pergamon, Oxford, 1980)

[82] A.Suzuki *et.al* Nucl.Instr.and Meth.,A329 (1993) 299

[83] W. Y. Chang, M. Goldhaber, R. Sagane, *Nature* **139** (1937) 962.

[84] V. McLane, C.L. Dunford, P.F. Rose, *Neutron Cross Sections, Vol. 2* (Academic Press, Boston, 1982) 48.

[85] R. B. Firestone, *Table Of Isotopes, Vol. 1* (John Wiley and Sons, New York, 1996) 20.

[86] E. D. Carlson, Phys. Rev. D 34, (1986) 1454
J. Bouchez *et al.*, Z. Phys. C32, (1986) 499

[87] J.N. Bachall, "Neutrino Astrophysics", Cambridge University, Cambridge (1998)

[88] Klaus. Winter, "Neutrino Physics", Cambridge University, Cambridge (2000)

[89] Thomas. K. Gaisser, "Cosmic Rays and Particle Physics", Cambridge University, Cambridge (1990)

[90] L. LYONS, "Statistics for nuclear and particle physicists" Cambridge university, Cambridge

[91] GEANT Detector Description and Simulation Tool, Cern Program Library W5013, (1994)

[92] William H. Press, "Numerical Recipes in FORTRAN 77", Cambridge University, Cambridge (1993)

[93] K. Hagiwara et al.l. (particle Data Group), Phys. Rev. D 66, 010001 (2002) (URL: http://pdg.lbl.gov)

[94] M. Nemoto, Master theisis, Tokai University (1998) (unpublished)

[95] C. Mitsuda, Master theisis, Niigata University (2000) (unpublished)

[96] Yusuke Koshio, PhD Thesis, University of Tokyo, Apr. 1998

[97] Measurement of the solar neutrino energy spectrum at Super-Kamiokande Hirokazu Ishino, PhD Thesis, University of Tokyo, Jan. 1999

[98] Nobuyuki Sakurai, PhD Thesis, University of Tokyo, Dec 2000

[99] Y.Koshio, master thesis, Tokyo University (1994) (unpublished)

[100] Y. Fukuda, *et al.*, (The Super-Kamiokande Collaboration), Phys. Lett. 452 (1999) 418-422

[101] Y.Takeuchi, *et al.*, Nucl. Instr. & Meth. A421 (1999) 334-341

[102] C.Mitsuda, *et al.*, Nucl. Instr. & Meth. A 497 (2003) 414-428

[103] Y. Fukuda, *et al.*, (The Super-Kamiokande Collaboration), Nucl. Instr. & Meth. A 458 (2001) 636-647

[104] Y. Fukuda, *et al.*, (The Super-Kamiokande Collaboration), Nucl. Instr. Meth. A421 (1999) 113-129

[105] M. Nakahata, private communication